RUHR-UNIVERSITÄT BOCHUM

RUB

Variational modeling of martensitic phase transformations

Philipp Junker

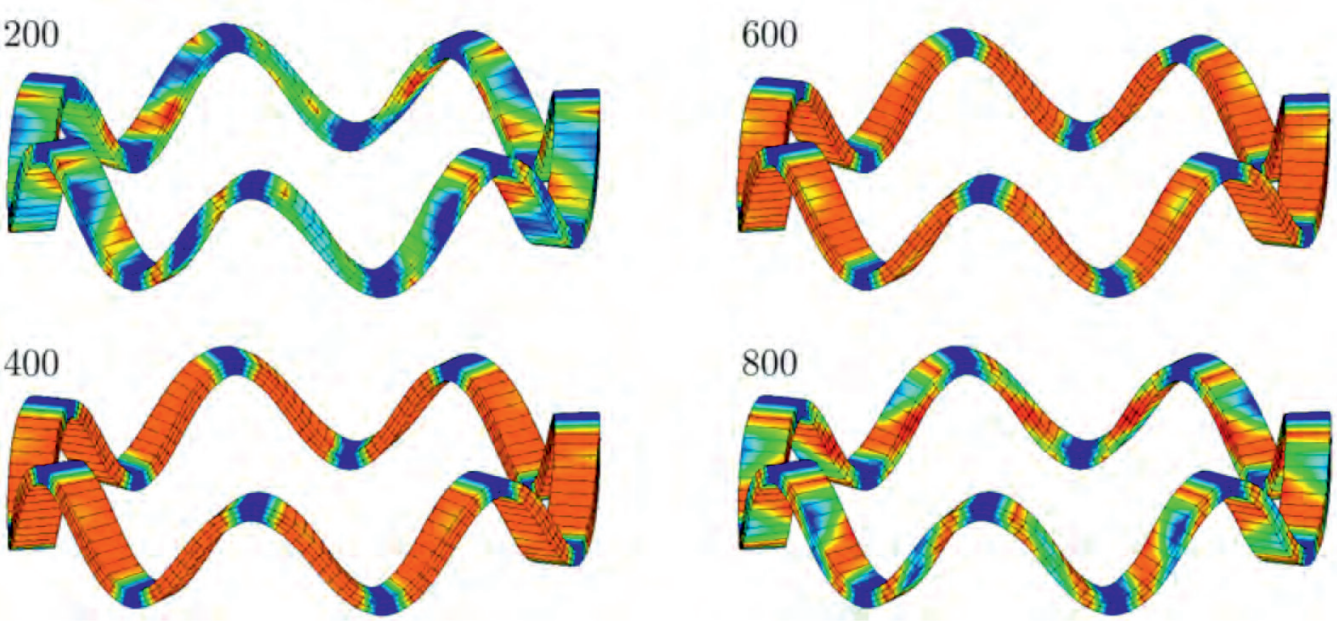

Variational Modeling of Martensitic Phase Transformations

—

Hamiltonian Principles, Experimental Validation, Numerical Approaches

als

Habilitationsschrift

vorgelegt der

Fakultät für Maschinenbau

an der

Ruhr-Universität Bochum

von

Dr.-Ing. Philipp Junker,
geb. 31.05.1983 in Bochum

Bochum 2016

— colored version online —

Contents

1 Introduction

1.1 Motivation and objectives

Phase transformation in solids are a topic of active research with a particular focus on shape memory alloys. This class of materials is characterized by the unique capability of *reversible* phase transitions that are also *mechanically* induced which is a strong deviation from regular metals. Here, "reversible" transformations in between the crystallographic phases austenite, martensite, ferrite, and bainite are induced *thermally*, a mechanical transformation e.g. in TRIP-steels (transformation induced plasticity) is permanent.

Shape memory alloys, in contrast, possess transformation strains, from austenite to variants of martensite and from one martensitic configuration to a different one, that are (nearly) volume preserving (e.i. the transformation strains are traceless). This capability allows for reversible phase transformations also during mechanical loads. This effect on the microstructural scale shows simultaneously a great influence on the macroscopic behavior of entire construction parts that are made of shape memory alloys: they are able to sustain large strains in a reversible way which opens a wide field of industrial applications such as medical engineering, actuator engineering, and aeronautics. However, the specific material reaction strongly depends both on the applied external loads and the ambient temperature. This complex thermo-mechanical coupling makes a precise, reliable, and predictive knowledge of the specific expected material behavior highly appreciated.

A famous tool in engineering is the application of simulation software which allows for a virtual investigation of the behavior of a construction part. This lowers the amount of experiments which in return reduces the necessary time for prototyping and hence costs. Most simulation software for the described purpose is based on a finite element calculation which essentially solves the balance of linear momentum in a numerical way. However, it remains to find a solution for the basic problem: the system of equations, that is given by the physical balance laws for mass, energy, and momentum and the entropy inequality, is undetermined. It is thus necessary to close it by postulating appropriate constitutive laws that interrelate mechanical strains to mechanical stresses in a material-dependent way. These material laws are thus also referred to as material models.

Various strategies exist for the derivation of material models. Most importantly, it is demanded that these models agree with the First and Second Law of Thermodynamics which is, obviously, a rather soft limitation for modeling techniques, and it is Hooke's law which is the most famous model that fulfills the aforementioned requirements. However, materials with a more complex behavior than a proportional relation between strains and stresses have to be treated in more sophisticated ways. For instance, rheological approaches model non-linear materials by application of so-called Hooke elements (springs), Newton elements (dampers), and St.-Venant elements (friction) which provide in a material-dependent way stresses as a direct function of strains.

A different strategy of modeling complex material behavior is the introduction of so-called internal variables which describe the changes of the underlying microstructure in time. Thereby, they can be interpreted in a physical sense and referred to experimental observations. In contrast to the rheological

approaches, an explicit formulation of the stresses $\boldsymbol{\sigma}$ follows directly from

$$\boldsymbol{\sigma} = \frac{\partial \Psi}{\partial \boldsymbol{\varepsilon}} \tag{1.1}$$

which is a result from the Second Law of Thermodynamics. Here, Ψ is the Helmholtz free energy (which is specified later) and $\boldsymbol{\varepsilon}$ are the strains. This relation is of great benefit since the Helmholtz free energy is a scalar-valued quantity and thus the inclusion of an orientation-dependent information is not possible at first glance. Consequently, if the "correct" energy has been found, stresses in all possible orientations can be derived consistently. On the other hand, the introduction of additional unknowns in terms of internal variables requires the formulation of equations that exactly describe the evolution of the internal variables in time and hence close the system of equations, e.g. by

$$\dot{\boldsymbol{\upsilon}} = f(\boldsymbol{\varepsilon}, \theta, \boldsymbol{\upsilon}, \dots) \tag{1.2}$$

which has to be specified for each material considered (θ is the temperature). The internal variable is denoted by $\boldsymbol{\upsilon}$ which has been assumed possessing tensor-valued dimension for sake of generality. The time derivative is indicated by $\dot{\boldsymbol{\upsilon}}$ for which these equations are usually referred to as evolution equations. In this regard, several different approaches are possible. For instance, a rate-dependent formulation constitutes as

$$\dot{\boldsymbol{\upsilon}} = \frac{1}{r_{\mathrm{v}}} \boldsymbol{p} \tag{1.3}$$

with a viscous parameter r_{v} and the thermodynamical driving forces $\boldsymbol{p} = -\partial \Psi / \partial \boldsymbol{\upsilon}$. Another famous example are rate-independent evolution equations

$$\dot{\boldsymbol{\upsilon}} = \underbrace{\frac{|\dot{\boldsymbol{\upsilon}}|}{r_{\mathrm{y}}}}_{=:\rho} \frac{\partial \phi}{\partial \boldsymbol{p}} \tag{1.4}$$

with a consistency parameter $\rho \geq 0$, a yield function $\phi = |\boldsymbol{p}| - r_{\mathrm{y}} \leq 0$ which indicates microstructural change only for $\phi = 0$ and the Kuhn-Tucker condition $\rho \phi = 0$. The parameter r_{y} indicates a yield criterion which is, again, a material-dependent quantity.

Modeling approaches of these fundamental form have been presented for a huge variety of material classes in literature. They are very successful for realistic and reliable modeling and consequently simulation of construction parts of different kinds. However, it can be problematic to directly derive evolution laws for materials in which internal variables have to fulfill complicated constraints (e.g. mass conservation): in these cases, the sole use of the driving forces as presented in Eqs. (1.3) and (1.4) is not sufficient and the postulation of the yield function ϕ is much more sophisticated. Additionally, the calibration of those direct models is sometimes difficult and a predictive character cannot be guaranteed. Fortunately, these limitations can be avoided by a variational-based treatment of the concept of internal variables. The entire process is described here in energetic terms which are orientation-independent quantities. Thus, if a calibration of such an energy-based description is able to display the experimentally observed material behavior correctly (which depends on the orientation, e.g. in terms of loads or microstructures), it can be assumed that the material model is also able to display the material behavior in other directions. This property is referred to as universality.

The objective of this thesis is the presentation of the benefits of variational material modeling by application to shape memory alloys. A brief introduction to variational calculus and to variational modeling is given below to ground a methodical basis. After these brief technical preliminaries, nine

chapters follow which show a continuous evolution of the modeling and simulation of shape memory alloys using variational techniques. Each of the chapters has been published as one scientific publication in renowned journals and thus passed through an evaluation process of the experts' community. A detailed list of the individual chapters along with a short summary is given in the following.

- Chapter 2: P. Junker, K. Hackl:
  Finite element simulations of poly-crystalline shape memory alloys based on a micromechanical model, Comput. Mech. **47(5)**: 505–517 (2011).
  This chapter presents the implementation of an existing variational material model into a finite element routine in which it is analyzed for construction parts for the first time. Several different boundary value problems are solved and a detailed inspection of the material behavior is carried out. To this end, the orientation distribution function is evaluated at different material points within the specimens and the influence of pre-texture is investigated.
  ▶ *PJ implemented the material model, produced all simulation results and wrote the vast majority of the publication.*

- Chapter 3: P. Junker, K. Hackl:
  A thermo-mechanically coupled field model for shape memory alloys, Continuum Mech. Therm. **26(6)**: 859–877 (2014).
  This chapter provides a different variational approach to the modeling of shape memory alloys. This approach, termed the principle of maximum dissipation, allows for the thermo-mechanically coupled modeling of phase transformations. Furthermore, the model is equipped by a localization aspect which in turn requires a regularization of the underlying energy. Along with the temperature field, which is computed in parallel to the displacement field and the regularizing field variable, a much more sophisticated finite element implementation is employed. Furthermore, a first attempt is presented on the estimation of the energetic material parameter indicating phase transformations based on experiments.
  ▶ *PJ derived the material model, including the estimation of the material parameter, and the finite element procedure, implemented it, performed all simulations and wrote the vast majority of the publication.*

- Chapter 4: P. Junker, K. Hackl:
  About the influence of heat conductivity on the mechanical behavior of poly-crystalline shape memory alloys, Int. J. Struct. Changes Sol. **3**: 49–62 (2011).
  This chapter builds on the previous model by inspecting here the interrelation between phase transformations and temperature to a greater degree. The latent heat produced by the phase transformations serves as a heat source or a heat sink. The temperature increase or decrease, respectively, modifies the caloric energy of the material and thus stabilizes or destabilizes the austenite phase. This, in turn, influences the thermodynamic driving force and damps or amplifies the phase transformation locally. The result are multiple transformation fronts and a complex thermo-mechanically coupled material behavior.
  ▶ *PJ derived the material model, implemented it, performed all simulations and wrote the vast majority of the publication.*

- Chapter 5: P. Junker:
  A Novel Approach to Representative Orientation Distribution Functions for Modeling and Simulation of Polycrystalline Shape Memory Alloys, Int. J. Numer. Meth. Eng. **98 (11)**: 799–818 (2014).
  This chapter presents a novel parameterization of the martensite strain orientation distribution

function. In contrast to the models used before, the orientation distribution function is not discretized in a static manner with a large amount of different discretized directions any more: Euler angles are introduced that allow for a dynamic (i.e. time-dependent) description of the orientation distribution function. This reduces the amount of necessary internal variables drastically and thus increases the calculation velocity by a factor of ten. Several examples for different initial values of the Euler angles are investigated for the shape memory alloys CuAlNi and NiTi. It closes with a comparison to the previous material model.
▶ *PJ is the sole author of the publication and thus responsible for the entire content.*

- Chapter 6: P. Junker, J. Makowski, K. Hackl:
The Principle of the Minimum of the Dissipation Potential for Non-Isothermal Processes, Continuum Mech. Therm. **26 (3)**: 259–268 (2014).
This chapter presents an enhancement of the variational principle of the minimum of the dissipation potential such that it is applicable to non-isothermal processes. In this regard, a unified and generalized heat conduction equation is derived in which the microstructural evolution of a material contributes to the generation of heat. Starting with thermodynamic fundamentals, the principle of the minimum of the dissipation potential is generalized and a unified variational framework for the derivation of thermo-mechanically coupled material models is established. The examples of plasticity and shape memory alloys are presented for demonstration purposes. They show that this novel approach yields much simpler equations compared to the principle of maximum dissipation and furthermore allows for a more intuitive physical interpretation.
▶ *PJ set up the general idea, derived all equations and wrote the vast majority of the publication.*

- Chapter 7: P. Junker, K. Hackl:
A condensed variational model for thermo-mechanically coupled phase transformations in polycrystalline shape memory alloys, J. Mech. Behav. Mat. **22 (3-4)**: 111–118 (2013).
This chapter employs the principle of the minimum of the dissipation potential for non-isothermal processes to the novel representation of the martensite strain orientation distribution function introduced in Chapter 5. The evolution equations for the crystallographic phases and the Euler angles are derived. Simultaneously, the unified heat conduction equation from Chapter 6 is specified for shape memory alloys. Numerical examples are presented for material point investigations. In this case, the time discretization results in a time-independent material behavior. To still show the influence of different loading conditions, the value for the heat capacity is varied. This treatment is not necessary if the gradient term does not vanish and the time-dependence is directly included. Variation of the value of heat capacity immediately shows that the formation of martensite is delayed for higher loading velocities which results in an increase of stresses instead of the plateau during phase transformation. Thus, the impact of thermal coupling is displayed well by the new material model.
▶ *PJ derived the material model, produced all numerical results and wrote the vast majority of the publication.*

- Chapter 8: P. Junker, S. Jaeger, O. Kastner, G. Eggeler, K. Hackl:
Variational prediction of the mechanical behavior of shape memory alloys based on thermal experiments, J. Mech. Phys. Solids **80**: 86–102 (2015).
This chapter presents a huge progress both in the modeling of shape memory alloys and the fundamental understanding of variational modeling. The material model derived in Chapter 5 is investigated for purely temperature-induced phase transformations which allows for a relation between the caloric energy and the dissipation parameter which is a material-dependent quantity. DSC (differential scanning calorimetry) experiments are performed for Ni51Ti49 from which the

caloric energy can be determined and thus the dissipation parameter. This thermally calibrated set of material data is applied to finite element simulation of tensile test of specimens with different geometry and at various temperatures. A comparison between the predictive simulations and mechanical experiments for the same tensile tests reveals that there exists a nearly perfect agreement between simulation and reality. Beside this being a further remarkable improvement of the modeling of shape memory alloys, it also serves as first demonstration example that a unique calibration of variational material models is sufficient for a predictive simulation which separates this modeling technique from others.
▶ *PJ derived the material model, produced all numerical results and wrote the majority of the publication, except of Section 8.3 and Appendix A.1.*

- Chapter 9: P. Junker:
  An accurate, fast and stable material model for shape memory alloys, Smart Mater. Struct. **23 (11)**: 115010 (2014).
  This chapter presents a further improvement of the model derived in Chapter 5 concerning numerical efficiency and stability. A homogenization of the individual martensitic twins is employed which results in only three martensitic variants. Furthermore, the evolution equations are formulated in an elasto-viscoplastic manner which ensures a very high numerical stability. Simple formulas are derived which allow for a model calibration and parameter identification based on stress/strain diagrams for tensile test. Various boundary value problems are solved for combined mechanical and thermal boundary conditions.
  ▶ *PJ is the sole author of the publication and thus responsible for the entire content.*

- Chapter 10: J. Waimann, P. Junker, K. Hackl:
  A coupled dissipation functional for modeling the functional fatigue in polycrystalline shape memory alloys, Eur. J. Mech. A-Solid : *accepted for publication* (2015).
  This chapter presents the inclusion of plastic effects into the material model which has also been used in Chapter 2. Thus, the crystallographic phases and the plastic strains serve as internal variables for this model whereas the plastic strains are formulated for each phase in each direction. The model is equipped with phenomenological approaches for a load-dependent relation between dissipated energy and plastic strains. This results in a decrease of the transformation stress which hence changes the shape of the hysteresis in a stress/strain diagram. Various numerical examples are presented for a material point analysis showing how the model can be calibrated to experimental data.
  ▶ *PJ developed the fundamental idea, contributed to the writing of the publication and to the interpretation of the numerical results.*

The contents of the individual chapters were developed in the time interval between 2011 and 2015. The Chapters 2, 3 and 4 were (partly) developed and published during the time when PJ was a PhD student. They are presented in this thesis to present a smooth and comprehensive basis for the modeling and simulation of shape memory alloys using variational principles. The Chapters 5 to 10 were developed during the time when PJ was a group leader in which J. Waimann was one member. The thesis closes with conclusions and an outlook to future perspectives.

1.2 Brief introduction to variational calculus

1.2.1 Basics

Variational calculus allows for the elegant mathematical investigation of so-called functionals which are specified later. A very convincing treatise concerning variational calculus is given by Elsgolc in [46]. Struwe presents an application towards nonlinear partial differential equations in [175], and another standard textbook is the one by Dacorogna (see [37]). In this section, a brief introduction to variational calculus is given to establish the basis for the later fundamentals which serve as framework for the subsequent chapters.

A functional $\mathcal{F}$ is a function which relates a number to each function. A classical example is the length of a curve, given by

$$\mathcal{F} = \int_{x_0}^{x_1} \sqrt{1 + (f'(x))^2}\, \mathrm{d}x = \mathcal{F}[f(x)] \tag{1.5}$$

or the surface area

$$\mathcal{F} = \int_{\partial\Omega} \sqrt{1 + z_{,x}^2 + z_{,y}^2}\, \mathrm{d}A = \mathcal{F}[z(x,y)] \tag{1.6}$$

where partial derivatives are abbreviated by a comma ($\partial z/\partial x = z_{,x}$; see Figure 1.1).

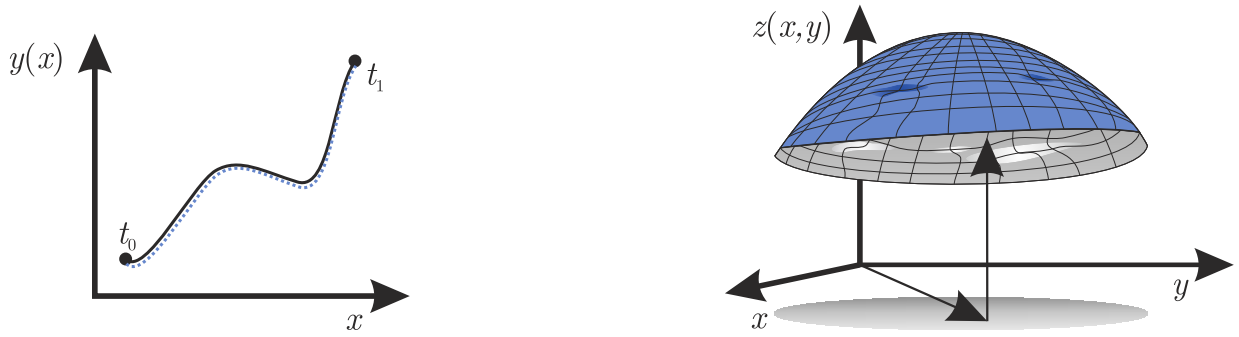

Figure 1.1: Two examples for functionals: length of a curve (left hand side) and surface area (right hand side).

The value of $\mathcal{F}$ obviously depends on the current function (here $f(x)$ or $z(x,y)$) for which it is evaluated. Although there are some similarities between functions and functionals, there also exist important differences. The properties of functionals can be compared to those of functions. This is carried out in Table 1.1.

1.2.2 The derivative as linear approximation

Scalar-valued functions A linearization of a function may be executed e.g. by application of a Taylor expansion. However, for an intuitive introduction to variational calculus, a modified approach is more suitable. First, a function $f(x)$ with $f : \mathbb{R} \to \mathbb{R}$ is investigated and the following coordinate transformation is employed

$$f(x) \to f(\bar{x} + \alpha\ \delta x) \tag{1.7}$$

functions	functionals
$f(x) = v$	$\mathcal{F}[f(x)] = w$
$x \mapsto v$	$f(x) \mapsto w$
f: function	$\mathcal{F}$: functional
x: variable	$f(x)$: function = "variable"
v: number	w: number
increment	variation of the argument
$\Delta x = x - x_0$	$\delta f = f(x) - f_0(x)$
$f(x)$ is continuous if small changes of x result in small changes in $f(x)$	$\mathcal{F}[f(x)]$ is continuous if small changes of $f(x)$ result in small changes in $\mathcal{F}[f(x)]$

Table 1.1: Properties of functions and functionals after [46].

Here, δx may be interpreted as a "normal vector" and α as the length in direction of δx, or equivalently as a coordinate transformation from x to δx. The quantity $\bar{x}$ serves as new origin. A plot is given in Figure 1.2. For the linearization around $\bar{x}$ the associated derivative is required which can be calculated by

$$\frac{\mathrm{d}}{\mathrm{d}\alpha} f(\bar{x} + \alpha\ \delta x)\Big|_{\alpha=0} = \lim_{\alpha \to 0} \frac{f(\bar{x} + \alpha\ \delta a) - f(\bar{x})}{\alpha} = f'(\bar{x})\ \delta x =: \mathrm{D}f(\bar{x})(\delta x) \tag{1.8}$$

Finally, the linearized form for $f(x)$ around $\bar{x}$ reads

$$\mathrm{L}f(\bar{x})(\delta x) = f(\bar{x}) + \mathrm{D}f(\bar{x})(\delta x) = f(\bar{x}) + f'(\bar{x})\ \delta x \tag{1.9}$$

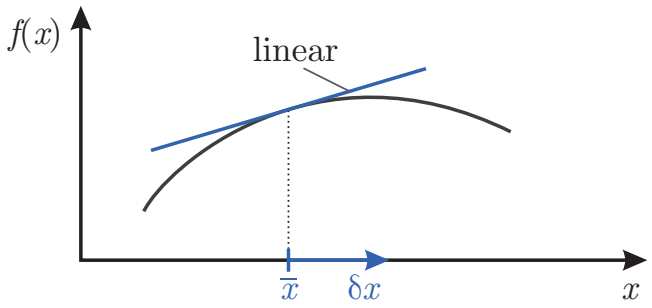

Figure 1.2: Linear approximation of a function $f(x)$ in point $\bar{x}$ and new direction δx.

For a function g that maps from the $\mathbb{R}^n$ to the $\mathbb{R}$, $g : \mathbb{R}^n \to \mathbb{R}$, a similar procedure is employed. It holds

$$g(\boldsymbol{x}) \to g(\bar{\boldsymbol{x}} + \alpha\ \delta \boldsymbol{x}) \tag{1.10}$$

and the derivative is calculated analogously by

$$\frac{\mathrm{d}}{\mathrm{d}\alpha} g(\bar{\boldsymbol{x}} + \alpha\ \delta \boldsymbol{x})\Big|_{\alpha=0} = \lim_{\alpha \to 0} \frac{g(\bar{\boldsymbol{x}} + \alpha\ \delta \boldsymbol{x}) - g(\bar{\boldsymbol{x}})}{\alpha} = \sum_i \frac{\partial g}{\partial x_i} \delta x_i = \nabla g \cdot \delta \boldsymbol{x} =: \mathrm{D}g(\bar{\boldsymbol{x}})(\delta \boldsymbol{x}) \tag{1.11}$$

with the gradient ∇g. Hence, the linearization is given by

$$\mathrm{L}g(\bar{\boldsymbol{x}})(\delta\boldsymbol{x}) = g(\bar{\boldsymbol{x}}) + \mathrm{D}g(\bar{\boldsymbol{x}})(\delta\boldsymbol{x}) = g(\bar{\boldsymbol{x}}) + \nabla g \cdot \delta\boldsymbol{x} \tag{1.12}$$

Vector functions A similar approximation is now applied to vector functions, thus $\boldsymbol{f} : \mathbb{R}^n \to \mathbb{R}^m$. Again, it holds

$$\boldsymbol{f}(\boldsymbol{x}) \to \boldsymbol{f}(\bar{\boldsymbol{x}} + \alpha\ \delta\boldsymbol{x}) \tag{1.13}$$

and the derivative reads

$$\frac{\mathrm{d}}{\mathrm{d}\alpha}\boldsymbol{f}(\bar{\boldsymbol{x}} + \alpha\ \delta\boldsymbol{x})\Big|_{\alpha=0} = \left(\frac{\partial f_i}{\partial x_j}\delta x_j\right) = \boldsymbol{J}\cdot\delta\boldsymbol{x} =: \mathrm{D}\boldsymbol{f}(\bar{\boldsymbol{x}})(\delta\boldsymbol{x}) \tag{1.14}$$

where the Jacobian

$$\boldsymbol{J} := \nabla \otimes \boldsymbol{f} = \nabla\boldsymbol{f} = \left(\frac{\partial f_i}{\partial x_j}\right) = \frac{\partial f_i}{\partial x_j}\boldsymbol{e}_i\boldsymbol{e}_j \tag{1.15}$$

has been introduced. The linearization is given by

$$\mathrm{L}\boldsymbol{f}(\bar{\boldsymbol{x}})(\delta\boldsymbol{x}) = \boldsymbol{f}(\bar{\boldsymbol{x}}) + \mathrm{D}\boldsymbol{f}(\bar{\boldsymbol{x}})(\delta\boldsymbol{x}) = \boldsymbol{f}(\bar{\boldsymbol{x}}) + \boldsymbol{J}\cdot\delta\boldsymbol{x} \tag{1.16}$$

Thus, in all cases a derivative evaluated in *point* $\bar{x}$ and *direction* δx is present in terms of the "directional derivatives" $f'(\bar{x})\ \delta x$, $\nabla f(\bar{\boldsymbol{x}})\cdot\delta\boldsymbol{x}$, and $\boldsymbol{J}(\bar{\boldsymbol{x}})\cdot\delta\boldsymbol{x}$, respectively. This procedure can now be expanded to the application on functionals.

1.2.3 Gâteaux derivative and stationary point

A functional maps a function, which is characterized by its specific function space, to a number, thus $\mathcal{F} : H^p \to \mathbb{R}$. For this thesis the use of the Sobolev space H^p as function space is sufficient. It is defined by

$$H^p(\Omega,\mathbb{R}) := \left\{ f : \Omega \to \mathbb{R} \;\middle|\; |f|_r < \infty,\ \text{with } 0 \le r \le p \right\} \tag{1.17}$$

where the Sobolev semi norm[1]

$$|f|_r := (f,f)_r^{1/2} \qquad \text{with } (f,f)_r = \int_\Omega \left(\frac{\partial^r f}{\partial x^r}\right)^2 \mathrm{d}x \tag{1.18}$$

is introduced.

Analogously to the previous section, the derivative of the functional $\mathcal{F}$ is required for the linearization. However, it is not immediately obvious how a derivative of a functional, thus a function which depends on functions, has to be calculated. To solve this problem, the former notation is employed. Then, a functional is called Gâteaux differentiable in *point* $\bar{f}$ and in *direction* δf

$$:\Longleftrightarrow \quad \exists \quad \mathrm{D}\mathcal{F}[\bar{f}](\delta x) := \lim_{\alpha\to 0}\frac{\mathcal{F}[\bar{f}+\alpha\ \delta f] - \mathcal{F}[\bar{f}]}{\alpha} \tag{1.19}$$

from which follows that the derivative of a functional is calculated by perturbation of the argument by

[1] Note that $|f|_r$ is "only" a *semi* norm since $|f|_r = 0$ is also possible for $f \neq 0$ i.e. $|f|_r = 0 \Leftrightarrow f = \text{const} \wedge r > 0$.

the variation of the same which is multiplied by a scalar factor α and a subsequent "regular" derivative with respect to α. Afterwards, α is set to zero.

Consequently, the linearization of a functional is given by

$$\mathrm{L}\mathcal{F}[\bar{f}](\delta f) = \mathcal{F}[\bar{f}] + \mathrm{D}\mathcal{F}[\bar{f}](\delta x) \tag{1.20}$$

This allows the following definition: $\bar{f}$ is called *stationary point* of $\mathcal{F}$

$$:\Longleftrightarrow \quad \mathrm{D}\mathcal{F}[\bar{f}](\delta f) = 0 \quad \forall \delta f \tag{1.21}$$

i.e. the derivative equals zero in point $\bar{f}$ all directions δf. It thus follows

$$\mathrm{D}\mathcal{F}[\bar{f}](\delta f) = 0 \quad \forall \delta f \qquad \Longleftrightarrow \qquad \mathcal{F}[\bar{f}] = w_{\min,\max} \tag{1.22}$$

as necessary condition for $\mathcal{F}$ being extremal in $\bar{f}$. The variation of the argument is denoted by δf, whereas the variation (of the functional) is just $\mathrm{D}\mathcal{F}[\bar{f}](\delta f) =: \delta\mathcal{F}$ in short.

1.3 Hamilton's principle and variational methods

1.3.1 Fundamental relations

The methods for material modeling which are used in the following chapters of this thesis are all based on variational strategies. They all share the fundamental idea that processes, which are observed in nature, tend to be extremal which roots back to Aristotle or even before (see [18]). This concept was embedded into a mathematically consistent setting in the late 1700's by Leibniz, Euler, Maupertuis, Lagrange, and others. A historical review and a critical investigation of the underlying assumptions of the three latter ones was given by Pulte (see [157]). The general procedure is the minimization of the energy-based quantity termed as "action". Thereby, the problem of brachistochrone could also be solved such as light refraction, the motion of a conservative oscillator, and many more. An energy-based description for static systems that points into an roughly comparable direction is the well-known principle of Castigliano and Menabrea (see [133, 31]). Here, the elastic energy is minimized with respect to the unknown displacements in order to calculate the resulting forces, or vice versa. An interesting historical review on the principle of Castigliano and Menabrea is given in [28].

A generalization of the principle of least action is Hamilton's principle (see [73, 74]) which can also be expanded in order to take non-conservative forces into account. A nice introduction to Hamilton's principle is given by Bedford (see [17]), while Bailey presents a clear distinction between different energy-based methods (see [9]).

Hamilton's principle is derived for a system of rigid bodies for which the position in time, described in terms of the generalized coordinates $(q_i(t)) = \boldsymbol{q}(t)$, is unknown. The system is described in energetic quantities, precisely in terms of the potential energy U, e.g. due to gravitation or spring forces, and in terms of the kinetic energy K. Then, Hamilton's principle postulates that the so-called action tends

to be stationary:

$$\mathcal{F}[\boldsymbol{q}(t)] \coloneqq \int_{t_0}^{t_1} \Big(K(t,\dot{\boldsymbol{q}}(t)) - U(t,\boldsymbol{q}(t))\Big)\mathrm{d}t \to \underset{\boldsymbol{q}(t)}{\mathrm{stat}} \tag{1.23}$$

for which it is assumed that the position of the system is known for the fixed points in time t_0 and t_1. The argument $K-U$ seems quite confusing and a direct interpretation or origin may be not obvious at this point. However, it is possible to interpret the action as will presented in Section 1.3.4. The stationary point of $\mathcal{F}[\boldsymbol{q}(t)]$ is calculated by use of the Gâteaux derivative

$$\delta\mathcal{F} = \int_{t_0}^{t_1} (\delta K - \delta U)\,\mathrm{d}t = \int_{t_0}^{t_1} \left(\frac{\partial K}{\partial \dot{\boldsymbol{q}}}\cdot\delta\dot{\boldsymbol{q}} - \frac{\partial U}{\partial \boldsymbol{q}}\cdot\delta\boldsymbol{q}\right)\mathrm{d}V = 0 \tag{1.24}$$

and a subsequent integration by parts yields

$$\delta\mathcal{F} = \int_{t_0}^{t_1} \left(\frac{\partial L}{\partial \boldsymbol{q}} - \frac{\mathrm{d}}{\mathrm{d}t}\frac{\partial L}{\partial \dot{\boldsymbol{q}}}\right)\cdot\delta\boldsymbol{q}\;\mathrm{d}t = 0 \qquad \forall\delta\boldsymbol{q} \tag{1.25}$$

where the Lagrangean $L \coloneqq K-U$ has been introduced. It thus follows from Equation (1.25) that

$$\frac{\partial L}{\partial \boldsymbol{q}} - \frac{\mathrm{d}}{\mathrm{d}t}\frac{\partial L}{\partial \dot{\boldsymbol{q}}} = \boldsymbol{0} \tag{1.26}$$

describes the positions $\boldsymbol{q}$ in time such that $\mathcal{F}$ in Equation (1.23) is stationary. In general, a differential equation results from a stationarity condition which is termed Euler equation. The equation (1.26), however, is usually referred to as Lagrange equation of second kind. It holds true also for the more general case $K = K(t,\boldsymbol{q}(t),\dot{\boldsymbol{q}}(t))$ and $U = U(t,\boldsymbol{q}(t),\dot{\boldsymbol{q}}(t))$.

For static systems, i.e. $K = 0$, Hamilton's principle according to Equation (1.24) reduces to

$$\delta U = \frac{\partial U}{\partial \boldsymbol{q}}\cdot\delta\boldsymbol{q} = 0 \quad \forall\delta\boldsymbol{q} \qquad \Leftrightarrow \qquad \frac{\partial U}{\partial \boldsymbol{q}} = \boldsymbol{0} \tag{1.27}$$

which equals the principle of Castigliano and Menabrea.

The potential energy allows also for the derivation of the generalized forces by

$$\tilde{\boldsymbol{p}} \coloneqq -\frac{\partial U}{\partial \boldsymbol{q}} \tag{1.28}$$

which are subsequently used to define the so-called virtual work $\delta\tilde{W}$ as

$$\delta\tilde{W} \coloneqq \tilde{\boldsymbol{p}}\cdot\delta\boldsymbol{q} \tag{1.29}$$

This expression can be inserted into Equation (1.25) which yields

$$\delta\mathcal{F} = \int_{t_0}^{t_1} \Big(\delta K + \delta\tilde{W}\Big)\mathrm{d}t = 0 \tag{1.30}$$

However, all forces that are acting along $\delta\boldsymbol{q}$ contribute to the virtual work, both conservative and non-conservatives ones. It is thus convenient to separate all conservative forces in $\delta\tilde{W}$ by introducing the potential energy and collecting the influence of the non-conservative forces, which cannot be derived from the (conserving) potential energy U, in W, resulting in the transformation $\delta\tilde{W} \to -\delta U + \delta W$.

Hence,

$$\delta\mathcal{F} = \int_{t_0}^{t_1} \Big(\delta K - \delta U + \delta W\Big)\mathrm{d}t = 0 \tag{1.31}$$

where $\delta W = \hat{\boldsymbol{p}} \cdot \delta \boldsymbol{q}$ is the virtual work due to non-conservative forces $\hat{\boldsymbol{p}}$. This implies that the forces $\tilde{\boldsymbol{p}}$ which can be derived from the potential energy according to Equation (1.28) are the conservative forces ($\tilde{\boldsymbol{p}} = -\partial U/\partial \boldsymbol{q}$). Equation (1.31) is referred to as Hamilton's principle for non-conservative systems.

1.3.2 Hamilton's principle for conservative continua

Hamilton's principle can also be applied to continuous systems. For this purpose, some thermodynamical quantities are recalled here (see e.g. [81, 130, 167, 189] for a more detailed elaboration). The Helmholtz free energy Ψ is defined as

$$\int_\Omega \Psi \, \mathrm{d}V \coloneqq \mathcal{E} - \int_\Omega \theta s \, \mathrm{d}V \tag{1.32}$$

with the internal energy $\mathcal{E}$, the absolute temperature θ, entropy s and the body's volume Ω. Employing a Legendre transformation on the Helmholtz free energy and subsequently Clapeyron's theorem (see [64]) results in the Gibbs free energy $\mathcal{G}$ defined by

$$\mathcal{G} \coloneqq \int_\Omega \Psi \, \mathrm{d}V - \int_\Omega \boldsymbol{b} \cdot \boldsymbol{u} \, \mathrm{d}V - \int_{\partial\Omega} \boldsymbol{t} \cdot \boldsymbol{u} \, \mathrm{d}A \tag{1.33}$$

where the body forces $\boldsymbol{b}$, the tractions $\boldsymbol{t}$, the displacements $\boldsymbol{u}$, and the surface area $\partial\Omega$ have been used. An alternative formulation (or interpretation) of the Gibbs free energy is its separation into two potentials Π_{in} and Π_{ex}

$$\mathcal{G} \coloneqq \Pi_{\mathrm{in}} + \Pi_{\mathrm{ex}} \tag{1.34}$$

Here, the internal potential is given by the Helmholtz free energy

$$\Pi_{\mathrm{in}} \coloneqq \int_\Omega \Psi \, \mathrm{d}V \tag{1.35}$$

which measures the amount of stored energy inside of a (deformable) body and the potential owing to external forces

$$\Pi_{\mathrm{ex}} \coloneqq -\int_\Omega \boldsymbol{b} \cdot \boldsymbol{u} \, \mathrm{d}V - \int_{\partial\Omega} \boldsymbol{t} \cdot \boldsymbol{u} \, \mathrm{d}A \tag{1.36}$$

The Gibbs free energy thus may be interpreted as the total (conservative) potential of a continuous body

$$\mathcal{G} = \Pi_{\mathrm{in}} + \Pi_{\mathrm{ex}} \tag{1.37}$$

Comparison to the Hamilton's principle as stated in Equation (1.24) thus yields ($K \to \mathcal{K}$, $U \to \mathcal{G}$, and neglecting dissipative forces)

$$\int_{t_0}^{t_1} \left(\delta\mathcal{K} - \delta\Pi_{\mathrm{in}} - \delta\Pi_{\mathrm{ex}}\right) \mathrm{d}t = \int_{t_0}^{t_1} \left(\delta\mathcal{K} - \delta\mathcal{G}\right) \mathrm{d}t = 0 \tag{1.38}$$

in which the kinetic energy for continuous media is given by

$$\mathcal{K} = \int_\Omega \frac{1}{2}\rho|\dot{\boldsymbol{u}}|^2 \, \mathrm{d}V \tag{1.39}$$

with the mass density ρ. Trivially, Hamilton's principle simplifies for static and conservative continua, implying $\dot{\boldsymbol{u}} = \boldsymbol{0}$, to

$$\delta \mathcal{G} = 0 \tag{1.40}$$

As presented in Section 1.3.4 in more detail, Equation (1.40) represents the so-called weak form of the balance of linear momentum. This expression is solved using the finite element method.

1.3.3 Materials with evolving microstructure

Variational approaches are employed in this thesis to derive material models that make use of "internal variables" which describe the underlying and time-dynamic microstructural state inside of a material. However, the principal variational methods explained above were derived before the concept of internal variables was introduced (see [83]): internal (state) variables were mentioned for the first time between 1820 and 1850 by Carnot [29], Joule [90], and Clausius [32] and embedded afterwards into a thermodynamical context by Helmholtz [191], Thomson [186], Maxwell [131], Gibbs [55], and Duhem [42] (for a detailed historical presentation see [83] and [129]). Consequently, a direct formal application of variational techniques to the treatment of internal variables was not possible since they were formulated only for macroscopic quantities such as generalized coordinates. However, it was recognized that indeed the aforementioned strategies can also be applied to micromechanical and microstructural processes as well. Before this was carried out, it was Onsager (see [146, 147]) who used a thermodynamic approach for the derivation of physical models which serves as linking element between the first fundamentals and the current methods. He recognized that thermodynamic fluxes $\dot{\boldsymbol{\upsilon}}$ and thermodynamic forces $\boldsymbol{p} = -\partial\Psi/\partial\boldsymbol{\upsilon}$ are related to each other owing to the (reduced) Clausius-Duhem inequality

$$\boldsymbol{p} \cdot \dot{\boldsymbol{\upsilon}} \geq 0 \tag{1.41}$$

which follows from the Second Law of Thermodynamics. Thus, he postulated

$$\dot{\boldsymbol{\upsilon}} = \boldsymbol{A} \cdot \boldsymbol{p} \tag{1.42}$$

with some positive and symmetric system matrix $\boldsymbol{A}$. Equation (1.42) can be regarded as a general strategy for the derivation of material models since it can be used also for the time-dependent evolution of internal variables (see the general work by Ziegler [199] and as an example for an application [117]). However, Onsager's principle is not a variational approach.

Roughly at the same time, Bridgman [24] and Eckart [43] established a link between thermodynamics and continuum mechanics. Later, it was Truesdell who opened the field of rational thermodynamics which includes usage of Equation (1.41) in [188], and also Coleman and Noll with their contribution to thermodynamics of materials with fading memory and internal variables [36, 33, 35]. It is also worth mentioning the work by Rice [160] and the work on the the structure of evolution equations given by Lubliner [124]. These important contributions along with others established the concept of internal variables in its current form.

Approximately ten years later, attempts to the application of variational principles to the modeling of materials by means of internal variables were made. Lubliner published in 1984 a work related to maximum dissipation for the calculation of the internal variables [125] so as Simo did in 1988 [168]. Ortiz and Repetto reported in 1999 on non-convex energy minimization which turned out to be beneficial for the modeling of materials with evolving (crystallographic) phases (see [149]) which

built on the very famous work of Ball and James who published the primal foundations in [10]. As compared to Hamilton's principle given above, it is obvious that these works are also directly related to variational modeling since energy minimizers are assumed to describe the associated microstructure realized in the material.

Related works on fundamentals for the variational modeling of materials were published by Hackl [65], Hackl and co-workers [30, 67, 69, 68] and Fischer and co-workers [181, 180]. Here, a way of deriving evolution equations based on variational strategies was used which was termed as the *principle of the minimum of the dissipation potential*. This principle was published in varying forms also in [127, 126, 72, 128] and compared to the complementary *principle of maximum dissipation* in [67]. The principle of the minimum of the dissipation potential was also expanded to the non-isothermal case in [103]. All of these works share the common basis that the dissipative forces (which contribute to δW) are included via a potential which had been first mentioned by Onsager in [146, 148].

The intention is now to forge a bridge from Hamilton's principle to the principle of the minimum of the dissipation potential just mentioned. Hence, the application of Hamilton's principle for materials with internal variables is presented in the subsequent section, during which the general case that includes also the gradient of the internal variables is treated first. Afterwards, the simplified case for vanishing gradients of $\boldsymbol{v}$ is presented.

1.3.4 Hamilton's principle for non-conservative continua

Hamilton's principle for conservative continua was given in Equation (1.24), and it is also valid for materials with internal variables as long as the associated processes of microstructure evolution conserve the elastic energy. This is, however, not true for many materials and their associated processes. Consequently, Hamilton's principle has to be expanded such that it is able to also account for non-conservative continua, similarly to the expansion for Hamilton's principle for non-conservative systems as stated in Equation (1.31). Therefore, a so-called dissipation functional $\mathcal{D}$ is introduced (see [146, 148]) which accounts for the amount of elastic energy that is converted into heat production and which is thus dissipative. For the sake of generality, the internal variables $\boldsymbol{v}$ are treated as vectorial quantities (in the case of tensorial dimensions, appropriate tensor products have to be substituted in the following derivations). The purpose of the dissipation functional is the derivation of the associated dissipative forces defined by $\hat{\boldsymbol{p}} = -\partial\mathcal{D}/\partial\dot{\boldsymbol{v}}$ (which must not be confused with the thermodynamic driving forces $\boldsymbol{p} = -\partial\Psi/\partial\boldsymbol{v}$). For non-conservative continua there are (at least) two variables which describe the material state: the displacement field $\boldsymbol{u}$ and the field of internal variables $\boldsymbol{v}$. The dissipative forces $\hat{\boldsymbol{p}}$ work consequently along the "path" $\boldsymbol{v}$ instead of $\boldsymbol{u}$. This is, of course, a deviation from Hamilton's principle which was postulated for systems that could completely be described (only) in terms of the single variable $\boldsymbol{q}$. Thus, the virtual work owing to dissipative forces in a continuum may be introduced as

$$\delta\mathcal{W} := \int_\Omega \hat{\boldsymbol{p}} \cdot \delta\boldsymbol{v} \, \mathrm{d}V \tag{1.43}$$

which allows for converting Equation (1.31) into its form for continuous bodies including internal variables as

$$\int_{t_0}^{t_1} (\delta\mathcal{K} - \delta\mathcal{G} + \delta\mathcal{W}) \, \mathrm{d}t = 0 \tag{1.44}$$

where $\delta W \rightarrow \delta \mathcal{W}$ has been used. In the quasi-static case, Equation (1.44) reads

$$\delta \mathcal{G} - \delta \mathcal{W} = 0 \tag{1.45}$$

which indicates that the virtual work of the conservative forces $\delta \mathcal{G}$ equals the virtual work of the dissipative forces $\delta \mathcal{W}$. Of course, the virtual work can be reformulated by aid of the dissipation functional as

$$\delta \mathcal{W} = - \int_\Omega \frac{\partial \mathcal{D}}{\partial \dot{\boldsymbol{v}}} \cdot \delta \boldsymbol{v} \, \mathrm{d}V \tag{1.46}$$

which transforms Equation (1.45) to its more convenient form

$$\delta \mathcal{G} + \int_\Omega \frac{\partial \mathcal{D}}{\partial \dot{\boldsymbol{v}}} \cdot \delta \boldsymbol{v} \, \mathrm{d}V = 0 \tag{1.47}$$

Obviously, the application of this formula demands the dissipative forces to be deducible from the dissipation functional $\mathcal{D}$ which might not be true for all cases (although no physically meaningful counterexample has been presented until today).

General case: $\mathcal{G} = \mathcal{G}(\boldsymbol{\varepsilon}, \boldsymbol{v}, \nabla \boldsymbol{v})$

In the most general case, the internal variables themselves and the associated gradient $\nabla \boldsymbol{v}$ contribute to the Gibbs free energy $\mathcal{G}$. According to Hamilton's principle in Equation (1.47), it holds

$$\delta \mathcal{G} + \int_\Omega \frac{\partial \mathcal{D}}{\partial \dot{\boldsymbol{v}}} \cdot \delta \boldsymbol{v} \, \mathrm{d}V = \delta_u \mathcal{G} + \delta_v \mathcal{G} + \int_\Omega \frac{\partial \mathcal{D}}{\partial \dot{\boldsymbol{v}}} \cdot \delta \boldsymbol{v} \, \mathrm{d}V = 0 \tag{1.48}$$

where the individual variations of $\mathcal{G}$ with respect to the displacements and the internal variables are denoted by $\delta_u \mathcal{G}$ and $\delta_v \mathcal{G}$, respectively. This yields

$$\begin{aligned} \delta \mathcal{G} - \delta \mathcal{W} = \int_\Omega \left(\frac{\partial \Psi}{\partial \boldsymbol{\varepsilon}} : \delta \boldsymbol{\varepsilon} + \frac{\partial \Psi}{\partial \boldsymbol{v}} \cdot \delta \boldsymbol{v} + \frac{\partial \Psi}{\partial \nabla \boldsymbol{v}} : \delta \nabla \boldsymbol{v} \right) \mathrm{d}V \\ - \int_\Omega \boldsymbol{b} \cdot \delta \boldsymbol{u} \, \mathrm{d}V - \int_{\partial \Omega} \boldsymbol{t} \cdot \delta \boldsymbol{u} \, \mathrm{d}A + \int_\Omega \frac{\partial \mathcal{D}}{\partial \dot{\boldsymbol{v}}} \cdot \delta \boldsymbol{v} \, \mathrm{d}V = 0 \quad \forall \delta \boldsymbol{u}, \delta \boldsymbol{v} \end{aligned} \tag{1.49}$$

The variation of the displacements $\boldsymbol{u}$ and the internal variables $\boldsymbol{v}$ can be chosen arbitrarily. Thus, the following conditions result from Equation (1.49)

$$\int_\Omega \frac{\partial \Psi}{\partial \boldsymbol{\varepsilon}} : \delta \boldsymbol{\varepsilon} \, \mathrm{d}V - \int_\Omega \boldsymbol{b} \cdot \delta \boldsymbol{u} \, \mathrm{d}V - \int_{\partial \Omega} \boldsymbol{t} \cdot \delta \boldsymbol{u} \, \mathrm{d}A = 0 \quad \forall \delta \boldsymbol{u} \tag{1.50}$$

$$\int_\Omega \frac{\partial \Psi}{\partial \boldsymbol{v}} \cdot \delta \boldsymbol{v} \, \mathrm{d}V + \int_\Omega \frac{\partial \Psi}{\partial \nabla \boldsymbol{v}} : \delta \nabla \boldsymbol{v} \, \mathrm{d}V + \int_\Omega \frac{\partial \mathcal{D}}{\partial \dot{\boldsymbol{v}}} \cdot \delta \boldsymbol{v} \, \mathrm{d}V = 0 \quad \forall \delta \boldsymbol{v} \tag{1.51}$$

The second equation (1.51) is called evolution equation for the internal variable $\boldsymbol{v}$. After specification of the Helmholtz free energy Ψ and the dissipation potential $\mathcal{D}$, it can be evaluated for a specific material. An example in which this strategy has been employed is given in [101].

Both equations (1.50,1.51) are integrated by parts, respectively. This yields for Equation (1.50)

$$\nabla \cdot \boldsymbol{\sigma} + \boldsymbol{b} = \boldsymbol{0} \tag{1.52}$$

$$\boldsymbol{\sigma} \cdot \boldsymbol{n} = \boldsymbol{t} \qquad \text{on } \partial \Omega \tag{1.53}$$

where the identity $\boldsymbol{\sigma} = \partial\Psi/\partial\boldsymbol{\varepsilon}$ has been used ($\boldsymbol{n}$ denotes a normal vector on the surface). Equation (1.52) constitutes as the balance of linear momentum (which is also known as Euler-Lagrange equation or Helmholtz equation) and Equation (1.53) is referred to as the Cauchy hypothesis. In turn, this allows to interpret the action $K - U$ as the (variational) potential form for the balance of forces for a system of rigid bodies.

Integration by parts of Equation (1.51) gives

$$\frac{\partial\Psi}{\partial\boldsymbol{\upsilon}} - \nabla\cdot\left(\frac{\partial\Psi}{\partial\nabla\boldsymbol{\upsilon}}\right) + \frac{\partial\mathcal{D}}{\partial\dot{\boldsymbol{\upsilon}}} = \mathbf{0} \tag{1.54}$$

$$\left(\frac{\partial\Psi}{\partial\nabla\boldsymbol{\upsilon}}\right)\cdot\boldsymbol{n} = \mathbf{0} \qquad \text{on } \partial\Omega \tag{1.55}$$

The first term in the Helmholtz equation in (1.54) is the negative of the driving force for the internal variable ("source term"). The second term indicates a contribution due to interfaces ("gradient term") whereas the third and last term introduces a viscous contribution ("transient term"). The entire equation has the same structure as the governing equation for phase field models when the transient term is replaced by $r_{\mathrm{v}}\dot{\boldsymbol{\varepsilon}}$ with some viscous parameter r_{v}. Equation (1.55) is the boundary condition ("flux term" for an "adiabatic" system). This general formulation of Hamilton's principle has also successfully been applied to the context of topology optimization [101] which shows that the principle is detached from material modeling but it can also by transferred to other physical problems.

Special case: $\mathcal{G} = \mathcal{G}(\boldsymbol{\varepsilon}, \upsilon)$

The introduction of the internal variables' gradient is not necessary in many cases which indicates that a local or pointwise evaluation is possible. Consequently, these models are usually referred to as material point models or Gauß point models. In the case of absent gradient of $\boldsymbol{\upsilon}$, the variation with respect to the internal variables in Equation (1.51) simplifies to

$$\int_\Omega \frac{\partial\Psi}{\partial\boldsymbol{\upsilon}}\cdot\delta\boldsymbol{\upsilon}\,\mathrm{d}V + \int_\Omega \frac{\partial\mathcal{D}}{\partial\dot{\boldsymbol{\upsilon}}}\cdot\delta\boldsymbol{\upsilon}\,\mathrm{d}V = 0 \quad \forall\delta\boldsymbol{\upsilon} \tag{1.56}$$

from which immediately follows that

$$\frac{\partial\Psi}{\partial\boldsymbol{\upsilon}} + \frac{\partial\mathcal{D}}{\partial\dot{\boldsymbol{\upsilon}}} = \mathbf{0} \tag{1.57}$$

Equation (1.57) can be integrated with respect to the internal variables' rate which yields the potential form

$$\frac{\partial\Psi}{\partial\boldsymbol{\upsilon}}\cdot\dot{\boldsymbol{\upsilon}} + \mathcal{D} + \mathcal{C} \to \operatorname*{stat}_{\dot{\boldsymbol{\upsilon}}} \tag{1.58}$$

with some arbitrary integration constant which is set to $\mathcal{C} = \partial\Psi/\partial\boldsymbol{\varepsilon} : \dot{\boldsymbol{\varepsilon}}$. This gives the Lagrangean

$$\mathcal{L} := \dot{\Psi} + \mathcal{D} \to \operatorname*{stat}_{\dot{\boldsymbol{\upsilon}}} \tag{1.59}$$

which is indeed referred to as the minimum of the dissipation potential. Hence, under consideration of the fact that the dissipative forces may be derived from a dissipation functional $\mathcal{D}$ and that no gradients of internal variables are present, the principle of the minimum of the dissipation potential coincides with Hamilton's principle for continuous bodies including dissipative variables.

1.3.5 Example for rate-independent and rate-dependent microstructural evolution

The great benefit for both variational principles discussed here (see Hamilton's principle in its most general form Equation (1.47) and for the special case in which gradients of internal variables are not present in Equation (1.59)) is the easy inclusion of constraints: they can be taken into account by adding them to the respective functional. As short example, a material exhibiting perfect plasticity is analyzed here.

The creation of dislocations and their movement is combined to a dissipative, non-reversible part of the strain which is referred to as plastic strain and denoted by $\boldsymbol{\varepsilon}^{\mathrm{p}}$. In a kinematically linear setting, the total strain is given by superposition of the elastic and plastic part. The Helmholtz free energy thus reads

$$\Psi = \frac{1}{2}(\boldsymbol{\varepsilon} - \boldsymbol{\varepsilon}^{\mathrm{p}}) : \mathbb{C} : (\boldsymbol{\varepsilon} - \boldsymbol{\varepsilon}^{\mathrm{p}}) \tag{1.60}$$

where the total strain is given by $\boldsymbol{\varepsilon}$ and the elasticity tensor of order four $\mathbb{C}$.

For a rate-independent material behavior, which is assumed for the plastically deforming material, the dissipation functional $\mathcal{D}$ is homogeneous of order one. This can be justified by a simple example. The most simple case for a dissipative force in a rate-independent setting is the force due to (dry) friction. It is a constant which points in opposite direction to the (assumed) moving direction: $R = -|\bar{R}|\mathrm{sgn}\dot{u}$. The associated dissipative potential which yields the friction force by $R = -\partial\tilde{\mathcal{D}}_R/\partial\dot{u}$ is thus

$$\tilde{\mathcal{D}}_R := |\bar{R}||\dot{u}| \tag{1.61}$$

which is indeed homogeneous of order one ($\tilde{\mathcal{D}}_R(\alpha\dot{u}) = \alpha\tilde{\mathcal{D}}_R(\dot{u})$). A schematic plot is given in Figure 1.3.

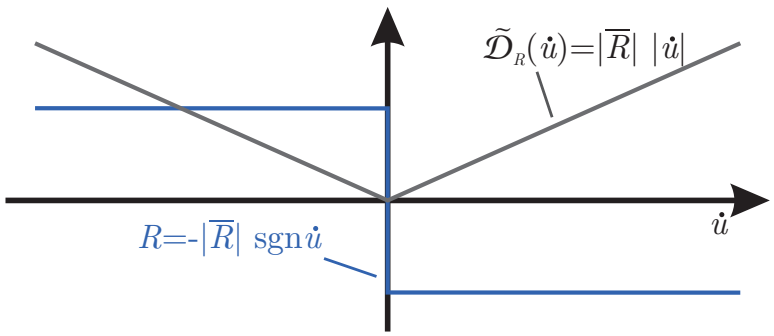

Figure 1.3: Friction force R and the associated dissipative potential $\tilde{\mathcal{D}}_R$ as functions of the (relative) displacement u.

In contrast to the dissipative potential $\tilde{\mathcal{D}}_R$ which depends on the (relative) velocity $\dot{u}$, the dissipation functional $\mathcal{D}$ depends on the rate of the internal variable [see e.g. Equation (1.47)] which is in the present case the rate of the plastic strains: $\dot{\boldsymbol{\upsilon}} = \dot{\boldsymbol{\varepsilon}}^{\mathrm{p}}$. Thus, the analogous formulation to Equation (1.61) is

$$\mathcal{D} = r|\dot{\boldsymbol{\varepsilon}}^{\mathrm{p}}| \tag{1.62}$$

with some material constant $r > 0$ which is referred to as dissipation parameter. A one-dimensional sketch is presented in Figure 1.4.

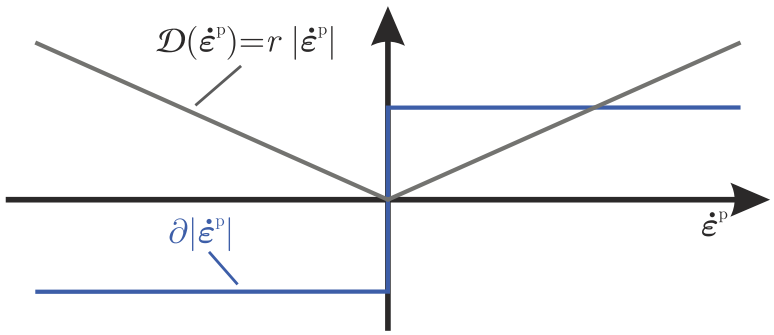

Figure 1.4: Dissipation functional $\mathcal{D} = r|\dot{\boldsymbol{\varepsilon}}^{\mathrm{r}}|$ for the one-dimensional case and its subdifferential according to Equation (1.67).

It is well-known that plastic deformations evolve in a volume-preserving way. This property is a constraint that has to be included into the material model, and while using variational modeling principles this can be archived in a straight forward way. Volume-preservation reads (in the case of linearized strains)

$$\varepsilon^{\mathrm{p}}_{ii} = c \tag{1.63}$$

where Einstein's summation convention has been employed. The constant c depends on the initial conditions and equals zero in most cases. However, the constraint has to be formulated in terms of the rates which gives (for all constants c)

$$\dot{\varepsilon}^{\mathrm{p}}_{ii} = 0 \tag{1.64}$$

This constraint is taken into account by means of a Lagrange parameter β, and the final form of the minimum of the dissipation potential constitutes as

$$\mathcal{L} = \dot{\Psi} + \mathcal{D} + \beta\dot{\varepsilon}^{\mathrm{p}}_{ii} \rightarrow \operatorname*{stat}_{\dot{\boldsymbol{\varepsilon}}^{\mathrm{p}}} \tag{1.65}$$

The stationarity condition demands

$$\frac{\partial\mathcal{L}}{\partial\dot{\boldsymbol{\varepsilon}}^{\mathrm{p}}} = \frac{\partial\Psi}{\partial\boldsymbol{\varepsilon}^{\mathrm{p}}} + r\partial|\dot{\boldsymbol{\varepsilon}}^{\mathrm{p}}| + \beta\ \mathbb{I} \ni \mathbf{0} \tag{1.66}$$

with the identity tensor of order two $\mathbb{I}$ and the subdifferential

$$\partial|\dot{\boldsymbol{\varepsilon}}^{\mathrm{p}}| = \begin{cases} \{|\dot{\boldsymbol{\varepsilon}}^{\mathrm{p}}| \leq 1\} & \text{for } |\dot{\boldsymbol{\varepsilon}}^{\mathrm{p}}| = \mathbf{0} \\ \dfrac{\dot{\boldsymbol{\varepsilon}}^{\mathrm{p}}}{|\dot{\boldsymbol{\varepsilon}}^{\mathrm{p}}|} & \text{else} \end{cases} \tag{1.67}$$

Owing to the set-property of the subdifferential, the stationary point in Equation (1.66) transforms into a differential inclusion, see also the plot in Figure 1.4. Note that the subdifferential may be interpreted as the negative of the dissipative force ($\rightarrow$ friction force).

Summation of all entries in Equation (1.66) with double indices results in

$$-p_{ii} + r\frac{\dot{\varepsilon}^{\mathrm{p}}_{ii}}{|\dot{\boldsymbol{\varepsilon}}^{\mathrm{p}}|} + 3\beta = 0 \tag{1.68}$$

where the driving force $p_{ij} = -\partial\Psi/\partial\varepsilon^{\mathrm{p}}_{ij}$ has been introduced:

$$\boldsymbol{p} = -\frac{\partial\Psi}{\partial\boldsymbol{\varepsilon}^{\mathrm{p}}} = \mathbb{C} : \left(\boldsymbol{\varepsilon} - \boldsymbol{\varepsilon}^{\mathrm{p}}\right) \equiv \boldsymbol{\sigma} \tag{1.69}$$

It follows from Equation (1.69) that the driving forces are indeed the mechanical stresses $\boldsymbol{\sigma}$.

Equation (1.68) allows to estimate the Lagrange parameter β when considering the constraint given in Equation (1.64) by

$$\beta = \frac{1}{3}\sigma_{ii} = \frac{1}{3}\mathrm{tr}\boldsymbol{\sigma} \tag{1.70}$$

where tr is the trace operator. Inserting this result back into the stationarity condition in Equation (1.66) finally results in

$$\dot{\boldsymbol{\varepsilon}}^{\mathrm{p}} = \frac{|\dot{\boldsymbol{\varepsilon}}^{\mathrm{p}}|}{r}\left(\boldsymbol{\sigma} - \frac{1}{3}\mathbb{I}\ \mathrm{tr}\boldsymbol{\sigma}\right) \qquad \text{for } |\dot{\boldsymbol{\varepsilon}}^{\mathrm{p}}| \neq 0 \tag{1.71}$$

The structure of Equation (1.71) is already well-known: the expression $\mathrm{dev}\boldsymbol{\sigma} := \boldsymbol{\sigma} - \mathbb{I}\ \mathrm{tr}\boldsymbol{\sigma}/3$ is the deviator which results in this framework just from the constraint of volume-preservation.

Equation (1.71) remains rather cumbersome to solve. Thus, it is transferred to its more conventional form

$$\dot{\boldsymbol{\varepsilon}}^{\mathrm{p}} = \rho\ \mathrm{dev}\boldsymbol{\sigma} \tag{1.72}$$

with a consistency parameter $\rho := |\dot{\boldsymbol{\varepsilon}}^{\mathrm{p}}|/r \geq 0$. For further mathematical simplification, a Legendre-Fenchel transformation of the dissipation potential $\mathcal{D}$ is employed. This gives

$$\mathcal{D}^{\star} = \sup_{\dot{\boldsymbol{\varepsilon}}^{\mathrm{p}}}\left\{\dot{\boldsymbol{\varepsilon}}^{\mathrm{p}} : \boldsymbol{p} - \mathcal{D} \;\middle|\; \dot{\varepsilon}^{\mathrm{p}}_{ii} = 0\right\} \tag{1.73}$$

Inserting Equation (1.72) into Equation 1.73 identically fulfills the constraint:

$$\begin{aligned}\mathcal{D}^{\star} &= \sup_{\dot{\boldsymbol{\varepsilon}}^{\mathrm{p}}}\left\{\frac{|\dot{\boldsymbol{\varepsilon}}^{\mathrm{p}}|}{r}\mathrm{dev}\boldsymbol{\sigma} : \mathrm{dev}\boldsymbol{\sigma} - r|\dot{\boldsymbol{\varepsilon}}^{\mathrm{p}}|\right\} \\ &= \sup_{\dot{\boldsymbol{\varepsilon}}^{\mathrm{p}}}\left\{\frac{|\dot{\boldsymbol{\varepsilon}}^{\mathrm{p}}|}{r}\left(\mathrm{dev}\boldsymbol{\sigma} : \mathrm{dev}\boldsymbol{\sigma} - r^2\right)\right\}\end{aligned} \tag{1.74}$$

The prefactor is obviously positive and may also take (at least theoretically) arbitrarily high values. It is hence necessary that the expression given in brackets is less or equal zero to bound the supremum. Thus, it serves as an indicator function

$$\phi := |\mathrm{dev}\boldsymbol{\sigma}|^2 - r^2 \overset{!}{\leq} 0 \tag{1.75}$$

for which plastic deformations may evolve if $\phi = 0$ ($|\mathrm{dev}\boldsymbol{\sigma}|^2 = \mathrm{dev}\boldsymbol{\sigma} : \mathrm{dev}\boldsymbol{\sigma}$). Hence, the dissipation parameter r constitutes in this example as a deviator-type norm of the yield stress. The entire system of equations for perfect plasticity is given by the evolution equation in Equation 1.72 in combination with Kuhn-Tucker conditions

$$\rho \geq 0, \qquad \phi \leq 0, \qquad \rho\phi = 0 \tag{1.76}$$

There exist other approaches for the dissipation functional $\mathcal{D}$ as e.g. a quadratic approach

$$\mathcal{D} = \frac{r_\mathrm{v}}{2}|\dot{\boldsymbol{\varepsilon}}^\mathrm{p}|^2 \tag{1.77}$$

In this case, the stationarity condition reads

$$\frac{\partial \mathcal{L}}{\partial \dot{\boldsymbol{\varepsilon}}^\mathrm{p}} = \frac{\partial \Psi}{\partial \boldsymbol{\varepsilon}^\mathrm{p}} + r_\mathrm{v}\ \dot{\boldsymbol{\varepsilon}}^\mathrm{p} = \mathbf{0} \tag{1.78}$$

which transforms to

$$\dot{\boldsymbol{\varepsilon}}^\mathrm{p} = \frac{1}{r_\mathrm{v}}\boldsymbol{p} = \frac{1}{r_\mathrm{v}}\boldsymbol{\sigma} \tag{1.79}$$

In the case of volume-preservation, an analogous procedure yields

$$\dot{\boldsymbol{\varepsilon}}^\mathrm{p} = \frac{1}{r_\mathrm{v}}\ \mathrm{dev}\boldsymbol{\sigma} \tag{1.80}$$

From Eqs. (1.79) and (1.80) it can be deduced that a quadratic approach for the dissipation functional results in rate-dependent evolution equations for a viscous material. Accordingly, the material parameter r_v is the viscosity in this case. The specific choice for the dissipation functional is thus a part of material modeling. However, the general structure (i.e. a homogeneous or quadratic approach) is already determined when the rate-(in)dependence of the material behavior has been specified.

2 A basis for the simulation of finite dimensional shape memory alloys

Published as: *P. Junker, K. Hackl*: Finite element simulations of poly-crystalline shape memory alloys based on a micromechanical model, *Comput. Mech.* **47(5): 505–517 (2011)**

We present a finite element implementation of a micromechanically motivated model for polycrystalline shape memory alloys, based on energy minimization principles. The implementation allows simulation of anisotropic material behavior as well as the pseudo-elastic and pseudo-plastic material response of whole samples. The evolving phase distribution over the entire specimen is calculated. The finite-element model predicts the material properties for a relatively small number of grains. For different points of interest in the specimen the model can be consistently evaluated with a significantly higher number of grains in a post-processing step, which allows to predict the reorientation of martensite at different loads. The influence of pre-texture on the material's properties, due to some previous treatment like rolling, is discussed.

2.1 Introduction

Shape memory alloys undergo solid to solid phase transformations during loading and unloading. These phase transformations are equivalent to changes in the lattice structure through which the material can minimize its elastic energy. Furthermore, most specimens are polycrystals with a huge number of crystallites in which the phase transformation takes place separately. Driven by the phase transformations, shape memory alloys can display either pseudo-elastic or pseudo-plastic behavior, depending on temperature. Hence, such materials offer a huge variety of industrial applications such as stents or micro-actuators, but micromechanical modeling of shape memory alloys remains a challenging topic in material science.

Our aim is the micromechanical simulation of the pseudo-elastic and pseudo-plastic material behavior of whole specimens made of shape-memory-alloys. As there exists a high number of different models of shape-memory alloys, we mention just a few of them. Phenomenological models for polycrystals were presented in [22, 79, 120]. Foundations for micromechanical models based on variational arguments were laid down in [10, 110, 138, 190]. Micromechanical models can be found in [60, 177] for single crystals, and in [174] for polycrystals. Finite element implementations were presented in [153] where a model introduced in [185] is used, [60, 174].

We use a micromechanical model for polycrystalline shape-memory alloys presented by [70]. This model synthesizes works in [61], [57], [77] and in [70] and is based on a relaxation of the elastic energy. Relaxation can be carried out for fixed volume fractions of the different phases (austenite and several martensite variants) and gives the energy minimizing elastic strains. In contrast to the work in [70], we extend the modeling from the material point level to the macroscopic scale of specimens. This is achieved by applying the finite element method to the variational equations for the minimum of the total potential. To find evolution equations for the volume fractions, we follow [149] by minimizing a Lagrange functional composed of the rate of the relaxed elastic energy and a dissipation functional.

The micromechanical model is solved using a Newton algorithm and implemented into a finite element code. We present some numerical results such as the distribution of the average austenite

and martensite volume fractions within the specimen, the orientation distribution of the variants in selected elements and load-displacement-curves for specimens with different pre-textures.

2.2 Micromechanical model for poly-crystalline shape memory alloys

2.2.1 Relaxation of the elastic energy

For describing the complex behavior of polycrystalline shape memory alloys, we minimize the elastic energy as shown in [70]. It is a well-known phenomenon that a shape memory alloy can minimize its elastic energy if the strain $\boldsymbol{\varepsilon}$ coincides with a certain so-called transformation strain $\boldsymbol{\eta}_i$ for one of the crystal variants i ($i = 0$ for the austenite phase, $i > 0$ for the different martensite phases). These transformation strains can be measured as shown in [163].

Depending on the system's temperature, either the austenite or the martensite phases are stable in an undeformed specimen. The temperature dependence leads to a difference in the chemical energies. This difference is called α_i and given with reference to the martensitic phases (all martenitic phases have the same chemical energy). Hence we can write $\alpha_i \neq 0$ only for the austenite. Therefore, we assume an elastic energy Ψ_i^j of the crystalline phase i in the crystallite j of the following form

$$\Psi_i^j(\boldsymbol{\varepsilon}_i^j) = \frac{1}{2}(\boldsymbol{\varepsilon}_i^j - \boldsymbol{\eta}_i^j) : \mathbb{C}_i^j : (\boldsymbol{\varepsilon}_i^j - \boldsymbol{\eta}_i^j) + \alpha_i \,, \tag{2.1}$$

with $\mathbb{C}_i^j$ as material constants, $\boldsymbol{\eta}_i^j$ as transformation strain, $\boldsymbol{\varepsilon}_i^j$ as strain of variant i in grains of direction j. To describe the orientation of every crystallite j in a polycrystal, we introduce rotation matrices $\boldsymbol{R}^j \in SO(3)$ which map the global Cartesian coordinate system to the orientation of the local cubic, and therefore Cartesian, austenite coordinate system. We account for the unstructured distribution of the different crystallite directions by choosing $\boldsymbol{R}^j$ randomly.

With $\boldsymbol{R}^j$ at hand, we can calculate the transformation strain of each variant i in the direction of each crystal j by

$$\boldsymbol{\eta}_i^j = \boldsymbol{R}^j \cdot \boldsymbol{\eta}_i \cdot \boldsymbol{R}^j \,, \tag{2.2}$$

and the elastic tensor of fourth order by

$$\mathbb{C}_{i,pqrs}^j = R_{tp}^j R_{uq}^j R_{vr}^j R_{ws}^j \mathbb{C}_{i,tuvw} \,. \tag{2.3}$$

Let us denote the volume fraction of grains with orientation $\boldsymbol{R}^j$ by ξ^j, collected into a vector $\boldsymbol{\xi} = (\xi^j)$. The constraint of mass conservation

$$\sum_{j=1}^{N} \xi^j = 1 \tag{2.4}$$

has to be satisfied, where N denotes to total number of grain orientations considered.

In this paper we will assume a pre-texture of the poly-crystal given by

$$\bar{\xi}^j = \max_{k=1,\ldots,6} [\boldsymbol{n}_{\text{pref}} \cdot \boldsymbol{R}^j \cdot \boldsymbol{n}_{\{1,0,0\},k}]^q \tag{2.5}$$

with

$$\boldsymbol{n}_{\{1,0,0\},k} \in \left\{ \begin{pmatrix} \pm 1 \\ 0 \\ 0 \end{pmatrix}, \begin{pmatrix} 0 \\ \pm 1 \\ 0 \end{pmatrix}, \begin{pmatrix} 0 \\ 0 \\ \pm 1 \end{pmatrix} \right\} .$$

In order to fulfill the constraint (2.4), we use

$$\xi^j = \frac{\bar{\xi}^j}{\sum_{j=1}^{N} \bar{\xi}^j} . \tag{2.6}$$

Here n_{pref} describes the preferred orientation belonging to a higher volume fraction of grains. This way previous treatments like rolling or deep-drawing can be taken into account. The exponent q controls the intensity of the pre-texture's influence, $q = 0$ referring to an isotropic texture.

In an analogous way to the volume fractions of the directions ξ^j, the volume fraction of each variant in each crystallite will be denoted by λ_i^j. Once again mass conservation requires

$$\sum_{i=0}^{n} \lambda_i^j = 1 \quad \forall\ j = 1, \ldots, N , \tag{2.7}$$

where n denotes the number of different phases ($n = 0$ being the austenitic phase).

The elastic energy of the entire polycrystal will be minimized over the strains in each phase and orientation $\boldsymbol{\varepsilon}_i^j$, with the constraint that the macroscopic strain $\boldsymbol{\varepsilon}$ is accommodated by the crystalline strains in each of the n phases and N crystallites (2.8),

$$\boldsymbol{\varepsilon} = \sum_{j=1}^{N} \sum_{i=0}^{n} \xi^j \lambda_i^j \boldsymbol{\varepsilon}_i^j . \tag{2.8}$$

Consequently the energy can be written for fixed volume fractions as the weighted sum of the energies for each phase in each grain orientation where the volume fractions of the phases, λ_i^j, and of the grain orientations, ξ^j, serve as weighting factors. Thus,

$$\Psi^{\text{rel}}(\boldsymbol{\varepsilon}, \boldsymbol{\lambda}) = \inf_{\boldsymbol{\varepsilon}_i^j} \left\{ \sum_{j=1}^{N} \sum_{i=0}^{n} \xi^j \lambda_i^j \Psi_i^j(\boldsymbol{\varepsilon}_i^j) \;\middle|\; \boldsymbol{\varepsilon} = \sum_{j=1}^{N} \sum_{i=0}^{n} \xi^j \lambda_i^j \boldsymbol{\varepsilon}_i^j \right\} . \tag{2.9}$$

Minimization yields [70]

$$\Psi^{\text{rel}}(\boldsymbol{\varepsilon}, \boldsymbol{\lambda}) = \frac{1}{2} (\boldsymbol{\varepsilon} - \boldsymbol{\eta}_{\text{eff}}) : \mathbb{C}_{\text{eff}} : (\boldsymbol{\varepsilon} - \boldsymbol{\eta}_{\text{eff}}) + \alpha_{\text{eff}} , \tag{2.10}$$

with

$$\mathbb{C}_{\text{eff}} = \left[\sum_{j=1}^{N} \sum_{i=0}^{n} \xi^j \lambda_i^j \left(\boldsymbol{C}_i^j \right)^{-1} \right]^{-1} , \quad \boldsymbol{\eta}_{\text{eff}} = \sum_{j=1}^{N} \sum_{i=0}^{n} \xi^j \lambda_i^j \boldsymbol{\eta}_i^j , \quad \alpha_{\text{eff}} = \sum_{j=1}^{N} \sum_{i=0}^{n} \xi^j \lambda_i^j \alpha_i .$$

2.3 Evolution of the volume fractions

The approach presented in the previous section is valid for given volume fractions. Of course, during loading and unloading, the state of strains and, therefore, the volume fractions of the phases change. Hence, it is necessary to describe these changes in time by evolution equations.

Following [149], we minimize a Lagrange functional consisting of the total power of the system and a dissipation functional [67] in order to find evolution equations for the phase fractions, $\dot{\boldsymbol{\lambda}} = (\dot{\lambda}_i^j)$. The Lagrangian consists of the derivative of the elastic energy with respect to time and of a dissipation functional. We assume that dissipation only occurs as a result of phase transitions. Therefore we make an ansatz for the dissipation functional as

$$\Delta(\dot{\boldsymbol{\lambda}}) = r\sqrt{\sum_{j=1}^{N}\xi^j\sum_{i=0}^{n}(\dot{\lambda}_i^j)^2}\,, \tag{2.11}$$

with r as a dissipation coefficient, [136]. The Lagrange functional then reads

$$\mathcal{L}(\boldsymbol{\lambda},\dot{\boldsymbol{\lambda}}) = \frac{\mathrm{d}}{\mathrm{d}t}\Psi^{\mathrm{rel}}(\boldsymbol{\varepsilon},\boldsymbol{\lambda}) + \Delta(\dot{\boldsymbol{\lambda}}) = \frac{\partial\Psi^{\mathrm{rel}}}{\partial\boldsymbol{\varepsilon}} : \dot{\boldsymbol{\varepsilon}} + \frac{\partial\Psi^{\mathrm{rel}}}{\partial\boldsymbol{\lambda}} : \dot{\boldsymbol{\lambda}} + \Delta(\dot{\boldsymbol{\lambda}})\,, \tag{2.12}$$

which we intend to minimize with respect to $\dot{\boldsymbol{\lambda}}$. In this equation, the term $-\partial\Psi^{\mathrm{rel}}/\partial\boldsymbol{\lambda}$ is identified as the thermodynamical driving force for phase change which is now denoted by $\boldsymbol{q}$. Differentiation of the relaxed energy Ψ^{rel} with respect to the volume fractions yields

$$\begin{aligned} q_i^j &= -\frac{\partial\Psi^{\mathrm{rel}}}{\partial\lambda_i^j} \\ &= \xi^j\left[\boldsymbol{\eta}_i^j : \mathbb{C}_{\mathrm{eff}} : (\boldsymbol{\varepsilon} - \eta_{\mathrm{eff}}) + \frac{1}{2}(\boldsymbol{\varepsilon} - \boldsymbol{\eta}_{\mathrm{eff}}) : \left(\mathbb{C}_{\mathrm{eff}} : (\mathbb{C}_i^j)^{-1} : \mathbb{C}_{\mathrm{eff}}\right) : (\boldsymbol{\varepsilon} - \boldsymbol{\eta}_{\mathrm{eff}}) - \alpha_i\right]. \end{aligned} \tag{2.13}$$

Again, the minimization requires the observation of mass conservation, as in (2.7). Furthermore, the volume fractions must not become negative. Therefore we introduce a Lagrange parameter β^j for mass conservation and a Kuhn-Tucker parameter γ_i^j for non-negativity. The Lagrangian now becomes

$$\bar{\mathcal{L}}(\boldsymbol{\lambda},\dot{\boldsymbol{\lambda}},\beta^j,\gamma_i^j) = -\boldsymbol{q}\dot{\boldsymbol{\lambda}} + \Delta + \sum_{j=1}^{N}\left(\beta^j\sum_{i=0}^{n}\dot{\lambda}_i^j\right) - \sum_{j=1}^{N}\sum_{i=0}^{n}\gamma_i^j\dot{\lambda}_i^j \tag{2.14}$$

The Kuhn-Tucker parameter is inactive if the volume fractions are positive; otherwise, γ_i^j is a number greater than zero, namely

$$\gamma_i^j = \begin{cases} = 0 & \text{for} \quad \lambda_i^j > 0 \vee (\lambda_i^j = 0 \wedge \dot{\lambda}_i^j > 0) \\ > 0 & \text{else} \end{cases}. \tag{2.15}$$

By choosing two sets, the passive set $\mathcal{B}^j$ and the active set $\mathcal{A}^j$, the mathematical derivation can be simplified and there is no need to specify the Kuhn-Tucker parameter. The passive set collects all those phases which have a volume fraction of zero within one crystallite or orientation, whereas the active set comprises all those phases which are in the passive set, but intent to grow, and furthermore

all phases which are not included in the passive set. Hence,

$$\mathcal{B}^j = \{i|\lambda_i^j = 0\} \,, \tag{2.16}$$

$$\mathcal{A}^j = \{i \in \mathcal{B}^j|\dot{\lambda}_i^j > 0\} \cup \{i \notin \mathcal{B}^j\} \,. \tag{2.17}$$

This yields the following set of evolution equations [70]

$$\begin{aligned} (\mathrm{dev}_{\mathcal{A}^j}\boldsymbol{q})_i^j &= r\xi^j \frac{\dot{\lambda}_i^j}{\sqrt{\sum_{j=1}^N \xi^j \sum_{i=0}^n (\dot{\lambda}_i^j)^2}} \quad \text{for} \quad i \in \mathcal{A}^j \quad \text{and} \quad \dot{\lambda}_i^j \neq 0 \,, \\ \left(\sum_{j=1}^N \frac{1}{\xi^j} \sum_{i=0}^n \left((\mathrm{dev}_{\mathcal{A}^j}\boldsymbol{q})_i^j\right)^2\right)^{1/2} &\leq r \qquad \text{for} \quad j \in \mathcal{A}^j \quad \text{and} \quad \dot{\lambda}_i^j = 0 \,, \\ (\mathrm{dev}_{\mathcal{A}^j}\boldsymbol{q})_i^j &= -\gamma_i^j < 0 \qquad\qquad \text{for} \quad i \notin \mathcal{A}^j \,, \end{aligned} \tag{2.18}$$

where $q_i^j - \frac{1}{n_{\mathcal{A}^j}} \sum_{k\in\mathcal{A}^j} q_k^j =: (\mathrm{dev}_{\mathcal{A}^j}\boldsymbol{q})_i^j$ is the *active deviator* and $n_{\mathcal{A}^j}$ is the number of variants in the active set.

These equations completely describe the evolution of the phase fractions. Nevertheless, we introduce the Legendre transformation of the dissipation functional

$$\mathcal{J}(\boldsymbol{q}) \quad = \quad \sup\left\{(\mathrm{dev}_{\mathcal{A}}\boldsymbol{q}) : \dot{\boldsymbol{\lambda}} - \Delta \,|\dot{\boldsymbol{\lambda}}\right\} \tag{2.19}$$

The functional $\mathcal{J}(\boldsymbol{q})$ has the form

$$\mathcal{J}(\boldsymbol{q}) = \begin{cases} 0 & \text{for} \quad \Phi(\boldsymbol{q}) \leq 0 \\ \infty & \text{else} \end{cases} \,, \tag{2.20}$$

with

$$\Phi(\boldsymbol{q}) := \sum_{j=1}^N \frac{1}{\xi^j} \sum_{i=0}^n \left((\mathrm{dev}_{\mathcal{A}^j}\boldsymbol{q})_i^j\right)^2 - r^2 \,. \tag{2.21}$$

Therefore, $\Phi(\boldsymbol{q})$ may be interpreted as 'yield function', well known from plasticity.

Then, the first equation from (2.18) gives

$$\dot{\lambda}_i^j = \frac{\rho}{\xi^j}[\mathrm{dev}_{\mathcal{A}^j} q_i^j]_{\mathcal{A}^j} \tag{2.22}$$

$$\rho := \frac{\Delta}{r^2} \geq 0 \,, \quad \Phi \leq 0 \,, \quad \rho\Phi = 0 \,, \quad \mathrm{dev}_{\mathcal{A}^j} q_i^j \leq 0 \quad \text{for} \;\; i \notin \mathcal{A}^j \tag{2.23}$$

where the last expression in (2.18) controls the evolution the active and the passive sets during the calculation.

2.4 Implementation within the finite elements method

2.4.1 Algorithm for the model

We use the notation introduced by [132] for the transformation of the strain and stress tensors to vectors and the elasticity tensor of fourth order to a matrix. The rotated elasticity constants can be obtained by first transforming them to matrices and afterwards rotating them by special 6×6 matrices which can be obtained from the original 3×3 rotation matrices. Inversion of the elasticity tensors is simplified by this notation, too.

In order to solve the problem numerically, we use a staggered Newton algorithm. During a *predictor* step, we evaluate a guess for the consistency parameter ρ which will then be updated by a *corrector* step in order to reach the exit criteria of $\Phi(\boldsymbol{q}) = 0$. The update of the active set can be realized by applying a step function to the obtained volume fractions during each step of the calculation. After that, a re-normalization is necessary.

2.4.2 Implementation into the finite element method

We implement the micomechanical model for polycrystalline shape memory alloys into the finite element program FEAP, [1]. The method is used to minimize the well know potential

$$\Pi = \int_\Omega \Psi^{\mathrm{rel}}\,\mathrm{d}V - \int_\Omega \boldsymbol{u}\cdot\boldsymbol{f}\,\mathrm{d}V - \int_{\partial\Omega}\boldsymbol{u}\cdot\boldsymbol{t}\,\mathrm{d}A \to \min_{\boldsymbol{u}} \tag{2.24}$$

with the body's volume Ω, the free energy Ψ^{rel} from (2.10), the displacements $\boldsymbol{u}$, the body forces $\boldsymbol{f}$ and the traction vector $\boldsymbol{t}$. Minimization yields

$$\boldsymbol{R}_{\boldsymbol{u}} := \int_\Omega \boldsymbol{B}^T\cdot\tilde{\boldsymbol{\sigma}}\,\mathrm{d}V - \int_\Omega \boldsymbol{N}_{\boldsymbol{u}}\cdot\boldsymbol{f}\,\mathrm{d}V - \int_{\partial\Omega}\boldsymbol{N}_{\boldsymbol{u}}\cdot\boldsymbol{t}\,\mathrm{d}A \stackrel{!}{=} \boldsymbol{0}\,. \tag{2.25}$$

Again, in (2.25) the notation of [132] is applied. $\boldsymbol{N}_{\boldsymbol{u}}$ denotes the shape functions, $\boldsymbol{B}$ the operator matrix connecting displacements and strain and the stress. The stress can be calculated according to

$$\boldsymbol{\sigma} = \frac{\partial\Psi^{\mathrm{rel}}}{\partial\boldsymbol{\varepsilon}} = \mathbb{C}_{\mathrm{eff}} : (\boldsymbol{\varepsilon} - \boldsymbol{\eta}_{\mathrm{eff}})\,, \tag{2.26}$$

from which the tangent matrix needed for the Newton algorithm can be calculated in a straightforward way.

The common Gauß integration is applied wherefore the material model has to be evaluated for every Gaußpoint. Then the strain calculated by the finite element approach is used to calculate the resulting stresses $\boldsymbol{\sigma}$ and tangent operator matrix, $\mathbb{C}_{\mathrm{eff}}$, with updated volume fractions $\boldsymbol{\lambda}$. The stresses and the tangent operator matrix form then the basis for an iteration step within the finite element code. If the residual is small enough the global load is increased further.

2.5 Results

2.5.1 Finite element calculations

The following plots show the results obtained from a mesh consisting of 1712 elements. We use one layer of hexahedral elements through the specimen thickness in order to impose plane stress conditions. From the point of view of the material model the calculation is completely three dimensional. For each element, we use eight Gaußpoints and tri-linear shape functions. The number of orientations within the finite element calculation was set to 100 which yields representative results as shown in [70]. We present results for exemplary problems without pre-texture (the exponent q in formula (2.6) was set to zero) and with pre-texture ($q = 2$). In this case we find a higher number of crystallites which are orientated in direction of the longitudinal axis of the specimen ($n_{\text{pref}} = (1, 0, 0)$).

As material data, we use the transformation strains and elastic constants for CuAlNi [163]. The elastic constants for the austenite and the martensite phases in Mehrabadi-Cowin notation are

$$\mathbb{C}_{\text{aust}} = \begin{pmatrix} 142.38 & 124.10 & 124.10 & 0 & 0 & 0 \\ 124.10 & 142.38 & 124.10 & 0 & 0 & 0 \\ 124.10 & 124.10 & 142.38 & 0 & 0 & 0 \\ 0 & 0 & 0 & 95.24 & 0 & 0 \\ 0 & 0 & 0 & 0 & 95.24 & 0 \\ 0 & 0 & 0 & 0 & 0 & 95.24 \end{pmatrix} \text{GPa} \tag{2.27}$$

and

$$\mathbb{C}_{\text{mart}} = \begin{pmatrix} 184.46 & 140.41 & 70.09 & 0 & 0 & 0 \\ 140.41 & 151.45 & 86.83 & 0 & 0 & 0 \\ 70.09 & 86.83 & 238.58 & 0 & 0 & 0 \\ 0 & 0 & 0 & 66.39 & 0 & 0 \\ 0 & 0 & 0 & 0 & 22.85 & 0 \\ 0 & 0 & 0 & 0 & 0 & 60.55 \end{pmatrix} \text{GPa} \,. \tag{2.28}$$

The transformation strains for the six martensite variants are summarized in Table 2.1, with $\bar{\alpha} = 0.0657501$, $\bar{\beta} = -0.0810031$ and $\bar{\gamma} = 0.0239604$. The transformation strain of austenite is equal to zero.

The pseudo-elastic results were computed using $\alpha_i = -0.025$ GPa for the chemical energy of the austenite phase and a dissipation coefficient $r = 0.012$ GPa.

As boundary conditions, we prescribe the displacements in $x-$direction (longitudinal) at one side of the body, while we enforce zero displacements at the other edge in $x-$ and $y-$direction.

Results shown in Fig. 2.1 and 2.2 present the average volume fraction of different phases ($\bar{\lambda}_i = \sum_{j=1}^{N} \xi^j \lambda_i^j$), namely that of the austenite phase and the martensite 3 phase, respectively. For each Gaußpoint, the volume fractions of all variants are averaged over the $N = 100$ orientations. The red

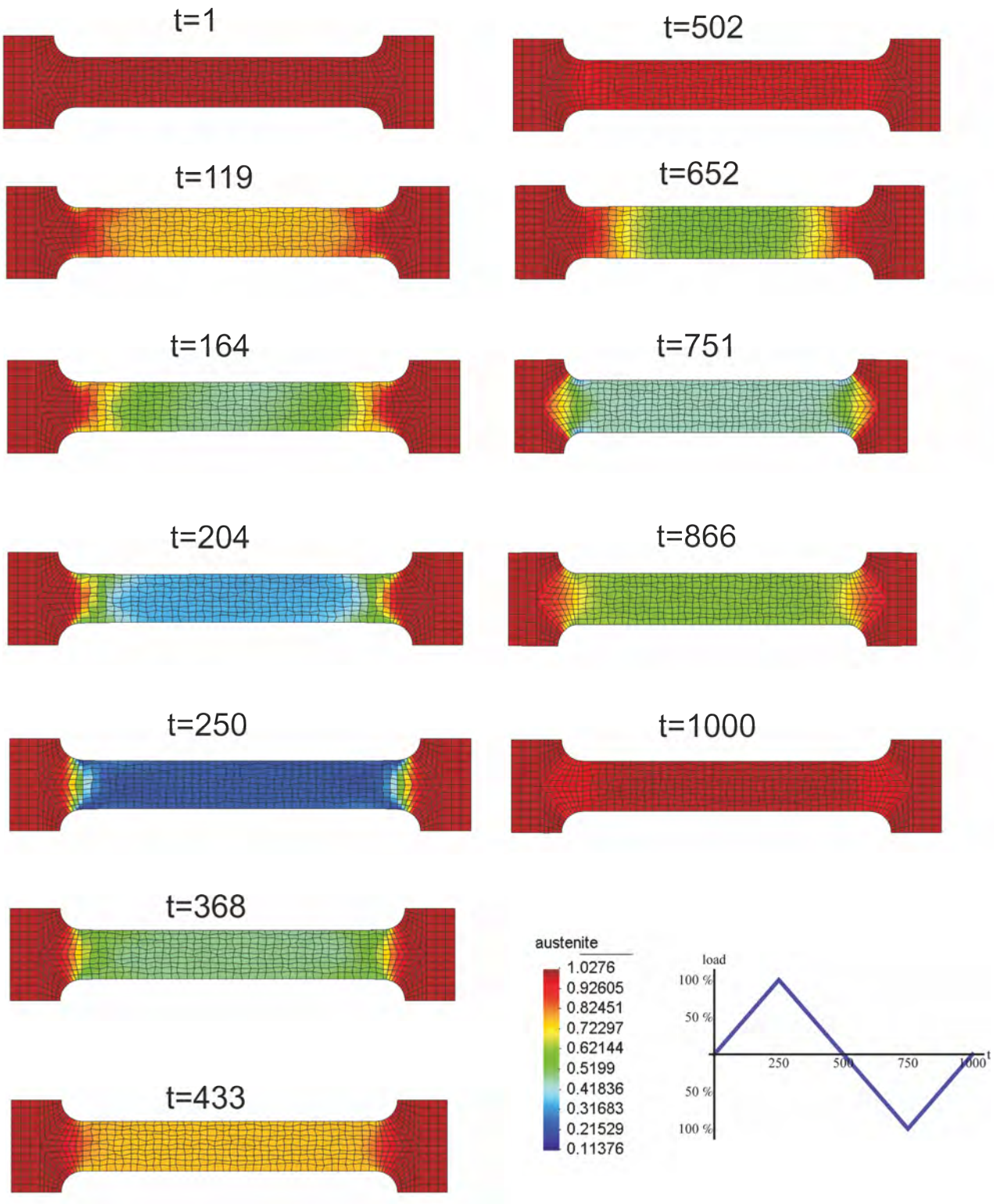

Figure 2.1: Average volume fraction during tension and compression of the austenite phase, $\bar{\lambda}_0$.

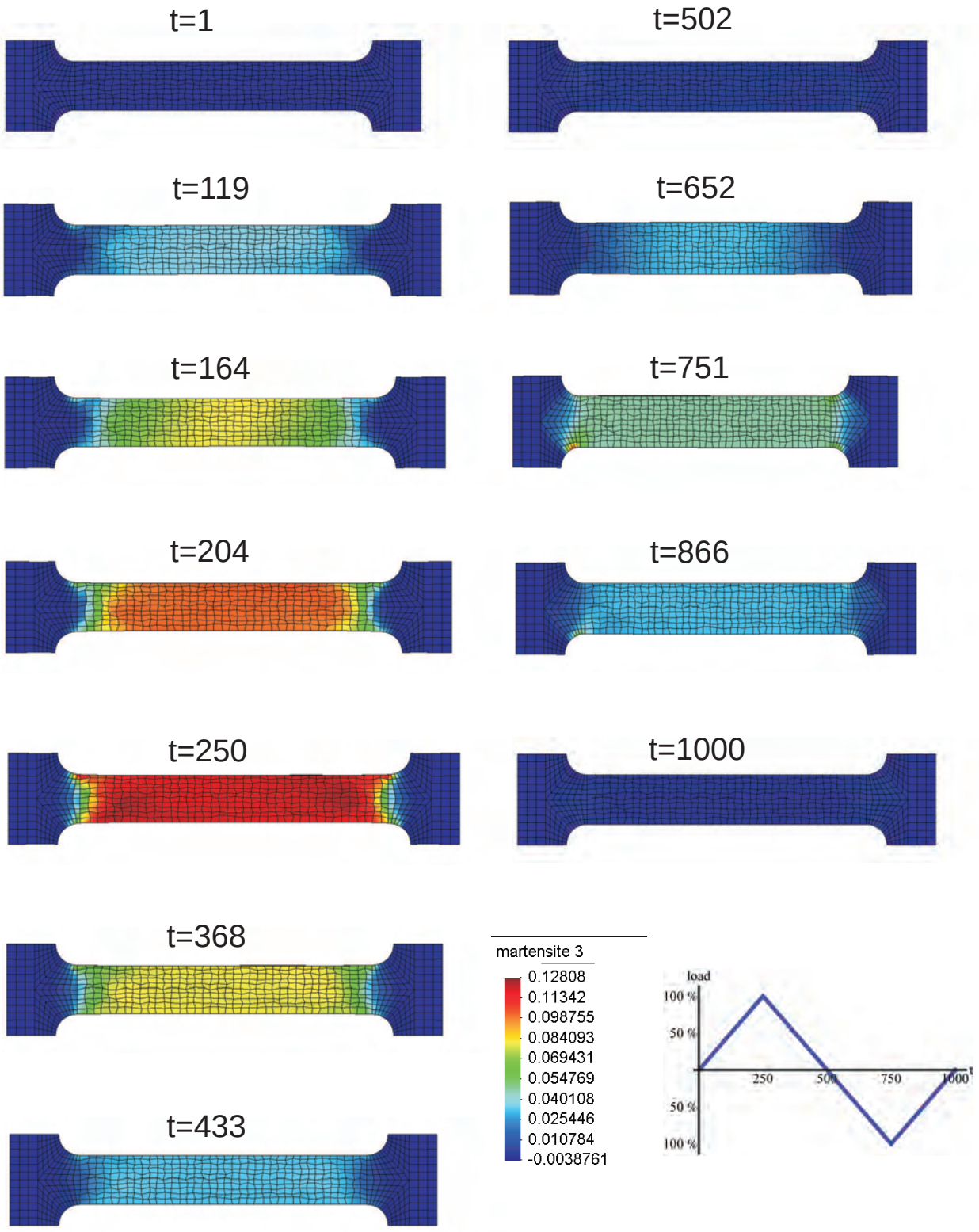

Figure 2.2: Average volume fraction during tension and compression of the martensite 3 phase, $\bar{\lambda}_3$.

Table 2.1: Transformation strains of the different martensite variants.

$$\boldsymbol{\eta}_1 = \begin{pmatrix} \bar{\beta} & 0 & 0 \\ 0 & \frac{\bar{\alpha}+\bar{\gamma}}{2} & \frac{\bar{\gamma}-\bar{\alpha}}{2} \\ 0 & \frac{\bar{\gamma}-\bar{\alpha}}{2} & \frac{\bar{\alpha}+\bar{\gamma}}{2} \end{pmatrix} \quad \boldsymbol{\eta}_2 = \begin{pmatrix} \bar{\beta} & 0 & 0 \\ 0 & \frac{\bar{\alpha}+\bar{\gamma}}{2} & \frac{\bar{\alpha}-\bar{\gamma}}{2} \\ 0 & \frac{\bar{\alpha}-\bar{\gamma}}{2} & \frac{\bar{\alpha}+\bar{\gamma}}{2} \end{pmatrix} \quad \boldsymbol{\eta}_3 = \begin{pmatrix} \frac{\bar{\alpha}+\bar{\gamma}}{2} & 0 & \frac{\bar{\gamma}-\bar{\alpha}}{2} \\ 0 & \bar{\beta} & 0 \\ \frac{\bar{\gamma}-\bar{\alpha}}{2} & 0 & \frac{\bar{\alpha}+\bar{\gamma}}{2} \end{pmatrix}$$

$$\boldsymbol{\eta}_4 = \begin{pmatrix} \frac{\bar{\alpha}+\bar{\gamma}}{2} & 0 & \frac{\bar{\alpha}-\bar{\gamma}}{2} \\ 0 & \bar{\beta} & 0 \\ \frac{\bar{\alpha}-\bar{\gamma}}{2} & 0 & \frac{\bar{\alpha}+\bar{\gamma}}{2} \end{pmatrix} \quad \boldsymbol{\eta}_5 = \begin{pmatrix} \frac{\bar{\alpha}+\bar{\gamma}}{2} & \frac{\bar{\gamma}-\bar{\alpha}}{2} & 0 \\ \frac{\bar{\gamma}-\bar{\alpha}}{2} & \frac{\bar{\alpha}+\bar{\gamma}}{2} & 0 \\ 0 & 0 & \bar{\beta} \end{pmatrix} \quad \boldsymbol{\eta}_6 = \begin{pmatrix} \frac{\bar{\alpha}+\bar{\gamma}}{2} & \frac{\bar{\alpha}-\bar{\gamma}}{2} & 0 \\ \frac{\bar{\alpha}-\bar{\gamma}}{2} & \frac{\bar{\alpha}+\bar{\gamma}}{2} & 0 \\ 0 & 0 & \bar{\beta} \end{pmatrix}$$

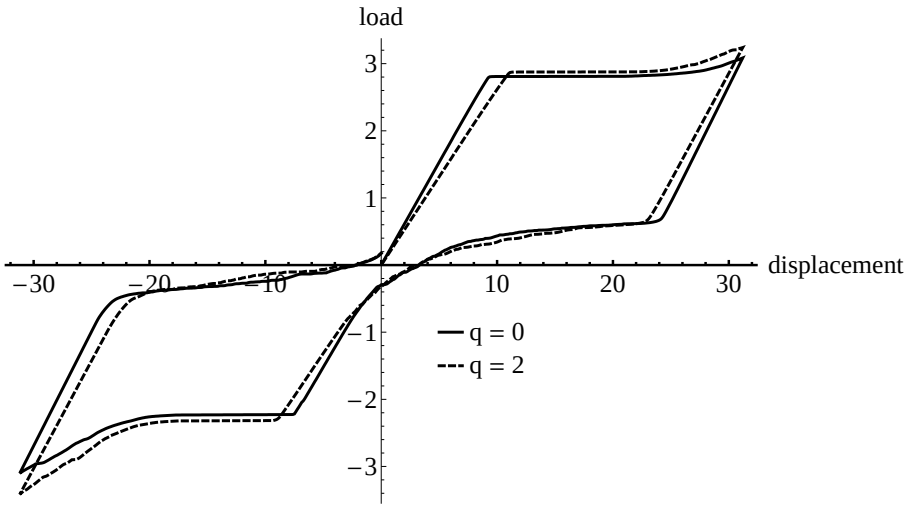

Figure 2.3: Load displacement curve for specimens with different pre-texture.

color indicates 100 percent of the specific phase, where the blue color coincides with zero percentage volume fraction. The minimum value for the austenitic phase is 11.4 %, the maximum value for the mastensitic 3 phase is 12.8 %. The evolution of the volume fractions show asymmetric behavior between tension and compression. Furthermore, the phase transition takes place in the part of the specimen where the maximum stresses occur. Interestingly the transformation starts in the shoulders of the specimen due to geometrically expected stress peaks. But in contrast to experimental results the subsequent transition takes place very homogeneously distributed over the geometry. The volume fractions of all phases are changing in the middle part of the body with a constant rate over space during tension and compression. Although front like transformations are observed in experiments, the global material reaction is mapped quite well which can be seen from the load-displacement curve, Fig. 2.3.

In Fig. 2.3 we show the average load-displacement curve. The dashed line represents the results for the same geometry under the same boundary conditions, but with a pre-texture. The preferred direction of the orientations is assumed to be parallel to the longitudinal axis of the specimen.

In contrast to the deviation of the phase distribution from experimentally observed behavior, the

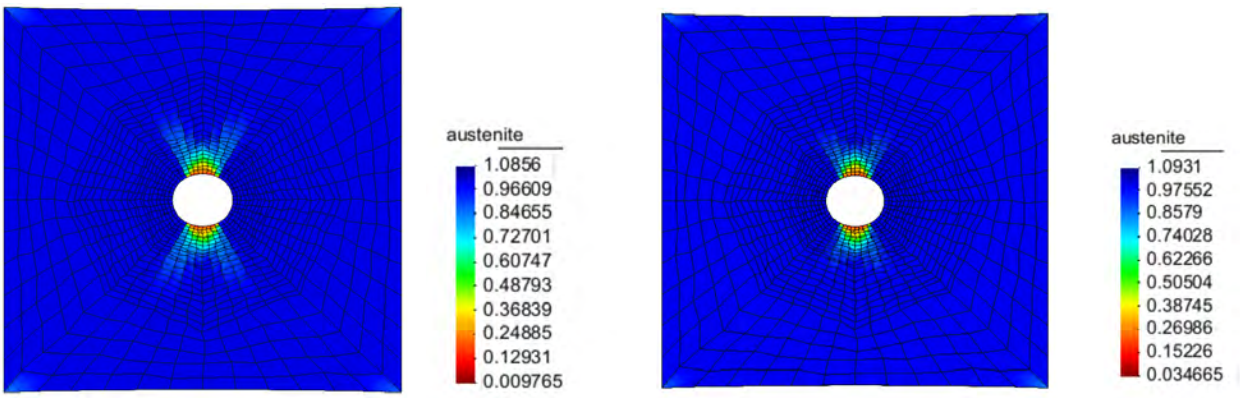

Figure 2.4: Distribution of the average austenitic phase ($\bar{\lambda}_0$) in a rectangular plate with centered hole at maximum load without (left) and with pre-texture (right).

resulting load-displacement diagrams display the typical characteristics of shape memory alloys. We see first the linear, pure austenitic material response when no transformation occurs. After reaching a critical point the curve runs parallel to the $x-$axes. This phenomenon, which is characteristic for shape-memory alloys, is observed during the transition from the austenitic to martensitic state. During unloading the occurring load reduces linearly again which is expected since in the first part of the unloading no transformation takes place. Analogously to the behavior during loading, again a critical point is reached and the martensite starts to change to austenite. In contrast to the loading state, during unloading we do not see the curve running parallel to the $x-$axes, but having a small slope. The slope of the curve increases as the deformation tends to zero. We still have, although relatively small, residual stress when the deformation equals zero. During compression a similar, but asymmetric behavior can be observed.

The application of a pre-texture has only a small influence on the occurring reaction force. Main differences can be found in the elastic region since the effective stiffness $\mathbb{C}_{\text{eff}}$ is calculated with a set of $\mathbb{C}_i^j$ which is orientated in a stronger way in the direction of the tension axes.

Additionally to the presented numerical results for a dog-bone shaped specimen under tension we investigate a rectangular plate with central hole which will exhibit more inhomogeneous stress states. The plate is fixed at the left hand side and pulled at the right hand side. We show the distribution of austenite and the maximum principal stress in the left hand sides of Fig. 2.4 and 2.5, respectively. As material parameters we use $\alpha = -0.045$ GPa and $r = 0.002$ GPa. Here, the distribution of stress is naturally more complicated in comparison to the basically one-dimensional stress state in tension tests. As expected stress peaks occur in the vicinity to the hole. Perpendicular to the horizontal direction the maximum principal stress is the highest. This is why phase transformations start here. At the maximum load the austenite vanishes with exception of an amount of approximately 9%.

On the right hand sides of Fig. 2.4 and 2.5 we present numerical results for a geometrically identical plate but now with a presumed pre-texture, $q = 2$. The distributions of austenite content and stress are similar. However, the transformed zone is larger compared to the case without pre-texture which causes that the residual austenite is higher in the case with pre-texture. Same observations are valid for the stress which is slightly more concentrated but has higher absolute values in the case with pre-texture.

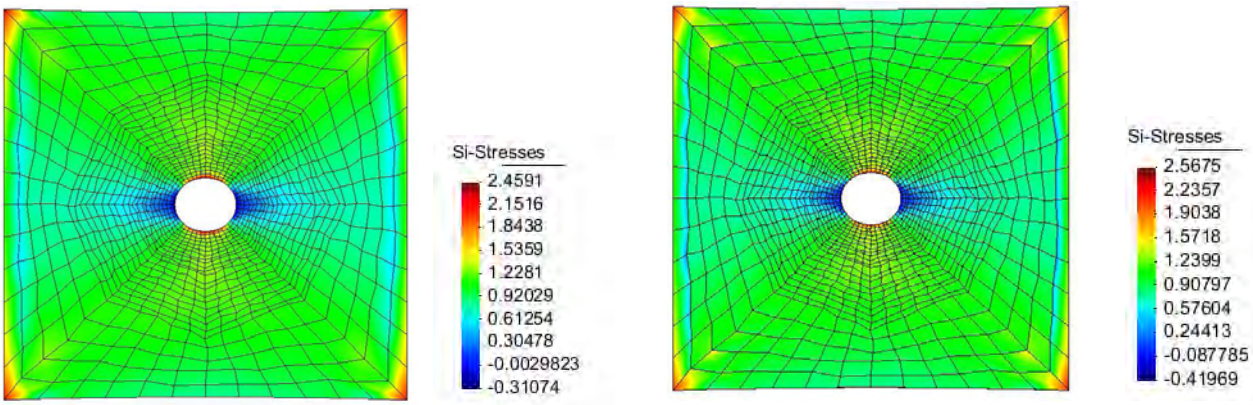

Figure 2.5: Distribution of the maximum principal stress in a rectangular plate with centered hole at maximum load without (left) and with pre-texture (right).

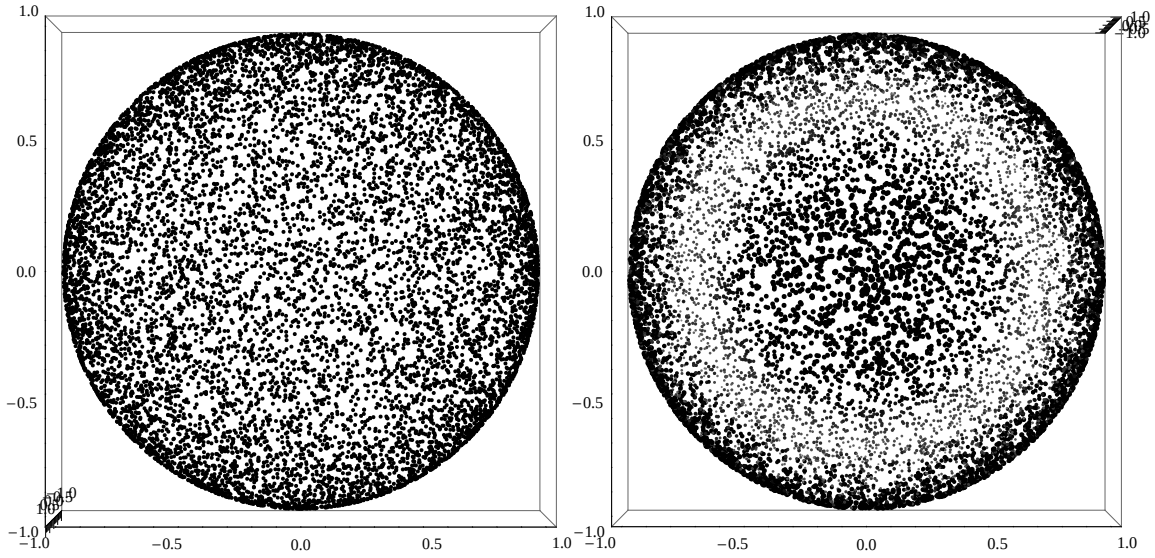

Figure 2.6: Polar plot in $\{1,0,0\}$-direction of the orientation distribution of martensite without (left) and with (right) pre-texure ($N = 10,000$).

2.5.2 Calculation of the orientation distribution

In order to save computing-time the finite-element calculations in the preceeding section have been performed with a small number of grains assumed in the material model. However, the stress-strain-behavior does not vary significantly between 100 and 10,000 orientations as can be seen from Fig. 2.7. This fact allows us to calculate detailed orientation-distributions in a post-processing step using a much higher number of grains.

The pole figures displayed in Fig. 2.8 and 2.9 are obtained from a succeeding calculation on the material point level with 10,000 orientations and the strains received from the finite element calculation for the dog-bone shaped tension test. The corresponding element is located in the center of the specimen. A

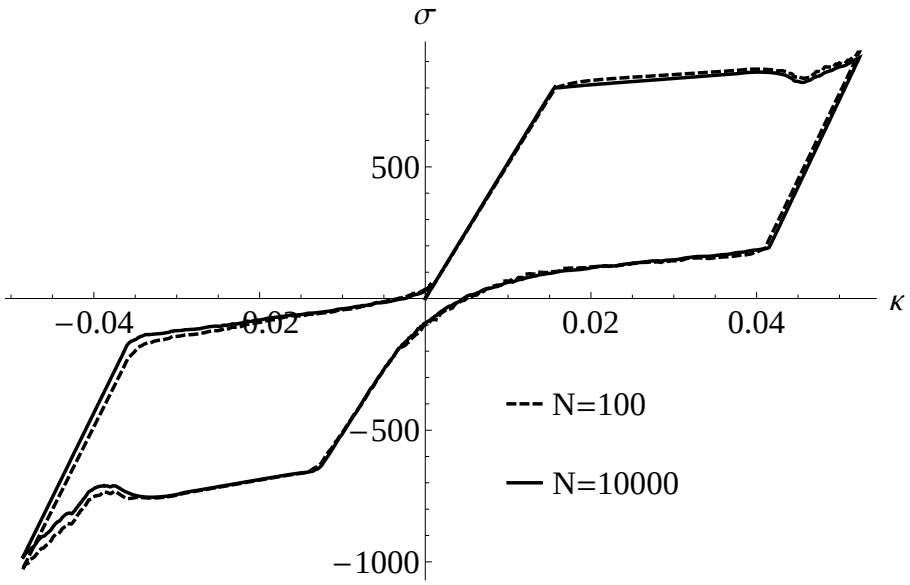

Figure 2.7: Comparison between stress-strain curves with $N = 100$ (used in FE calculation) and $N = 10,000$ (used in subsequent calculation for the pole figures) orientations. κ indicates the load state.

polar plot in $\{1,0,0\}$-direction of the orientation distribution of martensite for the case of a pre-texture with $q = 0$ and $q = 2$ is given in Fig. 2.6. Plotted are representative points scaled with their volume fraction $\boldsymbol{\xi}$ on the unit sphere.

In Fig. 2.8, the pole figures for the austenite phase for different pre-textures are shown in a comparative way, while Fig. 2.9 presents the pole figures for the martensite 3 phase. For all diagrams the first, third and last plot refer to zero prescribed displacement. The second plot indicates the distribution of preferred evolution directions at the end of the tension state whereas the fourth plot refers to the compression state. As already observed for the phase distribution, the pole figures show an asymmetric behavior during tension and compression. The pre-texture does not have a significant influence on the directions in which the evolution takes place.

Fig. 2.10 shows the pole figures without any pre-texture, $q = 0$ for the rectangular plate with hole. On the left hand side the results are given for an element located at the 12 o'clock position directly next to the hole. On the right hand side we present pole figures for the element again at the 12 o'clock position but this time with some distance to the hole. As expected the pole figures show a quite different behavior since the stress state differs. Most phase transformations are observed in directions which have an 'inclined' orientation with respect to the reference coordinate system.

To complete the analysis of re-orientation we present pole figures for the same elements in the plate as before but now for a calculation with some assumed pre-texture ($q = 2$), Fig.2.11. The results are comparable to the previous results without any pre-texture. In the case of a prescribed pre-texture the general reorientation demonstrated by the pole figures in Fig. 2.10 is more pronounced.

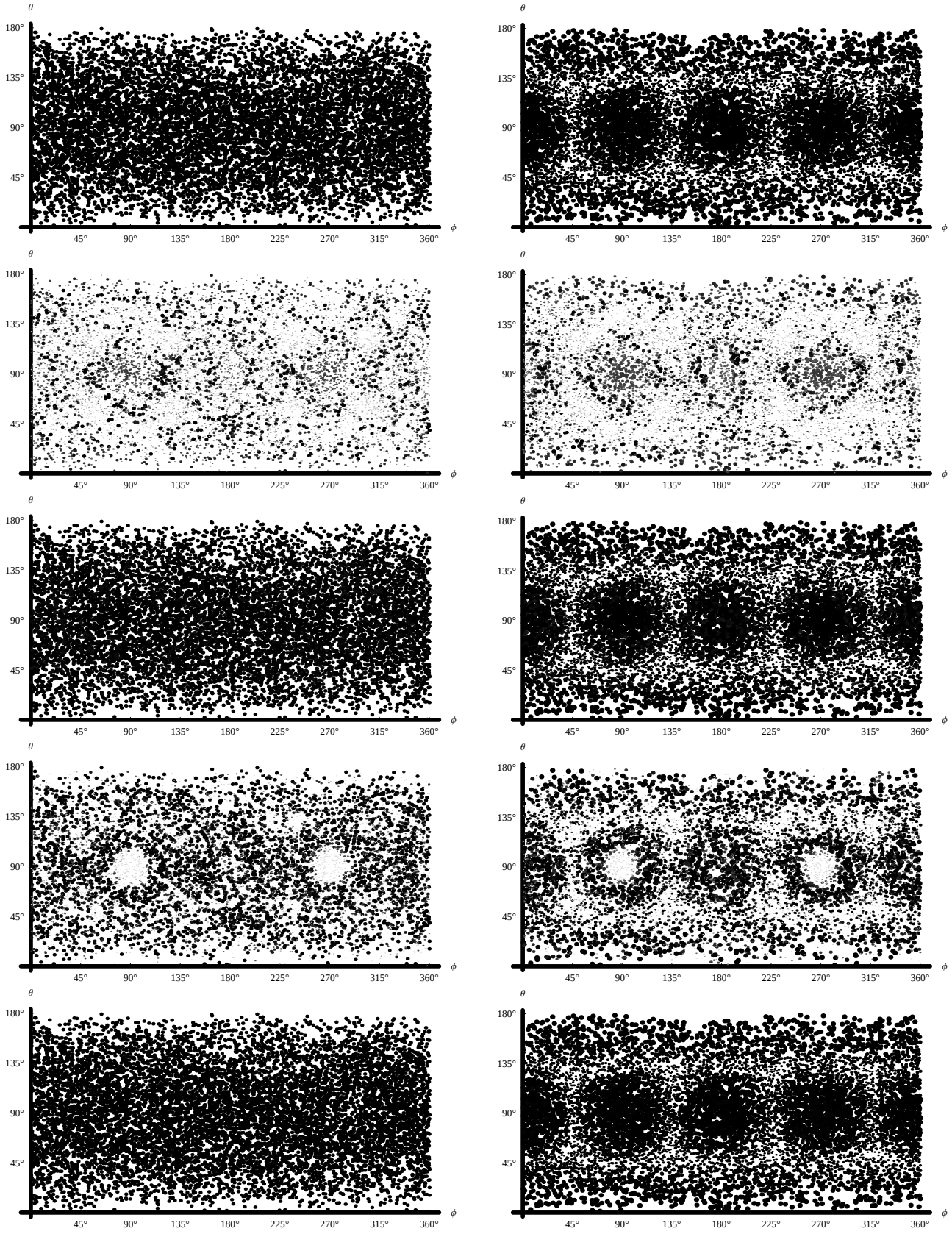

Figure 2.8: Pole figures for the austenite phase without ($q = 0$, left) and with ($q = 2$, right) pre-texture at the time points $t = \{1, 250, 500, 750, 1000\}$ (from top to bottom).

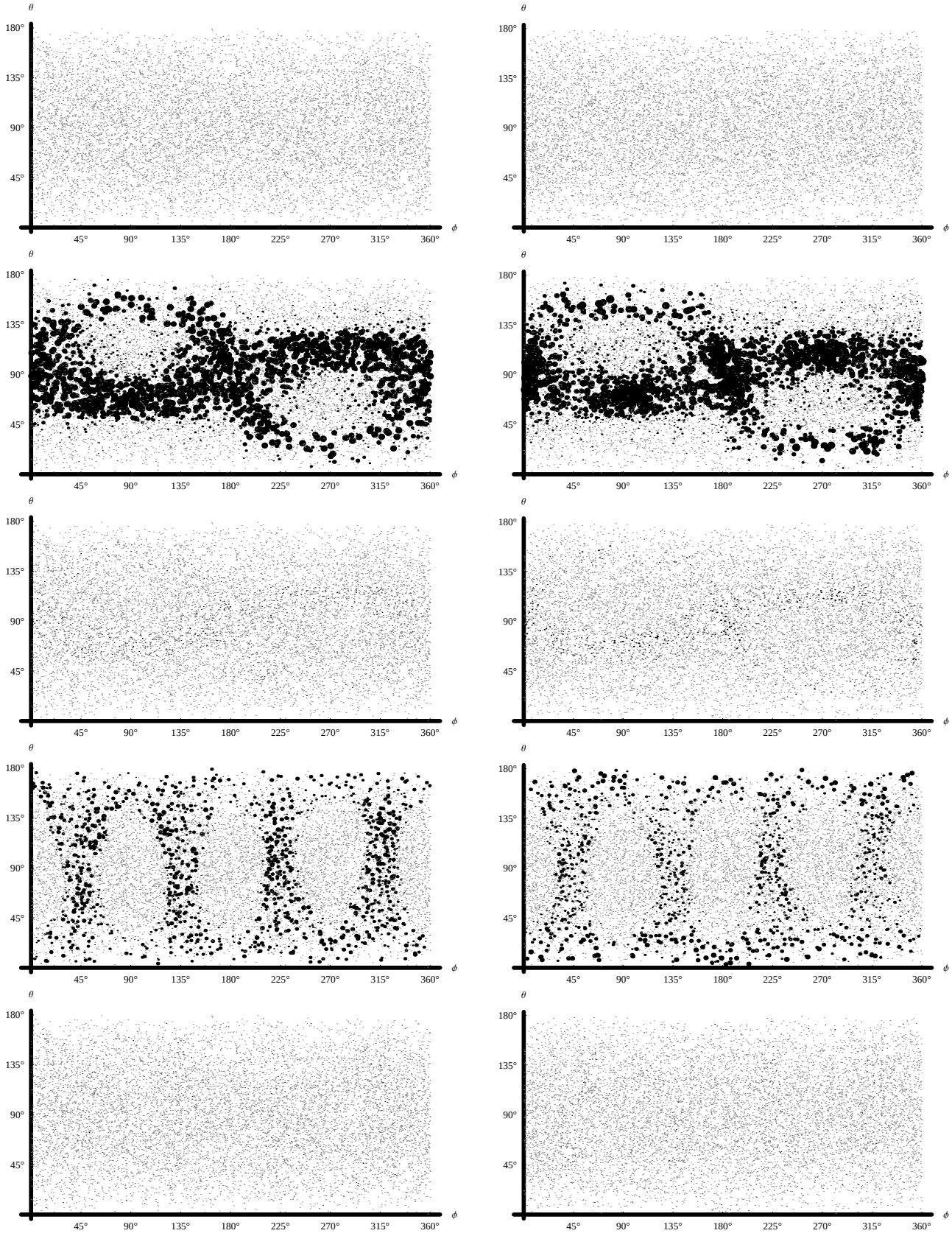

Figure 2.9: Pole figures for the martensite 3 phase without (q = 0, left) and with (q = 2, right) pre-texture at the time points $t = \{1, 250, 500, 750, 1000\}$ (from top to bottom).

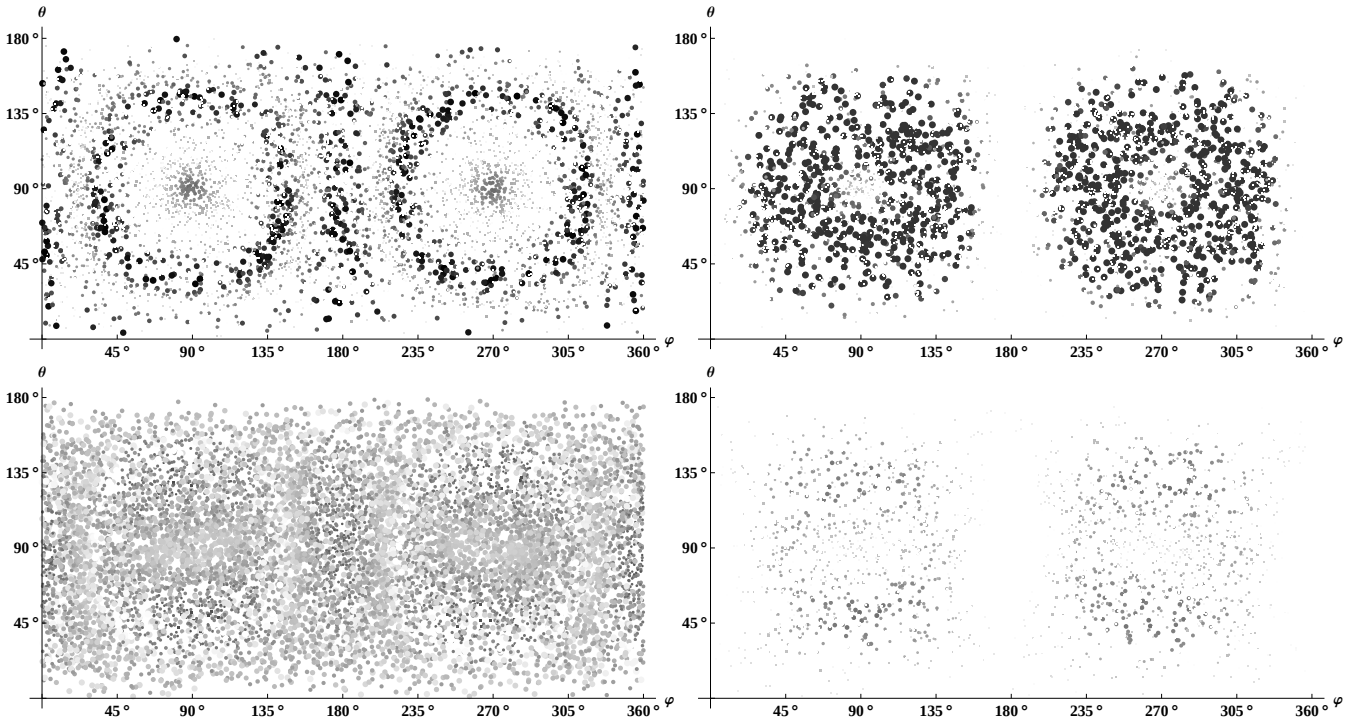

Figure 2.10: Pole figures for the austenite (top) and martensite 3 (bottom) without pre-texture for the 12 o'clock directly next to the hole (left) and with some distance to the hole (right) in a rectangular plate at maximum load without pre-texture.

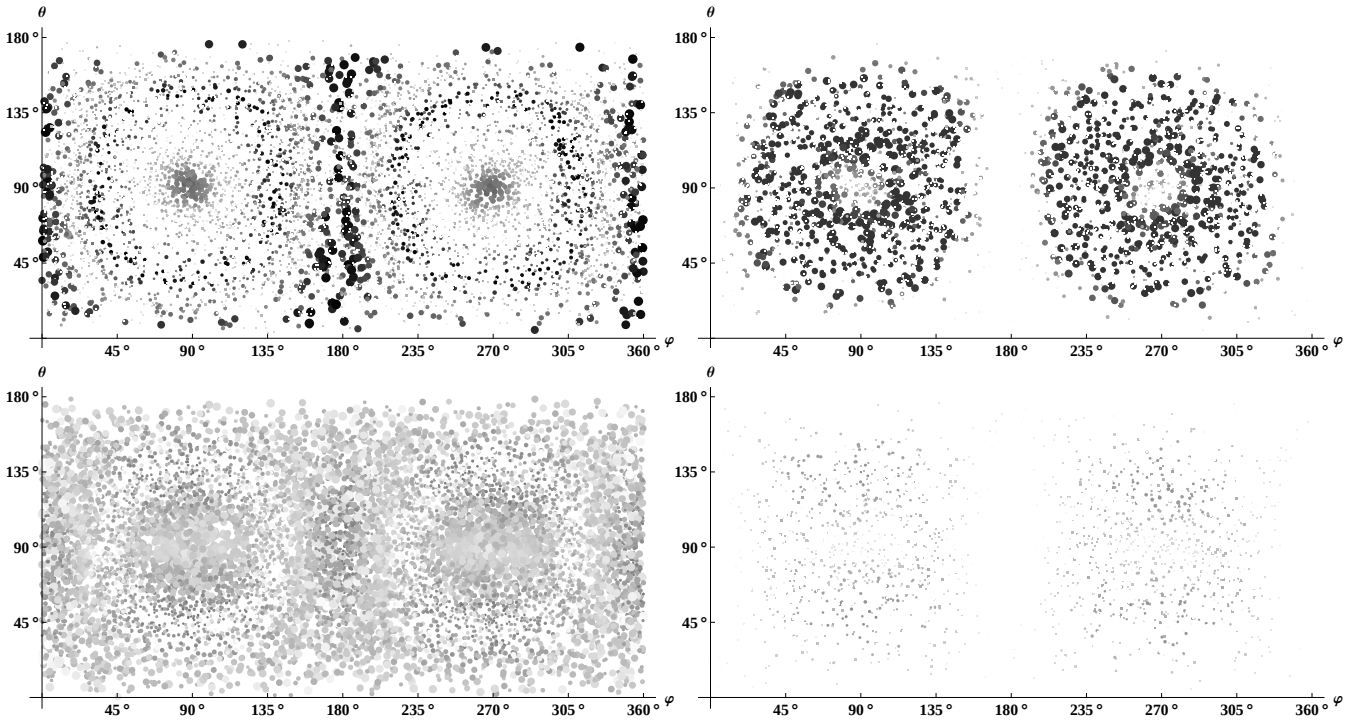

Figure 2.11: Pole figures for the austenite (top) and martensite 3 (bottom) without pre-texture for the 12 o'clock directly next to the hole (left) and with some distance to the hole (right) in a rectangular plate at maximum load with some pre-texture.

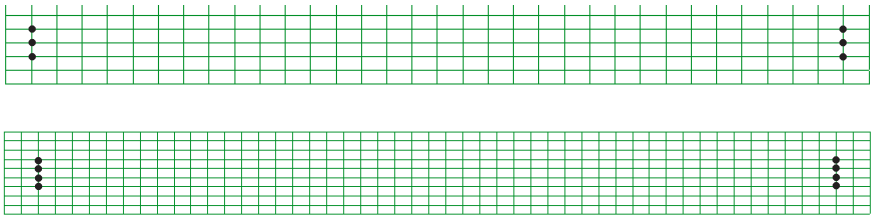

Figure 2.12: Different discretizations of a rectangular body and nodes with prescribed displacements.

2.5.3 Discussion of numerical performance

Obviously the material model has to be evaluated at every single Gauss point for every single iteration step. Thus, it is favored to keep the number of elements as small as possible. In order to study the accuracy of the method we employ in this section a rather simple geometry, namely a rectangular body. The boundary conditions are prescribed for the nodes which are marked in Fig. 2.12. This example is supposed to model a tension test of Nickel Titanium where a specimen is fixed at both ends, [162]. Hence, all displacements are set to zero except for the displacements in longitudinal direction at the nodes at the right hand side. These vary linearly in time.

First we show the results for a finite element implementation of the material model for a rather coarse mesh with 204 elements, Fig. 2.13. We see that, quite comparable to the dog-bone example above, the transformation starts where stress peaks occur, here where the body is fixed. This fact coincides well with experimental observations, [162]. In contrast, the subsequent behavior is different to experiments since the transformation proceeds homogeneously.

The result in Fig. 2.14 displays the same example, but here we use a rather fine mesh with 459 elements. The result of this fine discretization is very close to that one for the coarse discretization. The distribution of the austenitic phase is all the same. The only slight difference can be seen in the remaining amount of austenite which is insignificantly less than in the coarse mesh since some differences are expected due to the randomly chosen rotation matrices. We emphasize that the material model gives completely mesh independent results which can be seen in Figs. 2.13 and 2.14.

To complete the comparison of two different meshes we present the overall material response in a resulting force displacement diagram, Fig. 2.15. Here we see essentially no differences.

2.6 Conclusion

We have presented numerical results of a finite element implementation of a micromechanical model for polycrystalline shape memory alloys and analyzed the distribution of the different crystalline phases, preferred evolution directions in polycrystals and the global response of specimens with and without pre-texture by load-displacement diagrams for different examples.

Furthermore, we presented pole figures for the orientation distribution of the crystalline phases at a certain location of the geometry considered, which showed a tension-compression asymmetry. The

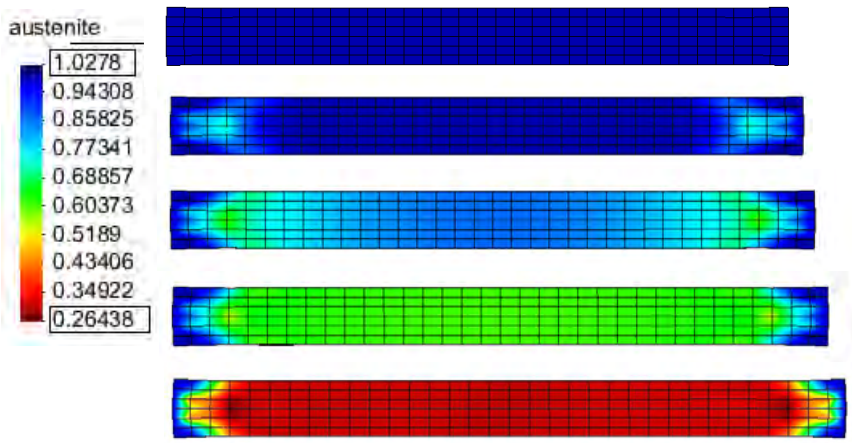

Figure 2.13: Austenite distribution of a stripe in a tension test, meshed with 204 elements.

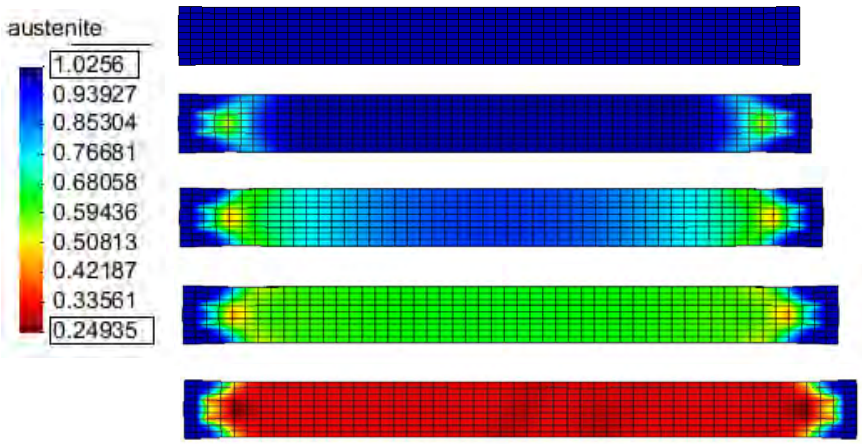

Figure 2.14: Austenite distribution of a stripe in a tension test, meshed with 459 elements.

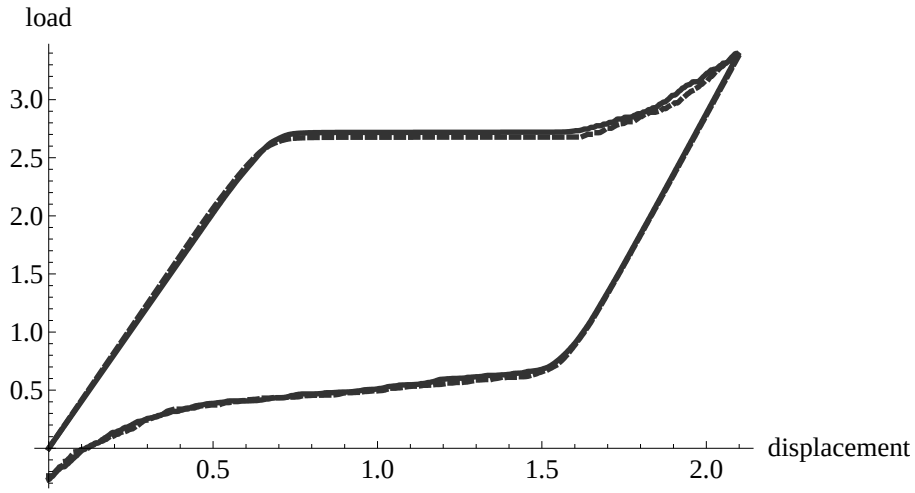

Figure 2.15: Comparison of the resulting force displacement of a stripe in a tension test, meshed with 204 (black line) and 459 (dashed line) elements respectively.

approach of using the finite element method to obtain the strain at a point of interest in the specimen together with a subsequent calculation at the material point-level employing a much higher number of crystallites has been justified by appropriate numerical tests. This approach allows to obtain a closer look on the martensitic reorientation during mechanical loading.

Concluding we presented an additional example for which we analyzed the numerical behavior by choosing two different discretizations, a fine one and a coarse one. The results for both discretizations differed only very slightly which proofs mesh independence of the material model. Due to the relatively high numerical effort of the finite element evaluation of the material model, a coarser mesh is more favorable. This approach is valid (until a certain threshold, of course) as the results proof empirically.

The current model leads to almost homogeneous phase transformations in regions with similar stress states. This material response does not completely coincide with experimental observations , [162]. Interestingly, previous investigations of the model used here in [70] proved that the model is capable to reproduce the main features of shape-memory alloys at the material point-level. The resulting load-displacement curves now in the scope of finite elements reflect the main characteristics of shape-memory alloys such as stress-plateau, hysteresis and tension-compression asymmetry. Therefore, it agrees regarding that aspect with experiments quantitatively, too.

In conclusion we can infer that the model in its current state can be developed further in order to reproduce a completely correct phase distribution over the geometry of the specimen. To model the experimentally observed front ('Lüdersband') like transformations, [162], a further trigger seems to be necessary since the stress enhancement due to the geometry obviously does not result in a sufficiently high raise of the driving forces. Thus, future work will focus on that topic. Furthermore the current model only reflects isothermal processes. The occurring solid to solid phase transformation is exothermic. The emitted heat then influences back the metamorphosis. Therefore another aim of ours is the derivation of a thermodynamically consistent model which takes the thermal coupling into account.

3 Heat conduction and localization

Published as: *P. Junker, K. Hackl*: A thermo-mechanically coupled field model for shape memory alloys, *Continuum Mech. Therm.* **26(6): 859–877 (2014)**

The impressive properties of shape memory alloys are produced by means of solid-to-solid phase transformations where thermal effects play an important role. In this paper we present a model for polycrystalline shape memory alloys which takes full thermo-mechanical coupling into account. Starting from the equations of the first and the second law of thermodynamics we derive evolution equations for the volume fractions of the different martensitic variants and a related equation for heat conduction. A thermodynamic analysis allows to formulate a complete expression for the dissipation caused by phase-transformation and heat flux. This allows to model the experimentally well documented transformation fronts in tension tests by a finite element scheme without further assumptions. Additionally, the number of required model parameters is very small in comparison with phenomenological approaches. Numerical examples are presented which show a good agreement with experimental observations.

3.1 Introduction

Shape memory alloys show a complex behavior. Pseudo-plasticity is the property related to the so-called "shape memory effect". Deformation applied to a construction part made from a pseudo-plastic alloy seems to be permanent. But surprisingly, heating the specimen will result in a spontaneous recovery of the original shape. This behavior is observed at relatively low temperatures. One has to distinguish here between the one way effect, which was just described, and the two way effect where a specimen will switch between two different ("deformed") configurations, controlled by temperature. Changing temperature will force the material to change its configuration. At higher temperatures a different material behavior can be observed. Here, the material behaves pseudo-elastically. This means that in contrast to "ordinary" metals, pseudo-elastic shape memory alloys may undergo very high strains elastically (up to 10%).

Which particular material behavior is present depends only on the current temperature, if the specific composition of the alloy is fixed. Since both pseudo-plasticity and pseudo-elasticity are accompanied by a hysteresis in the stress-strain diagram, both processes are dissipative, implying that heat is produced and the temperature changes during deformation. Since the material properties are highly dependent on the current temperature, it becomes obvious that thermal coupling should be included in a material model for shape memory alloys.

Two different structures can be formed by the crystal lattice of shape memory alloys. The cubic, high-symmetry lattice is called the austenitic phase and is stable at temperatures above the so-called transformation temperature. Furthermore there exists a number of less symmetric lattice structures which occur in states below the transformation temperature. These structures are known as the martensitic phase, of which several variants are related via symmetry. The exact number of these variants depends on the specific alloy. The ability to change between these crystal structures lies behind both the pseudo-elastic and pseudo-plastic behavior.

As of today, there exists a high number of different models for shape memory alloys which can be grouped into phenomenological and micromechanical ones. We would like to mention [22], [79], and [120] as examples for phenomenological ones. Foundations for micromechanical ones based on variational arguments were laid down in [10], [110], [138], and [190]. Micromechanical models are described in [60] and [177] for single crystals, and in [174] for polycrystals. Finite element implementations were presented in [153], where a model introduced in [185] is employed, [60], and [174]. In this paper we present a new approach which is able to capture all important features of shape memory alloys but needs only a minimum of modeling assumptions.

Our work relies on a micromechanical model for polycrystalline shape-memory alloys presented in [70]. This model synthesizes approaches in [61], [57], [77] and [94] and is based on energy relaxation, i.e. an approximation of the quasiconvex envelope of the elastic energy. A numerical implementation of the model and corresponding simulation results were presented in [97]. Although this model is in good agreement with experiments on a material point level, the numerical results for entire specimens show only limited coincidence with experimental findings. Specifically, it is known that in a tension test due to stress peaks at the supports phase transformation initializes. Starting from these localized transformation zones, the transformation proceeds in form of narrow fronts which are moving from the outer supports into the center of the specimen. After the front has passed, no further transformation is observed. The individual behavior highly depends on the inner microstructure of the material: due to processing effects (e.g. rolling, forging, wire drawing) the localized transformation can be symmetric or not, see [165] or [162] for example. Our objective, however, is to model whole specimens of shape memory alloys. Therefore, these effects have to be taken into account.

Temperature effects have an important impact on the phase transition since high temperature (relative to the transformation temperature) stabilizes the austenite whereas martensite is favored at low temperatures. The produced heat and the coupling between temperature and phase transformation therefore influences the material behavior. Experimental evidence for this can be found in [165] where a tension test under a relatively high tension velocity was investigated. The dissipation increases with higher velocity which results in higher heat production and thus higher temperature. Due to the stability of the austenitic phase at higher temperatures an increase of the number of transformation fronts as compared to the case of lower temperatures is observed.

Our approach is based on maximizing the rate of entropy production under the constraint of energy conservation, see [67], [69], [68]. This procedure yields evolution equations for the crystallographic phases and variants coupled to a corresponding heat conduction equation. Both, the equilibrium equation and the heat conduction equation, may be solved using a finite element approach.

As it will be shown, the model produces the localized transformation fronts. Special care has to be taken due to the softening character of the material behavior. Mesh dependent finite element results would be the outcome otherwise. Hence, we follow [95] and augment the elastic energy by a gradient term. For this we use a scheme presented in [39] and [40] for inelastic materials with softening.

In Section 3.2 we make use of the first and the second law of thermodynamics in order to derive an expression for the dissipation. Afterwards we employ the principle of maximum dissipation and obtain the evolution equations for the volume fractions of the crystallographic phases and variants as well as the heat conduction equation. In Section 3.3 the extension of the Helmholtz free energy by a non-local field function is carried out. The corresponding potential is minimized applying variational calculus and the heat conduction in its variational form is derived. In Section 3.4 we sketch the finite element

framework implemented in order to solve the previously derived variational equations. Section 3.5 is devoted to numerical results which are compared to the experimental ones of [162]. We display both the distribution of phases over the specimen as well as the temperature field. To emphasize the temperature dependence we furthermore show calculations with an increased loading speed and compare those to results in [165]. We conclude this paper in Section 3.6.

3.2 Material model

3.2.1 Thermodynamical principles

The equation of energy conservation can be formulated as [81]

$$\dot{\Psi} + s\,\dot{\theta} + \dot{s}\,\theta = \boldsymbol{\sigma} : \dot{\boldsymbol{\varepsilon}} + h - \nabla \cdot \boldsymbol{q} \tag{3.1}$$

with the time derivative of the Helmholtz free energy $\dot{\Psi}$, entropy s, absolute temperature θ, stress $\boldsymbol{\sigma}$, strain $\boldsymbol{\varepsilon}$, inner heat sources h and the vector of heat flux $\boldsymbol{q}$.

The second law of thermodynamics can be expressed by means of the non-conserving equation for entropy. It is given as

$$\dot{s}_{\mathrm{i}} = \frac{1}{\theta}\left(\boldsymbol{\sigma} : \dot{\boldsymbol{\varepsilon}} - \dot{\Psi} - s\,\dot{\theta}\right) + \boldsymbol{q} \cdot \nabla\frac{1}{\theta} \geq 0, \tag{3.2}$$

where $\dot{s}_{\mathrm{i}}$ is the rate of irreversible entropy production. Introducing the (rate of) dissipation $\mathcal{D} = \theta\dot{s}_{\mathrm{i}}$, Eq. (3.2) may also be written as $\mathcal{D} \geq 0$, see [69]. The Helmholtz free energy is a function of strain, temperature and the current microstructural state, expressed in terms of the internal variable $\boldsymbol{\lambda}$ which is specified in the next section. This allows using the identity

$$\dot{\Psi} = \frac{\partial\Psi}{\partial\boldsymbol{\varepsilon}} : \dot{\boldsymbol{\varepsilon}} + \frac{\partial\Psi}{\partial\boldsymbol{\lambda}} : \dot{\boldsymbol{\lambda}} + \frac{\partial\Psi}{\partial\theta}\dot{\theta}, \tag{3.3}$$

we can express the dissipation as

$$\mathcal{D} = \left(\boldsymbol{\sigma} - \frac{\partial\Psi}{\partial\boldsymbol{\varepsilon}}\right) : \dot{\boldsymbol{\varepsilon}} - \left(s + \frac{\partial\Psi}{\partial\theta}\right)\dot{\theta} - \frac{\partial\Psi}{\partial\boldsymbol{\lambda}} : \dot{\boldsymbol{\lambda}} - \frac{1}{\theta}\nabla\theta \cdot \boldsymbol{q}. \tag{3.4}$$

Let us decompose $\mathcal{D}$ into an energetic part $\mathcal{D}_{\mathrm{en}}$, a part due to phase transformation $\mathcal{D}_{\mathrm{ph}}$, and a part due to thermal flux $\mathcal{D}_{\mathrm{th}}$ as

$$\begin{aligned} \mathcal{D}_{\mathrm{en}} &= \left(\boldsymbol{\sigma} - \frac{\partial\Psi}{\partial\boldsymbol{\varepsilon}}\right) : \dot{\boldsymbol{\varepsilon}} - \left(s + \frac{\partial\Psi}{\partial\theta}\right)\dot{\theta}, \\ \mathcal{D}_{\mathrm{ph}} &= -\frac{\partial\Psi}{\partial\boldsymbol{\lambda}} : \dot{\boldsymbol{\lambda}}, \quad \mathcal{D}_{\mathrm{th}} = -\frac{1}{\theta}\nabla\theta \cdot \boldsymbol{q}. \end{aligned} \tag{3.5}$$

3.2.2 Evolution equations and heat conduction

In [70], [97], and [94] the principle of the minimum of the dissipation potential was used in order to derive evolution equations for internal variables, see [65], [149] and [30]. For the case of thermo-mechanical coupling studied here, it turns out to be more convenient to follow the idea of [146] to

maximize the entropy production (here $\mathcal{D}$) which is called principle of maximum dissipation. It has been shown in [67] that for many cases both principles yield the same or very close results.

To apply the principle of maximum dissipation to shape memory alloys, we claim that the dissipation due to phase transformation $\mathcal{D}_{\mathrm{ph}}$ in Eq. (3.5) depends only on the rates of the volume fractions of the crystallographic variants, and the dissipation due to thermal effects $\mathcal{D}_{\mathrm{th}}$ only on the heat flux:

$$\mathcal{D}_{\mathrm{ph}} = \bar{\mathcal{D}}_{\mathrm{ph}}(\dot{\boldsymbol{\lambda}}), \qquad \mathcal{D}_{\mathrm{th}} = \bar{\mathcal{D}}_{\mathrm{th}}(\boldsymbol{q}), \tag{3.6}$$

where for $\bar{\mathcal{D}}_{\mathrm{ph}}$ and $\bar{\mathcal{D}}_{\mathrm{th}}$ specific assumptions have to be made. Here, the volume fractions of the different crystallographic variants are collected in the vectorial quantity $\boldsymbol{\lambda} = (\boldsymbol{\lambda}^j) = (\lambda_i^j)$. The polycrystalline aspect of the material is taken into account by assigning a volume fraction vector $\boldsymbol{\lambda}^j$ to every assumed (grain) orientation $j \in \{1, \dots, N\}$. Here N is the number of different orientations assumed, each one being characterized by a rotation matrix $\boldsymbol{R}^j$. Within every orientation we identify the different variants by an index $i \in \{0, \dots, n\}$. The index 0 represents the austenite, and n number of martensitic variants. Then, λ_i^j gives the volume fraction of variant i within all the grains having orientation j. The volume fractions have to fulfill both mass conservation

$$\sum_{i=0}^{n} \dot{\lambda}_i^j = 0 \quad \forall\, j, \tag{3.7}$$

and positivity

$$\lambda_i^j \geq 0 \quad \forall\, i, j. \tag{3.8}$$

The principle of maximum dissipation now states, that $\mathcal{D}$ will be maximized with respect to the kinetic quantities $\dot{\boldsymbol{\varepsilon}}, \dot{\theta}, \dot{\boldsymbol{\lambda}}, \boldsymbol{q}$ under the constraints (3.6), (3.7), and (3.8). Let us for this purpose introduce a Lagrangian

$$\begin{aligned} \mathcal{L} =& \mathcal{D} + \beta_{\mathrm{ph}} \left(\mathcal{D}_{\mathrm{ph}} - \bar{\mathcal{D}}_{\mathrm{ph}}(\dot{\boldsymbol{\lambda}}) \right) + \beta_{\mathrm{th}} \left(\mathcal{D}_{\mathrm{th}} - \bar{\mathcal{D}}_{\mathrm{th}}(\boldsymbol{q}) \right) \\ &+ (1 + \beta_{\mathrm{ph}}) \left(\sum_{j=1}^{N} \kappa^j \sum_{i=0}^{n} \dot{\lambda}_i^j - \sum_{j=1}^{N} \sum_{i=0}^{n} \gamma_i^j \dot{\lambda}_i^j \right), \end{aligned} \tag{3.9}$$

where β_{ph}, β_{th}, and κ^j are Lagrange parameters and γ_i^j Kuhn-Tucker parameters associated with the constraints. We have Kuhn-Tucker conditions of the form

$$\begin{aligned} &\gamma_i^j = 0 \quad \text{for} \quad \lambda_i^j > 0 \vee \left(\lambda_i^j = 0 \wedge \dot{\lambda}_i^j > 0 \right), \\ &\gamma_i^j > 0 \quad \text{else.} \end{aligned} \tag{3.10}$$

The factor $1 + \beta_{\mathrm{ph}}$ in front of the Lagrange and Kuhn-Tucker terms is introduced for convenience. It only redefines the Lagrange and Kuhn-Tucker parameters and does not change the variational problem.

To find the stationary point of the Lagrange functional in Eq. (3.9) we calculate the variational derivatives of $\mathcal{L}$ with respect to the kinetic quantities $\dot{\boldsymbol{\varepsilon}}, \dot{\theta}, \dot{\boldsymbol{\lambda}}, \boldsymbol{q}$ and equate them to zero. Considering

(3.4), this yields

$$\frac{\partial \mathcal{L}}{\partial \dot{\boldsymbol{\varepsilon}}} = \mathbf{0} \quad \Leftrightarrow \quad \boldsymbol{\sigma} = \frac{\partial \Psi}{\partial \boldsymbol{\varepsilon}}, \tag{3.11}$$

$$\frac{\partial \mathcal{L}}{\partial \dot{\theta}} = 0 \quad \Leftrightarrow \quad s = -\frac{\partial \Psi}{\partial \theta}, \tag{3.12}$$

$$\frac{\partial \mathcal{L}}{\partial \dot{\boldsymbol{\lambda}}} = \mathbf{0} \quad \Leftrightarrow \quad -\beta_{\mathrm{ph}} \frac{\partial \bar{\mathcal{D}}_{\mathrm{ph}}}{\partial \dot{\boldsymbol{\lambda}}} + (1+\beta_{\mathrm{ph}}) \left(-\frac{\partial \Psi}{\partial \boldsymbol{\lambda}} + \boldsymbol{\kappa} - \boldsymbol{\gamma} \right) = \mathbf{0}, \tag{3.13}$$

$$\frac{\partial \mathcal{L}}{\partial \boldsymbol{q}} = \mathbf{0} \quad \Leftrightarrow \quad -\beta_{\mathrm{th}} \frac{\partial \bar{\mathcal{D}}_{\mathrm{th}}}{\partial \boldsymbol{q}} - (1+\beta_{\mathrm{th}}) \frac{1}{\theta} \nabla \theta = \mathbf{0}, \tag{3.14}$$

where $\boldsymbol{\kappa} = \kappa^j \boldsymbol{e}_i \boldsymbol{e}_j$, $\boldsymbol{\gamma} = \gamma_i^j \boldsymbol{e}_i \boldsymbol{e}_j$, and $\boldsymbol{e}_k$ denote unit vectors of dimension N. Eqs. (3.11) and (3.12) are the well-known constitutive relations of thermomechanics. They specifically imply $\mathcal{D}_{\mathrm{en}} = 0$. The equations (3.13) and (3.14) represent evolution laws. The Lagrange parameters β_{ph} and β_{th} can be found by multiplying Eq. (3.13) by $\dot{\boldsymbol{\lambda}}$, Eq. (3.14) by $\boldsymbol{q}$, and evaluating the constraints (3.6). Making use of the fact, that $\dot{\boldsymbol{\lambda}} : \boldsymbol{\kappa} = 0$ because of (3.7), and $\dot{\boldsymbol{\lambda}} : \boldsymbol{\gamma} = 0$ because of (3.10) we obtain

$$f_{\mathrm{ph}} := \frac{1+\beta_{\mathrm{ph}}}{\beta_{\mathrm{ph}}} = \frac{1}{\bar{\mathcal{D}}_{\mathrm{ph}}} \frac{\partial \bar{\mathcal{D}}_{\mathrm{ph}}}{\partial \dot{\boldsymbol{\lambda}}} : \dot{\boldsymbol{\lambda}}, \qquad f_{\mathrm{th}} := \frac{1+\beta_{\mathrm{th}}}{\beta_{\mathrm{th}}} = \frac{1}{\bar{\mathcal{D}}_{\mathrm{th}}} \frac{\partial \bar{\mathcal{D}}_{\mathrm{th}}}{\partial \boldsymbol{q}} \cdot \boldsymbol{q}. \tag{3.15}$$

In order to proceed further we will make specific assumptions on the form of the dissipation terms $\bar{\mathcal{D}}_{\mathrm{ph}}$ and $\bar{\mathcal{D}}_{\mathrm{th}}$ now. For the thermal dissipation we will employ $\bar{\mathcal{D}}_{\mathrm{th}} = \alpha_\theta |\boldsymbol{q}|^2$. This yields $f_{\mathrm{th}} = 2$ and we obtain from (3.14) the heat-conduction equation

$$-\frac{1}{\theta} \nabla \theta = \alpha_\theta \boldsymbol{q}, \tag{3.16}$$

identifying $1/(\theta \alpha_\theta)$ as thermal conductivity. Furthermore we assume the phase transformation to be a rate-independent process. This implies $\bar{\mathcal{D}}_{\mathrm{ph}}$ to be homogeneous of degree one in $\dot{\boldsymbol{\lambda}}$, i.e. $\bar{\mathcal{D}}_{\mathrm{ph}}(\alpha \dot{\boldsymbol{\lambda}}) = |\alpha| \bar{\mathcal{D}}_{\mathrm{ph}}(\dot{\boldsymbol{\lambda}})$. This yields $f_{\mathrm{ph}} = 1$. The decoupled formulation of the dissipation in Eq. (3.9), where the two separated Kuhn-Tucker parameters β_{ph} and β_{th} have been used, yields the two separated expressions f_{ph} and f_{th}. In contrast to [96] and [91], the application of the principle of maximum dissipation in the form presented here agrees with Zieglers's principle [201], although we chose a dissipation function for $\boldsymbol{q}$ that is not homogeneous.

Because $\bar{\mathcal{D}}_{\mathrm{ph}}$ is non-differentiable now at $\dot{\boldsymbol{\lambda}} = \mathbf{0}$, Eq. (3.13) becomes a differential-inclusion of the form

$$\mathbf{0} \in \partial_{\dot{\boldsymbol{\lambda}}} \bar{\mathcal{D}}_{\mathrm{ph}} + \frac{\partial \Psi}{\partial \boldsymbol{\lambda}} - \boldsymbol{\kappa} + \boldsymbol{\gamma}. \tag{3.17}$$

Here $\partial_{\dot{\boldsymbol{\lambda}}}$ denotes the subdifferential with respect to $\dot{\boldsymbol{\lambda}}$. For detailed explanations of the usage of non-smooth differential calculus for inelastic problems, see [30], [67].

We still have to solve for the remaining Lagrange and Kuhn-Tucker parameters. Let us for this purpose introduce two sets for each grain: a *passive* set $\mathcal{B}^j$ and an *active* set $\mathcal{A}^j$ as

$$\mathcal{B}^j = \left\{ i | \lambda_i^j = 0 \right\}, \tag{3.18}$$

$$\mathcal{A}^j = \left\{ i \in \mathcal{B}^j | \dot{\lambda}_i^j > 0 \right\} \cup \left\{ i \notin \mathcal{B}^j \right\}. \tag{3.19}$$

This formulation ensures that the volume fractions included in the active set fulfil the constraint of positivity identically. Thus, the Kuhn-Tucker parameters for all phases in the active set are zero:

$$\gamma_i^j = 0 \qquad \text{for} \qquad i \in \mathcal{A}^j. \tag{3.20}$$

In order to avoid mathematical complications when proceeding further let us make a specific ansatz for the dissipation

$$\mathcal{D}_{\mathrm{ph}} = r\sqrt{\sum_{j=1}^{N} \xi^j \sum_{i=0}^{n} \left(\dot{\lambda}_i^j\right)^2} = r|\dot{\boldsymbol{\lambda}}|_{\boldsymbol{\xi}}. \tag{3.21}$$

Now $[\partial_{\dot{\boldsymbol{\lambda}}} \bar{\mathcal{D}}_{\mathrm{ph}}]_j^i = 0$ for $i \in \mathcal{A}^j$ and summation over $\mathcal{A}^j$ in Eq. (3.17) gives

$$\kappa^j = -\frac{1}{n_{\mathcal{A}^j}} \sum_{k \in \mathcal{A}^j} \frac{\partial \Psi}{\partial \lambda_k^j}, \tag{3.22}$$

where $n_{\mathcal{A}^j}$ is the number of active elements in the specific grain j. Let us introduce the thermodynamically conjugate driving force to $\dot{\boldsymbol{\lambda}}$ as

$$\boldsymbol{P} := -\frac{\partial \Psi}{\partial \boldsymbol{\lambda}}. \tag{3.23}$$

Substituting Eq. (3.22) into the differential inclusion (3.17) we obtain

$$[\mathrm{dev}_{\mathcal{A}} \boldsymbol{P}]_i^j = r\xi^j \frac{\dot{\lambda}_i^j}{\sqrt{\sum_{j=1}^{N} \xi^j \sum_{k=0}^{n} \left(\dot{\lambda}_k^j\right)^2}} \qquad \text{for} \qquad i \in \mathcal{A}^j \quad \text{and} \quad \dot{\boldsymbol{\lambda}} \neq \mathbf{0}, \tag{3.24}$$

$$\left(\sum_{j=1}^{N} \frac{1}{\xi^j} \sum_{i=0}^{n} \left([\mathrm{dev}_{\mathcal{A}} \boldsymbol{P}]_i^j\right)^2\right)^{1/2} \leq r \qquad \text{for} \qquad \dot{\boldsymbol{\lambda}} = \mathbf{0}, \tag{3.25}$$

$$[\mathrm{dev}_{\mathcal{A}} \boldsymbol{P}]_i^j = -\gamma_i^j < 0 \qquad \text{for} \qquad i \notin \mathcal{A}^j\,, \tag{3.26}$$

where we introduced the active deviator

$$[\mathrm{dev}_{\mathcal{A}} \boldsymbol{P}]_i^j := P_i^j - \frac{1}{n_{\mathcal{A}^j}} \sum_{k \in \mathcal{A}^j} P_k^j. \tag{3.27}$$

We can bring Eqs. (3.24) and (3.25) into a more familiar form by introducing a yield function

$$\Phi := \frac{1}{N} \sum_{j=1}^{N} \frac{1}{\xi^j} \sum_{i=0}^{n} \left([\mathrm{dev}_{\mathcal{A}} \boldsymbol{P}]_i^j\right)^2 - r^2\,. \tag{3.28}$$

Then Eq. (3.25) takes the form $\Phi \leq 0$. Hence Φ indicates whether phase transformation occurs and has therefore a similar meaning as yield functions known from plasticity. Now Eq. (3.24) may be written as

$$\dot{\lambda}_i^j = \frac{\rho}{\xi^j} [\mathrm{dev}_{\mathcal{A}} \boldsymbol{P}]_i^j \qquad \text{for} \quad i \in \mathcal{A}^j, \tag{3.29}$$

and we obtain the Kuhn-Tucker conditions

$$\rho \geq 0, \quad \Phi \leq 0, \quad \rho\,\Phi = 0. \tag{3.30}$$

Finally inequality (3.26) serves as a consistency condition representing an update criterion for the active set. For a more extensive exposition of the derivation above, see [70].

For the energy we use the expression developed in [70] as

$$\Psi = \frac{1}{2}\left(\boldsymbol{\varepsilon} - \boldsymbol{\eta}_{\text{eff}}\right) : \mathbb{C}_{\text{eff}} : \left(\boldsymbol{\varepsilon} - \boldsymbol{\eta}_{\text{eff}}\right) + c_{\text{eff}}(\theta), \tag{3.31}$$

with effective quantities defined as

$$\begin{aligned} \eta_{\text{eff}} &= \sum_{j=1}^{N}\sum_{i=0}^{n} \xi^j \lambda_i^j \underbrace{\left(\boldsymbol{R}^j\right)^T \cdot \boldsymbol{\eta}_i \cdot \boldsymbol{R}^j}_{=:\,\boldsymbol{\eta}_i^j}, \quad \mathbb{C}_{\text{eff}} = \left[\sum_{j=1}^{N}\sum_{i=0}^{n} \xi^j \lambda_i^j \left(\mathbb{C}_i^j\right)^{-1}\right]^{-1}, \\ c_{\text{eff}}(\theta) &= \sum_{j=1}^{N}\sum_{i=0}^{n} \xi^j \lambda_i^j c_i(\theta). \end{aligned} \tag{3.32}$$

We do not consider any pretexture due to previous processing like rolling or drawing. Therefore, all grain directions have the same probability which yields $\xi^j = 1/N$.

The elasticity tensors rotated in the local coordinate system may be calculated by

$$\mathbb{C}^j_{ipqrs} = R^j_{tp} R^j_{uq} R^j_{vr} R^j_{ws} \mathbb{C}_{ituvw}. \tag{3.33}$$

In here, we use different, anisotropic elastic constants for the austenite and the martensite state and randomly chosen orientation matrices $\boldsymbol{R}$ for each orientation j. For the temperature dependent chemical energies for both austenite and martensite $c_i(\theta)$ we use the approach of [87] as

$$c_i(\theta) = c_\theta\left(\theta - \theta_R\right) - c_\theta\,\theta \ln\left(\frac{\theta}{\theta_R}\right) + a_i - b_i\theta, \tag{3.34}$$

with a constant c_θ, representing the heat capacity, phase depending constants a_i and b_i (these constants have the same value for all martensite states but differ between austenite and martensite) and the reference or room temperature θ_R.

The temperature is a variable in our model. Thus, we have to find an equation which describes the evolution of temperature. In order to do so, we employ the conservation of energy via Eq. (3.1). Substituting Eqs. (3.11), (3.12), and (3.23) we obtain

$$-\boldsymbol{P} : \dot{\boldsymbol{\lambda}} + \dot{s}\,\theta = -\nabla \cdot \boldsymbol{q} + h. \tag{3.35}$$

Using Eq. (3.12) we get

$$s = -\frac{\partial \Psi}{\partial \theta} = c_\theta \ln\left(\frac{\theta}{\theta_R}\right) + \sum_{j=1}^{N}\sum_{i=0}^{n} \xi^j \lambda_i^j b_i, \tag{3.36}$$

and

$$\dot{s} = c_\theta \frac{\dot{\theta}}{\theta} + \sum_{j=1}^{N}\sum_{i=0}^{n} \xi^j \dot{\lambda}_i^j b_i. \tag{3.37}$$

Inserting Eqs. (3.16) and (3.37) into Eq. (3.35), and assuming that there are no internal heat sources

$(h = 0)$ gives

$$c_\theta \dot{\theta} = \boldsymbol{P} : \dot{\boldsymbol{\lambda}} + \nabla \cdot \left(\frac{1}{\alpha_\theta} \frac{1}{\theta} \nabla \theta \right) - \theta \sum_{j=1}^{N} \sum_{i=0}^{n} \xi^j \dot{\lambda}_i^j b_i. \tag{3.38}$$

In conclusion, we have found evolution equations for both the volume fractions of the crystallographic phases and the temperature as

$$\dot{\lambda}_i^j = \frac{\rho}{\xi^j} \left[\operatorname{dev}_{\mathcal{A}^j} p_i^j \right]_{\mathcal{A}^j}, \tag{3.39}$$

$$c_\theta \dot{\theta} = \boldsymbol{P} : \dot{\boldsymbol{\lambda}} + \nabla \cdot \left(\frac{1}{\alpha_\theta} \frac{1}{\theta} \nabla \theta \right) - \theta \sum_{j=1}^{N} \sum_{i=0}^{n} \xi^j \dot{\lambda}_i^j b_i, \tag{3.40}$$

with the Kuhn-Tucker conditions

$$\rho \geq 0, \quad \Phi \leq 0, \quad \rho \Phi = 0, \tag{3.41}$$

and the consistency condition

$$\operatorname{dev}_{\mathcal{A}^j} \boldsymbol{P}_i^j \leq 0 \quad \text{for } i \notin \mathcal{A}^j, \tag{3.42}$$

which serves as update criteria for the active set.

3.2.3 Estimation of the dissipation coefficient r

We begin with a short digression and evaluate our material model for a differential scanning calorimetry (DSC) experiment. Here, a small sample is heated and cooled without any constraints for the displacements. Hence, a stress-free state is present during the entire process. For the simulation of the DSC process, we just vary the temperature in time and evaluate our model at the material point level. We use CuAlNi as example, taking the material data from [97], specifically $r = \text{const} = 0.01137$ GPa. This alloy can form six martensitic variants. Due to the symmetry of the process all martenistic variants in all grains behave in an equal way. We present the volume fraction of one variant in Fig. 3.1. This result deviates to some extent from the experimental findings in [48], where larger differences between the start and finish temperatures of the respective phase transformations have been observed. However, the hysteresis in the diagram opens up the possibility to calculate the dissipation parameter from experimentally determined quantities.

Recall that the yield function defined in Eq. (3.28) satisfies $\Phi = 0$ when phase transformation takes place. For the special case of thermal loading in a stress-free setting the active deviator has the form

$$[\operatorname{dev}_{\mathcal{A}^j} P]_i^j = \begin{cases} P_0^j - \dfrac{1}{n+1} \displaystyle\sum_{i=0}^{n} P_i^j & \forall j\,,\ i = 0 \quad \text{(austenite)}, \\ P_{i>0}^j - \dfrac{1}{n+1} \displaystyle\sum_{i=0}^{n} P_i^j & \forall j\,,\ i > 0 \quad \text{(martensite)}. \end{cases} \tag{3.43}$$

Here, the driving forces involve the chemical energies only (no mechanical loading) which are the same for all martensitic variants and do not depend on the orientation j. Moreover all phases become active in this case. Thus, for convenience we rename the driving forces as P_{A} for austenite and P_{M}

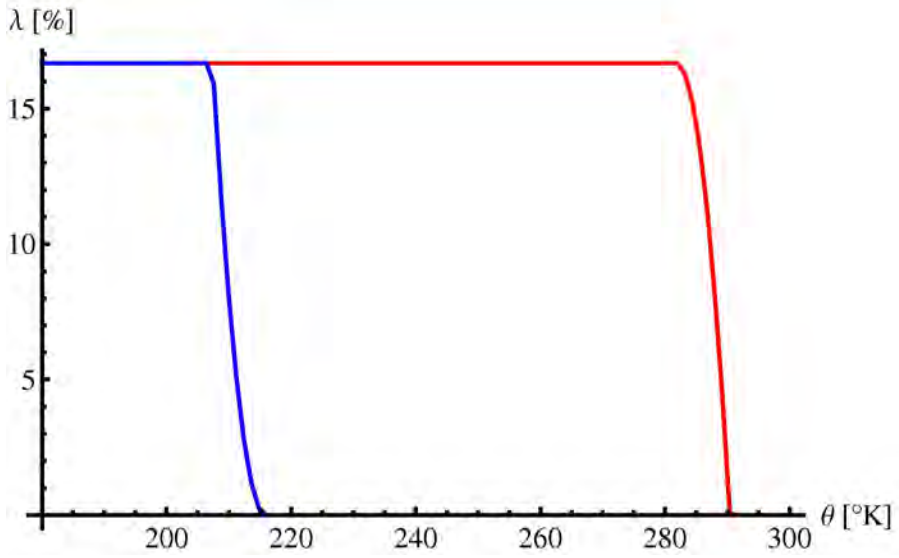

Figure 3.1: Phase fraction of one martensitic variant over time, $r = \text{const}$. Red curve is during heating, blue curve during cooling.

for martensite. Hence, the deviator reads

$$\begin{aligned} [\mathrm{dev}_{\mathcal{A}^j} P]_i^j &= \begin{cases} P_\mathrm{A}\left(1 - \dfrac{1}{n+1}\right) - \dfrac{n}{n+1} P_\mathrm{M} & \forall j\,,\ i = 0, \\ P_\mathrm{M}\left(1 - \dfrac{n}{n+1}\right) - \dfrac{1}{n+1} P_\mathrm{A} & \forall j\,,\ i > 0, \end{cases} \\ \Leftrightarrow \qquad [\mathrm{dev}_{\mathcal{A}^j} P]_i^j &= \begin{cases} \dfrac{n}{n+1}(P_\mathrm{A} - P_\mathrm{M}) & \forall j\,,\ i = 0 \quad \text{(austenite)}, \\ \dfrac{1}{n+1}(P_\mathrm{M} - P_\mathrm{A}) & \forall j\,,\ i > 0 \quad \text{(martensite)}. \end{cases} \end{aligned} \tag{3.44}$$

Inserting this result in the condition for transformation gives

$$\begin{aligned} & \Phi = 0 \\ \Leftrightarrow \qquad & \left[\sum_{j=1}^{N} \frac{1}{\xi^j} \sum_{i=0}^{n} \left([\mathrm{dev}_{\mathcal{A}^j} P]_i^j\right)^2\right] = r^2 \\ \Leftrightarrow \qquad & \left(\frac{n}{n+1}\right)^2 (-c_\mathrm{A} + c_\mathrm{M})^2 + \frac{n}{(n+1)^2}(-c_\mathrm{M} + c_\mathrm{A})^2 = r^2 \\ \Leftrightarrow \qquad & r = \sqrt{\frac{n}{n+1}}\,|\Delta c| \end{aligned} \tag{3.45}$$

with $|\Delta c| = |c_\mathrm{A} - c_\mathrm{M}|$ and the chemical energies c_A for austenite and c_M for martensite, respectively.

From Eq. (3.34) it can be seen that the difference in the chemical energies for austenite and martensite is a linear function of temperature, namely

$$\Delta c(\theta) := \Delta a - \Delta b\,\theta. \tag{3.46}$$

According to Eq. (3.45), the dissipation coefficient is proportional to the absolute value of the differences of the chemical energies. This fact coincides with the experimental observation in [48].

The transformation temperatures can be taken from experiments to calculate

$$\begin{aligned} r_{\mathrm{A}}^{s} &= \sqrt{\frac{n}{n+1}}\,|\Delta c(\theta_{\mathrm{A}}^{s})|\,, \quad r_{\mathrm{A}}^{f} = \sqrt{\frac{n}{n+1}}\,|\Delta c(\theta_{\mathrm{A}}^{f})| \\ r_{\mathrm{M}}^{s} &= \sqrt{\frac{n}{n+1}}\,|\Delta c(\theta_{\mathrm{M}}^{s})|\,, \quad r_{\mathrm{M}}^{f} = \sqrt{\frac{n}{n+1}}\,|\Delta c(\theta_{\mathrm{M}}^{f})|\,. \end{aligned} \tag{3.47}$$

This means we have to work with a non-constant dissipation parameter. However, due to the different temperature intervals for thermally driven phase transformation, temperature cannot be the variable describing the variation of r. In fact, the parameter chosen best is the average over all grains of the volume fraction of austenite, denoted as $\lambda_0 = \sum_{j=1}^{N} \xi^j \lambda_0^j$. This one will change its value during phase transformation from 0 to 1 or the other way around, without any direct dependence on the temperature interval. Hence, λ_0 may be interpreted as mathematical parameter describing both temperature intervals. Furthermore, there exists the possibility to transform from martensite to austenite (during heating) and backwards from austenite to martensite (during cooling). However, the differences in the chemical energies are not the same as pointed out before. So, an additional parameter is needed in order to distinguish between these two cases. Obviously, the sign of $\dot{\lambda}_0$ changes. Hence, this parameter is taken into account by formulating the dissipation coefficient as

$$r(\lambda_0, \dot{\lambda}_0) = \sqrt{\frac{n}{n+1}} \quad \begin{cases} r_{\mathrm{M}}^{f} + (r_{\mathrm{M}}^{s} - r_{\mathrm{M}}^{f})\,\lambda_0 & ,\ \dot{\lambda}_0 \le 0, \\ r_{\mathrm{A}}^{s} + (r_{\mathrm{A}}^{f} - r_{\mathrm{A}}^{s})\,\lambda_0 & ,\ \dot{\lambda}_0 > 0. \end{cases} \tag{3.48}$$

Using this non-constant dissipation coefficient and performing the same temperature-driven material point calculation as for the first example, we see a remarkable improvement in the model's quality: according to Fig. 3.2 the result is in very nice agreement to the experimental data from [48], where the starting and finishing temperatures for austenite and martensite where set to $\theta_{\mathrm{A}_s} = 265.0\,[\mathrm{K}]$, $\theta_{\mathrm{A}_f} = 280.0\,[\mathrm{K}]$, $\theta_{\mathrm{M}_s} = 230.0\,[\mathrm{K}]$ and $\theta_{\mathrm{M}_f} = 210.0\,[\mathrm{K}]$. Observe that the result depends only weakly on the exact values for Δa and Δb. This is due to the fact that not only the dissipation parameter depends on them but also the chemical energies in a way which has a neutralizing effect.

The presented approach for the dissipation coefficient is capable to describe in a thermodynamically sound way and based only on experimental data the temperature-induced transformation between austenite and martensite both during cooling and heating.

On the other hand, the formulation of r is not complete yet. In the case of pseudo-elasticity martensite evolves due to mechanical loading although austenite is the stable phase at that temperature. Hence, the ansatz for r - which so far is based only on thermal loading - has to be modified. For this purpose, let us assume that an initial austenitic configuration has been established by thermal transformation from martensite to austenite. After that the dissipation parameter is supposed to have the value r_{A}^{f}. When subsequently the austenite transforms to martensite in a pseudo-elastic (mechanical) manner, we assume that in the end r takes the same value as when martensite is beginning to transform to austenite during thermally driven transformations. This is $r = r_{\mathrm{A}}^{s}$.

When the specimen is unloaded, a martensite to austenite phase transition takes place. Here, we make similar assumptions as for the loading case: in the beginning of the reverse transformation, in

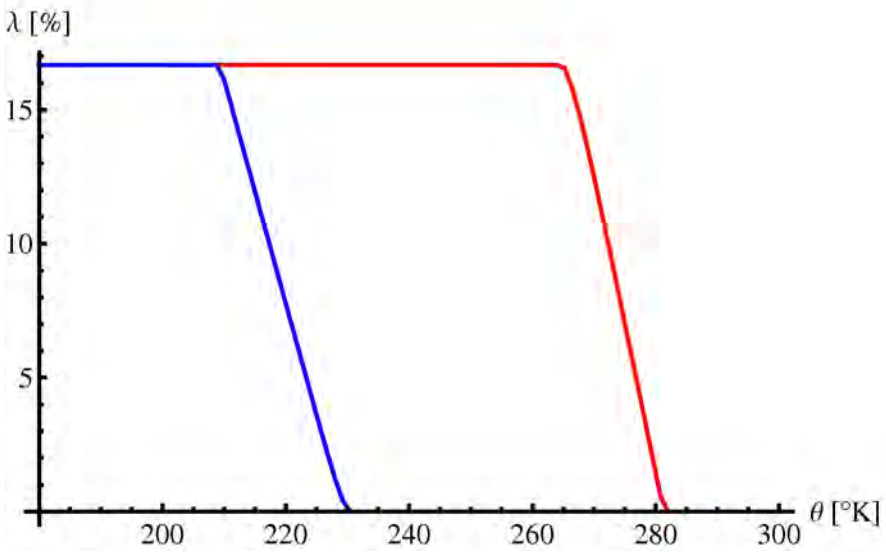

Figure 3.2: Phase fraction of one martensitic variant over time, r according to Eq. (3.48). Red curve is during heating, blue curve during cooling.

an idealized specimen no austenite is present but a specific composition of martensitic variants. Hence, this state is very comparable to the state when the thermally driven austenite to martensite phase transformation has finished. Consequently, r should start with the value of r_{M}^{f}. In the end, when no martensite is left and the material has completely transformed to austenite again, analogously r is r_{M}^{s}. This yields for the total dissipation parameter in dependence of λ_0 and $\dot{\lambda}_0$ and accounting for θ

$$r(\lambda_0,\dot{\lambda}_0,\theta) = \sqrt{\frac{n}{n+1}} \begin{cases} r_{\mathrm{M}}^{f} + (r_{\mathrm{M}}^{s} - r_{\mathrm{M}}^{f})\lambda_0 & ,\theta \le \theta_{\mathrm{A}}^{f} \wedge \dot{\lambda}_0 \le 0, \\ r_{\mathrm{A}}^{s} + (r_{\mathrm{A}}^{f} - r_{\mathrm{A}}^{s})\lambda_0 & ,\theta \le \theta_{\mathrm{A}}^{f} \wedge \dot{\lambda}_0 > 0, \\ r_{\mathrm{A}}^{s} + (r_{\mathrm{A}}^{f} - r_{\mathrm{A}}^{s})\lambda_0 & ,\theta > \theta_{\mathrm{A}}^{f} \wedge \dot{\lambda}_0 \le 0, \\ r_{\mathrm{M}}^{f} + (r_{\mathrm{M}}^{s} - r_{\mathrm{M}}^{f})\lambda_0 & ,\theta > \theta_{\mathrm{A}}^{f} \wedge \dot{\lambda}_0 > 0. \end{cases} \tag{3.49}$$

The first two conditions of Eq. (3.49) are valid for room temperatures below the austenite finish temperature. The sign of the rate distinguishes again between austenite → martensite and martensite → austenite transformations. If $\lambda_0 = 0$ and $\dot{\lambda}_0 = 0$, then the first case of Eq. (3.49) applies giving $r = r_{\mathrm{M}}^{f}$, the value for r for pseudo-plasticity.

The last two cases account for pseudo-elasticity since here the expressions for r are interchanged according to the explanation above. In combination, this formulation accounts for both pseudo-elastic and pseudo-plastic processes as well as heating and cooling.

A schematic plot of the dissipation parameter is given in Fig. 3.3

In [95], a rather artificial dependence of the entropy production on the local composition of the phases was assumed allowing to account for the different dissipation due to nucleation of martensite and its evolution. In contrast to that formulation, we found here a physically justified approach without any further assumptions.

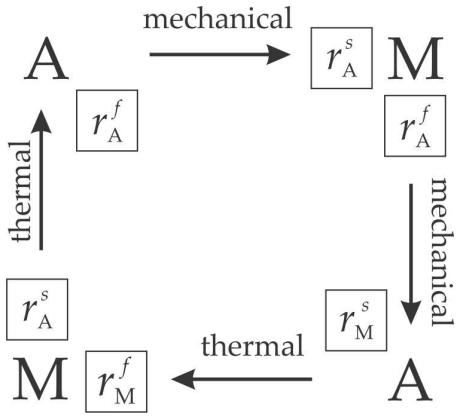

Figure 3.3: Schematic plot of the dissipation parameter. A indicates the austenite, M some martensitic composition.

3.3 Variational formulations

Our intention is the simulation of whole bodies made of shape memory alloys. Therefore we use a finite element approach in order to minimize the total energy of the system with the displacements as variables. A standard way to evaluate the presented model on a finite element layer would consist of minimizing the potential (or equivalently the Gibbs free energy $\mathcal{G} = \Pi$)

$$\Pi = \int_V \Psi \, \mathrm{d}V - \int_V \boldsymbol{u} \cdot (\rho \boldsymbol{f}) \, \mathrm{d}V - \int_{\partial V} \boldsymbol{u} \cdot \boldsymbol{t} \, \mathrm{d}A, \tag{3.50}$$

where $\boldsymbol{u}$ is the displacement, ρ the material's density, $\boldsymbol{f}$ the vector of body forces and $\boldsymbol{t}$ the tractions. Then, the material model has to be evaluated for every integration point where the specific internal configuration, represented by the volume fractions $\boldsymbol{\lambda}$, influences the stiffness. As mentioned above, the final expression for $\bar{\mathcal{D}}_{\mathrm{ph}}$ will cause a softening behavior. This means the minimization of (3.50) is an ill-posed mathematical problem and a standard finite element calculation would yield mesh dependent results. This phenomenon is obvious since phase transformations are boosted where they start leading to localized behavior.

In order to regularize the formulation above, we make use of the approach presented in [39], [40]. We introduce an extended energy given as

$$\Psi^{\mathrm{ext}}(\boldsymbol{\varepsilon}, \boldsymbol{\lambda}, \lambda_0, \varphi) = \Psi(\boldsymbol{\varepsilon}, \boldsymbol{\lambda}) + \frac{\beta_\varphi}{2} (\varphi + 1 - \lambda_0)^2 + \frac{c_\varphi}{2} |\nabla \varphi|^2, \tag{3.51}$$

with numerical parameters β_φ and c_φ. Here we have extended the energy Ψ by including a non-local field function φ. For β_φ large enough, φ is closely related to the total mount of martensite given by $1 - \lambda_0$. The term containing $\nabla\varphi$ then penalizes fluctuation of martensite content leading to the desired regularization.

Using the extended energy, we can calculate the driving forces P_i^j as

$$\begin{aligned} P_i^j &= -\frac{\partial}{\partial \lambda_i^j} \Psi^{\text{ext}}\left(\boldsymbol{\varepsilon}, \boldsymbol{\lambda}, \lambda_0, \varphi\right) \\ &= \xi^j \Big[\boldsymbol{\eta}_i^j : \mathbb{C}_{\text{eff}} : (\boldsymbol{\varepsilon} - \boldsymbol{\eta}_{\text{eff}}) \\ &\quad + \frac{1}{2} (\boldsymbol{\varepsilon} - \eta_{\text{eff}}) : \left(\mathbb{C}_{\text{eff}} : \left(\mathbb{C}_i^j \right)^{-1} : \mathbb{C}_{\text{eff}} \right) : (\boldsymbol{\varepsilon} - \eta_{\text{eff}}) - c_i(\theta) \Big] \\ &\quad + \underbrace{\xi^j \beta_\varphi \left(\varphi + 1 - \lambda_0\right) \delta_{0i}}_{\star} \, . \end{aligned} \tag{3.52}$$

In equation (3.52) the first part of the driving forces results from physical quantities while the second part ($\star$) derives from the extension of Ψ introduced above. The term ($\star$) connects the evolution of the volume fractions to the field function.

To find the minimum of the system's potential in Eq. (3.50) we calculate the variation of Π. These minimizing conditions read

$$\int_V \delta\boldsymbol{\varepsilon} : \frac{\partial \Psi}{\partial \boldsymbol{\varepsilon}} \, \mathrm{d}V - \int_V \delta \boldsymbol{u} \cdot (\rho \boldsymbol{f}) \, \mathrm{d}V - \int_{\partial V} \delta \boldsymbol{u} \cdot \boldsymbol{t} \, \mathrm{d}A = 0 \quad \forall \, \delta \boldsymbol{u}, \tag{3.53}$$

$$\int_V \beta_\varphi \left(\varphi + 1 - \lambda_0\right) \delta\varphi \, \mathrm{d}V + \int_V c_\varphi \nabla\varphi \cdot \nabla\delta\varphi \, \mathrm{d}V = 0 \quad \forall \, \delta\varphi. \tag{3.54}$$

For solving Eqs. (3.53) and (3.54) we use a finite element approach. Additionally, we have to solve the heat conduction equation in (3.40). This one may be interpreted as the Euler equation for a corresponding variational problem. Thus, we write a variational form of (3.40) as

$$\begin{aligned} \int_V c_\theta \, \dot{\theta} \, \delta\theta \, \mathrm{d} &= \int_V \boldsymbol{P} : \dot{\boldsymbol{\lambda}} \, \delta\theta \, \mathrm{d}V - \int_V \nabla \cdot \left(\frac{1}{\alpha_\theta} \frac{1}{\theta} \nabla\theta \right) \delta\theta \, \mathrm{d}V \\ &\quad - \int_V \theta \sum_{j=1}^{N} \sum_{i=0}^{n} \xi^j \dot{\lambda}_i^j b_i \, \delta\theta \, \mathrm{d}V \quad \forall \, \delta\theta. \end{aligned} \tag{3.55}$$

Partial integration gives

$$\begin{aligned} \int_V c_\theta \, \dot{\theta} \, \delta\theta \, \mathrm{d}V &= \int_V \boldsymbol{P} : \dot{\boldsymbol{\lambda}} \, \delta\theta \, \mathrm{d}V + \int_{\partial V} \boldsymbol{q} \cdot \boldsymbol{n} \, \delta\theta \, \mathrm{d}A + \int_V \frac{1}{\alpha_\theta} \frac{1}{\theta} \nabla\theta \cdot \nabla\delta\theta \, \mathrm{d}V \\ &\quad - \int_V \theta \sum_{j=1}^{N} \sum_{i=0}^{n} \xi^j \dot{\lambda}_i^j b_i \, \delta\theta \, \mathrm{d}V \quad \forall \, \delta\theta, \end{aligned} \tag{3.56}$$

where we made use of Eq. (3.16) giving the heat flux as $\boldsymbol{q} = -\frac{1}{\alpha_\theta} \frac{1}{\theta} \nabla\theta$.

3.4 Finite element approach

We are going to solve the coupled system of equations consisting of (3.53), (3.54), and (3.56) using the finite element method. Introducing standard tri-linear shape functions $\boldsymbol{N}_{\boldsymbol{u}}$, $\boldsymbol{N}_\varphi$, $\boldsymbol{N}_\theta$, and collecting the nodal values of the variables in vectors $\hat{\boldsymbol{u}}$, $\hat{\varphi}$, $\hat{\theta}$, the exact field functions are approximated by

$$\boldsymbol{u}(\boldsymbol{x}) = \boldsymbol{N}_{\boldsymbol{u}}(\boldsymbol{x}) \cdot \hat{\boldsymbol{u}}, \quad \varphi(\boldsymbol{x}) = \boldsymbol{N}_\varphi(\boldsymbol{x}) \cdot \hat{\boldsymbol{\varphi}}, \quad \theta(\boldsymbol{x}) = \boldsymbol{N}_\theta(\boldsymbol{x}) \cdot \hat{\boldsymbol{\theta}}, \tag{3.57}$$

where $\boldsymbol{x}$ is the position vector in space. Due to the different dimensions of the variables (the displacements are vectors, the field function and the temperature are scalars), $\boldsymbol{N_u}$ is a matrix while both $\boldsymbol{N}_\varphi$ and $\boldsymbol{N}_\theta$ are vectors. From Eq. (3.57), we find

$$\begin{aligned}
\delta\boldsymbol{u} &= \boldsymbol{N_u}\cdot\delta\hat{\boldsymbol{u}} \quad , \quad \tilde{\boldsymbol{\varepsilon}} = \boldsymbol{B}\cdot\hat{\boldsymbol{u}} \quad , \quad \delta\tilde{\boldsymbol{\varepsilon}} = \boldsymbol{B}\cdot\delta\hat{\boldsymbol{u}},\\
\delta\varphi &= \boldsymbol{N}_\varphi\cdot\delta\hat{\boldsymbol{\varphi}} \quad , \quad \nabla\varphi = \nabla\boldsymbol{N}_\varphi\cdot\hat{\boldsymbol{\varphi}} \quad , \quad \nabla\delta\varphi = \nabla\boldsymbol{N}_\varphi\cdot\delta\hat{\boldsymbol{\varphi}},\\
\delta\theta &= \boldsymbol{N}_\theta\cdot\delta\hat{\boldsymbol{\theta}} \quad , \quad \nabla\theta = \nabla\boldsymbol{N}_\theta\cdot\hat{\boldsymbol{\theta}} \quad , \quad \nabla\delta\theta = \nabla\boldsymbol{N}_\theta\cdot\delta\hat{\boldsymbol{\theta}}.
\end{aligned} \tag{3.58}$$

Here $\boldsymbol{B}$ is the usual displacement-strain operator and the strain $\tilde{\boldsymbol{\varepsilon}}$ in Mehrabadi-Cowin notation, [132]. The relations in (3.58) can now be introduced into the three variational equations (3.53), (3.54), (3.56) giving (for adiabatic processes, i.e. $\boldsymbol{q}\cdot\boldsymbol{n}=0$ at $\partial\Omega$) with stresses $\tilde{\boldsymbol{\sigma}}$ and stiffness $\tilde{\mathbb{C}}_{\text{eff}}$ in the notation of [132]

$$\int_V \boldsymbol{B}^T\cdot\tilde{\boldsymbol{\sigma}}\,\mathrm{d}V - \int_V \boldsymbol{N_u}\cdot(\rho\,\boldsymbol{f})\,\mathrm{d}V - \int_{\partial V}\boldsymbol{N_u}\cdot\boldsymbol{t}\,\mathrm{d}A = \boldsymbol{R_u} \overset{!}{=} \boldsymbol{0}, \tag{3.59}$$

$$\int_V \beta_\varphi\,(\boldsymbol{N}_\varphi\cdot\hat{\boldsymbol{\varphi}}+1-\lambda_0)\,\boldsymbol{N}_\varphi\,\mathrm{d}V + \int_V c_\varphi\,(\nabla\boldsymbol{N}_\varphi\cdot\nabla\boldsymbol{N}_\varphi\cdot\hat{\boldsymbol{\varphi}})\,\mathrm{d}V = \boldsymbol{R}_\varphi \overset{!}{=} \boldsymbol{0}, \tag{3.60}$$

$$\begin{aligned}
&\int_V c_\theta\,\boldsymbol{N}_\theta\cdot\dot{\hat{\boldsymbol{\theta}}}\,\mathrm{d}V - \int_V \boldsymbol{P}:\dot{\boldsymbol{\lambda}}\boldsymbol{N}_\theta\,\mathrm{d}V\\
&+\int_V \frac{1}{\alpha_\theta}\frac{\nabla\boldsymbol{N}_\theta\cdot\hat{\boldsymbol{\theta}}}{(\boldsymbol{N}_\theta\cdot\hat{\boldsymbol{\theta}})}\cdot\nabla\boldsymbol{N}_\theta\,\mathrm{d}V + \int_V \boldsymbol{N}_\theta\cdot\hat{\boldsymbol{\theta}}|\dot{\boldsymbol{\lambda}}:\boldsymbol{b}_\theta|\boldsymbol{N}_\theta\,\mathrm{d}V = \boldsymbol{R}_\theta \overset{!}{=} \boldsymbol{0},
\end{aligned} \tag{3.61}$$

with

$$|\dot{\boldsymbol{\lambda}}:\boldsymbol{b}_\theta| := \sum_{j=1}^{N}\sum_{i=0}^{n}\xi^j\dot{\lambda}_i^j b_i. \tag{3.62}$$

The system of equations in Eq. (3.59) is solved using a standard Newton scheme. Hence,

$$\begin{bmatrix}\boldsymbol{R_u}\\ \boldsymbol{R}_\varphi\\ \boldsymbol{R}_\theta\end{bmatrix}^{i+1} = \begin{bmatrix}\boldsymbol{R_u}\\ \boldsymbol{R}_\varphi\\ \boldsymbol{R}_\theta\end{bmatrix}^{i} + \boldsymbol{J}^i\cdot\begin{bmatrix}\Delta\hat{\boldsymbol{u}}\\ \Delta\hat{\boldsymbol{\varphi}}\\ \Delta\hat{\boldsymbol{\theta}}\end{bmatrix}^{i+1} = \begin{bmatrix}\boldsymbol{0}\\ \boldsymbol{0}\\ \boldsymbol{0}\end{bmatrix}, \tag{3.63}$$

with

$$\boldsymbol{J}^i = \begin{bmatrix}\frac{\partial\boldsymbol{R_u}}{\partial\hat{\boldsymbol{u}}} & \frac{\partial\boldsymbol{R_u}}{\partial\hat{\boldsymbol{\varphi}}} & \frac{\partial\boldsymbol{R_u}}{\partial\hat{\boldsymbol{\theta}}}\\ \frac{\partial\boldsymbol{R}_\varphi}{\partial\hat{\boldsymbol{u}}} & \frac{\boldsymbol{R}_\varphi}{\partial\hat{\boldsymbol{\varphi}}} & \frac{\partial\boldsymbol{R}_\varphi}{\partial\hat{\boldsymbol{\theta}}}\\ \frac{\partial\boldsymbol{R}_\theta}{\partial\hat{\boldsymbol{u}}} & \frac{\partial\boldsymbol{R}_\theta}{\partial\hat{\boldsymbol{\varphi}}} & \frac{\partial\boldsymbol{R}_\theta}{\partial\hat{\boldsymbol{\theta}}}\end{bmatrix}^i. \tag{3.64}$$

The entries of the Jacobian in Eq. (3.64) can be calculated by

$$\frac{\partial \boldsymbol{R}_{\boldsymbol{u}}}{\partial \hat{\boldsymbol{u}}} = \int_V \boldsymbol{B}^T \cdot \tilde{\mathbb{C}}_{\text{eff}} \cdot \boldsymbol{B} \, \mathrm{d}V, \tag{3.65}$$

$$\frac{\partial \boldsymbol{R}_{\boldsymbol{u}}}{\partial \hat{\boldsymbol{\varphi}}} = \int_V \boldsymbol{B}^T \cdot \frac{\partial \tilde{\boldsymbol{\sigma}}}{\partial \varphi} \otimes \boldsymbol{N}_\varphi \, \mathrm{d}V, \tag{3.66}$$

$$\frac{\partial \boldsymbol{R}_{\boldsymbol{u}}}{\partial \hat{\boldsymbol{\theta}}} = \int_V \boldsymbol{B}^T \cdot \frac{\partial \tilde{\boldsymbol{\sigma}}}{\partial \theta} \otimes \boldsymbol{N}_\theta \, \mathrm{d}V, \tag{3.67}$$

$$\frac{\partial \boldsymbol{R}_{\varphi}}{\partial \hat{\boldsymbol{u}}} = \int_V \beta_\varphi \boldsymbol{N}_\varphi \otimes \left(-\frac{\partial \lambda_0}{\partial \tilde{\boldsymbol{\varepsilon}}} \right) \cdot \boldsymbol{B} \, \mathrm{d}V, \tag{3.68}$$

$$\frac{\partial \boldsymbol{R}_{\varphi}}{\partial \hat{\boldsymbol{\varphi}}} = \int_V \beta_\varphi \left(1 - \frac{\partial \lambda_0}{\partial \varphi} \right) \boldsymbol{N}_\varphi \otimes \boldsymbol{N}_\varphi \, \mathrm{d}V + \int_V c_\varphi \left(\nabla \boldsymbol{N}_\varphi \right)^T \cdot \nabla \boldsymbol{N}_\varphi \, \mathrm{d}V, \tag{3.69}$$

$$\frac{\partial \boldsymbol{R}_{\varphi}}{\partial \hat{\boldsymbol{\theta}}} = \int_V \beta_\varphi \boldsymbol{N}_\varphi \otimes \left(-\frac{\partial \lambda_0}{\partial \theta} \right) \boldsymbol{N}_\theta \, \mathrm{d}V, \tag{3.70}$$

$$\begin{aligned} \frac{\partial \boldsymbol{R}_{\theta}}{\partial \hat{\boldsymbol{u}}} = & - \int_V \boldsymbol{N}_\theta \otimes \left(\frac{\partial (\boldsymbol{P} : \dot{\boldsymbol{\lambda}})}{\partial \tilde{\boldsymbol{\varepsilon}}} \cdot \boldsymbol{B} \right) \mathrm{d}V \\ & + \int_V \left(\boldsymbol{N}_\theta \cdot \hat{\boldsymbol{\theta}} \right) \boldsymbol{N}_\theta \otimes \left(\frac{\partial |\dot{\boldsymbol{\lambda}} : \boldsymbol{b}_\theta|}{\partial \tilde{\boldsymbol{\varepsilon}}} \cdot \boldsymbol{B} \right) \mathrm{d}V, \end{aligned} \tag{3.71}$$

$$\frac{\partial \boldsymbol{R}_{\theta}}{\partial \hat{\boldsymbol{\varphi}}} = - \int_V \frac{\partial (\boldsymbol{P} : \dot{\boldsymbol{\lambda}})}{\partial \varphi} \boldsymbol{N}_\varphi \otimes \boldsymbol{N}_\theta \, \mathrm{d}V + \int_V \boldsymbol{N}_\theta \cdot \hat{\boldsymbol{\theta}} \frac{\partial |\dot{\boldsymbol{\lambda}} : \boldsymbol{b}_\theta|}{\partial \varphi} \boldsymbol{N}_\varphi \otimes \boldsymbol{N}_\theta \, \mathrm{d}V \tag{3.72}$$

and for the last component, since we use as discretization for the temperature in time

$$\dot{\hat{\boldsymbol{\theta}}} = \left(\hat{\boldsymbol{\theta}}^{n+1} - \hat{\boldsymbol{\theta}}^{n} \right) \frac{1}{\Delta t}, \tag{3.73}$$

where n denotes the number of the load step,

$$\begin{aligned} \frac{\partial \boldsymbol{R}_{\theta}}{\partial \hat{\boldsymbol{\theta}}} = & \int_V \boldsymbol{N}_\theta \otimes \boldsymbol{N}_\theta \left[\frac{c_\theta}{\Delta t} - \frac{\partial (\boldsymbol{P} : \dot{\boldsymbol{\lambda}})}{\partial \theta} + |\dot{\boldsymbol{\lambda}} : \boldsymbol{b}_\theta| + \boldsymbol{N}_\theta \cdot \hat{\boldsymbol{\theta}} \frac{\partial |\dot{\boldsymbol{\lambda}} : \boldsymbol{b}_\theta|}{\partial \theta} \right] \mathrm{d}V \\ & + \int_V \frac{1}{\alpha_\theta} \left[\frac{\nabla \boldsymbol{N}_\theta^T \cdot \nabla \boldsymbol{N}_\theta}{(\boldsymbol{N}_\theta \cdot \hat{\boldsymbol{\theta}})} - \frac{\left((\nabla \boldsymbol{N}_\theta \cdot \hat{\boldsymbol{\theta}}) \cdot \nabla \boldsymbol{N}_\theta \right) \otimes \boldsymbol{N}_\theta}{(\boldsymbol{N}_\theta \cdot \hat{\boldsymbol{\theta}})^2} \right] \mathrm{d}V \end{aligned} \tag{3.74}$$

The remaining derivatives in the equations (3.66) till (3.72) and in Eq. (3.74) have to be calculated numerically.

3.5 Finite element results

We present finite element results for polycrystalline, pseudo-elastic Nickel Titanium. This shape memory alloy can form twelve different martensitic phases. The corresponding transformation strains are taken from [194] and collected in Table 3.1. The elastic constants for singlecrystalline austenite and martensite can be found according to [194] in Table 3.2. The polycrystalline behavior results from taking N randomly chosen orientations. The parameters used for the material model are presented in Table 3.3. The dependence of the chemical energies on temperature is depicted in Fig. 3.4. We do not account for heat exchanges with the surrounding, but assuming an adiabatic process.

Table 3.1: Transformation strains for cubic to monoclinic transforming NiTi after [194]. $\bar{\alpha} = 0.02381$, $\bar{\beta} = -0.02480$, $\bar{\delta} = 0.07528$, $\bar{\epsilon} = 0.04969$

$\boldsymbol{\eta}_1 = \begin{pmatrix} \bar{\alpha} & \bar{\delta} & \bar{\epsilon} \\ \bar{\delta} & \bar{\alpha} & \bar{\epsilon} \\ \bar{\epsilon} & \bar{\epsilon} & \bar{\beta} \end{pmatrix}$	$\boldsymbol{\eta}_2 = \begin{pmatrix} \bar{\alpha} & \bar{\delta} & -\bar{\epsilon} \\ \bar{\delta} & \bar{\alpha} & -\bar{\epsilon} \\ -\bar{\epsilon} & -\bar{\epsilon} & \bar{\beta} \end{pmatrix}$	$\boldsymbol{\eta}_3 = \begin{pmatrix} \bar{\alpha} & -\bar{\delta} & -\bar{\epsilon} \\ -\bar{\delta} & \bar{\alpha} & \bar{\epsilon} \\ -\bar{\epsilon} & \bar{\epsilon} & \bar{\beta} \end{pmatrix}$
$\boldsymbol{\eta}_4 = \begin{pmatrix} \bar{\alpha} & -\bar{\delta} & \bar{\epsilon} \\ -\bar{\delta} & \bar{\alpha} & -\bar{\epsilon} \\ \bar{\epsilon} & -\bar{\epsilon} & \bar{\beta} \end{pmatrix}$	$\boldsymbol{\eta}_5 = \begin{pmatrix} \bar{\alpha} & \bar{\epsilon} & \bar{\delta} \\ \bar{\epsilon} & \bar{\beta} & \bar{\epsilon} \\ \bar{\delta} & \bar{\epsilon} & \bar{\alpha} \end{pmatrix}$	$\boldsymbol{\eta}_6 = \begin{pmatrix} \bar{\alpha} & -\bar{\epsilon} & \bar{\delta} \\ -\bar{\epsilon} & \bar{\beta} & -\bar{\epsilon} \\ \bar{\delta} & -\bar{\epsilon} & \bar{\alpha} \end{pmatrix}$
$\boldsymbol{\eta}_7 = \begin{pmatrix} \bar{\alpha} & -\bar{\epsilon} & -\bar{\delta} \\ -\bar{\epsilon} & \bar{\beta} & \bar{\epsilon} \\ -\bar{\delta} & \bar{\epsilon} & \bar{\alpha} \end{pmatrix}$	$\boldsymbol{\eta}_8 = \begin{pmatrix} \bar{\alpha} & \bar{\epsilon} & -\bar{\delta} \\ \bar{\epsilon} & \bar{\beta} & -\bar{\epsilon} \\ -\bar{\delta} & -\bar{\epsilon} & \bar{\alpha} \end{pmatrix}$	$\boldsymbol{\eta}_9 = \begin{pmatrix} \bar{\beta} & \bar{\epsilon} & \bar{\epsilon} \\ \bar{\epsilon} & \bar{\alpha} & \bar{\delta} \\ \bar{\epsilon} & \bar{\delta} & \bar{\alpha} \end{pmatrix}$
$\boldsymbol{\eta}_{10} = \begin{pmatrix} \bar{\beta} & -\bar{\epsilon} & -\bar{\epsilon} \\ -\bar{\epsilon} & \bar{\alpha} & \bar{\delta} \\ -\bar{\epsilon} & \bar{\delta} & \bar{\alpha} \end{pmatrix}$	$\boldsymbol{\eta}_{11} = \begin{pmatrix} \bar{\beta} & -\bar{\epsilon} & \bar{\epsilon} \\ -\bar{\epsilon} & \bar{\alpha} & -\bar{\delta} \\ \bar{\epsilon} & -\bar{\delta} & \bar{\alpha} \end{pmatrix}$	$\boldsymbol{\eta}_{12} = \begin{pmatrix} \bar{\beta} & \bar{\epsilon} & -\bar{\epsilon} \\ \bar{\epsilon} & \bar{\alpha} & -\bar{\delta} \\ -\bar{\epsilon} & -\bar{\delta} & \bar{\alpha} \end{pmatrix}$

Table 3.3: Material parameters for the thermo-mechanically coupled model.

$\Delta a = -0.208199\,[\mathrm{GPa}]$	$\Delta b = -0.000775501\,[\mathrm{GPa}]$
$\theta^\star = 268.47\,[\mathrm{K}]$	$\theta_\mathrm{R} = 295.15\,[\mathrm{K}]$
$\theta^f_\mathrm{A} = 291.79\,[\mathrm{K}]$	$\theta^s_\mathrm{A} = 268.64\,[\mathrm{K}]$
$\theta^f_\mathrm{M} = 233.47\,[\mathrm{K}]$	$\theta^s_\mathrm{M} = 260.31\,[\mathrm{K}]$
$r^f_\mathrm{A} = 0.0174\,[\mathrm{GPa}]$	$r^s_\mathrm{A} = 0.0002\,[\mathrm{GPa}]$
$r^f_\mathrm{M} = 0.026\,[\mathrm{GPa}]$	$r^s_\mathrm{M} = 0.006\,[\mathrm{GPa}]$
$\beta_\varphi = 1.0\,[\mathrm{GPa}]$	$c_\varphi = 0.001\,[\mathrm{GPa}]$
$c_\theta = 0.0105\,[\mathrm{GPa/K}]$	$\alpha_\theta = 0.0075\,[\mathrm{mmK/W}]$

Table 3.2: Elastic constants for austenite and martensite after [194]

$$\mathbb{C}_\mathrm{aust} = \begin{pmatrix} 140 & 110 & 110 & 0 & 0 & 0 \\ 110 & 140 & 110 & 0 & 0 & 0 \\ 110 & 110 & 140 & 0 & 0 & 0 \\ 0 & 0 & 0 & 32 & 0 & 0 \\ 0 & 0 & 0 & 0 & 32 & 0 \\ 0 & 0 & 0 & 0 & 0 & 32 \end{pmatrix} \mathrm{GPa}$$

$$\mathbb{C}_\mathrm{mart} = \begin{pmatrix} 223 & 129 & 99 & 0 & 27 & 0 \\ 129 & 241 & 125 & 0 & -9 & 0 \\ 99 & 125 & 200 & 0 & 4 & 0 \\ 0 & 0 & 0 & 76 & 0 & -4 \\ 27 & -9 & 4 & 0 & 21 & 0 \\ 0 & 0 & 0 & -4 & 0 & 77 \end{pmatrix} \mathrm{GPa}$$

As example we perform simulations for a stripe of NiTi - the respective experiment can be found in [162]. The stripe is discretized with 234 elements. The general mesh including the nodes with prescribed displacements (zero at the left hand side and linearly varying at the right hand side) is

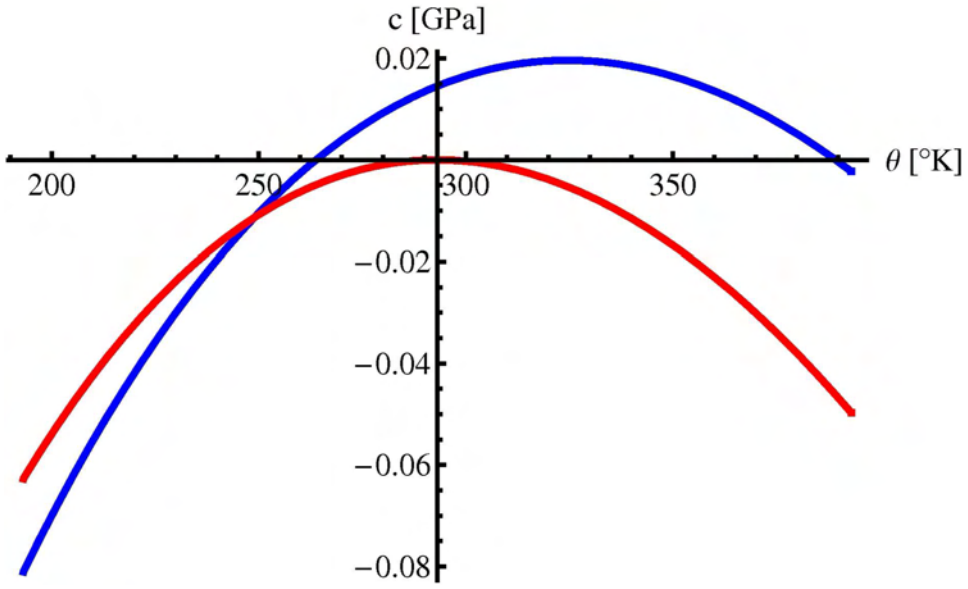

Figure 3.4: Chemical energies for austenite (red) and martensite (blue)

shown in Fig. 3.5.

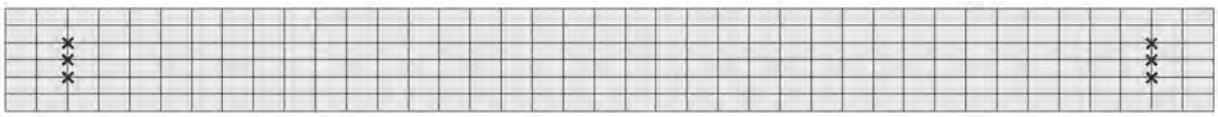

Figure 3.5: Finite element mesh for the stripe. Nodes with prescribed displacements are indicated by **x**. The dimensions are 35 mm x 3.3 mm x 0.68 mm. Same sample geometry was used in experiments.

The resultant system answer is depicted in Fig. 3.6. It can be seen that the general character of the material response is captured quite well. Although the character of the dissipation coefficient r causes softening, the decrease of stress is very small and there is no distinct stress drop as it was present for the results in [95]. Temperature, which is now an evolving variable, stabilizes the austenite. Hence, the strong influence of the decreasing dissipation parameter and consequently the threshold for the yield function is regularized. The experimental data are quantitatively not perfectly matched. Improvements in the values for the chemical energies could possibly correct this. However, without any ad hoc assumptions on load, geometry and temperature dependent quantities such as transformation stresses or (scalar) transformation strains, the general material behavior is simulated in a convincing way. Since at 22° C there exists an intermediate transformation from austenite to the so-called R-phase, for which we do not account, there is a difference in our simulations and the later part of the "elastic" region where that R-transformation takes place.

The influence of different loading velocities can be observed in Fig. 3.6 as well. When a higher loading velocity is applied more heat is generated. This results in a smoother curve since all phase transformations are influenced by temperature. Particularly in the beginning of the plateau the stress is slightly higher because the rate of transformation is reduced due to the stabilizing effect of temperature on the austenite. During unloading a curve almost parallel to the abscissa can be observed in the

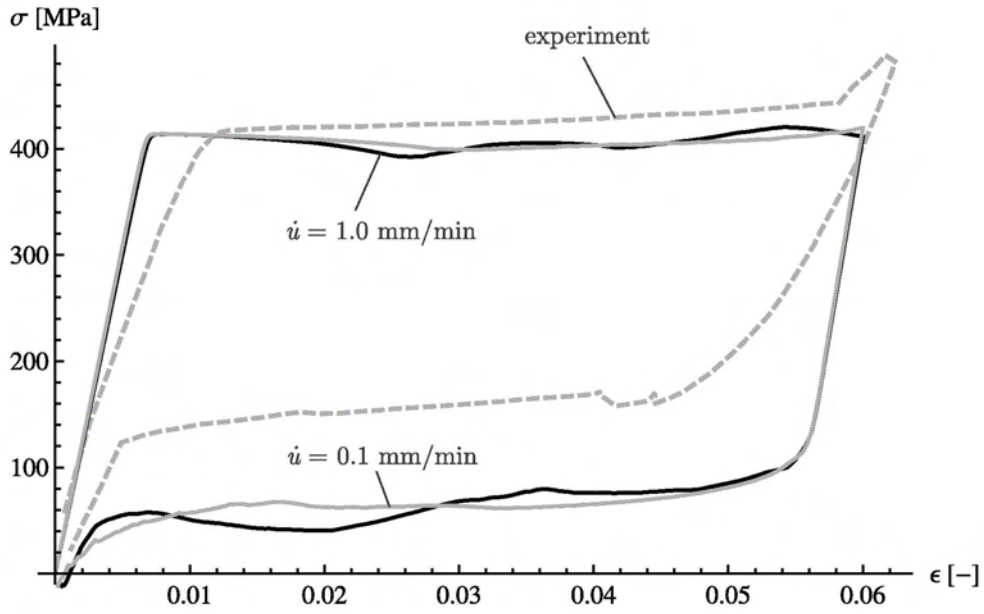

Figure 3.6: Thermo-mechanically coupled model. Stress-strain diagram for a stripe of NiTi at 22° C. Loading velocities are $\dot{u}_{x_1} = 1.0\,[\text{mm/min}]$ (black curve) and $\dot{u}_{x_1} = 0.1\,[\text{mm/min}]$ (gray curve). Experiment from [162].

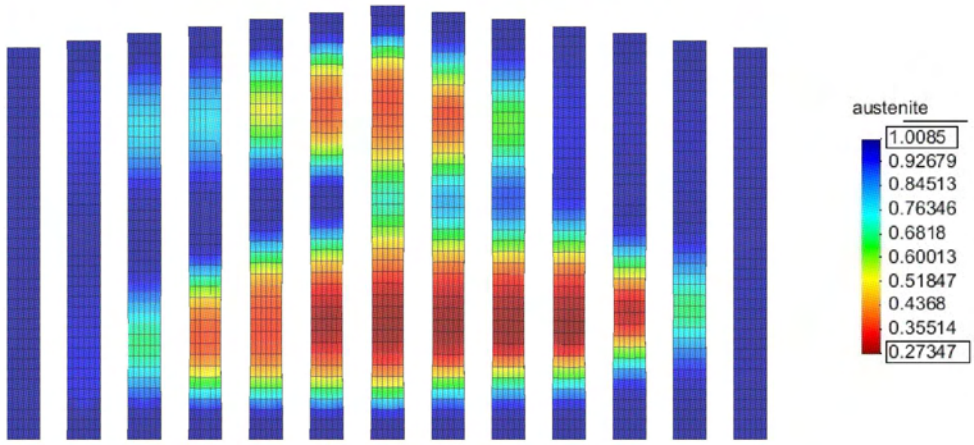

Figure 3.7: Thermo-mechanically coupled model. Distribution of austenite in a stripe of NiTi at 22° C. Loading velocity $\dot{u} = 0.1\,[\text{mm/min}]$.

plateau. Obviously, the agreement between simulation and experiment is not completely satisfying. In order to improve the results further parameter identification has to be carried out.

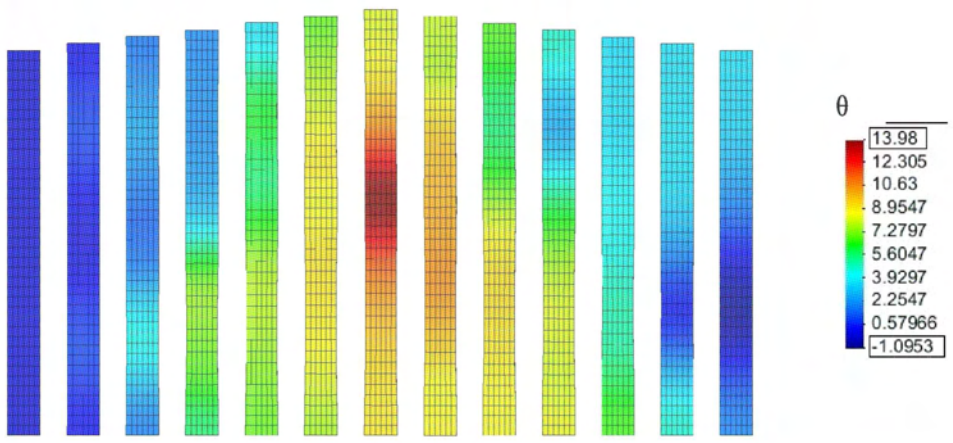

Figure 3.8: Thermo-mechanically coupled model. Distribution of temperature in a stripe of NiTi at 22° C. Loading velocity $\dot{u} = 0.1\,[\mathrm{mm/min}]$.

Although only a very slight softening was observed in the stress-strain diagram, the resulting localization of the phase transformation is desired as outcome since they correspond to experimental evidence. In Fig. 3.7 the distribution of austenite over time in the specimen corresponding to the results of Fig. 3.6 is displayed. Here, the loading velocity was chosen relatively small at $\dot{u} = 0.1\,\mathrm{mm/min}$. The phase transformation starts at the supports due to the thus-induced stress peaks and consequently at both sides distinct localized transformation zones evolve. Using anisotropic elastic constants and a set of $N = 30$ orientations results in a small orientation dependence. Due to the regularizing effect of temperature the deviations in the elastic constants from a purely isotropic material are smeared out in the beginning. Consequently, at both sides fronts evolve. However, later the influence of the anisotropic behavior is more pronounced since the transformation zones do not move with the same velocity.

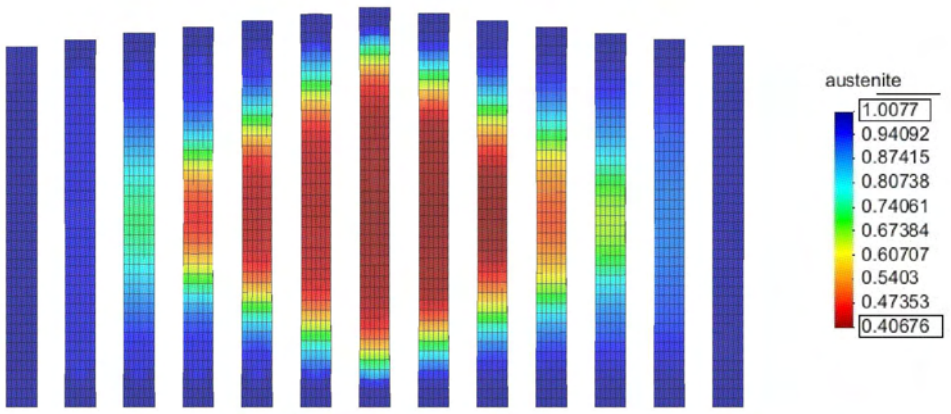

Figure 3.9: Thermo-mechanically coupled model. Distribution of austenite in a stripe of NiTi at 22° C. Loading velocity $\dot{u} = 1.0\,[\mathrm{mm/min}]$.

During unloading first the upper fronts vanish and afterwards the fronts in the lower parts collide after the front in the center has moved towards the support and the front next to the support has moved towards the center. This behavior was reported in the experiment, too, see [162].

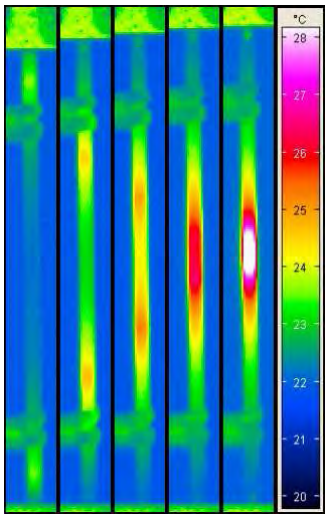

Figure 3.10: Experimentally measured distribution of the temperature over the specimen at various time steps (only the non-blue part shows the specimen; the background is blue). Courtesy of A. Schäfer and M.FX. Wagner, [162].

In Fig. 3.8 the corresponding distribution of temperature is presented. Here, only the deviation from the start temperature is shown. Due to phase transformation heat is produced. Therefore, analogously to the evolution of martensite the temperature first increases quite localized. While the transformation zones are moving, which serve as internal heat wells, the distribution of temperature is moving, too. Of course, due to its transient character the distribution of temperature is much more smeared out compared to the one of austenite. There occurs a peak in the distribution of temperature when the two heat fronts meet, see also Fig. 3.10.

When the specimen is unloaded a phase transformation from martensite back to austenite takes place. According to this, the temperature is decreasing again. Since the entire process is dissipative there is a lower temperature in the specimen than in the original state. In reality this gap of heat would be compensated by a heat flux from the surroundings into the specimen for which we do not account for in our adiabatic simulations.

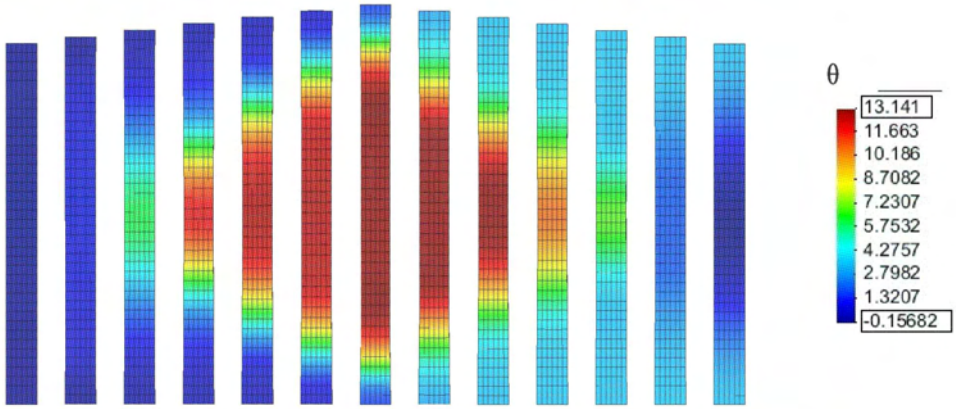

Figure 3.11: Thermo-mechanically coupled model. Distribution of temperature in a stripe of NiTi at 22° C. Loading velocity $\dot{u} = 1.0\,[\mathrm{mm/min}]$.

At higher loading velocities ($\dot{u}$ = 1 mm/min) the distribution of austenite is different, see Fig. 3.9. Here, transformation initializes again at the supports but due to the high evolution of temperature its stopped almost immediately. All further phase transition proceeds in the center of the specimen only which comes from the fact that the temperature is minimal there. Two distinct transformation fronts evolve which move through the specimen in the direction of the supports. The influence of the relatively high temperature can be seen in the remaining amount of austenite. With app. 40% it is quite high compared to the case of slow loading velocity. This is reasonable since temperature stabilizes the austenite and serves as driving force directed in the opposite direction of the mechanical ones. Thus, less material transforms. During unloading both fronts move back in the center of the specimen and meet again there.

Figure 3.11 shows the evolution of temperature at high loading velocities. Again, temperature evolves strongly connected to the phase transformations. The maximum value for temperature is slightly lower than in the example of slow loading. The absolute value of its minimum is even remarkably smaller. However, the amount of produced heat is higher. This can be seen from the temperature distribution which has high and low values respectively for a much broader spatial expansion in the stripe.

3.6 Conclusions and outlook

We presented a micromechanical model for polycrystalline shape memory alloys based on the principle of maximum dissipation. Relying on a minimum of assumptions, basically only on the form of Helmholtz free energy and dissipation, the most important characteristics of shape memory alloys can be captured. A way how to derive the dissipation parameter from more fundamental physical parameters is introduced. This is a marked improvement since it was an additional variable in other micromechanical models using the principle of maximum dissipation or the principle of the minimum of the dissipation potential. Other model parameters, which may be dependent on the load direction, geometry or temperature, do not have to be assumed. Although this has to be shown yet, we are optimistic that due to its energetic formulation and in combination with the small number of parameters the material model will have a quite universal applicability. In total, our model accounts for the dissipative character of martensitic solid-to-solid phase transitions as well as the localized evolution by means of the heat conduction equation. The dependence on the loading velocity is captured as well. In comparison to previous works the model predicts now the localization behavior, the temperature dependence and the influence of loading speed which is a definite progress in comparison with previous approached, e.g. in [94].

Future works will focus on the influence of heat conductivity on the material response and the simulation of pseudo-plastic material behavior and the one way effect. Additionally, further testing and improvement of the chemical energies will be part of our work. As reported in [195] and [196], interface (surface) energy plays a dominant role of the grain size tends to become very small. This important aspect has to be incorporated into a future version of the model, adopting procedures from [71] and [56].

4 Heat production, transformation fronts, and their interrelations

Published as: *P. Junker, K. Hackl*: About the influence of heat conductivity on the mechanical behavior of poly-crystalline shape memory alloys, *Int. J. Struct. Changes Sol.* **3: 49–62 (2011)**

Outgoing from energy conservation and the second law of thermodynamics we derive a thermo-mechanically coupled model for shape memory alloys. Additionally, we introduce a field function which allows for the modification of the dissipation coefficient. All together, the model is capable to display the localized phase transformation as well as temperature distribution which were observed in experiments.

This paper focuses on the influence of heat conductivity on numerical results for poly-crystalline shape memory alloys. The heat conductivity is identified in the approach for the entropy production. Slight changes of the entropy production ansatz yield interesting numerical results, capable of displaying experimental observations.

4.1 Introduction

The atoms in shape memory alloys may be arranged in different stable lattice structures, depending on temperature and load. These structures are well-known and denoted as *austenite* and *martensite*. At high temperatures the atoms are composed in a cubic arrangement which is called austenite. At low temperatures the material favors a less symmetric structure which can be converted from the austenite via shear and shuffle. Thus, there exists no unique transformation which maps the austenite to the sheared and shuffled state, but several which are coupled by symmetry relations. All those stable lattices are denoted by martensite whereas the variants of martensite are distinguished by means of fixed rotation matrices. From the deformation of the cubic austenitic lattice to the sheared and shuffled one of a particular martensitic variant a so-called transformation strain may be measured which serves as mechanical characterization.

Pseudo-elastic shape memory alloys are characterized by a fully reversible austenite $\leftrightarrow$ martensite phase transformation. That means starting from a purely austenitic specimen phase transformations evolve until a combination of different martensite variants is observed. During the process of phase transition a plateau in the stress-strain diagram indicates the change of internal state. The phase transformation has a dissipative character. Energy applied to the system via a prescribed displacement and the corresponding force is not only invested in phase transitions but also in heat. Hence, releasing the specimen results in a back-transformation, but with lower force. So, a hysteresis is observed.

Many models already exist capable of describing shape-memory alloys from different viewpoints. Phenomenological models were presented e.g. in [22], [79] and [120]. In contrast to those we intend to describe phase transformations from the micromechanical side to overcome the need to find many model parameters. Other micromechanical models for poly-crystals than ours may be found in [60], [177] and [174]. Different finite element implementations of models were presented in [153]. As far to our knowledge there exist no other model which is able to simultaneously describe phase transformation, localization and thermal coupling than ours.

A poly-crystal is a conglomerate of single crystals (grains) each having a different orientation. Depending on the direction of loads and the orientation of atoms a different material response may be expected. Therefore, in a poly-crystal there will always be crystals which are more favored to undergo phase transformations due to their orientation and some which will transform only slightly. In order to capture this property we use the relaxed free energy for poly-crystalline shape memory alloys introduced in [70]. We consider a material behavior free of re-crystallization which means that the orientation of grains does not change.

The aforementioned approach for the energy is taken to derive evolution equations for the crystalline phases and a heat conduction equation by means of maximization of the entropy production for which we make an appropriate ansatz. This approach allows us to take the coupling between phase transformation and heat into account. Introducing a field function for regularization similar to [39] allows a modification of a dissipation coefficient in a way that the *nucleation* of martensite costs more energy as compared to its *evolution*. The impact of this modification is the formation of moving transformation fronts similar to localized plastic strains (Lüders bands) in our numerical results which coincides with experimental observations of tension tests [162]. The complete approach results in a remarkable improvement of our results since the original model, derived in [70], gives a homogeneous transformation, [94]. The regularization is necessary since the modification of the dissipation results in a loss of ellipticity and consequently in mesh dependent finite element calculations.

In the experiments the shape of those transformation fronts is changing: the inclination angle differs from specimen to specimen and a "reorientation" is observed during its movement. Transformation fronts perpendicular to the longitudinal axes of a specimen in a tension test occur as well as inclined fronts with a certain angle. One reason for this phenomenon is considered to be the thermo-mechanical coupling of the occurring phase transformations.

In this paper we want to analyze the influence of the assumed ansatz on the entropy production. Since the dissipation coefficient for the heat flux may be identified as connected to heat conductivity, we present examples for different coefficients. The numerical results are brought into comparison and discussed.

4.2 Material Model

From thermodynamics we know that the total energy of a system is conserved. This property may be expressed by the well-known equation of energy conservation, [81],

$$\dot{\Psi} + \dot{\eta}\,\theta + \eta\,\dot{\theta} = \boldsymbol{\sigma} : \dot{\boldsymbol{\varepsilon}} + h - \nabla \cdot \boldsymbol{q}\,. \tag{4.1}$$

In (4.1) Ψ denotes the specific Helmholtz free energy and η entropy, θ temperature, σ stress, $\boldsymbol{\varepsilon}$ strain, h internal energy wells and $\boldsymbol{q}$ heat flux. Furthermore, the second law of thermodynamics has to hold which is taken here as

$$\Delta = \dot{\eta} - \frac{h}{\theta} + \nabla \cdot \left(\frac{\boldsymbol{q}}{\theta}\right) \geq 0\,, \tag{4.2}$$

where Δ is the irreversible entropy production. Combination of (4.1) and (4.2) by eliminating h gives the identity

$$\Delta = \frac{1}{\theta}\left(\boldsymbol{\sigma} : \dot{\boldsymbol{\varepsilon}} - \dot{\Psi} - \eta\,\dot{\theta}\right) + \boldsymbol{q} \cdot \nabla \frac{1}{\theta}, \tag{4.3}$$

which has to hold at every point in time.

We know that Δ is a function of the thermodynamical fluxes of the system under consideration and we have to make an assumption on this dependence. We follow [146] and [67] and maximize the entropy production Δ with respect to the thermodynamical fluxes in order to receive evolution equations. This approach is called *maximization of the dissipation* and gives for many cases same results as the *minimization of a dissipation potential* (see [67]) which was used for example in [200], [181] and [180]. This general approach was introduced for the thermodynamically coupled case in [69].

The maximization has to be carried out under several constraints. First, the identity (4.3) has to be fulfilled. Additionally, the phases may only evolve under the constraint of mass conservation and positivity. The mass conservation has to be achieved in every single grain. This may be brought to formulas via the introduction of volume fractions λ_i^j. The index j belongs to grains which are described by a randomly chosen rotation matrix $\boldsymbol{R}^j$. N denotes the maximum number of grain orientations assumed ($j \in \{1,\dots,N\}$). The different phases may be distinguished via the index i whereas $i = 0$ indicates austenite and $i > 0$ the corresponding martensitic phase ($i \in \{0,\dots,n\}$, n is the number of martensite variants). Then, mass conservation reads

$$\sum_{i=0}^{n} \dot{\lambda}_i^j = 0 \quad \forall\, j\,. \tag{4.4}$$

Since negative volume fractions do not make any physical sense, we demand

$$\lambda_i^j \geq 0 \quad \forall\, i,\, j\,. \tag{4.5}$$

We introduce the Lagrangian for our problem as

$$\mathcal{L} = \Delta + \beta\left\{\Delta - \frac{1}{\theta}\left(\boldsymbol{\sigma} : \dot{\boldsymbol{\varepsilon}} - \dot{\Psi} - \eta\dot{\theta}\right) - \boldsymbol{q}\cdot\nabla\frac{1}{\theta}\right\} + \sum_{j=1}^{N}\kappa^j\sum_{i=0}^{n}\dot{\lambda}_i^j - \sum_{j=1}^{N}\sum_{i=0}^{n}\gamma_i^j\dot{\lambda}_i^j \to \max_{\dot{\boldsymbol{\varepsilon}},\dot{\boldsymbol{\lambda}},\dot{\theta},\boldsymbol{q}}\,, \tag{4.6}$$

with Lagrange parameters β and κ^j for the constraints (4.3) and (4.4) and Kuhn-Tucker parameters γ_i^j for (4.5), respectively. The Kuhn-Tucker parameters are only active if the constraint of positivity is not fulfilled. Thus,

$$\gamma_i^j = \begin{cases} = 0 & \text{for } \lambda_i^j > 0 \vee \left(\lambda_i^j = 0 \wedge \dot{\lambda}_i^j > 0\right) \\ > 0 & \text{else} \end{cases}\,. \tag{4.7}$$

The Lagrangian $\mathcal{L}$ has to be maximized with respect to its free variables, which are the rates of strain, volume fraction and temperature and the heat flux. Finding the stationary values of $\mathcal{L}$ give

$$\frac{\partial\mathcal{L}}{\partial\dot{\boldsymbol{\varepsilon}}} = \boldsymbol{0} \quad\Leftrightarrow\quad \boldsymbol{\sigma} = \frac{\partial\Psi}{\partial\boldsymbol{\varepsilon}}\,, \tag{4.8}$$

$$\frac{\partial\mathcal{L}}{\partial\dot{\boldsymbol{\lambda}}} = \boldsymbol{0} \quad\Leftrightarrow\quad (1+\beta)\frac{\partial\Delta}{\partial\dot{\boldsymbol{\lambda}}} + \frac{\beta}{\theta}\frac{\partial\Psi}{\partial\boldsymbol{\lambda}} + \boldsymbol{\kappa} - \boldsymbol{\gamma} = \boldsymbol{0}\,, \tag{4.9}$$

$$\frac{\partial\mathcal{L}}{\partial\dot{\theta}} = 0 \quad\Leftrightarrow\quad \eta = -\frac{\partial\Psi}{\partial\theta}\,, \tag{4.10}$$

$$\frac{\partial\mathcal{L}}{\partial\boldsymbol{q}} = \boldsymbol{0} \quad\Leftrightarrow\quad (1+\beta)\frac{\partial\Delta}{\partial\boldsymbol{q}} - \beta\nabla\frac{1}{\theta} = \boldsymbol{0}\,, \tag{4.11}$$

with

$$\boldsymbol{\kappa} = \kappa^j\boldsymbol{e}_i\boldsymbol{e}_j\,, \quad \boldsymbol{\gamma} = \gamma_i^j\boldsymbol{e}_i\boldsymbol{e}_j\,, \qquad \boldsymbol{e}_k:\ \text{unit vectors}\,. \tag{4.12}$$

This approach of maximizing the entropy production yields the constitutive equations both for stress (4.8) and entropy (4.10). The equations (4.8) till (4.11) can be used to find expressions for the Lagrange parameters β and κ^j. Plugging those expressions back into the set of equations (4.8) and (4.11) we derive evolution equations for the phases

$$\begin{cases} \dfrac{f}{\theta} p_i^j - \dfrac{f}{\theta} \dfrac{1}{n_{\mathcal{A}^j}} \displaystyle\sum_{k \in \mathcal{A}^j} p_k^j &= \dfrac{\partial \Delta}{\partial \dot{\lambda}_i^j} \quad , \; i \in \mathcal{A}^j \\ \dfrac{f}{\theta} p_i^j - \dfrac{f}{\theta} \dfrac{1}{n_{\mathcal{A}^j}} \displaystyle\sum_{k \in \mathcal{A}^j} p_k^j &= -\dfrac{1}{1+\beta} \gamma_i^j \quad , \; i \notin \mathcal{A}^j \end{cases} , \tag{4.13}$$

where we applied the active set strategy. The active set collects all phases in each grain which fulfill the constraint of positivity (4.5) identically. Thus,

$$\mathcal{B}^j = \left\{ i | \lambda_i^j = 0 \right\} \tag{4.14}$$

$$\mathcal{A}^j = \left\{ i \in \mathcal{B}^j | \dot{\lambda}_i^j > 0 \right\} \cup \left\{ i \notin \mathcal{B}^j \right\} . \tag{4.15}$$

In Eq. (4.13) $p_i^j := -\partial \Psi / \partial \lambda_i^j$ denote the thermo-mechanically conjugated driving forces, $n_{\mathcal{A}^j}$ the number of active variants in each grain j and

$$f := \frac{\beta}{1+\beta} . \tag{4.16}$$

We have to make ansatzes for the energy and the entropy production. For the energy we take the approach of [70] in combination with [87] which is

$$\Psi^{\text{tot}} = \frac{1}{2} (\boldsymbol{\varepsilon} - \boldsymbol{\eta}_{\text{eff}}) : \mathbb{C}_{\text{eff}} : (\boldsymbol{\varepsilon} - \boldsymbol{\eta}_{\text{eff}}) + c_{\text{eff}}(\theta) \tag{4.17}$$

with

$$\boldsymbol{\eta}_{\text{eff}} = \sum_{j=1}^{N} \sum_{i=0}^{n} \frac{1}{N} \lambda_i^j \underbrace{\left(\boldsymbol{R}^j\right)^T \cdot \boldsymbol{\eta}_i \cdot \boldsymbol{R}^j}_{=: \boldsymbol{\eta}_i^j} , \quad \mathbb{C}_{\text{eff}} = \left[\sum_{j=1}^{N} \sum_{i=0}^{n} \frac{1}{N} \lambda_i^j \left(\mathbb{C}_i^j \right)^{-1} \right]^{-1} , \quad c_{\text{eff}}(\theta) = \sum_{j=1}^{N} \sum_{i=0}^{n} \frac{1}{N} \lambda_i^j c_i(\theta) , \tag{4.18}$$

where $\boldsymbol{\eta}_i$, $\mathbb{C}_i$ and c_i are the transformation strains, elastic constants and the temperature dependent chemical energy for each phase i. This energy is the result of a complete convexification of the entire energy of the system which can be expressed by the weighted sum of energies in all grains and all phases. By means of the randomly chosen rotation matrices $\boldsymbol{R}^j$ we can calculate the rotated elastic constants according to

$$\mathbb{C}_{i\,pqrs}^j = R_{tp}^j R_{uq}^j R_{vr}^j R_{ws}^j \mathbb{C}_{i\,tuvw} . \tag{4.19}$$

For the chemical energy part we follow [87] by

$$c_i(\theta) = c_\theta (\theta - \theta_{\text{R}}) - c_\theta \, \theta \ln \left(\frac{\theta}{\theta_{\text{R}}} \right) + a_i - b_i \theta , \tag{4.20}$$

where θ_{R} denotes the reference temperature, c_θ the specific heat (= heat capacity) and a_i and b_i phase dependent energetic and entropic constants, respectively. Finally we use (4.10) and our assumption

for the energy which gives the rate of entropy as

$$\dot{\eta} = c_\theta \frac{\dot{\theta}}{\theta} + \sum_{j=1}^{N} \sum_{i=0}^{n} \frac{1}{N} \dot{\lambda}_i^j b_i \,. \tag{4.21}$$

Plugging this back into (4.1) and introducing our ansatz for the entropy production

$$\Delta = r\left(|\boldsymbol{\lambda}_0|\right) |\dot{\boldsymbol{\lambda}}|_{\boldsymbol{\xi}} + \frac{\alpha_\theta}{2} |\boldsymbol{q}|^2 \,, \tag{4.22}$$

($r\left(|\boldsymbol{\lambda}_0|\right)$ and α_θ are dissipation coefficients for phase transformation and heat flux, respectively) where

$$|\dot{\boldsymbol{\lambda}}|_{\boldsymbol{\xi}} = \sqrt{\sum_{j=1}^{N} \frac{1}{N} \sum_{i=0}^{n} \left(\dot{\lambda}_i^j\right)^2} \,, \tag{4.23}$$

we receive the evolution law for the phases and the heat conduction equation as

$$\dot{\lambda}_i^j = \frac{\rho}{N} \frac{f}{\theta} \left[\mathrm{dev}_{\mathcal{A}^j} p_i^j\right]_{\mathcal{A}^j} \tag{4.24}$$

$$c_\theta \dot{\theta} = \boldsymbol{p} : \dot{\boldsymbol{\lambda}} - \nabla \cdot \left(\frac{f}{\alpha_\theta} \nabla \frac{1}{\theta}\right) - \theta \sum_{j=1}^{N} \sum_{i=0}^{n} \frac{1}{N} \dot{\lambda}_i^j b_i \,, \tag{4.25}$$

with the Kuhn-Tucker conditions

$$\rho \geq 0 \,, \quad \phi \leq 0 \,, \quad \rho\, \phi = 0 \tag{4.26}$$

and the consistency condition

$$\mathrm{dev}_{\mathcal{A}^j} p_i^j \leq 0 \quad \text{for } i \in \mathcal{A}^j \,. \tag{4.27}$$

In (4.27), $\mathrm{dev}_{\mathcal{A}^j} p_i^j := p_i^j - \sum_{k \in \mathcal{A}^j} p_k^j$ is called *active deviator*, $\phi = 1/N \left(f/\theta\, \mathrm{dev}_{\mathcal{A}} \boldsymbol{p}\right)^2 - r^2(|\boldsymbol{\lambda}_0|)$ a yield function and ρ a consistency parameter determined by the constraint $\phi \leq 0$.

The argument in the function of the dissipation coefficient r is the average amount of austenite at each material point, calculated by

$$|\boldsymbol{\lambda}_0| = \sum_{j=1}^{N} \frac{1}{N} \lambda_0^j \,. \tag{4.28}$$

This strategy allows us to account for different energy cost regarding the *nucleation* and the *evolution* of martensite by making an appropriate ansatz for r.

4.3 Finite Element Implementation

The material model presented in Section 4.2 holds on the material point level. As usual, this model can be applied to whole samples by introducing the elastic potential. This potential Π has to achieve a minimum. The consequential minimization conditions are then used to find the displacement field under some boundary conditions. The displacements cause strains which serve as input data for the material model whereas the internal state, which is described by the volume fractions, has an influence on the stiffness and hence back on the displacements. The system of equations has to be solved in an iterative way due to its non-linearity.

The potential we use is the very common potential

$$\Pi = \int_V \Psi \, \mathrm{d}V - \int_V \boldsymbol{u} \cdot (\rho \boldsymbol{f}) \, \mathrm{d}V - \int_{\partial V} \boldsymbol{u} \cdot \boldsymbol{t} \, \mathrm{d}A \tag{4.29}$$

which consists of the total free energy and terms due to internal and external loads ($\boldsymbol{u}$: displacements, ρ: density, $\boldsymbol{t}$: tractions on the surface). It is emphasized that it is not Ψ^{tot} which we have in (4.29), but an extended free energy denoted by Ψ. The extended free energy is composed of the Helmholtz free energy Ψ^{tot} and additional terms which are necessary for regularization purposes. Without any regularization the non-constant dissipation coefficient would yield mesh dependent results. The strategy to circumvent that effect is to introduce

$$\Psi = \Psi^{\mathrm{tot}} + \frac{\beta_\varphi}{2} \underbrace{(\varphi + 1 - |\boldsymbol{\lambda}_0|)^2}_{\text{coupling}} + \frac{c_\varphi}{2} \underbrace{|\nabla \varphi|^2}_{\text{higher order term}} \tag{4.30}$$

with numerical coefficients β_φ and c_φ. Penalizing the gradient of the field function φ will penalize the gradient of the internal variables due to their coupling. By this approach we adopt the idea of [39]. Although we introduce the field function mainly due to numerical reasons (mesh independence) it still may be interpreted as a *phase* field for the averaged crystallographic variants. Then, the higher order term reflects some average interface energy. The parameter c_φ controls the penalization of the interface energy. Thus, lower values of c_φ lead to interfaces which are sharper pronounced whereas higher values lead to interfaces which are more diffuse. In the results presented below we chose $c_\varphi = 0.1$. The numerical factor β_φ may be chosen arbitrarily since it hasn't any noticeable influence on the results as shown in [39]. From (4.30) we can calculate the driving forces for the volume fractions as

$$\begin{aligned} p_i^j &= -\frac{\partial}{\partial \lambda_i^j} \Psi \left(\boldsymbol{\varepsilon}, \boldsymbol{\lambda}, |\boldsymbol{\lambda}_0|, \varphi \right) \\ &= \frac{1}{N} \left[\boldsymbol{\eta}_i^j : \mathbb{C}_{\mathrm{eff}} : (\boldsymbol{\varepsilon} - \boldsymbol{\eta}_{\mathrm{eff}}) + \frac{1}{2} (\boldsymbol{\varepsilon} - \boldsymbol{\eta}_{\mathrm{eff}}) : \left(\mathbb{C}_{\mathrm{eff}} : \left(\mathbb{C}_i^j \right)^{-1} : \mathbb{C}_{\mathrm{eff}} \right) : (\boldsymbol{\varepsilon} - \boldsymbol{\eta}_{\mathrm{eff}}) - c_i(\theta) \right] \\ &\quad + \underbrace{\xi^j \beta_\varphi \left(\varphi + 1 - |\boldsymbol{\lambda}_0| \right)}_{\star}, \end{aligned} \tag{4.31}$$

with additional parts ($\star$) due to regularization. The stationary conditions of (4.29) are

$$\int_V \delta \boldsymbol{\varepsilon} : \frac{\partial \Psi}{\partial \boldsymbol{\varepsilon}} \, \mathrm{d}V - \int_V \delta \boldsymbol{u} \cdot (\rho \boldsymbol{f}) \, \mathrm{d}V - \int_{\partial V} \delta \boldsymbol{u} \cdot \boldsymbol{t} \, \mathrm{d}A = 0 \quad \forall \, \delta \boldsymbol{u} \tag{4.32}$$

$$\int_V \beta_\varphi \left(\varphi + 1 - |\boldsymbol{\lambda}_0| \right) \delta \varphi \, \mathrm{d}V + \int_V c_\varphi \nabla \varphi \cdot \nabla \delta \varphi \, \mathrm{d}V = 0 \quad \forall \, \delta \varphi \, , \tag{4.33}$$

which are solved by the finite element method. Additionally, we write the heat conduction equations in their variational form

$$\begin{aligned} \int_V c_\theta \, \dot{\theta} \, \delta \theta \, \mathrm{d}V = \int_V \boldsymbol{p} : \dot{\boldsymbol{\lambda}} \, \delta \theta \, \mathrm{d}V - \int_{\partial V} \underbrace{\frac{f}{\alpha_\theta} \nabla \frac{1}{\theta}}_{=\boldsymbol{q}} \cdot \boldsymbol{n} \, \delta \theta \, \mathrm{d}A + \frac{1}{\alpha_\theta} \int_V f \nabla \frac{1}{\theta} \cdot \nabla \delta \theta \, \mathrm{d}V \\ - \int_V \theta \sum_{j=1}^{N} \sum_{i=0}^{n} \frac{1}{N} \dot{\lambda}_i^j b_i \, \delta \theta \, \mathrm{d}V \quad \forall \, \delta \theta \end{aligned} \tag{4.34}$$

for which we apply finite elements, too.

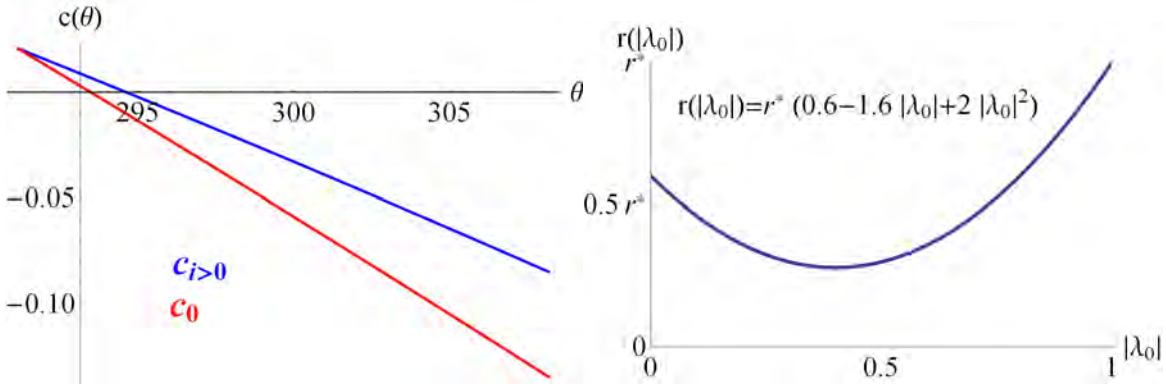

Figure 4.1: Left: chemical energies for austenite c_0 and all martensite variants $c_{i>0}$. Right: assumed function for the dissipation coefficient $r(|\boldsymbol{\lambda}_0|)$.

4.4 Numerical results

We present numerical results for a tensile test for pseudo-elastic Nickel Titanium. The corresponding transformation strains as well as the elastic constants are collected according to [194] in Tab. 4.1 and 4.2, respectively. In all cases the boundary conditions remain the same: for both sides we prescribe the displacements of all first two rows of nodes inside the discretization, i.e. the boundary nodes are excluded. On the left hand side all displacements are zero, whereas the displacements at the right hand side are prescribed in longitudinal direction. Through these boundary conditions the experimental conditions can be simulated best. The dimensions of the specimen are 35 mm, 3.3 mm and 0.68 mm (length, height, depth).

Although the rotation matrices are chosen randomly, we receive reproducible results since we calculate with a relatively high number of grains, exactly $N = 100$.

The plot of the assumed chemical energies for austenite and all variants of martensite is shown in Fig. (4.1) (left) as well as the plot of the dissipation coefficient as function of the average amount of austenite (right).

The functions for the chemical energies are

$$c_0(\theta) = 0.01(\theta - 293.15) - 0.01\,\theta \ln\frac{\theta}{293.15} + 2.61 - 0.0089\,\theta \qquad [\text{MPA}]\,, \tag{4.35}$$

$$c_{i\geq 0}(\theta) = 0.01(\theta - 293.15) - 0.01\,\theta \ln\frac{\theta}{293.15} + 1.76 - 0.0060\,\theta \qquad [\text{MPA}]\,. \tag{4.36}$$

The dissipation coefficient r is determined by the constraint that *nucleation* of martensite (r_{start}) costs more energy than its *evolution* (r_{av}). Furthermore, the completion of the transformation of austenite (r_{finish}) will again dissipate more energy as compared to the "average evolution" of martensite, due to the highly increasing number of interfaces (between austenite and martensite and between martensite and martensite). However, less energy is dissipated as compared to the case when the very first nucleation of martensitic grains takes place. The translation of these physical assumptions into a

mathematical scheme is done via

$$r_{\text{start}} = r(1) \tag{4.37}$$
$$r_{\text{finish}} = r(0) \tag{4.38}$$
$$r_{\text{av}} = \int_0^1 r(|\boldsymbol{\lambda}_0|)\, \mathrm{d}|\boldsymbol{\lambda}_0| \tag{4.39}$$
$$r_{\text{av}} < r_{\text{finish}} < r_{\text{start}} \,. \tag{4.40}$$

For the different dissipation coefficients we assume

$$r_{\text{start}} = r^\star \,, \qquad r_{\text{finish}} = \frac{3}{5} r^\star \qquad r_{\text{av}} = \frac{7}{15} r^\star \,, \tag{4.41}$$

with $r^\star = 0.018$ MPa/K. By quadratic interpolation this yields

$$r(|\boldsymbol{\lambda}_0|) = 0.018 \cdot (0.6 - 1.6|\boldsymbol{\lambda}_0| + 2|\boldsymbol{\lambda}_0|^2) \qquad [\text{MPA/K}] \,. \tag{4.42}$$

We mention that the exact values for r_{start}, r_{finish} and r_{av} are not essential since a variation gives similar results.

In the following we present different numerical results for the same boundary value problem described above. The only parameter we change is the value for the dissipation coefficient for the heat flux α_θ from Eq. (4.22), namely $\alpha_\theta = \{1.0, 2.5, 5.0\} \cdot 10^{-3}$ mmK/W.

In Fig. (4.2) we present the distribution of austenite at various steps in time for $\alpha_\theta = 1.0 \cdot 10^{-3}$ mmK/W. In this case the phase transformation initializes where the specimen is "clamped" (where the displacements are prescribed). Due to the released heat the increased temperature causes the material to evolve a further transformation zone. The relatively small value of α_θ results in a homogeneous temperature conduction so that in the center of the specimen the further front is created. Any small deviation of the front's orientation at the ends from being perpendicular to the longitudinal axes is damped out (the randomness of the orientation matrices yields very small stochastic variations). During further loading phase transformations can be observed in all three zones.

The corresponding distribution of temperature can be seen in Fig. (4.3). We present the temperature distribution for some selected points in time. It can be seen that the phase transformation serves as internal heat source since energy is dissipated during transition. During the increasing prescribed displacements the heat sources move through the specimen analogously to the transformation fronts.

In contrast to Fig. (4.2) we see a different behavior in Fig. (4.4). Here, we changed the dissipation coefficient slightly to $\alpha_\theta = 2.5 \cdot 10^{-3}$ mmK/W. However, the general material response in the beginning is similar. The transformation starts where stress peaks occur but almost simultaneously at two points in the specimen phase transitions initialize. Due to some inclination of the initial fronts the temperature field is not perpendicular either and caused by the a slower heat transport the additional phase transformation happens more closely to the ends. All the fronts proceed localized in a front like manner after their formation. Interestingly, the additional fronts are not perpendicular to the longitudinal axes anymore as they are in the previous case. Due to the changed heat conduction, the austenitic state is more stable in some areas and less stable in others. This influence results in a non-perpendicular but inclined direction in which the transformation spreads over the cross section.

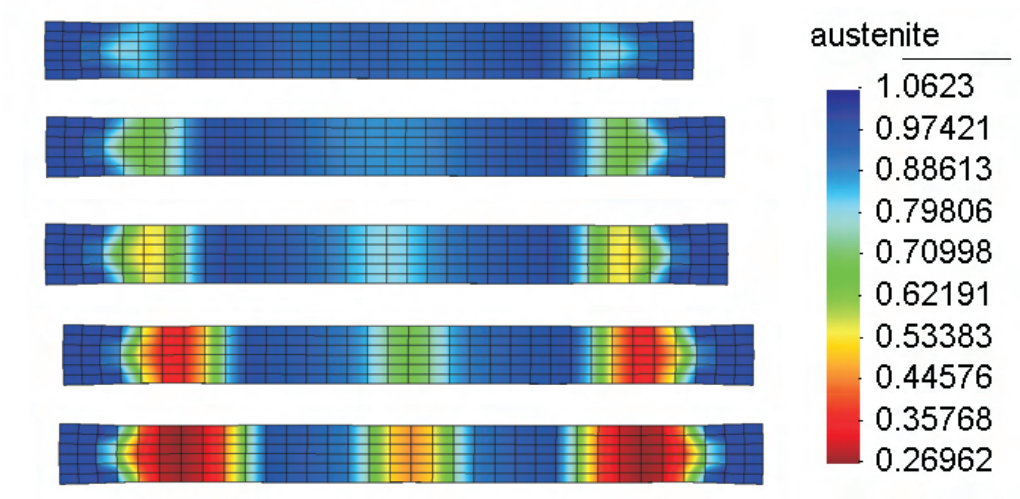

Figure 4.2: Distribution of the austenite phase over the specimen at different load steps, $\alpha_\theta = 1.0 \cdot 10^{-3}$ mmK/W.

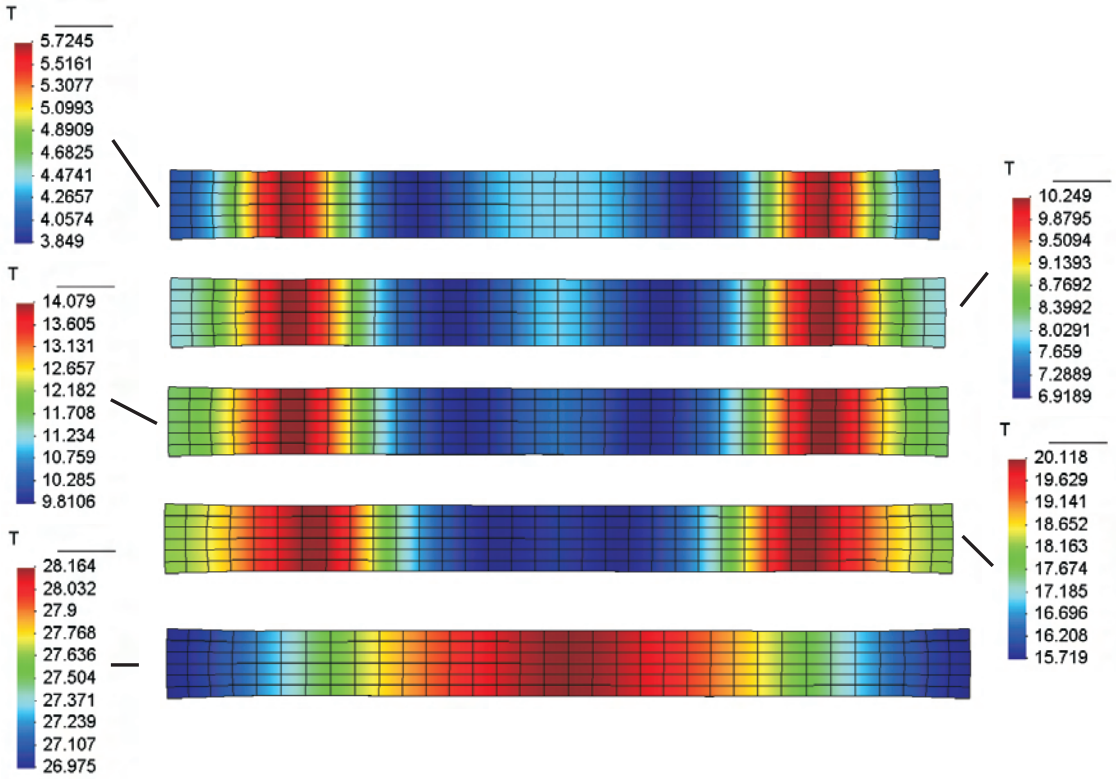

Figure 4.3: Distribution of the temperature over the specimen at different load steps with according legends, $\alpha_\theta = 1.0 \cdot 10^{-3}$ mmK/W.

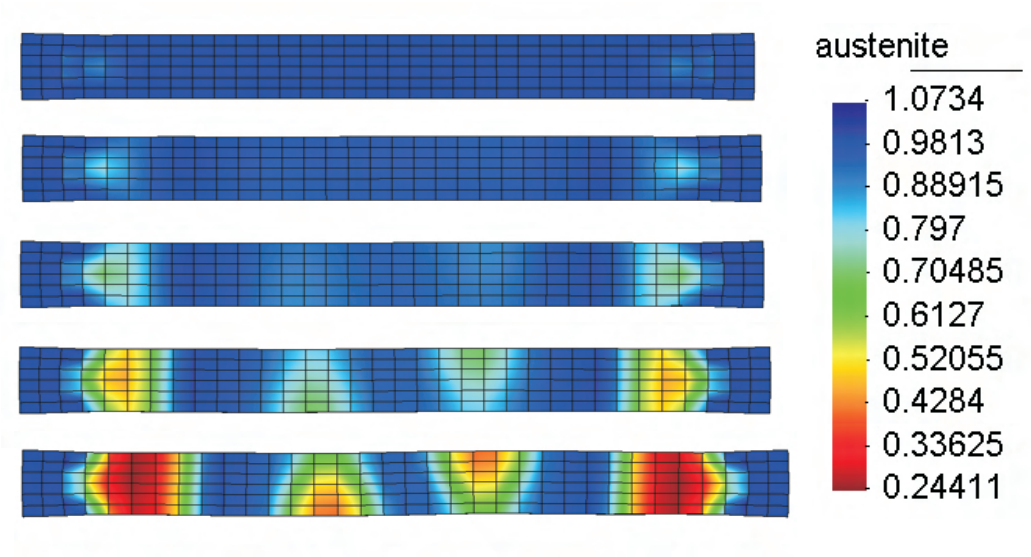

Figure 4.4: Distribution of the austenite phase over the specimen at different load steps, $\alpha_\theta = 2.5 \cdot 10^{-3}$ mmK/W.

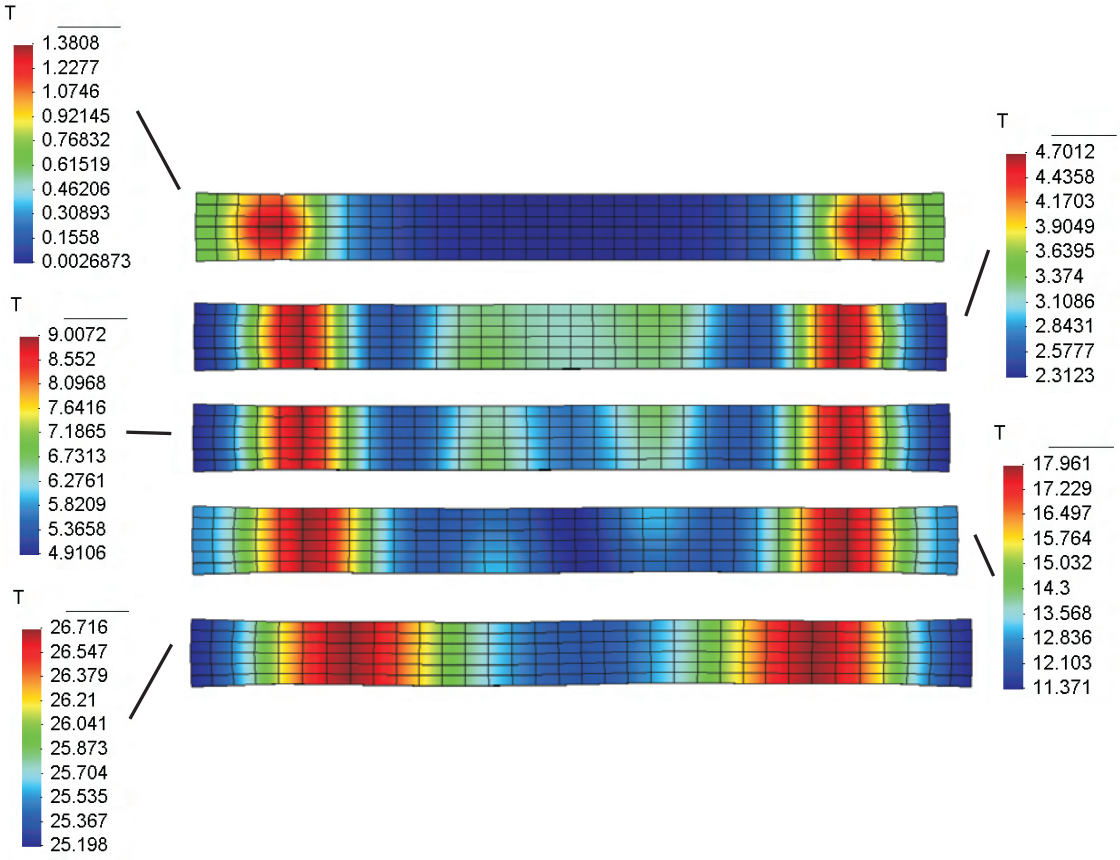

Figure 4.5: Distribution of the temperature over the specimen at different load steps with according legends, $\alpha_\theta = 2.5 \cdot 10^{-3}$ mmK/W.

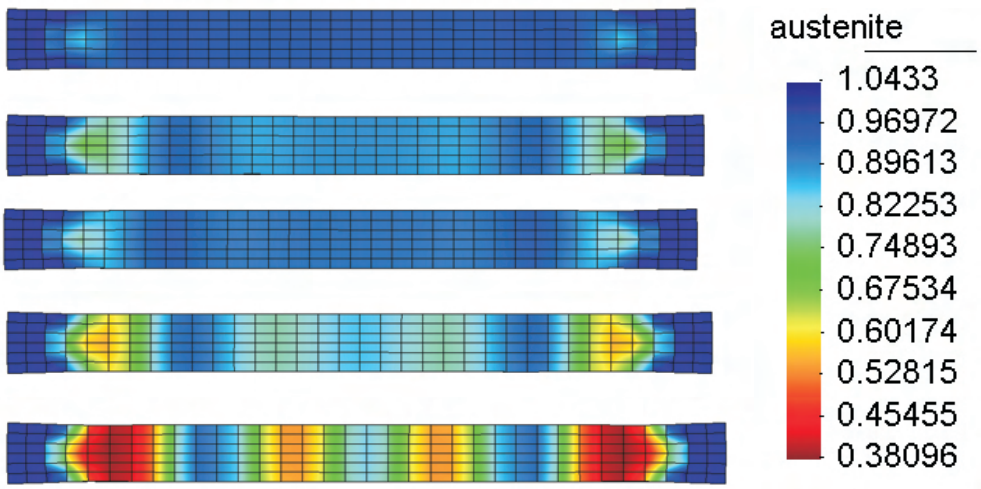

Figure 4.6: Distribution of the austenite phase over the specimen at different load steps, $\alpha_\theta = 5.0 \cdot 10^{-3}$ mmK/W.

The temperature distribution which corresponds to the second example is presented in Fig. 4.5. Since the temperature flows through the specimen its distribution is not as localized as the distribution of phases and the non-perpendicular front is smeared out. Again, the temperature sources move through the specimen.

The last example presented in this paper is based on a dissipation parameter for the heat flux of $\alpha_\theta = 5.0 \cdot 10^{-3}$ mmK/W. The resulting distribution of the austenitic phase is shown in Fig. 4.6. We recognize that again at the ends the initial phase transformation occurs. Here, the heat conductivity is the smallest one. Therefore the heat produced during the phase transformation at the ends of the specimen is not transported to the center very fast but remains mostly in the area of its release. Again, as in all examples here, the produced heat is high enough to stabilize the austenite in a remarkable way. Hence, again more zones of phase transformation occur, in this example quite close to the ends, similar as in the previous example. But in contrast to this one, any inclination of the initial zones does not affect the further developed zones since the "transporting variable", the temperature distribution, moves too slow according to the low heat conductivity. The impact of this fact is that the zones evolve perpendicular to the longitudinal axes of the specimen, similar as the first example, but now with two additional zones instead of only one.

In Fig. 4.7 the temperature distribution for some points in time is shown. It can be seen that obviously in the regions where the phase transformation has initialized the temperature is the highest.

Another interesting point is the global mechanical response of the specimen. This behavior can be captured in force displacement diagrams which we present in Fig. 4.8. It is obvious that all specimens react in a very similar way during the elastic regime. First when the phase transformations take place some slight differences can be recognized. All branches do not show a plateau during transformation which coincides well with experimental findings for tension test under high velocities, e.g. [165]. Due to temperature effects the localized transformation is less pronounced the faster the velocity is, as we have shown in our numerical results. Transformation is influenced by two opposing effects: on the

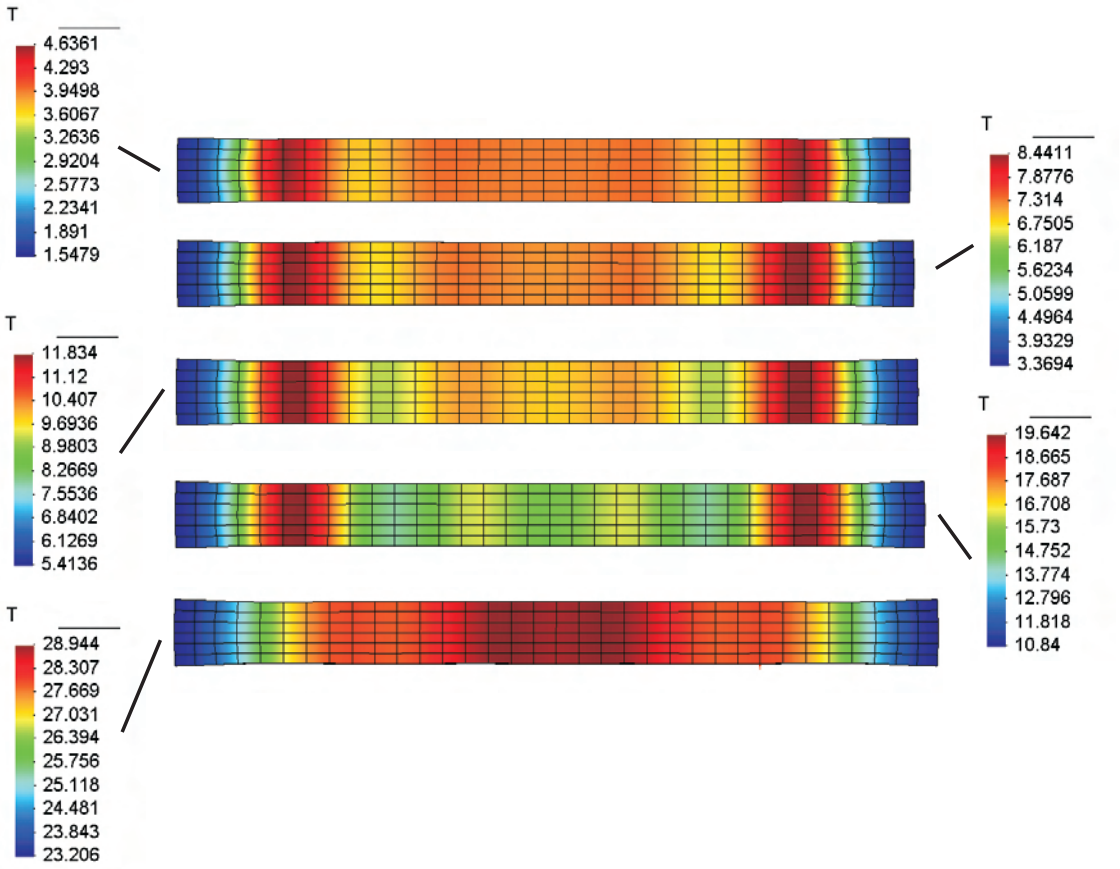

Figure 4.7: Distribution of the temperature over the specimen at different load steps with according legends, $\alpha_\theta = 5.0 \cdot 10^{-3}$ mmK/W.

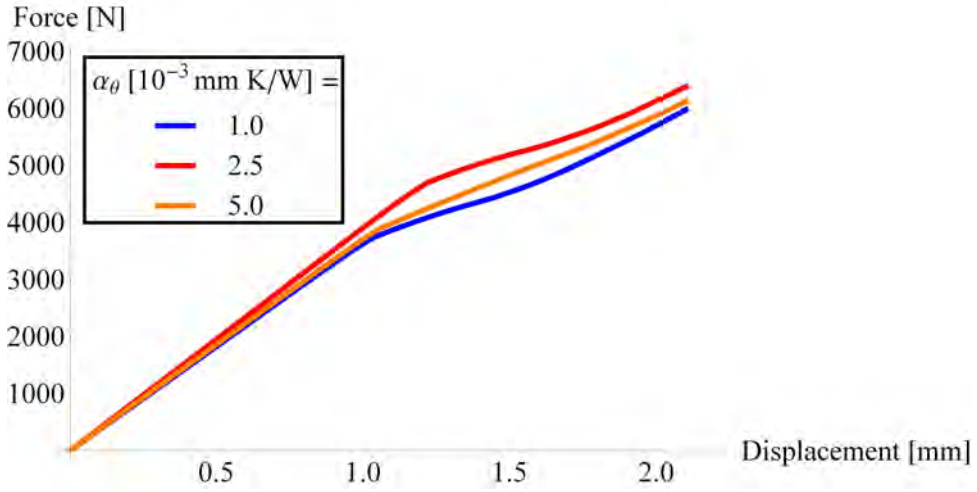

Figure 4.8: Force displacement diagram for the three different cases of dissipation coefficient.

one hand stress will favor the material to transform, on the other hand temperature will stabilize the austenitic phase. The interaction of both factors results in the non-linear but not plateau-like material behavior observed.

The blue branch in Fig. 4.8 corresponds to the distribution of austenite presented first. This branch has the highest similarity to a plateau which is reasonable due to the *initial* nucleation of the two fronts and a *subsequent* formation of the middle front. The orange branch belongs to the distribution of the austenitic phase with various fronts presented last. In that case the material response is almost linear during transformation but with a different slope than in the part without phase transformations. That corresponds to the fact that due to various fronts nearly everywhere in the specimen transformations are going on, but those are slowed due to the high production of heat. The last, red branch gives the material response for the case with transformation fronts with inclined angle. Here, we have a similar material response compared to the blue branch but with higher strains and stresses. At the first glance this result may seem surprising, but since a more localized distribution and less favorable transportation of heat in the specimen is present in this case the rate of transformation is slowed down. Due to the loss effective heat conduction the stabilizing effect on the austenitic phase is more pronounced and can be identified in the global material response.

4.5 Conclusions

Experimental results for a tension test are presented in [165]. There, the localized strain distribution was measured (which corresponds to a change of phase). The result is recalled in Fig. 4.9. We see that various inclinations of the front orientations may be observed in reality, e.g. the front in the upper end is changing its orientation during loading. Since our model is capable to display this phenomenon via a change of the dissipation coefficient α_θ, one reason for the change may be a locally different heat conductivity due to inhomogeneities in the alloy composition.

We presented numerical simulations of poly-crystalline shape memory alloys based on a micro-mechanically well motivated model. The model is able to predict the localized transformation as well as the corresponding distribution of temperature and their coupling. In this paper we focused on

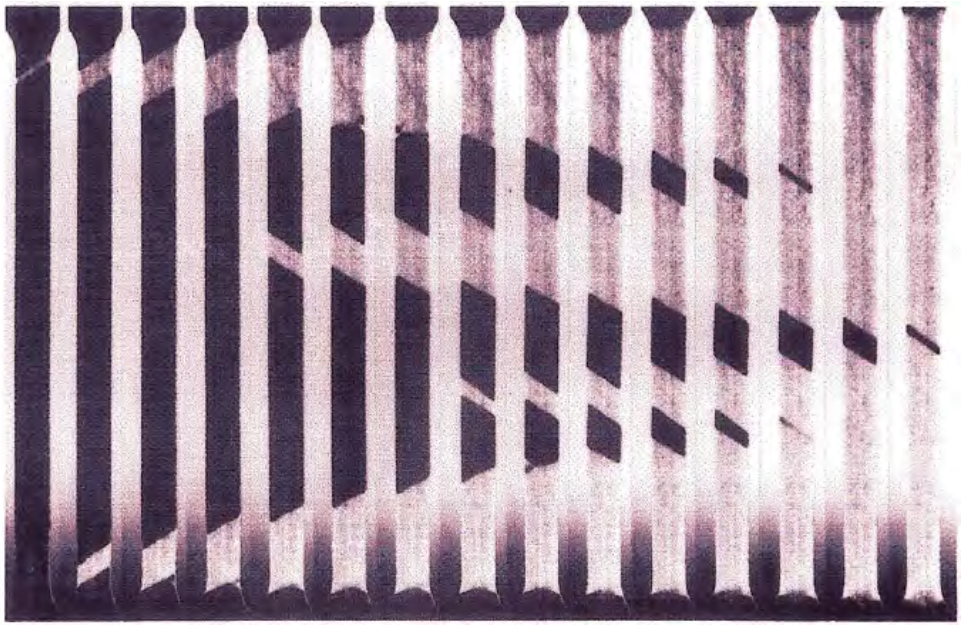

Figure 4.9: Experimentally measured phase distribution. Courtesy of A. Shaw.

the influence of the heat conductivity. Small changes of the dissipation coefficient cause the material to show different behavior. Due to to the randomly chosen rotation matrices the initial orientation of the first transformation front always differs very slightly. Thus, the temperature distribution shows as well some "initial direction" of the fronts. Those very small deviations are then more or less pronounced depending on the heat conductivity. Coupling of the whole system evokes that the direction of the transformation front depends on *where* and *with which orientation* additional fronts evolve. The evolution of all fronts is then coupled again.

This result may give a hint why a different material behavior is observed in the same test. The locally different heat conductivity in real specimens due to variation of the elementary composition of the alloy may be one reason for the observed changes in the orientation of the transformation fronts. Of course, the influence of dislocations and the current distribution of grain boundaries is not taken into account explicitly. On the other hand, those effects are always random so that we may interpret our randomly chosen orientations to reflect this point in some way.

Some future goals of ours are the implementation of locally random parameters for the dissipation coefficient and the analysis of pseudo-plastic problems via our model.

Table 4.1: Transformation strains for cubic to monoclinic transforming NiTi. $\bar{\alpha} = 0.02381$, $\bar{\beta} = -0.02480$, $\bar{\delta} = 0.07528$, $\bar{\epsilon} = 0.04969$

$$\boldsymbol{\eta}_1 = \begin{pmatrix} \bar{\alpha} & \bar{\delta} & \bar{\epsilon} \\ \bar{\delta} & \bar{\alpha} & \bar{\epsilon} \\ \bar{\epsilon} & \bar{\epsilon} & \bar{\beta} \end{pmatrix} \quad \boldsymbol{\eta}_2 = \begin{pmatrix} \bar{\alpha} & \bar{\delta} & -\bar{\epsilon} \\ \bar{\delta} & \bar{\alpha} & -\bar{\epsilon} \\ -\bar{\epsilon} & -\bar{\epsilon} & \bar{\beta} \end{pmatrix} \quad \boldsymbol{\eta}_3 = \begin{pmatrix} \bar{\alpha} & -\bar{\delta} & -\bar{\epsilon} \\ -\bar{\delta} & \bar{\alpha} & \bar{\epsilon} \\ -\bar{\epsilon} & \bar{\epsilon} & \bar{\beta} \end{pmatrix}$$

$$\boldsymbol{\eta}_4 = \begin{pmatrix} \bar{\alpha} & -\bar{\delta} & \bar{\epsilon} \\ -\bar{\delta} & \bar{\alpha} & -\bar{\epsilon} \\ \bar{\epsilon} & -\bar{\epsilon} & \bar{\beta} \end{pmatrix} \quad \boldsymbol{\eta}_5 = \begin{pmatrix} \bar{\alpha} & \bar{\epsilon} & \bar{\delta} \\ \bar{\epsilon} & \bar{\beta} & \bar{\epsilon} \\ \bar{\delta} & \bar{\epsilon} & \bar{\alpha} \end{pmatrix} \quad \boldsymbol{\eta}_6 = \begin{pmatrix} \bar{\alpha} & -\bar{\epsilon} & \bar{\delta} \\ -\bar{\epsilon} & \bar{\beta} & -\bar{\epsilon} \\ \bar{\delta} & -\bar{\epsilon} & \bar{\alpha} \end{pmatrix}$$

$$\boldsymbol{\eta}_7 = \begin{pmatrix} \bar{\alpha} & -\bar{\epsilon} & -\bar{\delta} \\ -\bar{\epsilon} & \bar{\beta} & \bar{\epsilon} \\ -\bar{\delta} & \bar{\epsilon} & \bar{\alpha} \end{pmatrix} \quad \boldsymbol{\eta}_8 = \begin{pmatrix} \bar{\alpha} & \bar{\epsilon} & -\bar{\delta} \\ \bar{\epsilon} & \bar{\beta} & -\bar{\epsilon} \\ -\bar{\delta} & -\bar{\epsilon} & \bar{\alpha} \end{pmatrix} \quad \boldsymbol{\eta}_9 = \begin{pmatrix} \bar{\beta} & \bar{\epsilon} & \bar{\epsilon} \\ \bar{\epsilon} & \bar{\alpha} & \bar{\delta} \\ \bar{\epsilon} & \bar{\delta} & \bar{\alpha} \end{pmatrix}$$

$$\boldsymbol{\eta}_{10} = \begin{pmatrix} \bar{\beta} & -\bar{\epsilon} & -\bar{\epsilon} \\ -\bar{\epsilon} & \bar{\alpha} & \bar{\delta} \\ -\bar{\epsilon} & \bar{\delta} & \bar{\alpha} \end{pmatrix} \quad \boldsymbol{\eta}_{11} = \begin{pmatrix} \bar{\beta} & -\bar{\epsilon} & \bar{\epsilon} \\ -\bar{\epsilon} & \bar{\alpha} & -\bar{\delta} \\ \bar{\epsilon} & -\bar{\delta} & \bar{\alpha} \end{pmatrix} \quad \boldsymbol{\eta}_{12} = \begin{pmatrix} \bar{\beta} & \bar{\epsilon} & -\bar{\epsilon} \\ \bar{\epsilon} & \bar{\alpha} & -\bar{\delta} \\ -\bar{\epsilon} & -\bar{\delta} & \bar{\alpha} \end{pmatrix}$$

Table 4.2: Elastic constants for austenite and martensite

$$\mathbb{C}_{\text{aust}} = \begin{pmatrix} 140 & 110 & 110 & 0 & 0 & 0 \\ 110 & 140 & 110 & 0 & 0 & 0 \\ 110 & 110 & 140 & 0 & 0 & 0 \\ 0 & 0 & 0 & 32 & 0 & 0 \\ 0 & 0 & 0 & 0 & 32 & 0 \\ 0 & 0 & 0 & 0 & 0 & 32 \end{pmatrix} \text{GPa} \quad \mathbb{C}_{\text{mart}} = \begin{pmatrix} 223 & 129 & 99 & 0 & 27 & 0 \\ 129 & 241 & 125 & 0 & -9 & 0 \\ 99 & 125 & 200 & 0 & 4 & 0 \\ 0 & 0 & 0 & 76 & 0 & -4 \\ 27 & -9 & 4 & 0 & 21 & 0 \\ 0 & 0 & 0 & -4 & 0 & 77 \end{pmatrix} \text{GPa}$$

5 A parametrization of the martensite strain orientation distribution function

Published as: *P. Junker*: A Novel Approach to Representative Orientation Distribution Functions for Modeling and Simulation of Polycrystalline Shape Memory Alloys, *Int. J. Numer. Meth. Eng.* **98 (11): 799–818 (2014)**

A micromechanical model for polycrystalline shape memory alloys (SMAs) was introduced in a series of papers by Hackl and co-authors. In order to model the polycrystalline aspect, they assumed a specific set of orientation distribution functions that had to be resolved with high numerical effort. Although this model displays interesting aspects, its use to simulate macroscopic specimens is problematic due to the long calculation time.

In this paper, we present a new approach to modeling and simulation of polycrystalline SMAs that is based on parameterization of a class of orientation distribution functions using only a few parameters. A variational concept is applied to derive evolution equations for these parameters. The resultant material model drastically reduces the calculation time and may thus provide an approach to efficient micromechanical simulation of specimens that are of engineering interest.

This study presents a variety of different numerical examples, such as pseudoelastic and pseudoplastic material behavior for CuAlNi and NiTi SMAs, to demonstrate the broad applicability of the material model. The numerical benefit of the presented modeling approach is demonstrated by comparative calculations of the new model versus the previous model.

5.1 Introduction

Smart materials are able to adapt to given external requirements such as load, temperature and magnetic fields by changing their material properties. A popular subgroup of smart materials are shape memory alloys. These metallic materials exhibit two different and fascinating characteristic phenomena: pseudoplasticity and pseudoelasticity. Both effects are characterized by plateaus (for polycrystals) and hysteresis in the stress/strain diagram. Nevertheless, there are important distinctions between pseudoplasticity and pseudoelasticity.

At lower temperatures, constant stresses occur after linear behavior in a stress/strain diagram during loading. When the specimen is unloaded an apparently irreversible strain remains at zero load. This material reaction during loading and unloading is termed pseudoplasticity. The deformations are only apparently permanent because heating the deformed specimen will result in recovery of the undeformed initial configuration. This combination of loading, unloading, heating, and cooling is referred to as the shape-memory effect or the one-way effect.

Different behavior is observed at higher temperatures: the deformed specimen returns into its original configuration during unloading. Both during loading and unloading, a plateau in the stress/strain diagram is observed together with a hysteresis. Therefore, the material behavior is not elastic but still pseudoelastic because the initial configuration is completely recovered. Pseudoelasticity is associated with deformations that remain elastic for large loads (e.g. strains up to 10%), whereas pseudoplasticity

allows actuators with large forces and distances.

Obviously, both macroscopic effects have to be accompanied by changes in the microscopic material configuration. The lattice structure of the unloaded crystal differs depending on the current temperature. At "high" temperatures, the atoms form a highly symmetrical cubic lattice, known as austenite, whereas at "low" temperatures, the atoms are arranged in less symmetrical lattices, known as martensite. The different martensitic variants can be converted into each other by symmetry relations. Because the actual state depends on the current temperature, there is a threshold temperature at which the austenite transforms into martensite and vice versa. This is known as the transformation temperature, which varies depending on the specific alloy and manufacturing processes (to be precise, there are four transformation temperatures that indicate start and finish for the austenite → martensite transformation, and for the martensite → austenite transformation).

Simulations of materials can be used to reduce the number of necessary experiments during prototyping. Our research group is contributing to the field of simulation with a material model for shape memory alloys that is based solely on energetic quantities and is derived from physical observations. In contrast to other models, for instance in [8], our primary goal is not the specimen's resulting global material response, for instance in terms of strains and stresses. Instead, we consider the physical processes that occur during the diffusionless solid-state phase transformation by modeling the evolution of the crystallographic microstructure taking place in shape memory alloys. Then, the resultant transformation strains and stresses are a yielding outcome of the simulation, and thus there is no need for these quantities to be known as input parameters. This provides a more universal applicability than phenomenological approaches.

Depending on the mechanical load, the material resets its "inner shape" by a rearrangement of the crystal structure. In the case of a single crystal, only the austenite phase is initially present in the case of pseudoelasticity. Due to the (nearly) volume-preserving transformation of austenite into a specific set of martensitic variants, the material is able to accommodate the external load by minimizing its free energy, [151].

If the temperature is the external driving force for phase transformation, there is no preferred direction, as mentioned previously. Hence, in this case the austenite will transform into "virgin" martensite in which every variant has the same volume fraction. The resultant martensitic configuration is the initial state from which pseudoplasticity starts. When a mechanical load is applied to a material that consists of this virgin distribution of martensitic variants, those variants with a "preferred" orientation in the load direction will grow at the expense of variants with a less favored orientation. This initial state cannot be restored during unloading, so that apparently irreversible strains remain at zero load. However, heating the material to create austenite and subsequent cooling will return it to the initial state of uniformly distributed martensite.

For both pseudoelasticity and pseudoplasticity, the described phase transformation has only a limited number of degrees of freedom in a single crystal. The number of martensitic variants is finite and depends on the specific kind of alloy. CuAlNi has six variants, whereas twelve can be identified in NiTi. This "natural" limitation of the number of degrees of freedom has a significant influence on the material behavior: the material transforms in a way that keeps stress constant during transformation only for specific load directions. It is thus obvious that the characteristic plateau in the stress/strain diagram only appears if the load is applied from specific directions. Additionally, the transformation stress depends on that relation of orientations. Overall, the material reaction in a tension test strongly

depends on the particular load direction, see [82].

In contrast, polycrystals are used in most industrial applications. Since a polycrystal is an ensemble of a very large number of single crystals (grains) with different orientations, the number of degrees of freedom is significantly increased. This allows the material to react under tension applied from different directions in a very comparable manner. Depending on the specific load direction and the individual grain orientation, different grains become "active" and will transform for different load directions. However, the global material behavior for this tension test will always result in a plateau in the stress/strain diagram.

This effect can be modeled by means of different general strategies. Phenomenological models for polycrystals were presented in [22], [79], and [120]. Foundations of micromechanical models based on variational arguments were laid down in [10], [110], [138], and [190]. Micromechanical models can be found in [11], [61], and [177] for single crystals, and in [174] for polycrystals. Finite element implementations are presented in [153], which uses a model introduced in [185], and also in [60] and [174].

There are models that take account of the polycrystalline effect by means of a certain set of orientation distribution functions in which the different grain orientations are discretized individually and the actual microstructural state is expressed in terms of volume fractions for all crystallographic phases (austenite and all variants of martensite): for the isothermal case, for instance, we refer to [70] which builds upon works in [61], [57], [71], and [77], and for the thermomechanically coupled case to [96, 91]. A general procedure for the derivation of thermomechanically coupled models is given in [103]. All of these approaches allow simulation of the described material reaction in a physically very reasonable way. However, for instance in the case of NiTi, there are twelve martensitic phases and one austenitic phase that have to be resolved for every single grain. The resulting total number of internal variables is then quite large, and the resultant (nonlinear) system of differential equations greatly increases the calculation time. Although these models are able to predict interesting features, for instance the favored orientation directions by means of pole-figures at different locations in a specimen, [94] and [97], faster models are desired for more complex geometries. For physical accuracy, they should still be based on energy methods. A model for the resolution of phases on a grain layer is presented in [84].

This paper presents an energetic model for polycrystalline shape memory alloys that considers micromechanical aspects and which also has high numerical efficiency. The micromechanical information is implemented by experimentally determined transformation strain tensors, which can be found for CuAlNi in [163] and for NiTi in [194]. Owing to its energy-based character, the model is independent of parameters that are highly influenced by geometry and loading conditions, such as transformation stresses and (scalar) transformation strains. To account for the polycrystalline character, we parametrize in our model a class of orientation distribution functions with only a very limited number of parameters: all individual grain orientations are condensed to one averaged or mean orientation, which is represented by one single, load-dependent orientation. There are several 3-dimensional parameterizations for the orientation, such as Euler angles, Rodrigues parameters, or quaternions, which may need a different number of parameters. We chose parametrization by means of Euler angles with three parameters, in contrast to the four used for the two other aforementioned strategies. This representation is much easier than using Rodrigues parameters, e.g. [16], or quaternions, [176]. Additionally, it was shown in [176] that no 3-dimensional parametrization is both global and nonsingular. This implies that the other parametrization techniques may have some advantages in special cases, but

they may perform worse for other cases. Therefore, we chose the parametrization that is the easiest and fastest for numerical implementation. The Euler angles serve as input for a rotation matrix that has some mathematical simplifications, such as taking the rotation matrix itself as variable (which was carried out for polycrystalline plasticity in [21] for instance). In such an approach, the entire rotation matrix is the unknown variable. Hence, it has to be ensured that the evolution equation always yields rotation matrices that have, naturally, certain characteristics compared (e.g. $\boldsymbol{Q}^T \cdot \boldsymbol{Q} = \boldsymbol{I}$).

The current internal state in terms of crystallographic phases is expressed by volume fractions for austenite and all martensitic variants. Using the variational principle of the minimum of the dissipation potential, we derive a material model that possesses all mentioned characteristics. An additional property of our model is the considerably reduced number of material parameters. Experimental data such as transformation strains and elastic constants (both as full tensors) serve as basic input, independent of the actual load state or geometry. Transformation stresses and strains known from tension tests result from the calculations. Due to the very limited number of internal variables, the material model presented here is extremely fast compared to the approach mentioned above, [71, 77, 96, 91], and drastically reduces the numerical effort.

We will first describe the derivation of the material model and then present the results of numerical experiments to demonstrate the model's abilities. Finally, we evaluate our material model by comparing it to the model presented in [70].

5.2 Material model

5.3 Principle of the minimum of the dissipation potential

We use the principle of the minimum of the dissipation potential to derive the evolution equations. This principle states

$$\mathcal{L} = \dot{\Psi} + \mathcal{D} + \text{cons} \rightarrow \min_{\dot{\boldsymbol{\xi}}} \tag{5.1}$$

The Lagrangian of Eq. (5.1) consists of the rate of the Helmholtz free energy $\dot{\Psi}$ and a dissipation functional $\mathcal{D}$. It has to be extended by material or process specific constraints *cons*, such as e.g. volume preservation or mass conservation, and deductively minimized with respect to the rates of the internal variables $\dot{\boldsymbol{\xi}}$. Other models based on this principle can be found in e.g. [138, 11, 70, 137] or [5], whereas [67] gives a more general explanation.

We use two types of internal variables in our model. To take the different crystallographic phases into account, we make use of Young measures, which serve as volume fractions. These are denoted by a vector $\boldsymbol{\lambda}$ that has the following entries: λ_0 indicates austenite, $\lambda_{i>0}$ collects the alloy-specific martensitic variants. Hence, $i \in \{0, \ldots, n\}$ holds, where n is the maximum number of martensites. The volume fractions belong to the first type of internal variables.

Furthermore, we allow the model to predict the orientation distribution function by means of one global, load-dependent rotation matrix $\boldsymbol{Q}$ that describes the averaged orientation of transforming grains. A simple way to define a rotation matrix is to introduce three Euler angles, collected in $\boldsymbol{\alpha} = \{\varphi, \nu, \omega\}$, on which $\boldsymbol{Q}$ depends, hence $\boldsymbol{Q} = \boldsymbol{Q}(\boldsymbol{\alpha})$. The Euler angles form the second type of internal variables.

In a polycrystalline ensemble, phase-transformation processes do not evolve in all grains homogeneously. Depending on the individual orientation of every grain and the direction of external loads, there are grains that show a more "favorable" orientation to transform compared to others, [82]. Experiments prove further that dislocations are formed by propagating transformation fronts when SMAs change their crystallographic phases, [151]. Due to the local stress field induced by dislocations, the nucleation of martensite is simplified in grains with a high number of dislocations, [151]. Since the dislocations, which are produced in grains with favorable orientation, trigger transformations, the evolution of "active" grains (grains that transform) is path dependent. Although it is beyond the intention of the model to account for the interaction of phase transformations and plasticity, we chose a dissipative approach for the modeling the path dependency of the averaged mean orientation of active grains, expressed by $\boldsymbol{\alpha}$. This yields the vector of all dissipative internal variables in Eq. (5.1) to be $\dot{\boldsymbol{\xi}} = \{\dot{\boldsymbol{\lambda}}, \dot{\boldsymbol{\alpha}}\}$.

In contrast to $\boldsymbol{\alpha}$ which may take every possible value, $\boldsymbol{\alpha} \in \mathbb{R}^3$, there are some constraints on the volume fractions. The first one is that all volume fractions need to be positive. Thus

$$\lambda_i \geq 0 \quad \forall\, i \tag{5.2}$$

Additionally, the volume fractions can be used to demand mass conservation, which is expressed in terms of their rates as

$$\sum_{i=0}^{n} \dot{\lambda}_i = 0 \tag{5.3}$$

To take the constraints of Eqs. (5.2) and (5.3) into account, we introduce Kuhn-Tucker parameters γ_i and a Lagrange multiplier β, respectively. The principle of the minimum of the dissipation potential for our problem then yields

$$\mathcal{L} = \dot{\Psi} + \mathcal{D} - \boldsymbol{\gamma} \cdot \dot{\boldsymbol{\lambda}} + \beta \sum_{i=0}^{n} \dot{\lambda}_i \rightarrow \min_{\dot{\boldsymbol{\lambda}}, \dot{\boldsymbol{\alpha}}} \tag{5.4}$$

The Helmholtz free energy is assumed to be a function of strain $\boldsymbol{\varepsilon}$, volume fractions $\boldsymbol{\lambda}$, and the current orientation $\boldsymbol{\alpha}$: $\Psi = \Psi(\boldsymbol{\varepsilon}, \boldsymbol{\lambda}, \boldsymbol{\alpha})$. Consequently, its rate with respect to time is

$$\dot{\Psi} = \frac{\partial \Psi}{\partial \boldsymbol{\varepsilon}} : \dot{\boldsymbol{\varepsilon}} + \frac{\partial \Psi}{\partial \boldsymbol{\lambda}} \cdot \dot{\boldsymbol{\lambda}} + \frac{\partial \Psi}{\partial \boldsymbol{\alpha}} \cdot \dot{\boldsymbol{\alpha}} \tag{5.5}$$

Inserting this result into Eq. (5.4), the minimization conditions of $\mathcal{L}$ with respect to the volume fractions $\dot{\boldsymbol{\lambda}}$ and to the rate of the Euler angles $\dot{\boldsymbol{\alpha}}$ are

$$\frac{\partial \mathcal{L}}{\partial \dot{\boldsymbol{\lambda}}} = \mathbf{0} \quad \Leftrightarrow \quad \frac{\partial \Psi}{\partial \boldsymbol{\lambda}} + \frac{\partial \mathcal{D}}{\partial \dot{\boldsymbol{\lambda}}} - \boldsymbol{\gamma} + \boldsymbol{\beta} = \mathbf{0} \tag{5.6}$$

$$\frac{\partial \mathcal{L}}{\partial \dot{\boldsymbol{\alpha}}} = \mathbf{0} \quad \Leftrightarrow \quad \frac{\partial \Psi}{\partial \boldsymbol{\alpha}} + \frac{\partial \mathcal{D}}{\partial \dot{\boldsymbol{\alpha}}} = \mathbf{0} \tag{5.7}$$

where $\boldsymbol{\beta} = \beta \mathbf{1}$, and $\mathbf{1}$ is a vector of length $n+1$ with all components equal to 1. These two equations can only be evaluated if representations for both the Helmholtz free energy Ψ and the dissipation functional $\mathcal{D}$ have been found. This is carried out in the next sections.

5.3.1 Energy

We derive the Helmholtz free energy for the material (point), as indicated before, by introducing the elastic part of the strains as the difference between the total strain and the respective transformation strain. The current orientation distribution function is described by the rotation matrix $\boldsymbol{Q} = \boldsymbol{Q}(\boldsymbol{\alpha})$. Thus, the energy for each phase Ψ_i reads individually

$$\Psi_i(\boldsymbol{\varepsilon}_i, \boldsymbol{Q}) = \frac{1}{2}\left(\boldsymbol{\varepsilon}_i - \boldsymbol{Q}^T \cdot \boldsymbol{\eta}_i \cdot \boldsymbol{Q}\right) : \mathbb{C}_i : \left(\boldsymbol{\varepsilon} - \boldsymbol{Q}^T \cdot \boldsymbol{\eta}_i \cdot \boldsymbol{Q}\right) + c_i(\theta) \tag{5.8}$$

where $\boldsymbol{\varepsilon}_i$ denotes the strain in the corresponding phase i, $\boldsymbol{\eta}_i$ the transformation strain (which is known from experiments and which is $\boldsymbol{\eta}_0 = \mathbf{0}$ for austenite) and c_i the caloric, temperature-dependent part of the energy. Here, we only consider an idealized isothermal process for which $c_i(\theta) = \text{const} = c_i$. The elastic constants of austenite and martensite are anisotropic for each individual grain (see [163, 194]). The presented approach for the orientation distribution function homogenizes the individual behavior at the "grain level" to a material point level, which reflects the combined behavior of the material. For the purpose of numerical efficiency, we therefore homogenize the elastic behavior by calculating the expectation values of the phase-dependent elastic constants $\mathbb{C}_i$. These isotropic elastic constants are found by averaging the anisotropic elastic constants over all possible grain directions, which is carried out with Eq. (5.9) (see [66] for details)

$$\mathbb{C}_{i,6\times6} = \left[\frac{\pi}{(2\pi)^3}\int_{\varphi=0}^{2\pi}\int_{\nu=0}^{\pi}\int_{\omega=0}^{2\pi} \boldsymbol{Q}_{6\times6} \cdot \left(\mathbb{C}^0_{i,6\times6}\right)^{-1} \cdot \boldsymbol{Q}^T_{6\times6} \,\sin\nu \,\mathrm{d}\varphi \,\mathrm{d}\nu \,\mathrm{d}\omega\right]^{-1} \tag{5.9}$$

where $\boldsymbol{Q}_{6\times6}$ and $\mathbb{C}_{i,6\times6}$ are the representations of $\boldsymbol{Q}$ and $\mathbb{C}_i$ respectively in the six-dimensional space of the Mehrabadi-Cowin notation [132]. The (anisotropic) elastic constants for austenite and martensite in the same notation are denoted by $\mathbb{C}^0_{i,6\times6}$. Of course, the resultant values for $\mathbb{C}_{i,6\times6}$ are isotropic, as expected for a polycrystal. Taking the expectation values of the elastic constants provides reproducible results for different random initial values of $\boldsymbol{\alpha}$. The inverse of the elastic constants accounts for the structure of the effective stiffness, which is derived in Eq. (5.12).

The total energy of the system can be expressed by the minimum of the weighted sum of the energies for each phase under the constraint that the weighted sum of all individual strains, $\boldsymbol{\varepsilon}_i$, gives the average macroscopic strain $\boldsymbol{\varepsilon}$. The weighting factors are the well-known volume fractions for each crystallographic phase i which we introduced as λ_i. Thus, the total energy for fixed volume fractions is

$$\Psi = \min_{\boldsymbol{\varepsilon}_i}\left\{\sum_{i=0}^{n}\lambda_i\Psi_i \;\middle|\; \boldsymbol{\varepsilon} = \sum_{i=0}^{n}\lambda_i\boldsymbol{\varepsilon}_i\right\} \tag{5.10}$$

This minimization problem is brought to the Lagrange function $\mathcal{L}^\star$ via

$$\mathcal{L}^\star = \sum_{i=0}^{n}\lambda_i\Psi_i + \boldsymbol{\sigma} : \left(\boldsymbol{\varepsilon} - \sum_{i=0}^{n}\lambda_i\boldsymbol{\varepsilon}_i\right) \tag{5.11}$$

Evaluation of the stationary point of Eq. (5.11), $\partial\mathcal{L}^\star/\partial\boldsymbol{\varepsilon}_i = \mathbf{0}$, gives Eq. (5.12) for the Lagrange parameter $\boldsymbol{\sigma}$

$$\boldsymbol{\sigma} = \bar{\mathbb{C}} : \left(\boldsymbol{\varepsilon} - \boldsymbol{Q}^T \cdot \bar{\boldsymbol{\eta}} \cdot \boldsymbol{Q}\right) \tag{5.12}$$

where

$$\bar{\mathbb{C}} = \left[\sum_{i=0}^{n} \lambda_i \left(\mathbb{C}_i\right)^{-1}\right]^{-1} \qquad \text{and} \qquad \bar{\boldsymbol{\eta}} = \sum_{i=0}^{n} \lambda_i \boldsymbol{\eta}_i \tag{5.13}$$

from which it follows that $\boldsymbol{\sigma}$ can be identified as the mechanical stress. Due to the character of a Reuß bound in $\bar{\mathbb{C}}$, the inverse of the elastic constants had to be taken in Eq. (5.9).

Plugging this result back into Eq. (5.10), gives for the Helmholtz free energy as

$$\Psi = \frac{1}{2}\left(\boldsymbol{\varepsilon} - \boldsymbol{Q}^T \cdot \bar{\boldsymbol{\eta}} \cdot \boldsymbol{Q}\right) : \bar{\mathbb{C}} : \left(\boldsymbol{\varepsilon} - \boldsymbol{Q}^T \cdot \bar{\boldsymbol{\eta}} \cdot \boldsymbol{Q}\right) + \bar{c} \tag{5.14}$$

where $\bar{c} = \sum_{i=0}^{n} \lambda_i c_i$ as averaged temperature-dependent part of the energy (see also [71] or [70]).

5.3.2 Dissipation functional

In addition to the energy, we need to make assumptions concerning the dissipation functional. As in previous works, e.g. [11], [97], and [70], we chose the dissipation functional to consist of the norm of the rate of the volume fractions $\dot{\boldsymbol{\lambda}}$, and newly of the skew symmetric matrix of angular velocities $\boldsymbol{\Omega} := \dot{\boldsymbol{Q}} \cdot \boldsymbol{Q}^{-1}$, weighted with some parameters r_λ and r_α, thus:

$$\mathcal{D} = r_\lambda |\dot{\boldsymbol{\lambda}}| + r_\alpha ||\boldsymbol{\Omega}|| = r_\lambda |\dot{\boldsymbol{\lambda}}| + \sqrt{2}\, r_\alpha \left(\dot{\varphi}^2 + \dot{\nu}^2 + 2\dot{\varphi}\,\dot{\omega}\,\cos\nu + \dot{\omega}^2\right)^{1/2} \tag{5.15}$$

The use of $\boldsymbol{\Omega}$, instead of $\dot{\boldsymbol{\alpha}}$ for instance, ensures frame-independence. The respective derivatives then yield

$$\frac{\partial \mathcal{D}}{\partial \dot{\boldsymbol{\lambda}}} = r_\lambda \frac{\dot{\boldsymbol{\lambda}}}{|\dot{\boldsymbol{\lambda}}|} \qquad \text{and} \qquad \frac{\partial \mathcal{D}}{\partial \dot{\boldsymbol{\alpha}}} = \sqrt{2}\frac{r_\alpha}{||\boldsymbol{\Omega}||} \begin{pmatrix} \dot{\varphi} + \dot{\omega}\cos\nu \\ \dot{\nu} \\ \dot{\omega} + \dot{\varphi}\cos\nu \end{pmatrix} \tag{5.16}$$

for $\dot{\boldsymbol{\lambda}} \neq \boldsymbol{0}$ and $\dot{\boldsymbol{\alpha}} \neq \boldsymbol{0}$, respectively. This approach ensures rate-independent evolution equations, as presented in Section 5.3.3 (see [11], [96] or [70] for other examples with the same structure in the dissipation functional).

5.3.3 Evolution equations

We account for the constraint of positivity by applying the active set strategy in which an active set $\mathcal{A}$ is defined according to

$$\mathcal{A} \quad = \quad \{i \,|\, \lambda_i \neq 0\} \cup \left\{i \,|\, \lambda_i = 0 \wedge \dot{\lambda}_i > 0\right\} \tag{5.17}$$

All variants that are element of $\mathcal{A}$ fulfill the constraint of positivity, Eq. (5.2), identically and may therefore evolve. During a numerical treatment of the model, this active set has to be updated for every single time step.

The constraint of mass conservation Eq. (5.3) implies for the derivative of the dissipation potential

with respect to the rate of the volume fractions

$$\sum_{k\in\mathcal{A}} \frac{\partial \mathcal{D}}{\partial \dot{\lambda}_k} = \frac{r_\lambda}{|\dot{\boldsymbol{\lambda}}|} \sum_{k\in\mathcal{A}} \dot{\lambda}_k = 0 \tag{5.18}$$

This property can be used to determine the Lagrange parameter β. Taking the sum of the entries with active phases in Eq. (5.6), we calculate

$$\beta = -\frac{1}{n_\mathcal{A}} \sum_{k\in\mathcal{A}} \frac{\partial \Psi}{\partial \lambda_k} \tag{5.19}$$

where $n_\mathcal{A}$ denotes the number of active phases according to Eq. (5.17). The thermodynamical conjugated driving forces are identified to be

$$\boldsymbol{p}^\lambda := -\frac{\partial \Psi}{\partial \boldsymbol{\lambda}} \tag{5.20}$$

for the volume fractions and

$$p_\varphi := -\frac{\partial \Psi}{\partial \varphi}\,, \qquad p_\nu := -\frac{\partial \Psi}{\partial \nu}\,, \qquad p_\omega := -\frac{\partial \Psi}{\partial \omega} \tag{5.21}$$

for the Euler angles.

Evaluation of the stationary conditions in Eq. (5.6) by inserting the derivatives of the dissipation functional, Eq. (5.16), and under consideration of Eqs. (5.19) and (5.20) gives

$$\begin{cases} p_i^\lambda - \dfrac{1}{n_\mathcal{A}} \displaystyle\sum_{k\in\mathcal{A}} p_k^\lambda = \dfrac{\partial \mathcal{D}}{\partial \dot{\lambda}_i} & ,\ i \in \mathcal{A} \\ p_i^\lambda - \dfrac{1}{n_\mathcal{A}} \displaystyle\sum_{k\in\mathcal{A}} p_k^\lambda = -\gamma_i < 0 & ,\ i \notin \mathcal{A} \end{cases} \tag{5.22}$$

The expression

$$\mathrm{dev}_\mathcal{A} p_i^\lambda := p_i^\lambda - \frac{1}{n_\mathcal{A}} \sum_{k\in\mathcal{A}} p_k^\lambda \tag{5.23}$$

is termed the *active deviator*.

Inserting the derivative of $\mathcal{D}$ with respect to the Euler angles, Eq. (5.16), into the stationarity conditions in Eq. (5.7) yields

$$\frac{\partial \Psi}{\partial \varphi} + \sqrt{2} r_\alpha \frac{\dot{\varphi} + \dot{\omega}\cos\nu}{\|\boldsymbol{\Omega}\|} = 0 \tag{5.24}$$

$$\frac{\partial \Psi}{\partial \nu} + \sqrt{2} r_\alpha \frac{\dot{\nu}}{\|\boldsymbol{\Omega}\|} = 0 \tag{5.25}$$

$$\frac{\partial \Psi}{\partial \varphi} + \sqrt{2} r_\alpha \frac{\dot{\omega} + \dot{\varphi}\cos\nu}{\|\boldsymbol{\Omega}\|} = 0 \tag{5.26}$$

This system of equations can be solved for the rates of the respective angles:

$$\dot{\varphi} = \rho_\alpha (p_\varphi - p_\omega \cos\nu) \tag{5.27}$$
$$\dot{\nu} = \rho_\alpha p_\nu (1 - \cos^2\nu) \tag{5.28}$$
$$\dot{\omega} = \rho_\alpha (p_\omega - p_\varphi \cos\nu) \tag{5.29}$$

where Eq. (5.21) has been used. The consistency parameter is defined as $\rho_\alpha := \|\boldsymbol{\Omega}\| / (\sqrt{2} r_\alpha (1 - \cos^2\nu))$.

Although we have already found the entire set of evolution equations, we now perform a Legendre transformation $\mathcal{J}$ of the dissipation functional $\mathcal{D}$ given in Eq. (5.15) for mathematical simplification. This yields

$$\begin{aligned} \mathcal{J}_\lambda &= \sup_{\dot{\boldsymbol{\lambda}}} \left\{ \boldsymbol{p}^\lambda \cdot \dot{\boldsymbol{\lambda}} - \mathcal{D} \;\middle|\; \mathcal{A} \right\} \\ &= \sup_{\dot{\boldsymbol{\lambda}}} \left\{ \frac{|\dot{\boldsymbol{\lambda}}|}{r_\lambda} \underbrace{\left(\sum_{i=0}^{n} \left(\mathrm{dev}_{\mathcal{A}} p_i^\lambda \right)^2 - r_\lambda^2 \right)}_{=: \Phi_\lambda(\boldsymbol{p}^\lambda) \overset{!}{\leq} 0} \;\middle|\; \mathcal{A} \right\} \end{aligned} \tag{5.30}$$

for the volume rates.

A second Legendre transformation gives, similar to the volume fractions, an indicator function as to whether or not reorientation takes place. Hence,

$$\begin{aligned} \mathcal{J}_\alpha &= \sup_{\dot{\boldsymbol{\alpha}}} \left\{ p^\varphi \dot{\varphi} + p^\nu \dot{\nu} + p^\omega \dot{\omega} - \sqrt{2} r_\alpha \left(\dot{\varphi}^2 + \dot{\nu}^2 + 2\dot{\varphi}\dot{\omega}\cos\nu + \dot{\omega}^2 \right)^{1/2} \right\} \\ &= \sup_{\dot{\boldsymbol{\alpha}}} \left\{ \frac{\|\boldsymbol{\Omega}\|}{\sqrt{2} r_\alpha (1 - \cos^2\nu)} \right. \qquad (5.31) \\ &\quad \underbrace{\left. \left(p_\varphi^2 + p_\nu^2 (1 - \cos^2\nu) + p_\omega^2 - 2 p_\varphi p_\omega \cos\nu - \sqrt{2} r_\alpha^2 (1 - \cos^2\nu) \right) \right\}}_{=: \Phi_\alpha(\boldsymbol{p}^\alpha) \overset{!}{\leq} 0} \qquad (5.32) \end{aligned}$$

Thus, both Legendre transformations, Eqs. (5.30) and (5.31), contain expressions, denoted by Φ_λ and Φ_α respectively, that bound the supremum problem. Since the rates may take arbitrary values, the aforementioned factors have to be less than or equal to zero. Therefore, they serve as (two) yield functions with the yield limits r_λ and r_α known from (multisurface) plasticity. This gives the evolution equations for the phases from Eq. (5.6) and for the angles from Eq. (5.7) as

$$\dot{\boldsymbol{\lambda}} = \rho_\lambda \left(\mathrm{dev}_{\mathcal{A}} \boldsymbol{p}^\lambda \right)_{\mathcal{A}} \tag{5.33}$$
$$\dot{\boldsymbol{\alpha}} = \rho_\alpha \boldsymbol{p}^\alpha \tag{5.34}$$

with $\rho_\lambda := |\dot{\boldsymbol{\lambda}}|/r_\lambda$ as consistency parameter and

$$\boldsymbol{p}^\alpha := \begin{pmatrix} p_\varphi - p_\omega \cos\nu \\ p_\nu(1-\cos^2\nu) \\ p_\omega - p_\varphi \cos\nu \end{pmatrix} \tag{5.35}$$

The entire set is closed with the two Kuhn-Tucker conditions

$$\rho_\lambda \geq 0 \qquad \Phi_\lambda \leq 0 \qquad \rho_\lambda\, \Phi_\lambda = 0 \tag{5.36}$$

$$\rho_\alpha \geq 0 \qquad \Phi_\alpha \leq 0 \qquad \rho_\alpha\, \Phi_\alpha = 0 \tag{5.37}$$

and the consistency condition

$$\mathrm{dev}_{\mathcal{A}} p_i^\lambda \leq 0 \qquad \text{for } i \notin \mathcal{A} \tag{5.38}$$

that updates the active set.

5.3.4 Driving forces

The driving forces still have to be calculated. For the volume fractions they are

$$\begin{aligned} p_i^\lambda = -\frac{\partial \Psi}{\partial \lambda_i} &= \left(\boldsymbol{Q}^T \cdot \boldsymbol{\eta}_i \cdot \boldsymbol{Q}\right) : \bar{\mathbb{C}} : \left(\boldsymbol{\varepsilon} - \boldsymbol{Q}^T \cdot \bar{\boldsymbol{\eta}} \cdot \boldsymbol{Q}\right) \\ &\quad + \frac{1}{2}\left(\boldsymbol{\varepsilon} - \boldsymbol{Q}^T \cdot \bar{\boldsymbol{\eta}} \cdot \boldsymbol{Q}\right) : \left[\bar{\mathbb{C}} : (\mathbb{C}_i)^{-1} : \bar{\mathbb{C}}\right] : \left(\boldsymbol{\varepsilon} - \boldsymbol{Q}^T \cdot \bar{\boldsymbol{\eta}} \cdot \boldsymbol{Q}\right) - c_i \end{aligned} \tag{5.39}$$

(see also [70]). The Euler angles are introduced by means of the rotation matrix $\boldsymbol{Q}$, thus $\boldsymbol{Q} = \boldsymbol{Q}(\boldsymbol{\alpha})$. Hence, the driving forces for the angles are

$$p_\varphi = -\frac{\partial \Psi}{\partial \varphi} = -\frac{\partial \Psi}{\partial \boldsymbol{Q}} : \frac{\partial \boldsymbol{Q}}{\partial \varphi} \tag{5.40}$$

$$p_\nu = -\frac{\partial \Psi}{\partial \nu} = -\frac{\partial \Psi}{\partial \boldsymbol{Q}} : \frac{\partial \boldsymbol{Q}}{\partial \nu} \tag{5.41}$$

$$p_\omega = -\frac{\partial \Psi}{\partial \omega} = -\frac{\partial \Psi}{\partial \boldsymbol{Q}} : \frac{\partial \boldsymbol{Q}}{\partial \omega} \tag{5.42}$$

The first part of the driving forces is identical for all angles and yields

$$-\frac{\partial \Psi}{\partial \boldsymbol{Q}} = 2\left[\bar{\boldsymbol{\eta}} \cdot \boldsymbol{Q} \cdot \bar{\mathbb{C}} : \left(\boldsymbol{\varepsilon} - \boldsymbol{Q}^T \cdot \bar{\boldsymbol{\eta}} \cdot \boldsymbol{Q}\right)\right] \tag{5.43}$$

There are several possible ways to define the specific rotation matrix $\boldsymbol{Q}$ by means of rotations around different axes and around the respective angles. We chose the following

$$\boldsymbol{Q}(\boldsymbol{\alpha}) = \begin{pmatrix} \cos\varphi\cos\omega - \cos\nu\sin\varphi\sin\omega & -\cos\nu\cos\omega\sin\varphi - \cos\varphi\sin\omega & \sin\nu\sin\varphi \\ \cos\omega\sin\varphi + \cos\nu\cos\varphi\sin\omega & \cos\nu\cos\varphi\cos\omega - \sin\varphi\sin\omega & -\cos\varphi\sin\nu \\ \sin\nu\sin\omega & \cos\omega\sin\nu & \cos\nu \end{pmatrix} \tag{5.44}$$

The entries for $\partial \boldsymbol{Q}/\partial \boldsymbol{\alpha} = (\partial \boldsymbol{Q}/\partial\varphi, \partial \boldsymbol{Q}/\partial\nu, \partial \boldsymbol{Q}/\partial\omega)$ are then

$$\frac{\partial \boldsymbol{Q}}{\partial \varphi} = \begin{pmatrix} -\cos\omega\sin\varphi - \cos\nu\cos\varphi\sin\omega & -\cos\nu\cos\varphi\cos\omega + \sin\varphi\sin\omega & \cos\varphi\sin\nu \\ \cos\varphi\cos\omega - \cos\nu\sin\varphi\sin\omega & -\cos\nu\cos\omega\sin\varphi - \cos\varphi\sin\omega & \sin\nu\sin\varphi \\ 0 & 0 & 0 \end{pmatrix}$$

$$\frac{\partial \boldsymbol{Q}}{\partial \nu} = \begin{pmatrix} \sin\nu\sin\varphi\sin\omega & \cos\omega\sin\nu\sin\varphi & \cos\nu\sin\varphi \\ -\cos\varphi\sin\nu\sin\omega & -\cos\varphi\cos\omega\sin\nu & -\cos\nu\cos\varphi \\ \cos\nu\sin\omega & \cos\nu\cos\omega & -\sin\nu \end{pmatrix}$$

$$\frac{\partial \boldsymbol{Q}}{\partial \omega} = \begin{pmatrix} -\cos\nu\cos\omega\sin\varphi - \cos\varphi\sin\omega & -\cos\varphi\cos\omega + \cos\nu\sin\varphi\sin\omega & 0 \\ \cos\nu\cos\varphi\cos\omega - \sin\varphi\sin\omega & -\cos\omega\sin\varphi - \cos\nu\cos\varphi\sin\omega & 0 \\ \cos\omega\sin\nu & -\sin\nu\sin\omega & 0 \end{pmatrix}$$

Of course, if a different approach for the rotation matrix in Eq. (5.44) is chosen, the derivatives have to be recalculated.

5.3.5 Numerical implementation

The presented material model has a structure similar to multisurface plasticity, [170]: there are two evolution equations in combination with two Kuhn-Tucker conditions (see Eqs. (5.33) to (5.37)). Furthermore, the set of active phases has to be updated according to Eq. (5.38). Since the structure of these models may seem complex, we present here one possible solution scheme in Algorithm 1.

We chose an explicit Newton scheme because the tangent operator in an implicit Newton scheme is hard to find for this material model. Due to its complexity, the numerical tangent may be even faster. Therefore, we accept the need for smaller time increments when using an explicit scheme, but maintain the easier numerical implementation. For the treatment of the yield functions in combination with the Kuhn-Tucker conditions, we use a staggered solution scheme: starting from the previous time step, the updates of the volume fractions and the Euler angles are found individually. In order to fulfill $\Phi_\lambda \leq 0$ and $\Phi_\alpha \leq 0$ simultaneously, we use both updated internal variables for a final calculation and testing of both yield functions. If negative values for the consistency parameters ρ_λ or ρ_α should occur, the algorithm is aborted. As tolerances for the gradient and for zero, we use gtol = 10^{-8} and ztol = 10^{-10}, respectively.

Although the presented numerical treatment is possibly the easiest, and maybe not the most stable one, we did not encounter any numerical problems for varying initial values nor due to bad stability. Nevertheless, a detailed treatment in a finite element scheme has to be discussed.

5.4 Numerical experiments

We present the results of numerical experiments for CuAlNi at high temperatures (pseudoelasticity) and at low temperatures (pseudoplasticity). Furthermore, we compare different initial values

Input: t^{j+1}, $\boldsymbol{\varepsilon}^{j+1}$
CALCULATE: $(\mathrm{dev}_{\mathcal{A}}\boldsymbol{p}_\lambda)^j = (\mathrm{dev}_{\mathcal{A}}\boldsymbol{p}_\lambda)^j\,(\boldsymbol{\varepsilon}^{j+1}, \boldsymbol{\lambda}^j, \boldsymbol{\alpha}^j) \Rightarrow \Phi_\lambda$,
CALCULATE: $\boldsymbol{p}_\alpha^j = \boldsymbol{p}_\alpha^j(\boldsymbol{\varepsilon}^{j+1}, \boldsymbol{\lambda}^j, \boldsymbol{\alpha}^j) \Rightarrow \Phi_\alpha$
SET: $\boldsymbol{\lambda}^{j+1} = \boldsymbol{\lambda}^j$, $\mathcal{A}^{j+1} = \mathcal{A}^j$, $\boldsymbol{\alpha}^{j+1} = \boldsymbol{\alpha}^j$, $\rho_\lambda = 0$, $\rho_\alpha = 0$
if $\Phi_\lambda \le 0 \;\wedge\; \Phi_\alpha \le 0$ **then**
  CONTINUE with next time step: $t^{j+1} \to t^{j+2}$
else
  while $\Phi_\lambda > \mathrm{ztol} \;\vee\; \Phi_\alpha > \mathrm{ztol}$ **do**
    while $\Phi_\alpha > \mathrm{ztol}$ **do**
      $\boldsymbol{\alpha}^{j+1} = \boldsymbol{\alpha}^j + \rho_\alpha \boldsymbol{p}_\alpha^j$
      CALCULATE: $\boldsymbol{p}_\alpha^{j+1} = \boldsymbol{p}_\alpha(\boldsymbol{\varepsilon}^{j+1}, \boldsymbol{\lambda}^j, \boldsymbol{\alpha}^{j+1}) \Rightarrow \Phi_\alpha$
      if $\Phi_\alpha > \mathrm{ztol}$ **then**
        $\boldsymbol{\alpha}^{\mathrm{tr}} = \boldsymbol{\alpha}^j + (\rho_\alpha + \mathrm{gtol})\boldsymbol{p}_\alpha^j$
        CALCULATE: $\boldsymbol{p}_\alpha^{\mathrm{tr}} = \boldsymbol{p}_\alpha(\boldsymbol{\varepsilon}^{j+1}, \boldsymbol{\lambda}^j, \boldsymbol{\alpha}^{\mathrm{tr}}) \Rightarrow \Phi_\alpha^{\mathrm{tr}}$
        $\rho_\alpha \to \rho_\alpha - \frac{\Phi_\alpha}{\Phi_\alpha^{\mathrm{tr}} - \Phi_\alpha}\mathrm{gtol}$
      end
    end
    while $\Phi_\lambda > \mathrm{ztol}$ **do**
      $\boldsymbol{\lambda}^{j+1} = \boldsymbol{\lambda}^j + \rho_\lambda\,(\mathrm{dev}_{\mathcal{A}}\boldsymbol{p}_\lambda)^j$
      CALCULATE: $(\mathrm{dev}_{\mathcal{A}^{j+1}}\boldsymbol{p}_\lambda)^{j+1} = (\mathrm{dev}_{\mathcal{A}^{j+1}}\boldsymbol{p}_\lambda)\,(\boldsymbol{\varepsilon}^{j+1}, \boldsymbol{\lambda}^{j+1}, \boldsymbol{\alpha}^j) \Rightarrow \Phi_\lambda$
      if $\Phi_\lambda > \mathrm{ztol}$ **then**
        $\boldsymbol{\lambda}^{\mathrm{tr}} = \boldsymbol{\lambda}^j + (\rho_\lambda + \mathrm{gtol})\,(\mathrm{dev}_{\mathcal{A}^{j+1}}\boldsymbol{p}_\lambda)^j$
        CALCULATE: $(\mathrm{dev}_{\mathcal{A}^{j+1}}\boldsymbol{p}_\lambda)^{\mathrm{tr}} = (\mathrm{dev}_{\mathcal{A}^{j+1}}\boldsymbol{p}_\lambda)\,(\boldsymbol{\varepsilon}^{j+1}, \boldsymbol{\lambda}^{\mathrm{tr}}, \boldsymbol{\alpha}^j) \Rightarrow \Phi_\lambda^{\mathrm{tr}}$
        $\rho_\lambda \to \rho_\lambda - \frac{\Phi_\lambda}{\Phi_\lambda^{\mathrm{tr}} - \Phi_\lambda}\mathrm{gtol}$
      end
      UPDATE: $\mathcal{A}^{j+1}$ according to Eq. (5.38)
    end
    $\boldsymbol{\alpha}^{j+1} = \boldsymbol{\alpha}^j + \rho_\alpha \boldsymbol{p}_\alpha^j$
    $\boldsymbol{\lambda}^{j+1} = \boldsymbol{\lambda}^j + \rho_\lambda\,(\mathrm{dev}_{\mathcal{A}^{j+1}}\boldsymbol{p}_\lambda)^j$
    CALCULATE: $\boldsymbol{p}_\alpha^{j+1} = \boldsymbol{p}_\alpha(\boldsymbol{\varepsilon}^{j+1}, \boldsymbol{\lambda}^{j+1}, \boldsymbol{\alpha}^{j+1}) \Rightarrow \Phi_\alpha$
    CALCULATE: $(\mathrm{dev}_{\mathcal{A}^{j+1}}\boldsymbol{p}_\lambda)^{j+1} = (\mathrm{dev}_{\mathcal{A}^{j+1}}\boldsymbol{p}_\lambda)\,(\boldsymbol{\varepsilon}^{j+1}, \boldsymbol{\lambda}^{j+1}, \boldsymbol{\alpha}^{j+1}) \Rightarrow \Phi_\lambda$
  end
  if $\rho_\lambda < -\mathrm{ztol} \;\vee\; \rho_\alpha < -\mathrm{ztol}$ **then**
    ABORT
  end
  UPDATE: $\boldsymbol{\lambda}^j \to \boldsymbol{\lambda}^{j+1}$, $\mathcal{A}^j \to \mathcal{A}^{j+1}$, $\boldsymbol{\alpha}^j \to \boldsymbol{\alpha}^{j+1}$
end

Algorithm 1: Numerical implementation of the material model. $(\cdot)^{j+1}$ indicates the actual point in time, $(\cdot)^j$ the previous one.

for the Euler angles and prove empirically independence of the specific choice. We then calculate tension/compression tests for NiTi, again for pseudoelastic and pseudoplastic material responses in order to demonstrate the model's capability to display the material reaction for alloys with different microstructures. Finally, we compare our model to the one in [70] on the basis of CPU times and stress/strain diagrams.

5.4.1 Pseudoelasticity: CuAlNi

We apply our material model first to CuAlNi. The experimentally observed transformation strains are taken from [163] and collected in Table 5.1. The elastic constants are also given in [163] – here we present only the expectation values, given in Table 5.2. In order to create conditions similar to a tension/compression test, we chose the prescribed strain to be

$$\boldsymbol{\varepsilon} = \epsilon \begin{pmatrix} 1 & 0 & 0 \\ 0 & -0.4 & 0 \\ 0 & 0 & -0.4\nu \end{pmatrix}$$

where $\epsilon \in \{-0.02, \dots, 0.06\}$. We emphasize that the choice of strain is obsolete if such (material point) models are embedded in a finite element scheme. Thus, the structure of the strain tensor does not need to be chosen because it is a direct outcome of the resultant displacement field.

Table 5.1: Transformation strains for cubic to orthorhombic transforming CuAlNi after [163]. $\bar{\alpha} = -0.0810031$, $\bar{\beta} = 0.0448553$, $\bar{\delta} = -0.0208949$.

$$\boldsymbol{\eta}_1 = \begin{pmatrix} \bar{\alpha} & 0 & 0 \\ 0 & \bar{\beta} & \bar{\delta} \\ 0 & \bar{\delta} & \bar{\beta} \end{pmatrix} \quad \boldsymbol{\eta}_2 = \begin{pmatrix} \bar{\alpha} & 0 & 0 \\ 0 & \bar{\beta} & -\bar{\delta} \\ 0 & -\bar{\delta} & \bar{\beta} \end{pmatrix} \quad \boldsymbol{\eta}_3 = \begin{pmatrix} \bar{\beta} & 0 & \bar{\delta} \\ 0 & \bar{\alpha} & 0 \\ \bar{\delta} & 0 & \bar{\beta} \end{pmatrix}$$

$$\boldsymbol{\eta}_4 = \begin{pmatrix} \bar{\beta} & 0 & -\bar{\delta} \\ 0 & \bar{\alpha} & 0 \\ -\bar{\delta} & 0 & \bar{\beta} \end{pmatrix} \quad \boldsymbol{\eta}_5 = \begin{pmatrix} \bar{\beta} & \bar{\delta} & 0 \\ \bar{\delta} & \bar{\beta} & 0 \\ 0 & 0 & \bar{\alpha} \end{pmatrix} \quad \boldsymbol{\eta}_6 = \begin{pmatrix} \bar{\beta} & -\bar{\delta} & 0 \\ -\bar{\delta} & \bar{\beta} & 0 \\ 0 & 0 & \bar{\alpha} \end{pmatrix}$$

For all subsequent pseudoelastic calculations of CuAlNi, the caloric part of the Helmholtz free energy for austenite is $c_0 = -25$ [MPa], $c_{i>0} = 0$ [MPa] and the dissipation coefficient $r_\lambda = 7$ [MPa]. Due to the isotropy of the virgin crystallographic states (pure austenite or uniform distribution of martensitic variants), we cannot make any physically meaningful estimate for the initial averaged grain orientation of the entire polycrystal. Therefore, we take it as a (uniformly distributed) random value from

$$\boldsymbol{\alpha} = \{2\pi X_1, \arccos(-1 + 2X_2), 2\pi X_3\}$$

with $X_i \in \{0, \dots, 1\}$ as random numbers. In order to prove empirically independence of this initial guess, we take two sets of random values. These are set 1

$$\boldsymbol{\alpha}_1 = \{2.6260, 1.8406, 5.9814\}$$

and set 2, both in rad,

$$\boldsymbol{\alpha}_2 = \{5.9725, 1.2051, 3.4680\}$$

Table 5.2: Expectation values for the elastic constants of austenite and martensite in CuAlNi calculated from the anisotropic data of [163].

$$\mathbb{C}^{\mathrm{CuAlNi}}_{0,6x6} = \begin{pmatrix} 156.83 & 116.88 & 116.88 & 0 & 0 & 0 \\ 116.88 & 156.83 & 116.88 & 0 & 0 & 0 \\ 116.88 & 116.88 & 156.83 & 0 & 0 & 0 \\ 0 & 0 & 0 & 39.95 & 0 & 0 \\ 0 & 0 & 0 & 0 & 39.95 & 0 \\ 0 & 0 & 0 & 0 & 0 & 39.95 \end{pmatrix} \text{GPa}$$

$$\mathbb{C}^{\mathrm{CuAlNi}}_{i>0,6x6} = \begin{pmatrix} 168.63 & 109.48 & 109.48 & 0 & 0 & 0 \\ 109.48 & 168.63 & 109.48 & 0 & 0 & 0 \\ 109.48 & 109.48 & 168.63 & 0 & 0 & 0 \\ 0 & 0 & 0 & 59.16 & 0 & 0 \\ 0 & 0 & 0 & 0 & 59.16 & 0 \\ 0 & 0 & 0 & 0 & 0 & 59.16 \end{pmatrix} \text{GPa}$$

The dissipation parameter for the reorientation is set stepwise to $r_\alpha = \{7, 3, 2\}$ [MPa]. The numerical results are presented in Figure 5.1.

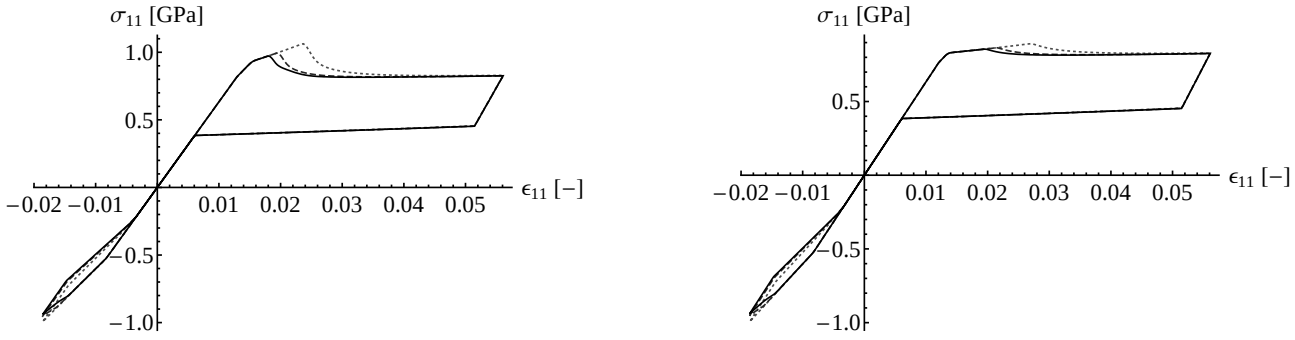

Figure 5.1: CuAlNi: stress/strain diagram for pseudoelasticity. Set 1 (left) and set 2 (right) were used for the initial Euler angles. The values for the dissipation coefficient are respectively $r_\alpha = \{7, 3, 2\}$ [MPa]; the respective curves are dotted, dashed, and solid.

The respective curves are plotted as dotted, dashed, and solid. When a certain amount of martensite has been formed, reorientation takes place. Reorientation may be interpreted in a polycrystalline sense in that initial grains which transform affect grains with a different orientation so that they also undergo phase transformations. The averaged direction of grains with active phase transformations thus changes. The impact on the global material behavior in terms of stresses is strong: the stresses drop and then produce a nearly perfect plateau. This corresponds to experimental tension tests with

polycrystalline shape memory alloys, see [151].

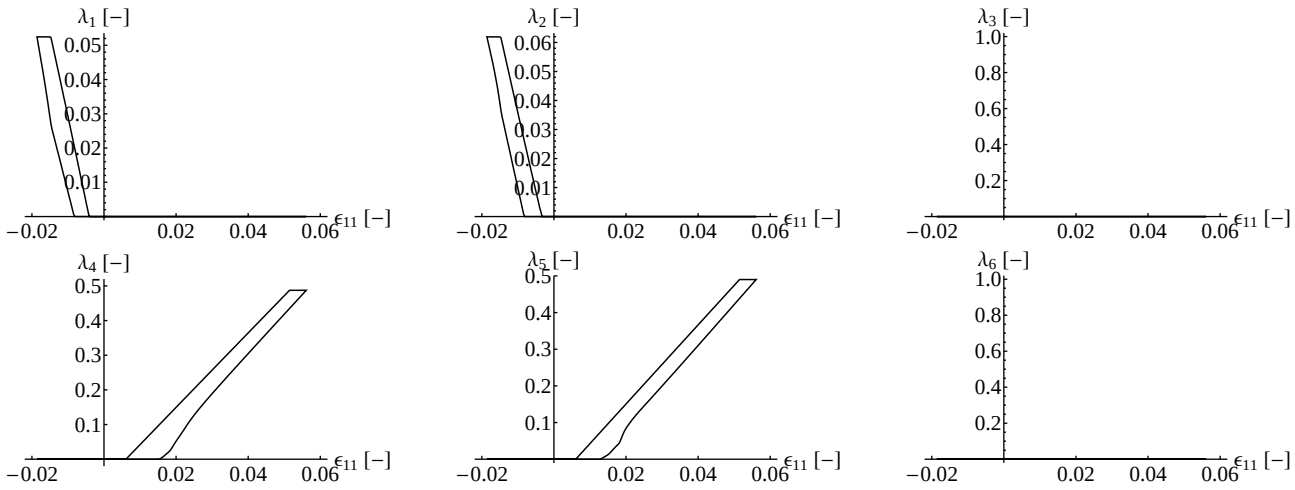

Figure 5.2: CuAlNi: volume fractions for all martensitic variants for pseudoelasticity. Set 1 is used for the initial Euler angles, $r_\alpha = 2$ [MPa].

During compression, still hysteresis is present. However, no plateau arises. This is in agreement with simulations for CuAlNi using a fully polycrystalline model (see [70]), and provided in both models by the micromechanical information carried by the experimental transformation strains. The simulations in [70] are recalculated for comparison and depicted in Figure 5.10. In contrast to these calculations, the stress in our case drops in the beginning. This effect can be controlled by the choice of the dissipation parameter r_α. However, in our calculations there is no increase in the stresses at the end of the plateau, in contrast to [70] which is in better agreement with experimental observations.

For set 2 (Figure 5.1, right), decreasing the dissipation parameter for reorientation reduces the initial zone in the plateau where material softening takes place, as for set 1 (left). A similar effect can be observed during compression. By chance, the second initial guess points the averaged direction of the pseudopolycrystal into a direction that allows the material to adapt to the external load direction quite easily. Hence, only very few rotations and therefore also stress drops are observed during loading. This proves empirically that inclusion of reorientation effects is necessary if a single crystal is to be used for modeling polycrystalline material behavior. The choice of the initial grain orientation is not important: the material will show a very similar reaction, which can be seen from a comparison of the plots at left- and right-hand plots in Figures 5.1 and 5.10. Only in the beginning, when the respective favored direction evolves, are there differences in stress. However, these are very small, which empirically shows a reproducibility, even for different Euler angles.

We plot diagrams only for the volume fractions simulated with $\boldsymbol{\alpha}_1$ because the other plots of phase fraction evolution are quite similar to the presented ones, as expected. The volume fractions evolve in a very smooth way. This can be seen in Figure 5.2 (since the results are nearly identical for the other choices of r_α, we present here only those for $r_\alpha = 2$ [MPa].). During tension, only martensite variants 4 and 5 phase evolve, and during compression only variants 1 and 2. No meta-phase or intermediate phase occurs. In both cases the respective two martensitic variants evolve at the same time.

An illustration of the change in the crystal's orientation is given in Figure 5.3. This shows the relative change of the specific Euler angles for set 1 (left) and set 2 (right) ($r_\alpha = 1$ [MPa]). For both sets, very

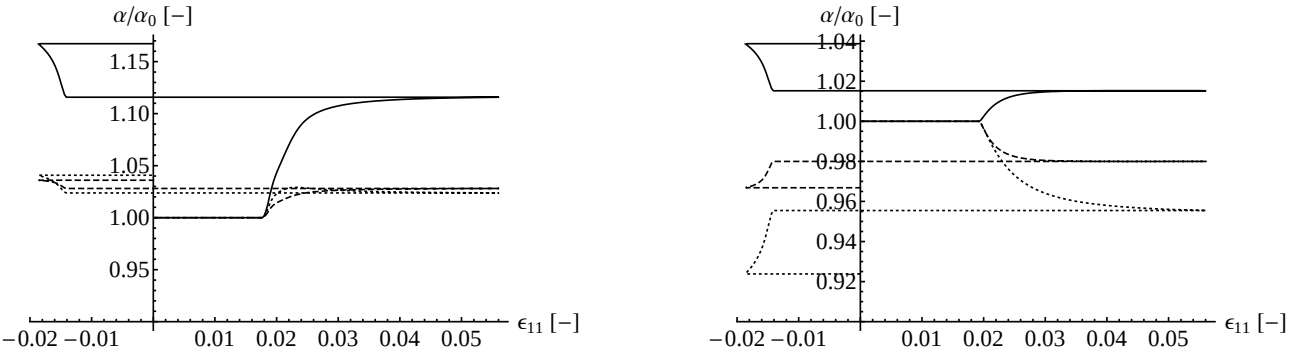

Figure 5.3: CuAlNi: relative change of the individual angles during time for pseudoelasticity. Left: set 1 is used for the initial Euler angles, right: set 2. The respective lines (dotted, dashed, solid) correspond to the three entries of $\boldsymbol{\alpha} = \{\varphi, \nu, \omega\}$ where $\boldsymbol{\alpha}_0$ are the respective initial values. $r_\alpha = 1.0$ [MPa].

drastic changes in grain orientation are present at the beginning of the distinct load states very drastic changes in grain orientation are present. Once a favorable direction has been reached, this direction remains constant until the load state is modified. The crystal undergoes much smaller changes of Euler angles using set 2 compared to set 1. This is reasonable due to the "better agreement" of initial crystal orientation and load direction. The load direction is the same for both tension and compression. However, due to the tension/compression asymmetry, a reorientation takes place when the material is compressed. This indicates that one single static calculation of one optimum orientation that would yield comparable results to the previous model in [70] is not possible: only a dynamical estimation of the average orientation of the transforming grains yields results that are in good agreement with experiments on polycrystals in terms of (nearly) constant plateau stresses, e.g. [151].

5.4.2 Pseudoplasticity: CuAlNi

To show that the model is able to easily display pseudoplasticity, we set the caloric part of the free energy for austenite to $c_0 = 20$ [MPa] and $c_{i>0} = 0$ [MPa] for all calculations in this section. The dissipation coefficient for phase transformation is set in analogy to [70] to $r_\lambda = 80$ [MPa]. We present the results on numerical experiments for CuAlNi and use the same two sets of initial values for the Euler angles as for the pseudoelastic simulations given above. The strain is taken as

$$\boldsymbol{\varepsilon} = \epsilon \begin{pmatrix} 1 & 0 & 0 \\ 0 & -0.5 & 0 \\ 0 & 0 & -0.5 \end{pmatrix}$$

where $\epsilon \in \{-0.095, \ldots, 0.056\}$.

Since we assume that room temperature is much lower than the finish temperature of martensite, we have no austenite at zero strain (with respect to temperature strain), but a uniform distribution of all martensitic variants (from which the transformation strain can be calculated). This is known as disoriented martensite. We again decrease the dissipation coefficient for the Euler angles, r_α, step-by-step in order to investigate its influence. A set of results with varying dissipation coefficient using both initial angles is presented in Figure 5.4. It can be seen, that first a linear material reaction is

present. Then, after reaching a certain threshold, the first slope changes after which the stresses drop. Finally, the curve changes into a plateau – in analogy to the results for pseudoelasticity. After the phase transformation is complete (here: orientation of martensite), a linear branch continues. During unloading, a linear reaction takes place initially before the (negative) stress stays constant. In this state, the plateau stress has the same absolute value as during loading.

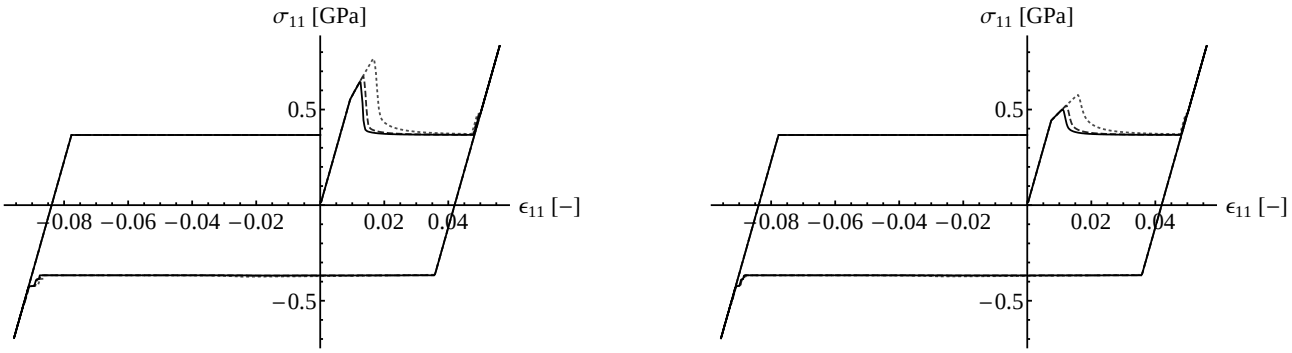

Figure 5.4: CuAlNi: stress/strain diagram for pseudoplasticity. The used sets for the initial Euler angles are: set 1 (left) and set 2 (right). The values for the dissipation coefficient are respectively $r_\alpha = \{7, 3, 2\}$ [MPa]; the respective curves are as dotted, dashed, and solid.

During compression, the same path is followed until the phase transformation has finished. If the specimen is unloaded, the stress returns linearly back to the negative of its original plateau value and then remains constant.

Again, to confirm the independence of the material model's results from the initial guess for the Euler angles, we now present the results of numerical simulations for the second set of angles also for the case of pseudoplasticity (Figure 5.4, right). The choice for the dissipation coefficients is the same, along with all other values for chemical energies and the dissipation coefficient for the phase transformation. A reduction of the dissipation parameter for reorientation reduces the stress drop when phase transformation initializes, thus when the path of the fixed single crystal is left, and the polycrystalline behavior is displayed. In contrast to the initial set 1 (Figure 5.4, left), the stress drop is less intense (for this random guess for set 2).

The evolution of the volume fractions for the case $r_\alpha = 2$ [MPa] is shown in Figure 5.5 where all curves show monotonic slopes. During tension, the variants 3 to 6 evolve quite equivalently at the expense of variants 1 and 2. In contrast, at maximum compression, the main variants are 1 and 2 (each 40%) and less intense are variants 3 to 6 (each 5%).

The evolution of the Euler angles for $r_\alpha = 2$ [MPa] is presented in Figure 5.6 (all other results look similar). We see that severe changes in the crystal orientation take place. These are not symmetric with respect to the abscissa, which is obvious since the reorientation is modeled in a dissipative way. Additionally, the initial state for compression differs from tension. After reorientation has taken place during the first loading steps under tension, only very small adaptations to the load can be found.

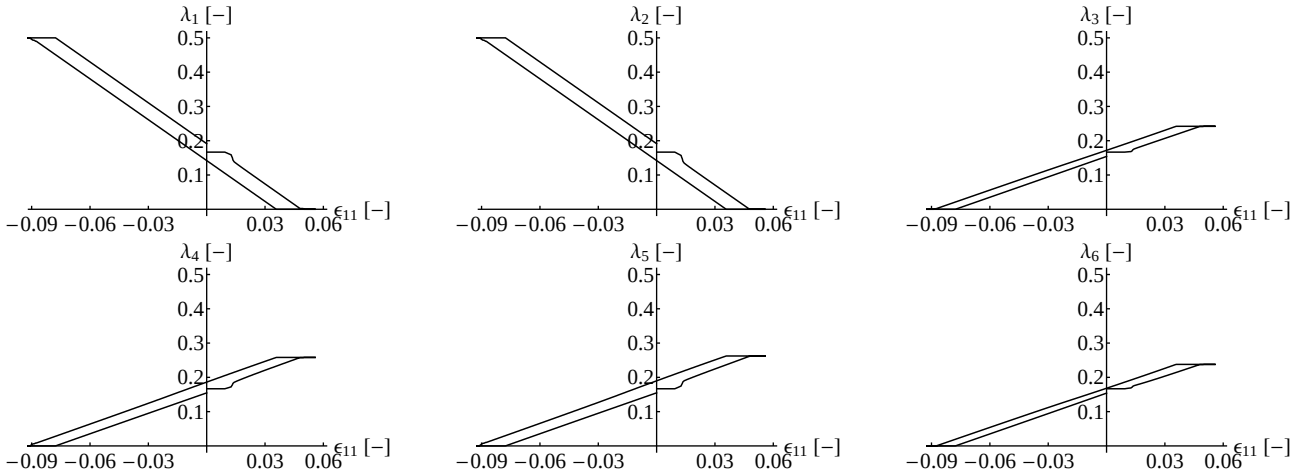

Figure 5.5: CuAlNi: volume fractions for all martensitic variants for pseudoplasticity. Set 1 is used for the initial Euler angles, $r_\alpha = 2$ [MPa].

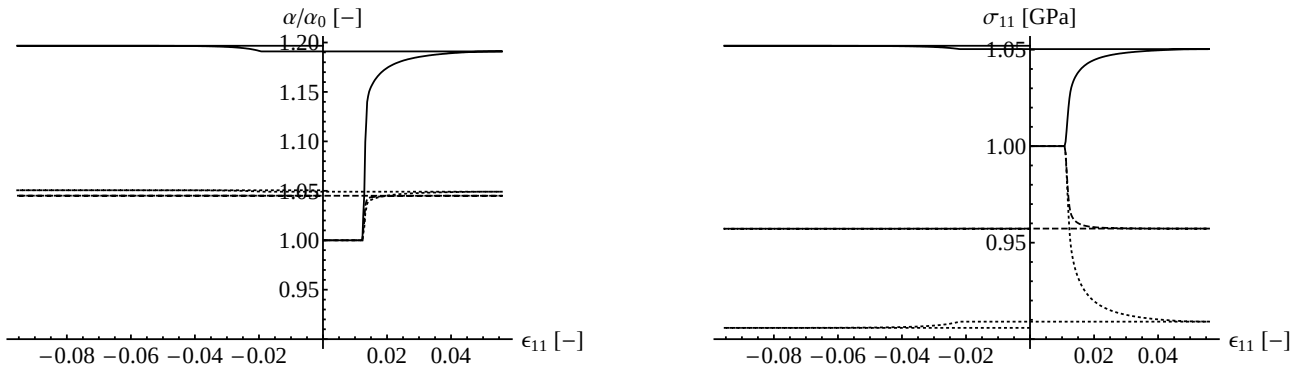

Figure 5.6: CuAlNi: relative change of the individual angles during time for pseudoplasticity. Left: set 1 is used for the initial Euler angles, right: set 2. The respective lines (dotted, dashed, solid) correspond to the three entries of $\boldsymbol{\alpha} = \{\varphi, \nu, \omega\}$ where $\boldsymbol{\alpha}_0$ are the respective initial values. $r_\alpha = 2.0$ [MPa].

5.4.3 NiTi

The general framework of the presented material model is applicable to every shape memory alloy. In order to demonstrate this, we perform numerical simulations of NiTi in this section. The transformation strains are taken from [194] and given in Table 5.3. The expectation values for the elastic constants of austenite and martensite in NiTi are given in Table 5.4, calculated from the elastic constants also from [194] (martensite) and [151] (austenite). Since NiTi may form twelve different variants of martensite, n now runs from 0 (austenite) to 12. The guesses for the initial Euler angles are the same as those used for CuAlNi in the previous sections.

Table 5.3: Transformation strains for cubic to monoclinic transforming NiTi after [194]. $\bar{\alpha} = 0.02381$, $\bar{\beta} = -0.02480$, $\bar{\delta} = 0.07528$, $\bar{\epsilon} = 0.04969$.

$$\boldsymbol{\eta}_1 = \begin{pmatrix} \bar{\alpha} & \bar{\delta} & \bar{\epsilon} \\ \bar{\delta} & \bar{\alpha} & \bar{\epsilon} \\ \bar{\epsilon} & \bar{\epsilon} & \bar{\beta} \end{pmatrix} \quad \boldsymbol{\eta}_2 = \begin{pmatrix} \bar{\alpha} & \bar{\delta} & -\bar{\epsilon} \\ \bar{\delta} & \bar{\alpha} & -\bar{\epsilon} \\ -\bar{\epsilon} & -\bar{\epsilon} & \bar{\beta} \end{pmatrix} \quad \boldsymbol{\eta}_3 = \begin{pmatrix} \bar{\alpha} & -\bar{\delta} & -\bar{\epsilon} \\ -\bar{\delta} & \bar{\alpha} & \bar{\epsilon} \\ -\bar{\epsilon} & \bar{\epsilon} & \bar{\beta} \end{pmatrix}$$

$$\boldsymbol{\eta}_4 = \begin{pmatrix} \bar{\alpha} & -\bar{\delta} & \bar{\epsilon} \\ -\bar{\delta} & \bar{\alpha} & -\bar{\epsilon} \\ \bar{\epsilon} & -\bar{\epsilon} & \bar{\beta} \end{pmatrix} \quad \boldsymbol{\eta}_5 = \begin{pmatrix} \bar{\alpha} & \bar{\epsilon} & \bar{\delta} \\ \bar{\epsilon} & \bar{\beta} & \bar{\epsilon} \\ \bar{\delta} & \bar{\epsilon} & \bar{\alpha} \end{pmatrix} \quad \boldsymbol{\eta}_6 = \begin{pmatrix} \bar{\alpha} & -\bar{\epsilon} & \bar{\delta} \\ -\bar{\epsilon} & \bar{\beta} & -\bar{\epsilon} \\ \bar{\delta} & -\bar{\epsilon} & \bar{\alpha} \end{pmatrix}$$

$$\boldsymbol{\eta}_7 = \begin{pmatrix} \bar{\alpha} & -\bar{\epsilon} & -\bar{\delta} \\ -\bar{\epsilon} & \bar{\beta} & \bar{\epsilon} \\ -\bar{\delta} & \bar{\epsilon} & \bar{\alpha} \end{pmatrix} \quad \boldsymbol{\eta}_8 = \begin{pmatrix} \bar{\alpha} & \bar{\epsilon} & -\bar{\delta} \\ \bar{\epsilon} & \bar{\beta} & -\bar{\epsilon} \\ -\bar{\delta} & -\bar{\epsilon} & \bar{\alpha} \end{pmatrix} \quad \boldsymbol{\eta}_9 = \begin{pmatrix} \bar{\beta} & \bar{\epsilon} & \bar{\epsilon} \\ \bar{\epsilon} & \bar{\alpha} & \bar{\delta} \\ \bar{\epsilon} & \bar{\delta} & \bar{\alpha} \end{pmatrix}$$

$$\boldsymbol{\eta}_{10} = \begin{pmatrix} \bar{\beta} & -\bar{\epsilon} & -\bar{\epsilon} \\ -\bar{\epsilon} & \bar{\alpha} & \bar{\delta} \\ -\bar{\epsilon} & \bar{\delta} & \bar{\alpha} \end{pmatrix} \quad \boldsymbol{\eta}_{11} = \begin{pmatrix} \bar{\beta} & -\bar{\epsilon} & \bar{\epsilon} \\ -\bar{\epsilon} & \bar{\alpha} & -\bar{\delta} \\ \bar{\epsilon} & -\bar{\delta} & \bar{\alpha} \end{pmatrix} \quad \boldsymbol{\eta}_{12} = \begin{pmatrix} \bar{\beta} & \bar{\epsilon} & -\bar{\epsilon} \\ \bar{\epsilon} & \bar{\alpha} & -\bar{\delta} \\ -\bar{\epsilon} & -\bar{\delta} & \bar{\alpha} \end{pmatrix}$$

For pseudoelastic simulations, we set the strain as above, but now with $\epsilon \in \{-0.013, \ldots, 0.067\}$ and $\bar{\nu} = 0.41$. The temperature-dependent part of the energy is chosen to be $c_0 = -25$ [MPa] ($c_{i>0} = 0$ [MPa]) and the dissipation parameter for phase transformation $r_\lambda = 7$ [MPa]. Our intention is to show that the material model is also valid for shape memory alloys other than CuAlNi. For this purpose, we only present the stress/strain curves.

Table 5.4: Expectation values for the elastic constants of austenite and martensite in NiTi calculated from the anisotropic data from [151] and [194].

$$\mathbb{C}^{\mathrm{NiTi}}_{0,6x6} = \begin{pmatrix} 149.36 & 105.32 & 105.32 & 0 & 0 & 0 \\ 105.32 & 149.36 & 105.32 & 0 & 0 & 0 \\ 105.32 & 105.32 & 149.36 & 0 & 0 & 0 \\ 0 & 0 & 0 & 44.04 & 0 & 0 \\ 0 & 0 & 0 & 0 & 44.04 & 0 \\ 0 & 0 & 0 & 0 & 0 & 44.04 \end{pmatrix} \text{GPa}$$

$$\mathbb{C}^{\mathrm{NiTi}}_{i>0,6x6} = \begin{pmatrix} 205.05 & 120.78 & 120.78 & 0 & 0 & 0 \\ 120.78 & 205.05 & 120.78 & 0 & 0 & 0 \\ 120.78 & 120.78 & 205.05 & 0 & 0 & 0 \\ 0 & 0 & 0 & 84.28 & 0 & 0 \\ 0 & 0 & 0 & 0 & 84.28 & 0 \\ 0 & 0 & 0 & 0 & 0 & 84.28 \end{pmatrix} \text{GPa}$$

To conclude the numerical experiments, we finally present results for pseudoplastic NiTi. In order to do so, we set $c_0 = 20$ [MPa] ($c_{i>0} = 0$ [MPa]) and $r_\lambda = 80$ [MPa]. The stress/strain curves for both sets of initial angles (solid: set 1, dashed: set 2) are presented in Figure 5.7 (left), again with $r_\alpha = 2$ [MPa]. Similarly to CuAlNi, NiTi also adapts to the external load by reorientation until a favored averaged grain orientation is established. While reorientation takes place, the stress drops until an almost perfect plateau is established. Again, the zone of stress drop and consequently the height of the stress peak is controlled by the dissipation parameter r_α: larger values produce larger zones and higher stresses – smaller values allow smaller zones and smaller stresses. Again, the initial sets of angles influence this effect. Contrary to CuAlNi, set 1 in NiTi is accompanied by smaller stress drops than set 2.

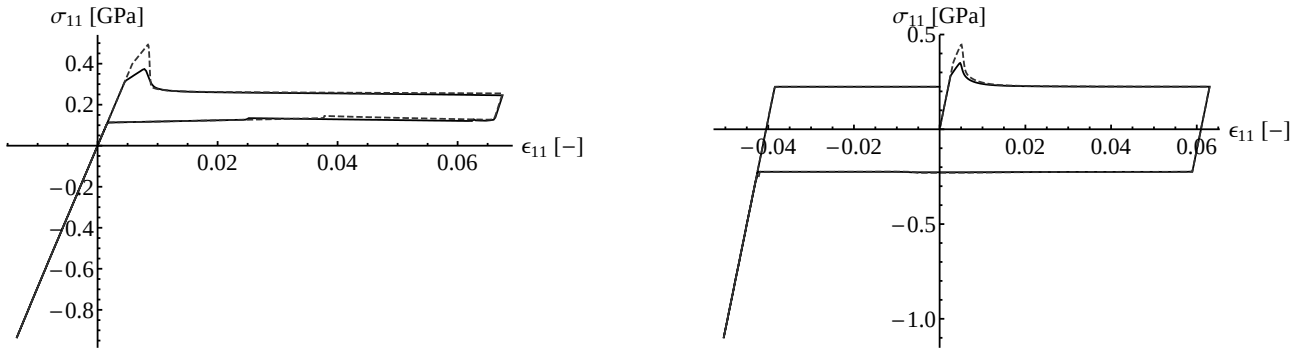

Figure 5.7: NiTi: stress/strain diagram. Left: pseudoelasticity, right: pseudoplasticity. The value for the dissipation coefficient is $r_\alpha = 1$ [MPa]. Solid line: set 1, dashed line: set 2.

The stress remains nearly constant during unloading as well. However, for relatively small values of r_α, a reorientation takes place during unloading (approximately at $\epsilon = 0.047$). This is accompanied

by a small drop in stress. Contrary to compressed CuAlNi, in NiTi both sets show phase transitions during compression that do not influence σ_{11}. Therefore, the material behavior is the same for both results.

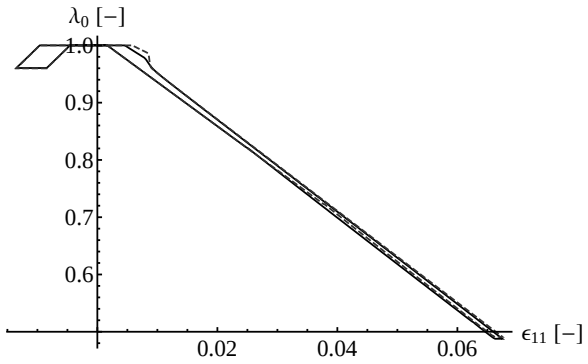

Figure 5.8: NiTi: volume fraction of austenite (λ_0) over strain. Solid line: set 1, dashed line: set 2. r_α = 1.0 [MPa]. At a final strain of 0.067 the remaining amount of austenite is app. 0.5. This indicates that phase transformation is finished at at a strain of app. 0.12 %.

Figure 5.8 shows the volume fraction of austenite for set 1 (solid) and set 2 (dashed). There is only a minor influence of the initial set of Euler angles on the evolution of austenite. Although the 11-component of stress is almost linear, austenite transforms also during compression to martensite (the effective stiffness is affected by the reducing amount of austenite). The reason for this different material reaction compared to CuAlNi lies in the micromechanical information, provided by the respective transformation strains $\boldsymbol{\eta}_i$. Due to the different crystallographic structure of the different martensite variants, e.g. orthorhombic in CuAlNi and monoclinic in NiTi, the material reaction varies and we find different tension/compression asymmetries for CuAlNi and NiTi. However, both alloys transform during tension and compression, see Fig. 5.8. A final comparison to experimental data is left for future work where finite element implementations of the model can be used to create numerical conditions that are comparable to the experimental ones.

With respect to pseudoplasticity, once again there is good agreement between both initial sets of orientation, despite the stress drop in the beginning (Figure 5.7, right). As in the case of pseudoelasticity, set 2 lies in a less favored orientation than set 1 for NiTi, which is in contrast to CuAlNi. Compared to CuAlNi, the stress plateau is now much larger. Additionally, it exhibits again a tension/compression asymmetry.

The relative change of the Euler angles $\boldsymbol{\alpha}$ for pseudoelastic NiTi is plotted in Figure 5.9. At the left-hand side we see the evolution of set 1, at the right hand side that of set 2. The angles of set 2 change much more than those of set 1, which coincides with the observation in the stress/strain diagrams.

The changes during compression indicate that phase transformation takes place during this loading state as well. However, it does not influence the σ_{11} component in the plots.

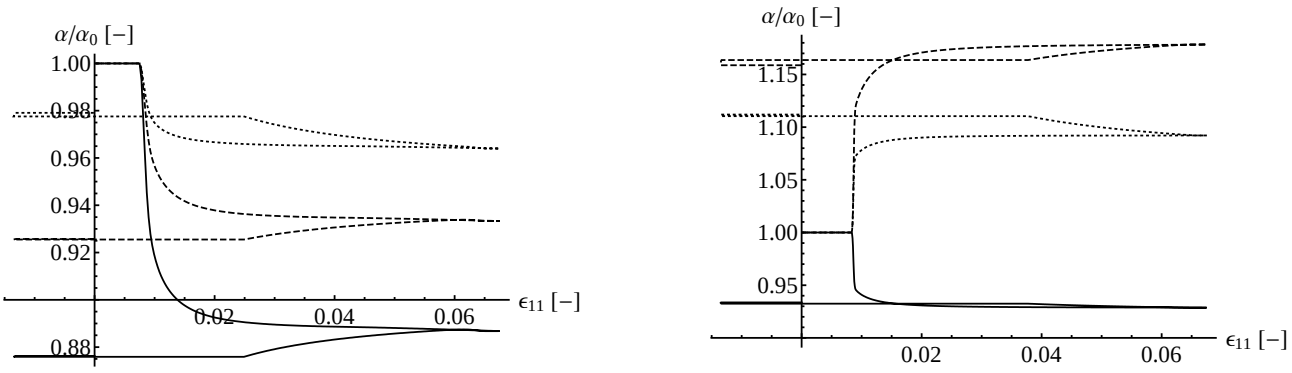

Figure 5.9: NiTi: relative change of the individual angles during time for pseudoelasticity. Left: set 1 is used for the initial Euler angles, right: set 2. The respective lines (dotted, dashed, solid) correspond to the three entries of $\boldsymbol{\alpha} = \{\varphi, \nu, \omega\}$ where $\boldsymbol{\alpha}_0$ are the respective initial values. $r_\alpha = 1.0$ [MPa].

5.4.4 Comparison with previous models

The underlying concept of the presented material model shares some similarities to that presented in [70]. However, the new approach for the evolving orientation distribution function has a remarkable influence on the calculation time. To demonstrate this, we performed simulations with the model of [70] for CuAlNi with a number of 100 randomly chosen grain orientations. This number ensures reproducible results. The respective CPU times are collected in Table 5.5 for the cases of pseudoelasticity and pseudoplasticity. They show that the current model is able to drastically reduce the necessary numerical effort: CPU time is reduced by up to 89.9% for pseudoelastic simulations and up to 91.2% for pseudoplastic material behavior because more martensitic variants become active in this case. The impact of this time saving will become even more evident in future finite element simulations.

Table 5.5: Comparison of the required CPU time in seconds for the new (set 1 and set 2) and the old material models presented in [70].

	new material model		old material model	time saving [%]
	$\boldsymbol{\alpha}_1$	$\boldsymbol{\alpha}_2$		
pseudoelastic	4.88	4.52	44.83	up to 89.9
pseudoplastic	7.56	8.09	85.92	up to 91.2

Figure 5.10 compares the calculated stresses of the old and new models. For the pseudoelastic simulations, the two models yield very similar results. The main difference occurs at the beginning and at the end of the plateau. The area of the hysteresis, which is a measure for the dissipated power, is almost identical. Although the same material parameters are used for both models in the simulations of pseudoplasticity, the width of the hysteresis is larger for the old model. However, the length of the plateau is much smaller than expected for SMAs. Additionally, the plateau in the old material model is not as "stable" as in the new model. Therefore, it is hard to tell which model would yield the more accurate results. This could be carried out in a future work by an experimental comparison when both models are implemented in a finite element code.

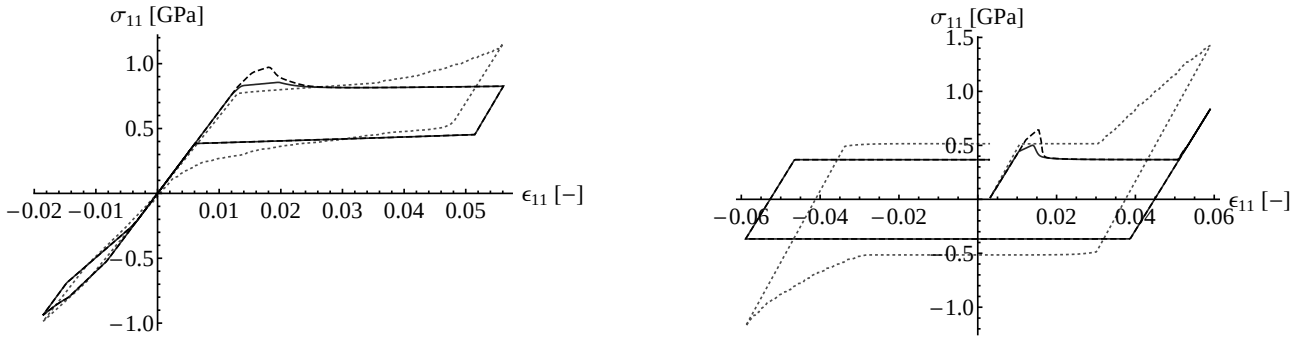

Figure 5.10: Comparison between the new and old material models: set 1 is dashed, set 2 is solid, old model is dotted. Left: pseudoelastic, right: pseudoplastic. $r_\alpha = 2.0$ [MPa].

5.5 Conclusions and outlook

We have presented a potential-based approach for the effective simulation of polycrystalline shape memory alloys by the evolution of a class of orientation distribution functions. Starting from the principle of the minimum of the dissipation potential, we derived the evolution equations for the internal variables, volume fractions, and Euler angles of the representative averaged grain orientation. Micromechanical aspects are included in the model using experimentally determined transformation strains. We performed numerical experiments for different sets of initial guesses for the Euler angles and proved empirically by numerical analysis that the influence of the initial set is of minor importance for the entire global material reaction. Furthermore, we presented the results for pseudoelastic and pseudoplastic material behaviors for which the micromechanical information included causes e.g. a tension/compression asymmetry. The applicability of the model to different kinds of shape memory alloys was confirmed by simulations for CuAlNi and NiTi, which exhibit different possible microstructures due to the varying number of martensite variants. All performed simulations gave a good reproducibility. A drop of varying intensity was only observed at the beginning of the respective stress plateau, and this can be controlled by the model parameter r_α. It was shown that the calculation time can be reduced by up to 90% compared to previous models.

In order to investigate the global material reaction, we plan to apply our model to entire specimens of shape memory alloys. We will implement the model into a finite element code to enable simulation of specimens with arbitrary geometry. Subsequently, we will analyze the behavior of the model in that (numerical) context and the influence of the softening character when phase transformation initializes. For mesh-dependent finite element results, we will follow [39] or [95] for regularization. Finally, the inclusion of thermal coupling is of great interest, and a possible procedure for this is given in [103].

6 A unified variational approach for thermo-mechanically coupled material models

Published as: *P. Junker, J. Makowski, K. Hackl*: The Principle of the Minimum of the Dissipation Potential for Non-Isothermal Processes, *Continuum Mech. Therm.* **26 (3): 259–268 (2014)**

In this paper we contribute to the methodology of material modeling by presenting a potential-based approach for non-isothermal inelastic processes. It is based on the principle of the minimum of the dissipation potential which was used previously only in the isothermal context. In contrast to the principle of maximum dissipation, the presented procedure results in mathematically simplified equations. Due to its variational character, the inclusion of constraints is very simple. After derivation of our method, we use the examples of non-isothermal perfect plasticity and shape memory alloys for demonstration of the validity and performance of the concept.

6.1 Introduction

According to the underlying concept of continuum mechanics, the fundamental laws of physics (balance of linear and angular momentum) and thermodynamics (balance of energy and entropy inequality) apply to all material bodies covered by a particular material model of continuous media (Cauchy continua, Cosserat or polar continua, multi-director continua, etc.), see e.g. [63], [130] or [189]. It is also well-known that the system of field equations (equations of motion and local equation of energy balance) and side conditions (initial, boundary and jump conditions) derived from the basic principles is, in general, under-determined. The lacking equations and relations, which have to be added are called the constitutive equations, [36], [33], [38], [189]. They characterize special classes of materials and their behavior in response to applied forces (stresses) and temperature.

Special classes for which the constitutive equations have been extensively studied in the past include materials with fading memory, materials of differential, rate or integral type, and many other kinds extensively discussed in the classical treaties, e.g. [35], [38], [125], [160] and [189]. In addition, special methodologies have been developed to ensure that the proposed constitutive models are consistent with the laws of thermodynamics. The Coleman-Noll procedure and the Müller-Liu procedure are the most prominent ones (see [36], [33], [122] or [189]). It should be obvious, however, that thermodynamics and general theory of constitutive equations provide only a framework and do not give the specifics of the formulation of the constitutive equations for various materials. These specifics must be brought into the theory by additional constitutive assumptions.

The constitutive theory of elastic materials, including the concept of Cauchy and Green elasticity and the more recent concept of hypo-elasticity, are well-developed and routinely used in the mathematical analysis of the behavior of materials (see details in [81], [167] and [189]). However, the theories of inelastic materials whose behavior is accompanied by energy dissipation and the theories accounting for thermal and electro-magnetic effects are still extensively discussed in the literature. There are several ways of accounting for the dissipative effects accompanying irreversible deformation of material bodies. The oldest and simplest way is to introduce a viscous stress which depends on the rate of strain, as is in the classical Navier-Stokes theory of linearly viscous fluids [189]. Another description of dissipation assumes that the entire past history of the strain influences the stress in a manner compatible with a

principle of fading memory, [36], [33], [189]. A third approach is to postulate the existence of internal state variables. This theory of materials with internal variables, originally developed by Coleman and Gurtin [35], provides a natural framework to investigate the structure of conservation laws from the viewpoint of continuum thermomechanics. It is now widely accepted that constitutive models of inelastic behavior may be successfully treated within this framework. Early investigations along these lines have been discussed in [108]. Further essential development of this theory has been presented by halphen1975materiaux and Nguyen [72] resulting in the new concept of so-called standard media. A survey may be found in the paper by Germain, Nguyen, and Suquet [53].

Central to the structure of any internal variable theory of inelastic materials are the evolution equations which describe the time rates of the internal variables. There are two basic issues: one concerns the form which the evolution equation should take for a particular class of inelastic phenomena, and the other concerns the construction of specific internal variables for that class of materials. In rather recent papers by Hackl and Fischer [67], followed by extensive studies presented in [70, 94, 96, 91], a novel approach has been presented to derive evolution laws for internal variables. This approach is based on the principle of maximum dissipation, first formulated by Onsager for the special problems of heat conduction and diffusion, [146]. The approach developed in the above cited papers has been successfully applied to both coupled and non-coupled processes in materials, [69, 68].

In general, three very common methodical schemes for the development of material models based on the theory of internal variables are the introduction of yield functions for rate-independent materials, the principle of the minimum of the dissipation potential, and the principle of maximum dissipation. All of these share the fact that there exist no thermodynamical explanation for the respective mathematical formulation. A yield function is an indicator function for separating different regimes of material behavior. The dissipation potential, see Eq. (6.14), is the sum of the rate of the Helmholtz free energy and a dissipation functional. However, there is no thermodynamic law requiring that this sum has to be minimal. The principle of maximum dissipation expands the prior method by taking into account both the first and second law of thermodynamics but still: there is no such principle that dissipation always has to be a maximum. So, no matter which method is chosen: everyone has its difficulty to claim thermodynamical justification. However, all methods are just (mathematical) tools to derive models whose governing equations agree with the second law of thermodynamics and are therefore convenient to predict material behavior

Each method has its own benefits and advantages. Maybe it is the most direct way to introduce a yield function from which the evolution equations of the internal variables describing the underlying microstructural state of the material can be derived. If there are materials for which it is very complicated to formulate an appropriate yield function directly, for instance due to complex constraints, the principle of the minimum of the dissipation potential offers an elegant way to consider theses side conditions. Then, the entire problem is brought to a variational level by a Lagrange functional where constraints can just be added easily by using Lagrange or Kuhn-Tucker parameters respectively. A subsequent Legendre transformation of the Lagrange functional results in a characteristic function associated with a yield function, so that the entire model is closed. Until now, this principle has been formulated for isothermal processes only.

The principle of maximum dissipation expands the mentioned advantage of the principle of the minimum of the dissipation potential by the option of including temperature effects. However, the resultant model equations contain a higher mathematical complexity which influences the possible numerical treatment, [69, 68].

In this paper, we discuss the principle of the minimum of the dissipation potential for non-isothermal processes. By comparison with the second law of thermodynamics, this principle can be reformulated in order to take thermal coupling into account, this time without the negative effect of increased complexity of the governing equations as present for the principle of maximum dissipation. The general structure of the evolution equations is presented as well as a generalized heat conduction equation.

After deriving the general framework of the principle of the minimum of the dissipation potential, we chose non-isothermal perfect plasticity and shape memory alloys as examples to demonstrate how to use the presented approach. Furthermore, we give a hint how it is embedded in a functional form.

6.2 Thermodynamic basis

First, let us recall concepts of the thermodynamics used in order to clarify notations. The first law of thermodynamics is expressed by the balance of energy which is given as [167], [189]

$$\dot{\mathcal{E}} + \dot{\mathcal{K}} = \mathcal{W} + \mathcal{Q} \tag{6.1}$$

where a dot $\dot{(\,)}$ represents the time derivative. The internal energy is denoted by $\mathcal{E}$, the kinetic energy by $\mathcal{K}$, the mechanical power is given by $\mathcal{W}$ and $\boldsymbol{Q}$ is the rate of the heat supply. Let us introduce the (specific) Helmholtz free energy Ψ by

$$\int_\Omega \Psi \,\mathrm{d}V = \mathcal{E} - \int_\Omega \theta s \,\mathrm{d}V \tag{6.2}$$

where Ω denotes the body's volume, θ is (absolute) temperature and s the entropy density per unit volume. Furthermore, the mechanical power is given as

$$\mathcal{W} = \int_\Omega \boldsymbol{f} \cdot \boldsymbol{w} \,\mathrm{d}V + \int_{\partial\Omega} \boldsymbol{t}^\star \cdot \boldsymbol{w} \,\mathrm{d}A \,. \tag{6.3}$$

Here, $\boldsymbol{f}$ are external body forces, such as gravitation, $\boldsymbol{w}$ the velocity and $\boldsymbol{t}^\star$ externally acting traction forces. Application of the Cauchy hypothesis $\boldsymbol{\sigma} \cdot \boldsymbol{n} = \boldsymbol{t}^\star$ ($\boldsymbol{n}$: normal vector on the surface) and considering the balance of linear momentum ($\mathrm{div}\boldsymbol{\sigma} + \boldsymbol{f} = \rho\dot{\boldsymbol{w}}$), the mechanical power can be reformulated as

$$\mathcal{W} = \int_\Omega \left(\frac{\mathrm{d}}{\mathrm{d}t} \frac{1}{2} \rho |\boldsymbol{w}|^2 + \boldsymbol{\sigma} : \dot{\boldsymbol{\epsilon}} \right) \mathrm{d}V, \tag{6.4}$$

where ρ is the material's density, $\boldsymbol{\sigma}$ denotes stress and $\boldsymbol{\epsilon}$ strain. The rate of heat supply is [167], [189]

$$\boldsymbol{Q} = \int_\Omega h \,\mathrm{d}V - \int_{\partial\Omega} \boldsymbol{q} \cdot \boldsymbol{n} \,\mathrm{d}A = \int_\Omega \left(h - \nabla \cdot \boldsymbol{q} \right) \mathrm{d}V \tag{6.5}$$

with $\nabla \cdot \boldsymbol{q} \equiv \mathrm{div}\boldsymbol{q}$ and h as internal heat source due to nuclear fission or fusion, radiation, chemical processes and others. The kinetic energy is

$$\mathcal{K} = \int_\Omega \frac{1}{2} \rho |\boldsymbol{w}|^2 \,\mathrm{d}V. \tag{6.6}$$

These formulations yield for the balance of energy, Eq. (6.1),

$$\dot{\Psi} + \frac{\mathrm{d}}{\mathrm{d}t}(\theta s) = \boldsymbol{\sigma} : \dot{\boldsymbol{\epsilon}} + h - \nabla \cdot \boldsymbol{q}. \tag{6.7}$$

Let us recall the reduced form of the second law of thermodynamics which is [167], [189]

$$\theta \dot{s} = \boldsymbol{\sigma} : \dot{\boldsymbol{\epsilon}} - \dot{\Psi} - s\dot{\theta} - \frac{1}{\theta}\boldsymbol{q} \cdot \nabla\theta \geq 0 \tag{6.8}$$

Since in general the Helmholtz free energy is a function of strains, temperature and generalized (tensorial) internal variables $\boldsymbol{\lambda}$, its rate is [35], [125]

$$\dot{\Psi} = \frac{\partial \Psi}{\partial \boldsymbol{\epsilon}} : \dot{\boldsymbol{\epsilon}} + \frac{\partial \Psi}{\partial \theta}\dot{\theta} + \frac{\partial \Psi}{\partial \boldsymbol{\lambda}} : \dot{\boldsymbol{\lambda}}\,. \tag{6.9}$$

Furthermore, the constitutive equations for stress and entropy are [167], [189]

$$\boldsymbol{\sigma} = \frac{\partial \Psi}{\partial \boldsymbol{\epsilon}} \qquad \text{and} \qquad s = -\frac{\partial \Psi}{\partial \theta} \tag{6.10}$$

which follows without any further assumptions from the second law of thermodynamics, Eq. (6.8). Let us define $\mathcal{D} = \theta \dot{s}$ as dissipation. Then, a final form of the balance of energy, Eq. (6.7), reads

$$\mathcal{D} = \theta \dot{s} = \boldsymbol{p} : \dot{\boldsymbol{\lambda}} + h - \nabla \cdot \boldsymbol{q} \tag{6.11}$$

where we introduced $\boldsymbol{p} := -\partial\Psi/\partial\boldsymbol{\lambda}$ as conjugated thermodynamical driving forces acting on the internal variables $\boldsymbol{\lambda}$.

Finally, let us decompose the Helmholtz free energy into three additive parts: the first one is called mechanical part and depends usually on strain, the internal variables, and, for instance concerning thermal expansion, on temperature. The second part is solely a function of temperature, where the third part may depend both on temperature *and* the internal variables. Hence, we assume Ψ in the following general form

$$\Psi(\boldsymbol{\epsilon}, \theta, \boldsymbol{\lambda}) = \Psi_{\mathrm{mech}}(\boldsymbol{\epsilon}, \theta, \boldsymbol{\lambda}) + c(\theta - \theta_{\mathrm{ref}}) - c\theta \log\left(\frac{\theta}{\theta_{\mathrm{ref}}}\right) + \bar{\Psi}_{\theta}(\theta, \boldsymbol{\lambda}) \tag{6.12}$$

where we followed [50] for the purely temperature-dependent part of the energy which was derived from general conclusions independent of a specific material. In Eq. (6.12), θ_{ref} indicates some reference temperature and c heat capacity. The mechanical part of the energy Ψ_{mech} as well as the mixture term $\bar{\Psi}_{\theta}$ have to be specified for every considered material individually.

Finally, the total Gibbs energy $\mathcal{G}$ is defined as

$$\mathcal{G} = \int_{\Omega} \Psi \,\mathrm{d}V - \int_{\Omega} \boldsymbol{f} \cdot \boldsymbol{u} \,\mathrm{d}V - \int_{\partial\Omega} \boldsymbol{t}^{\star} \cdot \boldsymbol{u} \,\mathrm{d}A\,. \tag{6.13}$$

6.3 The principle of the minimum of the dissipation potential for isothermal processes

The principle of the minimum of the dissipation potential is commonly stated as (c.f. [67, 70, 94, 96, 91])

$$\mathcal{L}^\star = \dot{\Psi}(\boldsymbol{\epsilon}, \boldsymbol{\lambda}) + \bar{\mathcal{D}}^\star(\dot{\boldsymbol{\lambda}}) \rightarrow \min_{\dot{\boldsymbol{\lambda}}} \tag{6.14}$$

where $\bar{\mathcal{D}}^\star$ denotes the dissipation functional for which an appropriate ansatz has to be chosen. We emphasize that previously only isothermal processes have been modeled by this approach. Hence, the Helmholtz free energy is then independent of temperature. The evolution equations for the internal variables are then found by evaluating the stationarity conditions of $\mathcal{L}^\star$ with respect to $\dot{\boldsymbol{\lambda}}$. Material dependent constraints can be taken into account easily by just adding them and using Lagrange or Kuhn-Tucker parameters respectively. Thus, this principle allows a very elegant method for material modeling.

Since the principle of the minimum of the dissipation potential may also be written in functional form using for instance the total potential Π (see e.g. [44, 65, 150, 154, 202, 135])

$$\Pi = \int_\Omega \int_{t^n}^{t^{n+1}} \left(\dot{\Psi} + \bar{\mathcal{D}}^\star\right) \mathrm{d}t \, \mathrm{d}V - \int_\Omega \int_{t^n}^{t^{n+1}} \boldsymbol{f} \cdot \dot{\boldsymbol{u}} \, \mathrm{d}t \, \mathrm{d}V - \int_{\partial\Omega} \int_{t^n}^{t^{n+1}} \boldsymbol{t}^\star \cdot \dot{\boldsymbol{u}} \, \mathrm{d}t \, \mathrm{d}A \,, \tag{6.15}$$

thus providing the basis for numerical approximation schemes, a possibility to apply this principle to non-isothermal processes might prove advantageous. In Eq. (6.15), the current and the previous time point are indicated by t^{n+1} and t^n, respectively, while $\boldsymbol{u}$ denotes the displacement field. Minimizing Π with respect to $\boldsymbol{u}^{n+1}$ and $\boldsymbol{\lambda}^{n+1}$ yields the current fields of displacements and internal variables (the minimization condition of Eq. (6.15) for the current internal variables results in discretized evolution equations as obtained from Eq. (6.14)).

For Eq. (6.15), a physical interpretation can be given: let us define the total dissipation Δ as

$$\Delta = \int_\Omega \bar{\mathcal{D}}^\star \, \mathrm{d}V \,. \tag{6.16}$$

Then, Eq. (6.15) is identical to the minimization of the rate of the Gibbs energy, compare to Eq. (6.13), plus dissipation, under the constraint given by the boundary conditions for the displacements,

$$\dot{\mathcal{G}} + \Delta \rightarrow \min_{\dot{\boldsymbol{u}}, \dot{\boldsymbol{\lambda}}} \,. \tag{6.17}$$

This property will be important at a later point.

Equation (6.14) can be simplified since $\mathcal{L}^\star$ is minimized only with respect to the rate of the internal variables, so

$$\mathcal{L}^\star = \frac{\partial \Psi}{\partial \boldsymbol{\lambda}} : \dot{\boldsymbol{\lambda}} + \bar{\mathcal{D}}^\star \tag{6.18}$$

where an ansatz according to $\bar{\mathcal{D}}^\star = r|\dot{\boldsymbol{\lambda}}|$ yields evolution equations which are of a rate-independent type. The scalar quantity r is called dissipation parameter and serves, as shown later, as threshold separating the elastic and the inelastic material behavior. Other approaches are possible, too, as for instance $\bar{\mathcal{D}}^\star = r_2|\dot{\boldsymbol{\lambda}}|^2/2$ yielding evolution equations of a rate-dependent type.

We are going to show now how Eq. (6.18) can be reformulated. In order to do so, we insert Eqs. (6.9)

and (6.10) into Eq. (6.8) and find

$$\mathcal{D} = -\frac{\partial \Psi}{\partial \boldsymbol{\lambda}} : \dot{\boldsymbol{\lambda}} - \frac{1}{\theta} \boldsymbol{q} \cdot \nabla \theta \tag{6.19}$$

For isothermal processes the dissipation is therefore $\mathcal{D}^\star = -(\partial \Psi / \partial \boldsymbol{\lambda}) : \dot{\boldsymbol{\lambda}}$. Comparison to Eq. (6.18) yields

$$\mathcal{L}^\star \equiv \bar{\mathcal{D}}^\star - \mathcal{D}^\star \rightarrow \min_{\dot{\boldsymbol{\lambda}}} \ . \tag{6.20}$$

According to Eq. (6.20), the principle of the minimum of the dissipation potential given in Eq. (6.14) as well as the total potential in Eq. (6.15) can be reformulated,

$$\Pi = \int_\Omega \int_{t^n}^{t^{n+1}} \left(\bar{\mathcal{D}}^\star - \mathcal{D}^\star \right) \mathrm{d}t \, \mathrm{d}V - \int_\Omega \int_{t^n}^{t^{n+1}} \boldsymbol{f} \cdot \dot{\boldsymbol{u}} \, \mathrm{d}t \, \mathrm{d}V - \int_{\partial\Omega} \int_{t^n}^{t^{n+1}} \boldsymbol{t}^\star \cdot \dot{\boldsymbol{u}} \, \mathrm{d}t \, \mathrm{d}A \ , \tag{6.21}$$

This observation seems to be unimportant at first glance, however, it is not since it allows to account for thermal coupling.

6.4 The principle of the minimum of the dissipation potential for non-isothermal processes

The dissipation $\mathcal{D}$ is uniquely given by Eq. (6.19), even for the non-isothermal case. On the other hand, the purpose of the entire scheme of minimizing the dissipation potential is to include side conditions very easily where $\bar{\mathcal{D}}^\star$ serves as 'ingredient' to receive evolution equations which are of the desired type (rate-independent or rate-dependent). It was shown in [67] that in many cases this method of material modeling yields identical evolution equations as the principle of maximum dissipation. This is valid as long as the dissipation functional $\bar{\mathcal{D}}^\star$ fulfills certain conditions.

Of course, if non-isothermal processes are to be modeled, the ansatz for the dissipation functional $\bar{\mathcal{D}}^\star$ has to be adapted: temperature is now an additional unknown variable for which the corresponding heat conduction equation has to be found. It is possible to expand $\bar{\mathcal{D}}^\star$ in a way that it displays the rate-dependent character of the heat conduction equations by introducing $\bar{\mathcal{D}} = \bar{\mathcal{D}}^\star + \bar{\mathcal{D}}^\theta$. Here, $\bar{\mathcal{D}}^\star$ represents the mechanical part of the dissipation potential, as before, and $\bar{\mathcal{D}}^\theta$ its additional thermal contribution. Then, the dissipation potential for the non-isothermal case reads

$$\mathcal{L} = \bar{\mathcal{D}} - \mathcal{D} = \bar{\mathcal{D}}^\star + \bar{\mathcal{D}}^\theta + \frac{\partial \Psi}{\partial \boldsymbol{\lambda}} : \dot{\boldsymbol{\lambda}} + \frac{1}{\theta} \boldsymbol{q} \cdot \nabla \theta \rightarrow \min_{\dot{\boldsymbol{\lambda}}, \boldsymbol{q}} \ , \tag{6.22}$$

whose stationarity conditions have to be evaluated with respect to all unknown variables which are the rate of the internal variables $\dot{\boldsymbol{\lambda}}$ and, newly, the heat flux $\boldsymbol{q}$.

For the evaluation of the stationarity condition $\partial \mathcal{L} / \partial \dot{\boldsymbol{\lambda}} = \boldsymbol{0}$, specific approaches for $\bar{\mathcal{D}}^\star$ and $\bar{\mathcal{D}}^\theta$ have to be chosen. Let us consider the rate-independent case, thus $\bar{\mathcal{D}}^\star = r|\dot{\boldsymbol{\lambda}}|$. Then, the derivative of the absolute value function $r|\dot{\boldsymbol{\lambda}}|$ has to be found. This is not uniquely defined for $\dot{\boldsymbol{\lambda}} = \boldsymbol{0}$. Therefore, its so-called subdifferential denoted by $\partial(r|\dot{\boldsymbol{\lambda}}|)$ is introduced as

$$\partial(r|\dot{\boldsymbol{\lambda}}|) = \begin{cases} r \dfrac{\dot{\boldsymbol{\lambda}}}{|\boldsymbol{\lambda}|} =: r \ \mathrm{sign}\, \dot{\boldsymbol{\lambda}} \ , & \boldsymbol{\lambda} \neq \boldsymbol{0} \\ \dot{\boldsymbol{\Gamma}} \mid |\dot{\boldsymbol{\Gamma}}| \leq r \ , & \dot{\boldsymbol{\lambda}} = \boldsymbol{0} \end{cases} \tag{6.23}$$

The second condition in Eq. (6.23) is the set of all hyper-planes tangential to $r|\dot{\boldsymbol{\lambda}}|$ at $\dot{\boldsymbol{\lambda}} = \mathbf{0}$. Since in general a subdifferential is thus a mathematical set, equations turn into inclusions: $\partial\mathcal{L}/\partial\dot{\boldsymbol{\lambda}} \ni \mathbf{0}$. For mathematical simplification of the resultant governing equations, a Legendre transformation of the original Lagrangean can be performed which defines a yield function.

Furthermore, we chose $\bar{\mathcal{D}}^\theta = \frac{\alpha}{2}|\boldsymbol{q}|^2$ which is the same approach as it is used for the principle of maximum dissipation, e.g. [91]. The stationarity conditions of $\mathcal{L}$ in Eq. (6.22) are

$$r \operatorname{sign} \dot{\boldsymbol{\lambda}} = \boldsymbol{p} \quad , \; \dot{\boldsymbol{\lambda}} \neq \mathbf{0} \tag{6.24}$$

$$\alpha\, \boldsymbol{q} = -\frac{1}{\theta} \nabla\theta \; . \tag{6.25}$$

The first equation, Eq. (6.24), is identical to the well known evolution equations for rate-independent internal variables. Equation (6.25) gives an expression which is very similar to Fourier's law and which allows to derive the heat conduction equation. Note that a different approach for $\bar{\mathcal{D}}^\theta$ would yield different constitutive laws for the heat flux: for instance $\bar{\mathcal{D}}^\theta = \frac{\alpha}{2\theta}|\boldsymbol{q}|^2$ would yield the common Fourier's law.

Inserting $\mathcal{L} = \bar{\mathcal{D}} - \mathcal{D}$ into Eq. (6.15) allows to re-interpret the potential in Eq. (6.15) as

$$\dot{\mathcal{G}} + \Delta \to \min_{\dot{\boldsymbol{u}},\dot{\boldsymbol{\lambda}},\boldsymbol{q}} \; , \tag{6.26}$$

compare to Eq. (6.20). Hence, for non-isothermal processes the rate of the Gibbs free energy plus the total dissipation are minimized with respect to the heat flux, too.

As there exists no functional which serves as a potential for the heat conduction equation, a different way has to be chosen for its formulation. In order to do so, conservation of energy is used as given in Eq. (6.11)

$$\theta\, \dot{s} = \boldsymbol{p} : \dot{\boldsymbol{\lambda}} + h - \nabla \cdot \boldsymbol{q} \; . \tag{6.27}$$

Since entropy is given via the relation $s = -\partial\Psi/\partial\theta$, its rate can be found through

$$\dot{s} = \frac{\mathrm{d}}{\mathrm{d}t}\left(-\frac{\partial\Psi}{\partial\theta}\right) \tag{6.28}$$

Using the presented approach for the temperature-dependent parts of the Helmholtz free energy according to Eq. (6.12), the rate of entropy, calculated according to Eq. (6.28), reads

$$\dot{s} = c\frac{\dot{\theta}}{\theta} - \underbrace{\frac{\mathrm{d}}{\mathrm{d}t}\left(\frac{\partial\Psi_{\mathrm{mech}}(\boldsymbol{\epsilon},\theta,\boldsymbol{\lambda})}{\partial\theta} + \frac{\partial\bar{\Psi}_\theta(\theta,\boldsymbol{\lambda})}{\partial\theta}\right)}_{=:\dot{p}_\theta} \; . \tag{6.29}$$

Observe that due to the time dependence of $\boldsymbol{\lambda}$ its rate appears in $\dot{s}$, as well. Using this result in combination with Eq. (6.25) into Eq. (6.27), we finally find a general form for the heat conduction equation which is

$$c\dot{\theta} - \nabla \cdot \left(\frac{1}{\alpha\theta} \nabla\theta\right) = \boldsymbol{p} : \dot{\boldsymbol{\lambda}} + \dot{p}_\theta\, \theta + h \; . \tag{6.30}$$

In Eq. (6.30), the term $1/\alpha$ is identified as the heat conductivity. Additionally, it can be seen that there are two heat sources which enter the equation: one part due to the mechanical driving forces,

given through $\boldsymbol{p} : \dot{\boldsymbol{\lambda}}$, and a second part $\dot{p}_\theta\, \theta$ which we call 'structural heating' in analogy to [171].

The general approach for material modeling using the principle of the minimum of the dissipation potential for non-isothermal processes can be applied to various materials. We present two examples: perfect plasticity representing materials with changing microstructure and secondly shape memory alloys representing phase transforming materials.

6.5 Examples

6.5.1 Perfect plasticity

The Helmholtz free energy in the case of perfect plasticity reads

$$\Psi^{\mathrm{p}} = \frac{1}{2}(\boldsymbol{\epsilon} - \boldsymbol{\epsilon}^{\mathrm{p}}) : \mathbb{C} : (\boldsymbol{\epsilon} - \boldsymbol{\epsilon}^{\mathrm{p}}) + c(\theta - \theta_{\mathrm{ref}}) + c\,\theta \log\left(\frac{\theta}{\theta_{\mathrm{ref}}}\right) , \tag{6.31}$$

where $\boldsymbol{\epsilon}$ is the total strain, $\boldsymbol{\epsilon}^{\mathrm{p}}$ is the plastic strain which serves simultaneously as internal variable and $\mathbb{C}$ are the elastic constants. We assume here that no thermal deformation is present. In the chemical part of the energy we have no dependence on the plastic strain so that $\bar{\Psi}^{\mathrm{p}}_\theta(\theta, \boldsymbol{\lambda}) = 0$. We expect rate-independent material behavior for which $\bar{\mathcal{D}} = r|\dot{\boldsymbol{\epsilon}}^{\mathrm{p}}| + \frac{\alpha}{2}|\boldsymbol{q}|^2$ may be assumed. Since plasticity evolves in a volume preserving way ($\mathrm{tr}\dot{\boldsymbol{\epsilon}}^{\mathrm{p}} = 0$), we introduce this property by a Lagrange multiplier κ in the entire Lagrangean

$$\mathcal{L}^{\mathrm{p}} = r|\dot{\boldsymbol{\epsilon}}^{\mathrm{p}}| + \frac{\alpha}{2}|\boldsymbol{q}|^2 + \frac{\partial \Psi^{\mathrm{p}}}{\partial \boldsymbol{\epsilon}^{\mathrm{p}}} : \dot{\boldsymbol{\epsilon}}^{\mathrm{p}} + \frac{1}{\theta}\,\boldsymbol{q} \cdot \nabla\theta + \kappa \dot{\epsilon}^{\mathrm{p}}_{ii} \to \min_{\dot{\boldsymbol{\epsilon}}^{\mathrm{p}}, \boldsymbol{q}} , \tag{6.32}$$

where Einstein's summation convention is applied. Evaluation of the stationarity conditions of Eq. (6.32) with respect to $\boldsymbol{q}$ yields again Eq. (6.25), while that one with respect to the rate of plastic strains is

$$r\ \mathrm{sign}\,\dot{\epsilon}^{\mathrm{p}}_{ij} - p_{ij} + \kappa\delta_{ij} \ni 0 , \tag{6.33}$$

where $p_{ij} = -\partial\Psi^{\mathrm{p}}/\partial\epsilon^{\mathrm{p}}_{ij}$ are the driving forces for the plastic strains. Summing up over all components with identical indices, Eq. (6.33) gives

$$\kappa = \frac{1}{3} p_{kk} \tag{6.34}$$

due to the constraint of volume preservation. Plugging this result back into Eq. (6.33) we get the evolution equations for the plastic strains as

$$r\ \mathrm{sign}\,\dot{\epsilon}^{\mathrm{p}}_{ij} = \begin{cases} p_{ij} - \dfrac{1}{3}\delta_{ij} p_{kk} \equiv (\mathrm{dev}\boldsymbol{p})_{ij} , & \dot{\boldsymbol{\epsilon}}^{\mathrm{p}} \neq \boldsymbol{0} \\ \dot{\Gamma}_{ij} \mid |\dot{\boldsymbol{\Gamma}}| < r , & \dot{\boldsymbol{\epsilon}}^{\mathrm{p}} = \boldsymbol{0} \end{cases} . \tag{6.35}$$

The driving forces $\boldsymbol{p}$ turn out to be given by the stresses: $\boldsymbol{p} = \boldsymbol{\sigma}$. Thus, we received the well known evolution equations for plasticity where the deviator $\mathrm{dev}\boldsymbol{\sigma}$ plays an important role just by means of the principle of the minimum of the dissipation potential. A Legendre transformation of the Lagrangean in Eq. (6.32) yields an indicator function denoted by ϕ which is identified as the yield function. Basic calculations result in

$$\phi = |\mathrm{dev}\boldsymbol{\sigma}|^2 - r^2 \overset{!}{\leq} 0 . \tag{6.36}$$

From Eq. (6.36) it can be seen that the dissipation parameter r serves as a 'deviator type norm' of the tensorial yield stress. Thermal coupling is given by application of formula Eq. (6.30) to the Helmholtz free energy for this example presented in Eq. (6.31). Here, we do not consider any heat supply due to internal heat sources, hence $h = 0$. This is

$$c\dot{\theta} - \nabla \cdot \left(\frac{1}{\alpha\theta} \nabla\theta \right) = \boldsymbol{\sigma} : \dot{\boldsymbol{\epsilon}}^{\mathrm{p}} \, . \tag{6.37}$$

Now, we have found the heat conduction equation describing temperature evolution due to plastic deformation and thermal coupling results without any further assumptions, Eq. (6.37). However, by introducing an appropriate ansatz for a temperature-dependent dissipation parameter, thus $r = r(\theta)$, a more detailed coupling is the outcome. Hardening effects could be introduced by furthermore defining $r = r(\boldsymbol{\alpha})$, expanding $\bar{\mathcal{D}}$ by $r_2|\dot{\boldsymbol{\alpha}}|$ and Ψ^{p} by $\frac{1}{3} H \boldsymbol{\alpha}^2$.

6.5.2 Shape memory alloys

For the modeling of shape memory alloys (SMAs) an approach following [70] for the Helmholtz free energy is chosen

$$\Psi^{\mathrm{sma}} = \frac{1}{2}(\boldsymbol{\epsilon} - \hat{\boldsymbol{\eta}}) : \hat{\mathbb{C}} : (\boldsymbol{\epsilon} - \hat{\boldsymbol{\eta}}) + c(\theta - \theta_{\mathrm{ref}}) + c\theta \log\left(\frac{\theta}{\theta_{\mathrm{ref}}} \right) + \bar{\Psi}_{\theta}^{\mathrm{sma}}(\theta, \boldsymbol{\lambda}) \tag{6.38}$$

with $\bar{\Psi}_{\theta}^{\mathrm{sma}} = (\boldsymbol{a} - \boldsymbol{b}\,\theta) : \boldsymbol{\lambda}$ and $\boldsymbol{a}$ and $\boldsymbol{b}$ as material constants. Here, $\hat{\boldsymbol{\eta}}$ and $\hat{\boldsymbol{C}}$ indicate the effective transformation strain and effective elastic constants, respectively, which depend on the volume fraction of the different crystallographic phases denoted by $\boldsymbol{\lambda}$. These volume fractions are the internal variables in this example for which the constraints of positivity and mass conservation apply. Using the principle of maximum dissipation, the following set of field equations was derived, see [96, 91]

$$r \operatorname{sign} \dot{\boldsymbol{\lambda}} = \begin{cases} f \operatorname{dev}_{\mathcal{A}} \boldsymbol{p} \, , & \dot{\boldsymbol{\lambda}} \neq \boldsymbol{0} \\ \dot{\boldsymbol{\Gamma}} \mid |\dot{\boldsymbol{\Gamma}}| < r \, , & \dot{\boldsymbol{\lambda}} = \boldsymbol{0} \end{cases} \tag{6.39}$$

$$c\,\dot{\theta} - \nabla \left(f \frac{1}{\alpha\theta} \nabla\theta \right) = \boldsymbol{p} : \dot{\boldsymbol{\lambda}} - \boldsymbol{b} : \dot{\boldsymbol{\lambda}}\,\theta \tag{6.40}$$

with the *active deviator* $\operatorname{dev}_{\mathcal{A}} p_{ij} = p_{ij} - \frac{1}{n_{\mathcal{A}_j}} \sum_{k \in \mathcal{A}_j} p_{kj}$ and the driving forces $\boldsymbol{p} = -\partial \Psi^{\mathrm{SMA}} / \partial \boldsymbol{\lambda}$. Here, an active set strategy has been applied in order to account for the constraint of positivity. The active set is denoted by $\mathcal{A}$ and $n_{\mathcal{A}_j}$ gives the number of active elements in $\mathcal{A}_j$. Using a Legendre transformation, Eq. (6.39) can be once again reformulated with the aid of the yield function,

$$\phi = |f \operatorname{dev}_{\mathcal{A}} \boldsymbol{p}|^2 - r^2 \tag{6.41}$$

and the Kuhn-Tucker conditions $|\dot{\boldsymbol{\lambda}}|/r =: \rho \geq 0$, $\phi \leq 0$ and $\rho\phi = 0$. The factor f in Eqs. (6.39) to (6.41) is given by

$$f = \frac{\frac{\partial \bar{\mathcal{D}}}{\partial \dot{\boldsymbol{\lambda}}} : \dot{\boldsymbol{\lambda}} + \frac{\partial \bar{\mathcal{D}}}{\partial \boldsymbol{q}} \cdot \boldsymbol{q}}{\bar{\mathcal{D}}} = \frac{2r|\dot{\boldsymbol{\lambda}}| + 2\alpha|\boldsymbol{q}|^2}{2r|\dot{\boldsymbol{\lambda}}| + \alpha|\boldsymbol{q}|^2} \, . \tag{6.42}$$

From Eq. (6.42) it can be seen that the prefactor f complicates the entire system of governing equations significantly. Therefore, only bounds for f have been used in previous works which are 1 when $r|\dot{\boldsymbol{\lambda}}|$ is dominant in $\bar{\mathcal{D}}$ and 2 when $\alpha|\boldsymbol{q}|^2/2$ is the governing term. Although the influence of this

approximation is not huge an additional error source arises from it.

We demonstrate now how our new approach yields similar but simpler equations. In the case of our example Eq. (6.22) specifies to

$$\mathcal{L}^{\mathrm{sma}} = r|\dot{\boldsymbol{\lambda}}| + \frac{\alpha}{2}|\boldsymbol{q}|^2 + \frac{\partial \Psi^{\mathrm{sma}}}{\partial \boldsymbol{\lambda}} : \dot{\boldsymbol{\lambda}} + \frac{1}{\theta}\boldsymbol{q}\cdot\nabla\theta + \boldsymbol{\kappa} : \dot{\boldsymbol{\lambda}} - \boldsymbol{\gamma} : \dot{\boldsymbol{\lambda}} \to \min_{\dot{\boldsymbol{\lambda}},\boldsymbol{q}} \tag{6.43}$$

with Lagrange parameters $\boldsymbol{\kappa}$ and Kuhn-Tucker parameters $\boldsymbol{\gamma}$ which account for the constraints of mass conservation and positivity. Application of the presented scheme of the minimum of the dissipation potential for non-isothermal processes leads in this case to the evolution equation for the volume fractions

$$r \operatorname{sign} \dot{\boldsymbol{\lambda}} = \begin{cases} \operatorname{dev}_{\mathcal{A}} \boldsymbol{p} \,, & \dot{\boldsymbol{\lambda}} \neq \boldsymbol{0} \\ \dot{\Gamma} | \dot{\Gamma} < r \,, & \dot{\boldsymbol{\lambda}} = \boldsymbol{0} \,. \end{cases} \tag{6.44}$$

A Legendre transformation gives the yield function

$$\phi = |\operatorname{dev}_{\mathcal{A}} \boldsymbol{p}|^2 - r^2 \leq 0 \tag{6.45}$$

which serves as indicator for phase transformations. The heat conduction equation yields, again following the method presented in this paper and again setting $h = 0$,

$$c\,\dot{\theta} - \nabla\cdot\left(\frac{1}{\alpha\theta}\nabla\theta\right) = \boldsymbol{p} : \dot{\boldsymbol{\lambda}} \underbrace{-\boldsymbol{b} : \dot{\boldsymbol{\lambda}}}_{=\dot{\boldsymbol{p}}_\theta}\theta \,. \tag{6.46}$$

Now, since there exists a specific dependence of the chemical part of Ψ^{sma} on the internal variable, the structural heating $\dot{\boldsymbol{p}}_\theta\theta$ enters the heat conduction equation in this example.

Comparison between the corresponding equations of both approaches discussed, Eq. (6.44) as related to Eq. (6.39), Eq. (6.45) as related to Eq. (6.41), and Eq. (6.46) as related to Eq. (6.40), shows that f does not appear anymore neither in the evolution equation, nor yield function, nor heat conduction equation.

Hence, as we presented in this paper, using the principle of the minimum of the dissipation potential for non-isothermal processes allows the formulation of a thermally coupled material model which is as convincing as those derived from other modeling principles but which exhibits a simpler and more convenient mathematical structure. Interestingly, the prefactor f can be avoided as well when using the principle of maximum dissipation as it has been shown in [69, 68]. However, one has to pay the price of maximizing the contribution to dissipation of every single process individually, which might be arguable in physical terms. In contrast to this, the principle of the minimum of the dissipation potential for non-isothermal processes operates without this extra assumption.

6.6 Conclusions

The conventional approach to the thermodynamics of materials with internal variables is based on the specification of the free energy and the evolution law for each particular internal variable. This is a difficult task particularly for problems requiring many internal variables, because many constitutive functions must be specified independently. In contrast, the approach based on the principle of the

minimum of the dissipation potential requires the specification of only two scalar constitutive functions, free energy and dissipation functional, independently of the number of internal variables. This method has been successfully applied in the analysis of numerous inelastic phenomena with the restriction to isothermal processes. The extension to non-isothermal processes presented in this paper provides a firm basis for the thermodynamics of materials with internal variables in which thermal coupling is not neglected. Two specific problems considered in this work, rate-independent elasto-plasticity and shape memory alloys, illustrate the basic idea of the presented approach.

7 Condensed modeling of the thermo-mechanical behavior of shape memory alloys

Published as: *P. Junker, K. Hackl*: A condensed variational model for thermo-mechanically coupled phase transformations in polycrystalline shape memory alloys, *J. Mech. Behav. Mat.* **22 (3-4): 111–118 (2013)**

We derive an energy-based material model for thermo-mechanically coupled phase transformation in polycrystalline shape memory alloys. For the variational formulation of the model, we use the principle of the minimum of the dissipation potential for non-isothermal processes for which only a minimal number of constitutive assumptions has to be made. By introducing a condensed formulation for the representative orientation distribution function, the resulting material model is numerically highly-efficient. For a first analysis, we present results of material point calculations where the evolution of temperature as well as its influence on the mechanical material response is investigated.

7.1 Introduction

Shape memory alloys are materials which posses the highly symmetric austenitic crystal lattice at high temperatures and a composition of martensitic variants of lower symmetry at low temperatures. This can be observed for other alloys, too. However, the unique property of shape memory alloys, which characterizes this class of materials, is that the transformation strain is nearly volume preserving. As a consequence, it is possible to induce the phase transformation from austenite to martensite and vice versa or from one martensitic configuration to another by mechanical loads since they are not inhibited by volumetric eigenstresses. Dependent on the current room temperature, and thus the virgin crystallographic state, shape memory alloys can show the effect of pseudo-elasticity or pseudo-plasticity which are both accompanied by plateaus in the stress-strain diagrams. For more details we refer e.g. to [152].

At high temperatures, austenite is the prevalent phase. A previous stress-induced phase transformation from austenite to a certain composition of martensitic variants results again in the austenitic configuration when the external load is removed. Hence, this material behavior is called pseudo-elastic.

At low temperatures, where a uniform distribution of martensites forms the initial crystallographic state, an external mechanical load forces the material to accommodate its internal microstructure via detwinning. This means that some martensitic variants which have a more favorable orientation than others, grow at the expense of the remaining ones. Since a martensitic crystal lattice has only low symmetry, it is easy to imagine that the initial configuration of uniformly distributed martensite cannot be recovered when the external load is removed. Hence, the material relaxes elastically but a remaining deformation indicates a deviation from a state with uniformly distributed martensitic variants. If such a specimen is heated, thermally induced phase transformation takes place from the specific martensitic configuration to the austenitic one. Subsequent cooling restores the initial state of undeformed uniformly distributed martensite. Therefore, the observed material behavior is termed pseudo-plastic. The described so-called one-way-effect gives rise to the notion “shape memory alloys”.

Various experiments, for example in [166], show that due to the dissipative character of phase transi-

tions, which can be identified by the hysteresis observed in stress-strain diagrams, mechanical energy is partly converted into heat. The resultant change in temperature on the other hand has a direct consequence for the phase transformations: since a higher temperature stabilizes the austenite, phase transformation is slowed down if temperature is increased. This implies that the hysteresis in the stress-strain diagram increases its slope the higher the temperature is. This effect is more pronounced if more energy is converted into heat, [166].

In this paper, we present a material model for the simulation of polycrystalline shape memory alloys which accounts for thermal coupling. The model uses a novel approach involving a condensed orientation distribution function. This one is based on representing the entire texture of the polycrystalline aggregate by its average orientation. This way the number of degrees of freedom is reduced drastically and the numerical effort by orders of magnitude compared to previous works, [93]. We use the variational concept of the minimum of the dissipation potential for non-isothermal processes, as presented in [103], which allows to derive a thermo-mechanically coupled material model. Additionally this approach results in a more concise mathematical structure of the equations as compared to the principle of maximum dissipation, [103]. As recently shown, [102], a variational or energy-based material model has the advantage that it must be calibrated only once. Afterwards, results of comparable quality can be obtained for different load states and geometries at different temperatures. In [102] it has been demonstrated that an isothermal energetic material model for shape memory alloys can even be calibrated via *thermal* experiments (DSC measurements) in order to simulate *mechanical* tension tests for different specimens at different room temperatures. This concept is expanded in this paper by the thermo-mechanically coupled version of the material model.

This work is based on a model in [71] and [70] which has been investigated within a finite element scheme in [97]. A thermo-mechanically coupled version of this model, based on the principle of maximum dissipation, was presented in [91] and [99]. Previous models for shape memory alloys based on phenomenological concepts can be found for instance in [25], [8], [22] or [174]. A selection of other micromechanical models are derived in [11], [60] or [177].

7.2 Material model

The principle of the minimum of the dissipation potential for non-isothermal processes states that

$$\mathcal{L} = \bar{\mathcal{D}} - \mathcal{D} \rightarrow \min_{\dot{\xi}, \boldsymbol{q}}, \tag{7.1}$$

see [103]. In Eq. (7.1), $\dot{\xi}$ are the rates of the internal variables of the specific material model, $\boldsymbol{q}$ is the heat flux vector and $\mathcal{D}$ is the thermodynamic dissipation which is given by the second law of thermodynamics. This is

$$\mathcal{D} = -\dot{\psi} - \frac{1}{\theta}\boldsymbol{q} \cdot \nabla\theta, \tag{7.2}$$

with the Helmholtz free energy ψ and the (absolute) temperature θ. According to [93], we introduce two kinds of internal variables, namely a vector of volume fractions of the crystallographic phases denoted by $\boldsymbol{\lambda} = (\lambda_i)$, λ_0 representing the austenite and λ_i, $i \in \{1, \ldots, \bar{n}\}$ the specific martensitic variants where $\bar{n}$ is alloy dependent, and a set of three Euler angles $\boldsymbol{\alpha}$ which indicates the average or mean orientation direction of the polycrystalline arrangement. Thus, the rate of the internal variables is $\dot{\xi} = \{\dot{\boldsymbol{\lambda}}, \dot{\boldsymbol{\alpha}}\}$. We denote by $\bar{\mathcal{D}}$ the so-called dissipation potential introduced in [44] comprising the

material-dependent dissipative terms. We decompose the dissipation potential into a transformational and a thermal part as $\bar{\mathcal{D}} = \bar{\mathcal{D}}^{\mathrm{tr}} + \bar{\mathcal{D}}^{\mathrm{th}}$. Moreover we follow [93] to set $\bar{\mathcal{D}}^{\mathrm{tr}} = r_\lambda|\dot{\boldsymbol{\lambda}}| + r_\alpha|\dot{\boldsymbol{\alpha}}|$ and [103] to set $\bar{\mathcal{D}}^{\mathrm{th}} = \mu|\boldsymbol{q}|^2/(2\theta)$ where r_λ and r_α are the dissipation parameters for phase transformation and reorientation, respectively, and μ is the reciprocal of the heat conductivity, [103].

The Lagrangean $\mathcal{L}$ in Eq. (7.1) is not minimized with respect to the rates of the strains. Hence, we drop the term $(\partial\psi/\partial\boldsymbol{\epsilon}) : \dot{\boldsymbol{\epsilon}}$ and find

$$\mathcal{L} = r_\lambda|\dot{\boldsymbol{\lambda}}| + r_\alpha|\dot{\boldsymbol{\alpha}}| + \frac{\mu}{2\theta}|\boldsymbol{q}|^2 + \frac{\partial\psi}{\partial\boldsymbol{\lambda}}\cdot\dot{\boldsymbol{\lambda}} + \frac{\partial\psi}{\partial\boldsymbol{\alpha}}\cdot\dot{\boldsymbol{\alpha}} + \frac{1}{\theta}\boldsymbol{q}\cdot\nabla\theta - \boldsymbol{\gamma}\cdot\dot{\boldsymbol{\lambda}} + \beta\sum_{i=0}^{\bar{n}}\dot{\lambda}_i \to \min_{\dot{\boldsymbol{\lambda}},\dot{\boldsymbol{\alpha}},\boldsymbol{q}} . \tag{7.3}$$

The last two terms in Eq. (7.3), $-\boldsymbol{\gamma}\cdot\boldsymbol{\lambda}$ and $\beta\sum_{i=0}^{\bar{n}}\dot{\lambda}_i$, are introduced to include the constraints of positivity and mass conservation, respectively, by means of the Lagrange parameter β and the Kuhn-Tucker parameters $\boldsymbol{\gamma} = (\gamma_i)$. For more details, we refer to [93].

The stationarity condition of $\mathcal{L}$ with respect to the rates of the volume fractions reads, due to the non-differentiability of $|\dot{\boldsymbol{\lambda}}|$ at $\dot{\boldsymbol{\lambda}} = \mathbf{0}$, the differential inclusion

$$r_\lambda\frac{\dot{\boldsymbol{\lambda}}}{|\dot{\boldsymbol{\lambda}}|} + \frac{\partial\psi}{\partial\boldsymbol{\lambda}} - \boldsymbol{\gamma} + \boldsymbol{\beta} \ni \mathbf{0}, \tag{7.4}$$

where $\boldsymbol{\beta} = \beta\mathbf{1}$ and $\mathbf{1}$ denotes the $\bar{n}+1$-dimensional vector with value 1 in all components.

The stationarity condition of $\mathcal{L}$ with respect to the rates of the Euler angles gives

$$r_\alpha\frac{\dot{\boldsymbol{\alpha}}}{|\dot{\boldsymbol{\alpha}}|} + \frac{\partial\psi}{\partial\boldsymbol{\alpha}} \ni \mathbf{0}. \tag{7.5}$$

Finally, stationarity of $\mathcal{L}$ with respect to $\boldsymbol{q}$ yields

$$\boldsymbol{q} = -\frac{1}{\mu}\nabla\theta \tag{7.6}$$

which is nothing else but Fourier's law.

It turns out to be convenient to invert Eqs. (7.4) and (7.5) which amounts to performing a Legendre transformation of the dissipation potentials $\bar{\mathcal{D}}^{\mathrm{tr}}$ and $\bar{\mathcal{D}}^{\mathrm{th}}$, see [93] for details. For this purpose, let us introduce an active set (of variants) $\mathcal{A}$ as

$$\mathcal{A} = \{i|\lambda_i \neq 0\} \cup \left\{i \,\middle|\, \lambda_i = 0 \wedge \dot{\lambda}_i > 0\right\} \tag{7.7}$$

to account for the constraint of positivity and furthermore $\boldsymbol{p}^\lambda = -\partial\psi/\partial\boldsymbol{\lambda}$ and $\boldsymbol{p}^\alpha = -\partial\psi/\partial\boldsymbol{\alpha}$ as thermodynamically conjugated driving forces. Inserting this into Eq. (7.4) we find

$$\begin{cases} p_i^\lambda - \dfrac{1}{\bar{n}_{\mathcal{A}}}\displaystyle\sum_{k\in\mathcal{A}} p_k^\lambda = r_\lambda\dfrac{\dot{\lambda}_i}{|\dot{\boldsymbol{\lambda}}|} & , i \in \mathcal{A}, \\ p_i^\lambda - \dfrac{1}{\bar{n}_{\mathcal{A}}}\displaystyle\sum_{k\in\mathcal{A}} p_k^\lambda = -\gamma_i < 0 & , i \notin \mathcal{A}. \end{cases} \tag{7.8}$$

Following [93], we introduce the active deviator as

$$\mathrm{dev}_{\mathcal{A}}\boldsymbol{p}^{\lambda} := \boldsymbol{p}^{\lambda} - \frac{1}{\bar{n}_{\mathcal{A}}} \sum_{k\in\mathcal{A}} p_k^{\lambda}\mathbf{1} \tag{7.9}$$

with $\bar{n}_{\mathcal{A}}$ as number of active phases. This allows to define yield functions $\Phi_\lambda \le 0$ and $\Phi_\alpha \le 0$ which indicate whether phase transformation and / or re-orientation take place, respectively. They are given as

$$\Phi_\lambda = \left|\mathrm{dev}_{\mathcal{A}}\boldsymbol{p}^{\lambda}\right|^2_{\mathcal{A}} - r_\lambda^2, \tag{7.10}$$

and

$$\Phi_\alpha = \boldsymbol{p}^{\alpha}\cdot\boldsymbol{p}^{\alpha} - r_\alpha^2, \tag{7.11}$$

where $|\boldsymbol{p}|^2_{\mathcal{A}} = \sum_{i\in\mathcal{A}} p_i^2$, see [93]. We take the formula given in [103] to derive the heat conduction equation. Using our approach for $\bar{\mathcal{D}}^{\mathrm{th}}$, it is given as

$$\kappa\dot{\theta} - \nabla\cdot\left(\frac{1}{\mu}\nabla\theta\right) = \boldsymbol{p}^{\lambda}\cdot\dot{\boldsymbol{\lambda}} + \boldsymbol{p}^{\alpha}\cdot\dot{\boldsymbol{\alpha}} + \dot{p}_\theta\,\theta, \tag{7.12}$$

where κ denotes the heat capacity. Structural heating $\dot{p}_\theta\,\theta$ is defined via

$$p_\theta = -\frac{\partial\psi}{\partial\theta}. \tag{7.13}$$

For the Helmholtz free energy we take the approach from [93], now including temperature dependent parts, as

$$\psi = \frac{1}{2}\left(\boldsymbol{\epsilon} - \boldsymbol{Q}^T\cdot\bar{\boldsymbol{\eta}}\cdot\boldsymbol{Q}\right) : \bar{\mathbb{C}} : \left(\boldsymbol{\epsilon} - \boldsymbol{Q}^T\cdot\bar{\boldsymbol{\eta}}\cdot\boldsymbol{Q}\right) + \bar{c}(\theta), \tag{7.14}$$

where $\boldsymbol{Q} = \boldsymbol{Q}(\boldsymbol{\alpha})$ denotes a rotation matrix, and the effective transformation strain $\bar{\boldsymbol{\eta}}$, the effective stiffness tensor $\bar{\mathbb{C}}$ and the effective caloric part of the energy $\bar{c}(\theta)$ are given by

$$\bar{\boldsymbol{\eta}} = \sum_{i=0}^{\bar{n}} \lambda_i\boldsymbol{\eta}_i, \qquad \bar{\mathbb{C}} = \left[\sum_{i=0}^{\bar{n}} \lambda_i\left(\mathbb{C}_i\right)^{-1}\right]^{-1}, \qquad \bar{c}(\theta) = \sum_{i=0}^{\bar{n}} \lambda_i c_i(\theta). \tag{7.15}$$

According to [50, 102], the temperature-dependent caloric part of the energy is given as

$$c_i(\theta) = a_i - b_i\theta, \tag{7.16}$$

where we have omitted terms which are identical for all phases and which therefore are not relevant for our formulation.

We are now able to write the final system of evolution equations as

$$\dot{\boldsymbol{\lambda}} = \rho_\lambda\left(\mathrm{dev}_{\mathcal{A}}\boldsymbol{p}^{\lambda}\right)_{\mathcal{A}}, \tag{7.17}$$

$$\dot{\boldsymbol{\alpha}} = \rho_\alpha\boldsymbol{p}^{\alpha} \tag{7.18}$$

with $\rho_\lambda := |\dot{\boldsymbol{\lambda}}|/r_\lambda$ and $\rho_\alpha := |\dot{\boldsymbol{\alpha}}|/r_\alpha$ as consistency parameters. The Kuhn-Tucker conditions

$$\rho_\lambda \ge 0, \qquad \Phi_\lambda \le 0, \qquad \rho_\lambda\Phi_\lambda = 0, \tag{7.19}$$

$$\rho_\alpha \ge 0, \qquad \Phi_\alpha \le 0, \qquad \rho_\alpha\Phi_\alpha = 0, \tag{7.20}$$

close the system of equations, in combination with the consistency condition

$$\mathrm{dev}_{\mathcal{A}} p_i^{\lambda} \leq 0 \qquad \text{for } i \notin \mathcal{A} \tag{7.21}$$

which updates the active set. The heat conduction equation reads

$$\kappa\dot{\theta} - \nabla \cdot \left(\frac{1}{\mu} \nabla\theta \right) = \boldsymbol{p}^{\lambda} \cdot \dot{\boldsymbol{\lambda}} + \boldsymbol{p}^{\alpha} \cdot \dot{\boldsymbol{\alpha}} - \boldsymbol{b} \cdot \dot{\boldsymbol{\lambda}}\, \theta \tag{7.22}$$

with $\boldsymbol{b} = (b_{\mathrm{A}}, b_{\mathrm{M}}, \ldots, b_{\mathrm{M}})$, where b_{A} and b_{M} denote the entropic constants for austenite and martensite respectively.

In order to evaluate the material model, it is necessary to derive the driving forces. For the volume fractions they are

$$\begin{aligned} p_i^{\lambda} = & \left(\boldsymbol{Q}^T \cdot \boldsymbol{\eta}_i \cdot \boldsymbol{Q} \right) : \bar{\mathbb{C}} : \left(\boldsymbol{\varepsilon} - \boldsymbol{Q}^T \cdot \bar{\boldsymbol{\eta}} \cdot \boldsymbol{Q} \right) \\ & + \frac{1}{2} \left(\boldsymbol{\varepsilon} - \boldsymbol{Q}^T \cdot \bar{\boldsymbol{\eta}} \cdot \boldsymbol{Q} \right) : \left[\bar{\mathbb{C}} : (\mathbb{C})^{-1} : \bar{\mathbb{C}} \right] : \left(\boldsymbol{\varepsilon} - \boldsymbol{Q}^T \cdot \bar{\boldsymbol{\eta}} \cdot \boldsymbol{Q} \right) - c_i(\theta) \,, \end{aligned} \tag{7.23}$$

see also [93]. The rotation matrix is given in terms of Euler angles as

$$\boldsymbol{Q}(\boldsymbol{\alpha}) = \begin{pmatrix} \cos\varphi\cos\omega - \cos\nu\sin\varphi\sin\omega & -\cos\nu\cos\omega\sin\varphi - \cos\varphi\sin\omega & \sin\nu\sin\varphi \\ \cos\omega\sin\varphi + \cos\nu\cos\varphi\sin\omega & \cos\nu\cos\varphi\cos\omega - \sin\varphi\sin\omega & -\cos\varphi\sin\nu \\ \sin\nu\sin\omega & \cos\omega\sin\nu & \cos\nu \end{pmatrix} \tag{7.24}$$

with $\boldsymbol{\alpha} = \{\varphi, \nu, \omega\}$ and $\varphi, \omega \in [0, 2\pi]$, $\nu \in [0, \pi]$. Now we can calculate the corresponding driving forces as

$$\boldsymbol{p}^{\alpha} = -\frac{\partial\psi}{\partial\boldsymbol{\alpha}} = -\frac{\partial\psi}{\partial\boldsymbol{Q}} : \frac{\partial\boldsymbol{Q}}{\partial\boldsymbol{\alpha}} \tag{7.25}$$

While the first term in Eq. (7.25) reads

$$-\frac{\partial\psi}{\partial\boldsymbol{Q}} = 2 \left[\bar{\boldsymbol{\eta}} \cdot \boldsymbol{Q} \cdot \bar{\mathbb{C}} : \left(\boldsymbol{\varepsilon} - \boldsymbol{Q}^T \cdot \bar{\boldsymbol{\eta}} \cdot \boldsymbol{Q} \right) \right] \,, \tag{7.26}$$

the entries of the second part $\partial \boldsymbol{Q}/\partial \boldsymbol{\alpha} = (\partial \boldsymbol{Q}/\partial \varphi, \partial \boldsymbol{Q}/\partial \nu, \partial \boldsymbol{Q}/\partial \omega)$ are

$$\frac{\partial \boldsymbol{Q}}{\partial \varphi} = \begin{pmatrix} -\cos\omega\sin\varphi - \cos\nu\cos\varphi\sin\omega & -\cos\nu\cos\varphi\cos\omega + \sin\varphi\sin\omega & \cos\varphi\sin\nu \\ \cos\varphi\cos\omega - \cos\nu\sin\varphi\sin\omega & -\cos\nu\cos\omega\sin\varphi - \cos\varphi\sin\omega & \sin\nu\sin\varphi \\ 0 & 0 & 0 \end{pmatrix}, \tag{7.27}$$

$$\frac{\partial \boldsymbol{Q}}{\partial \nu} = \begin{pmatrix} \sin\nu\sin\varphi\sin\omega & \cos\omega\sin\nu\sin\varphi & \cos\nu\sin\varphi \\ -\cos\varphi\sin\nu\sin\omega & -\cos\varphi\cos\omega\sin\nu & -\cos\nu\cos\varphi \\ \cos\nu\sin\omega & \cos\nu\cos\omega & -\sin\nu \end{pmatrix}, \tag{7.28}$$

$$\frac{\partial \boldsymbol{Q}}{\partial \omega} = \begin{pmatrix} -\cos\nu\cos\omega\sin\varphi - \cos\varphi\sin\omega & -\cos\varphi\cos\omega + \cos\nu\sin\varphi\sin\omega & 0 \\ \cos\nu\cos\varphi\cos\omega - \sin\varphi\sin\omega & -\cos\omega\sin\varphi - \cos\nu\cos\varphi\sin\omega & 0 \\ \cos\omega\sin\nu & -\sin\nu\sin\omega & 0 \end{pmatrix}. \tag{7.29}$$

7.3 Material point analysis

The evolution equations for the volume fractions and the Euler angles, Eqs. (7.19), (7.20), can be evaluated if the strain is known as a function of time. Hence, for our purpose of analyzing the material point behavior of the model no modifications are necessary. In contrast, the temperature gradient Eq. (7.22) in cannot be evaluated at a material point level. There are several possibilities to reduce the equation in an appropriate way. One would be to consider the isothermal case, where all heat is immediately transported away when produced. Obviously, this case is of minor interest since it ignores thermal coupling completely. Therefore, we choose to investigate another possibility which is an adiabatic process. In such a system, no heat may enter or leave the system. Thus, for our case all heat produced in the material point is converted directly into temperature changes. We find the material point heat conduction equation in its reduced form as

$$\kappa\dot{\theta} = \boldsymbol{p}^{\lambda} \cdot \dot{\boldsymbol{\lambda}} + \boldsymbol{p}^{\alpha} \cdot \dot{\boldsymbol{\alpha}} - \boldsymbol{b} \cdot \dot{\boldsymbol{\lambda}}\,\theta. \tag{7.30}$$

Due to its high non-linearity, we solve the system of governing equations, Eqs. (7.17), (7.18) and (7.30), numerically. A detailed numerical treatment as well as the algorithm used are given in [93].

On inspection of the equations we find that our model is rate-independent for a material point analysis, i.e. the results do not change when altering the velocities of the process. Especially, for an adiabatic process the loading velocity, defined as $\dot{\boldsymbol{\epsilon}}$, has no influence on the heat production and thus temperature evolution. This means we can replace the rates in Eq. (7.30) by increments

$$\Delta\theta = \theta^{n+1} - \theta^{n}\,, \qquad \Delta\boldsymbol{\lambda} = \boldsymbol{\lambda}^{n+1} - \boldsymbol{\lambda}^{n}\,, \qquad \Delta\boldsymbol{\alpha} = \boldsymbol{\alpha}^{n+1} - \boldsymbol{\alpha}^{n}. \tag{7.31}$$

The unknown values of temperature, volume fractions and Euler angles at the end of the time increment are indicated by $(\cdot)^{n+1}$, the known ones at the beginning by $(\cdot)^{n}$. On substitution, we obtain the time discretized form of the heat conduction equation. We are using a forward Euler scheme for the solution

as

$$\kappa\left(\theta^{n+1}-\theta^{n}\right)=\left(\boldsymbol{p}^{\lambda}\right)^{n}\cdot\Delta\boldsymbol{\lambda}+\left(\boldsymbol{p}^{\alpha}\right)^{n}\cdot\Delta\boldsymbol{\alpha}-\boldsymbol{b}\cdot\Delta\boldsymbol{\lambda}\,\theta^{n+1} \tag{7.32}$$

from which the current temperature can be calculated as

$$\theta^{n+1}=\frac{\kappa\theta^{n}+\left(\boldsymbol{p}^{\lambda}\right)^{n}\cdot\Delta\boldsymbol{\lambda}+\left(\boldsymbol{p}^{\alpha}\right)^{n}\cdot\Delta\boldsymbol{\alpha}}{\kappa+\boldsymbol{b}\cdot\Delta\boldsymbol{\lambda}}\,. \tag{7.33}$$

The driving forces are evaluated using the known quantities at the beginning of the time increment. The discretized versions of Eqs. (7.17) and (7.18) then read

$$\begin{aligned}\Delta\boldsymbol{\lambda}&=\hat{\rho}_{\lambda}\left(\mathrm{dev}_{\mathcal{A}}\left(\boldsymbol{p}^{\lambda}\right)^{n}\right)_{\mathcal{A}}\,,\\ \Delta\boldsymbol{\alpha}&=\hat{\rho}_{\alpha}\left(\boldsymbol{p}^{\alpha}\right)^{n}\,.\end{aligned} \tag{7.34}$$

The yield conditions are evaluated at the end of the time increment:

$$\begin{aligned}\Phi_{\lambda}(\boldsymbol{\lambda}^{n+1},\boldsymbol{\alpha}^{n+1})&=0,\\ \Phi_{\alpha}(\boldsymbol{\lambda}^{n+1},\boldsymbol{\alpha}^{n+1})&=0.\end{aligned} \tag{7.35}$$

The update of the variables is now calculated in a staggered scheme. In a first step Eqs. (7.34) and (7.35) are solved for $\boldsymbol{\lambda}^{n+1}$, $\boldsymbol{\alpha}^{n+1}$, and the discretized consistency parameters $\hat{\rho}_{\lambda}$, $\hat{\rho}_{\alpha}$. In a second step, the temperature is updated according to Eq. (7.33).

7.4 Numerical experiments

We apply our material model to Nickel Titanium which can form twelve martensitic variants, yielding $\bar{n}=12$. The respective transformation strains for the different martensitic variants after [194] are collected in Tab. 7.1 ($\boldsymbol{\eta}_0=\boldsymbol{0}$). For the elastic constants of austenite and martensite we use the expectation values, as proposed and calculated in [93], based on experimental data of [151] and [194].

The values for the caloric part of the Helmholtz free energy, $\Delta c(\theta)\coloneqq c_0(\theta)-c_{i>0}(\theta)=\Delta a-\Delta b\,\theta$, are taken from [102] as $\Delta a=0.258\,\mathrm{GPa}$ and $\Delta b=0.001\,\mathrm{GPa/K}$. The initial temperature is set to $\theta^0=323.15°\mathrm{K}$ which implies $\Delta c(\theta^0)=-0.065\,\mathrm{GPa}$. Also in [102], the dissipation parameter for phase transformation has been calculated to be $r_{\lambda}=0.013\,\mathrm{GPa}$.

In [93], it has been shown that the value for r_{α} controls the intensity of stress drop when phase transformation initializes and the plateau has not yet been completely established. Here, we choose it to be $r_{\alpha}=0.001\,\mathrm{GPa}$.

The only remaining parameter is the heat capacity. As pointed out previously, on a material point level for the adiabatic case the amount of produced heat is independent of the loading velocities. In other words, it is completely determined by the material parameters. Consequently, for demonstration of our material model we vary the only parameter which is not fixed yet: the heat capacity κ. This allows to influence the magnitude of temperature change and therefore to investigate the material model for different cases. In a finite element setting, this modification is not necessary since then the temperature gradient in the heat conduction equation is still present and the dependence on the loading velocity is still given. However, for this first analysis we present various sets of simulations with

different values of the heat capacity, specifically $\kappa = \{0.010, 0.015, 0.030, 0.050\}$ GPa/K. The larger the heat capacity is, the smaller the change in temperature. Hence, we expect higher temperatures for smaller heat capacity and therefore a larger influence on the mechanical material response compared to an isothermal case.

Strain is the input variable. We perform a numerical tri-axial tension test for which we set

$$\boldsymbol{\epsilon} = \chi \begin{pmatrix} 1 & 0 & 0 \\ 0 & -0.41 & 0 \\ 0 & 0 & -0.41 \end{pmatrix} \tag{7.36}$$

with $\chi \in [0, 0.06]$ linearly varying in time. The material is subjected to loading and unloading, consequently χ increases linearly from zero to its maximum value and then decreases linearly again until it reaches zero. As randomly chosen initial set for the Euler angles we take $\boldsymbol{\alpha}_0 = \{2.62596, 1.84057, 5.98139\}$ (in rad).

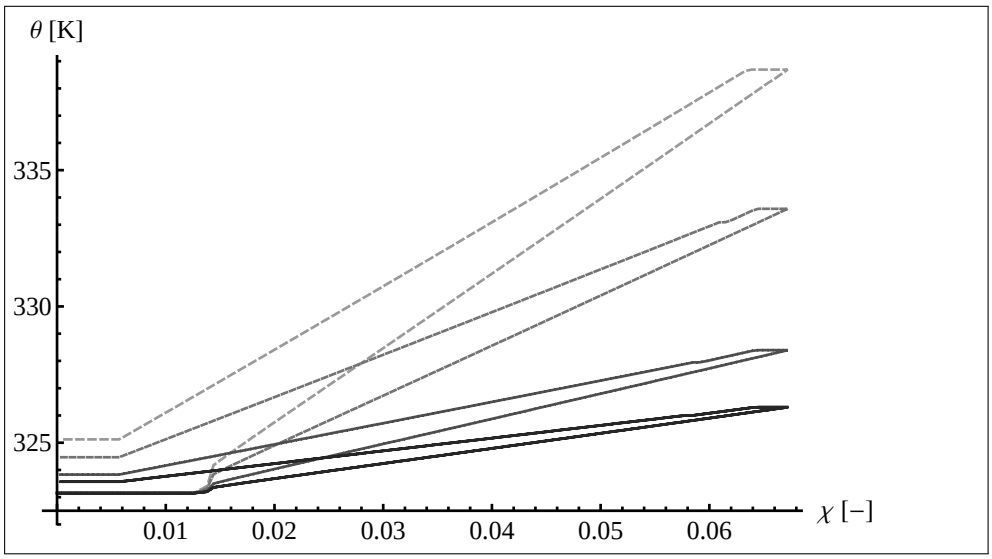

Figure 7.1: Temperature over strain with varying heat conductivity $\kappa = \{0.010, 0.015, 0.030, 0.050\}$ GPa/K. Higher temperature evolution is observed at lower values of κ.

At first, we show the evolution of temperature over strain in Fig. 7.1. We see that in the beginning, temperature is constant. At a strain of approximately $\chi = 0.0125$ phase transformation initializes, see also Fig. 7.3, which causes temperature to increase. Depending on the specific choice of the heat conductivity, the increase of heat differs: it is lowest for $\kappa = 0.050$ [GPa/K] and highest for $\kappa = 0.010$ [GPa/K]. When the material is unloaded, the elevated temperature remains constant until the phase transformation from the martensitic composition starts which was established during loading back to austenite. In contrast to the transformation from the thermodynamically stable phase of austenite to martensite when the material was loaded, the back transformation is endothermic. Thus, during unloading the material absorbs heat which causes temperature to decrease. When the back transformation has finished, temperature remains constant again, but at a higher value than at the beginning. This effect is expected since phase transformations in shape memory alloys are dissipative. Therefore a part of the mechanically applied power is transformed into to heat. This aspect is captured

by our material model as demonstrated in Fig. 7.1.

The value for the heat capacity determines the amount of produced heat not only in terms of final values of temperature but also influences shape and size of the hysteresis in the temperature-strain diagram in Fig. 7.1.

Thermo-mechanical coupling in shape memory alloys takes place bilaterally: due to phase transformations temperature increases which in turn has an impact on the evolution of phase transformation. This phenomenon can be observed in Fig. 7.2. Here, the evolution of the austenitic phase over strain is presented. We see that in the beginning there is hardly any difference between the cases with varying heat capacity. However, at maximum load the diagram shows that the amount of remaining austenite is approximately about 2% higher for the simulation with low heat capacity and thus high temperature (gray, dashed curve) compared to the case with large heat capacity (black curve).

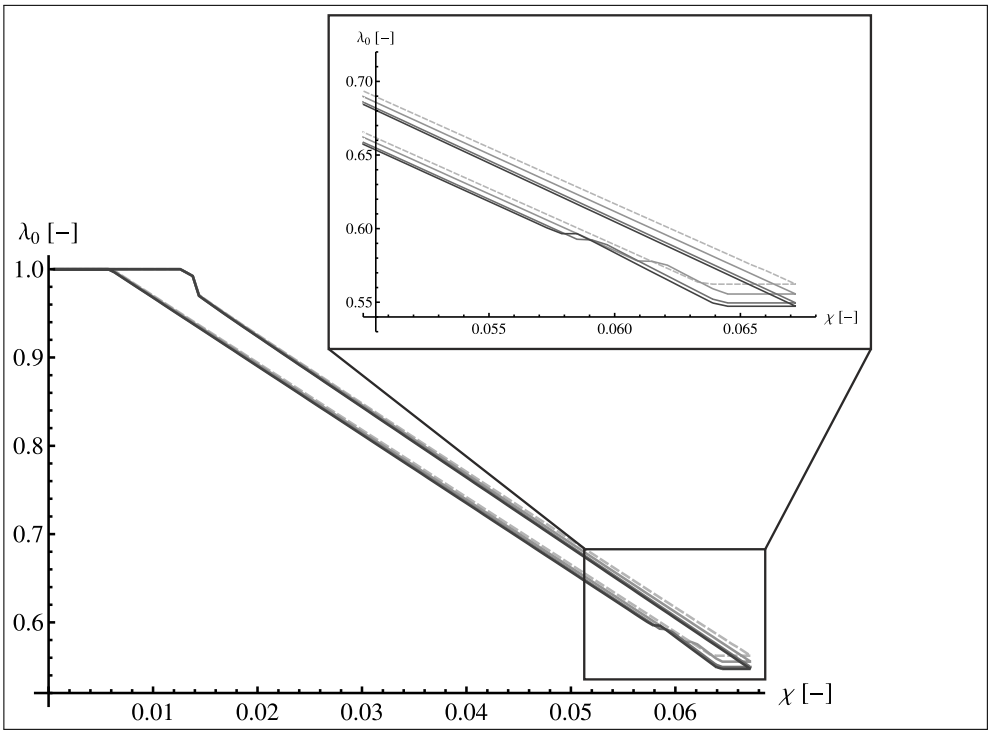

Figure 7.2: Volume fraction of austenite over strain with varying heat conductivity $\kappa = \{0.010, 0.015, 0.030, 0.050\}$ GPa/K, including a zoom of the end region.

Although it may seem at first glance that a difference of approximately 2% in the remaining amount of austenite is of minor importance, the contrary is true as demonstrated in Fig. 7.3. Here, the corresponding stress-strain diagrams are plotted for the simulations with different values for κ. At the very beginning, the material behaves linearly elastic. Then, at a strain of $\chi = 0.0125$ a stress drop takes place when phase transformation starts. This first part of the material reaction is almost independent of the specific choice for the heat conductivity, which is expected since during that part the increase in temperature is not yet very pronounced, see Fig. 7.1.After the stress drop we find the well-known plateau behavior which is typical during phase transformation in shape memory alloys. While the load increases further, the difference in the evolution of temperature increases which stabilizes the austenite as discussed previously, Fig. 7.2. This effect is discussed in greater detail in [93]. Although the resulting change in the evolution of austenite is not very huge, it is large enough

to have a pronounced impact on the resultant stress: while stress remains quite constant for a small temperature increase, the stress plateau shows a distinct inclination which is the more pronounced the higher the temperature is. This aspect corresponds well to experiments [166].

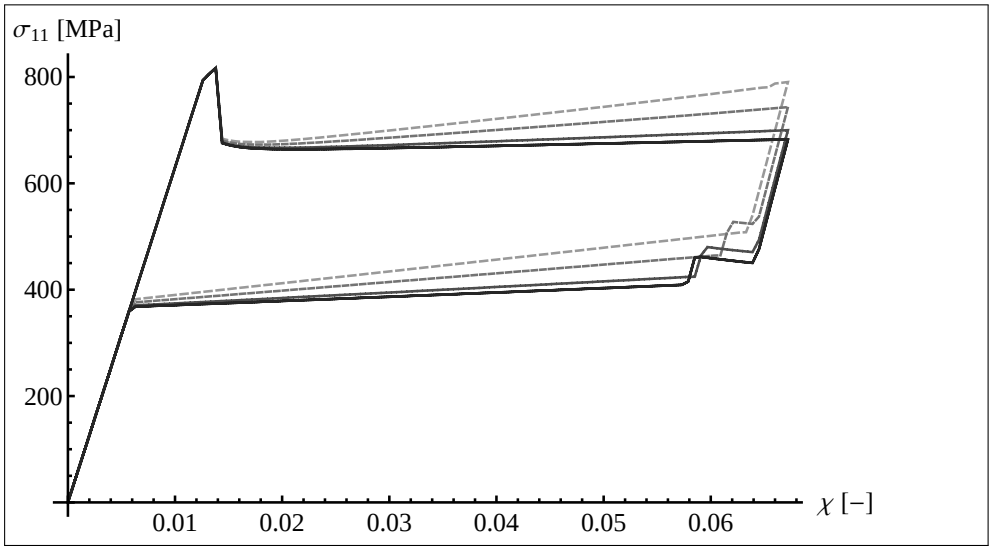

Figure 7.3: Stress σ_{11} over strain for varying heat conductivity$\kappa = \{0.010, 0.015, 0.030, 0.050\}$ GPa/K.

The material model accounts for the polycrystalline martensitic texture by the specific approach for the representative orientation distribution function in terms of evolving Euler angles. For more details we refer to [93]. The relative value of the Euler angles is presented in Fig. 7.4. Here, all angles start at a relative value of 1. We see that the evolution of the Euler angles differs. For instance, one angle diminishes only by approximately 2% while another angle reduces its value by approximately 12%. This depends on the choice of the initial set of angles, see [93]. Again we see some influence when temperature increases with different loading rates. However, here the differences are quite small.

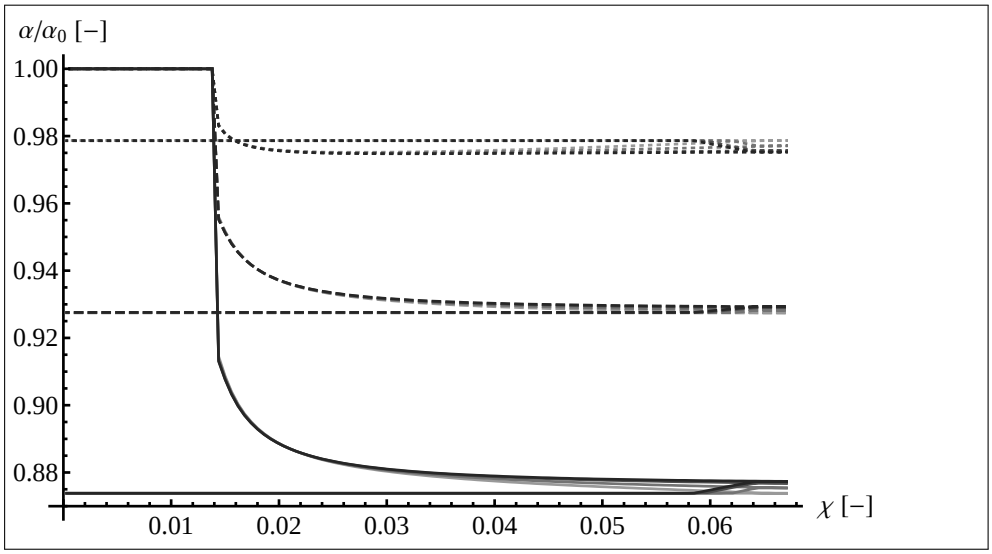

Figure 7.4: Relative value of the Euler angles over strain for varying heat conductivity $\kappa = \{0.010, 0.015, 0.030, 0.050\}$ GPa/K, $\boldsymbol{\alpha}_0 = \{2.62596, 1.84057, 5.98139\}$.

It can be seen that all angles evolve quite drastically when phase transformation initializes. After this

initial drop they remain almost constant. The evolution of the orientation of the average direction of phase transforming grains is dissipative. Thus, the evolution of the relative values for $\boldsymbol{\alpha}$ contributes to the evolution of temperature, as well. This explains the non-linear behavior of the temperature-strain curves in Fig. 7.1 right at the beginning of temperature evolution. This means we see a similar effect as for the evolution of the volume fraction of austenite: although the difference in the evolution of Euler angles seems to be quite small for different values for κ, these small differences have a measurable impact on temperature evolution.

7.5 Conclusions

Based on the variational principle of the minimum of the dissipation potential for non-isothermal processes we derived a thermo-mechanically coupled material model for polycrystalline shape memory alloys. The application of this variational principle yields more concise governing equations in comparison to the principle of maximum dissipation, [67]. In order to increase numerical efficiency, we adapted the condensed formulation for the distribution orientation functions from [93]. Finally, we presented in this paper first results for the thermo-mechanically coupled material model on a material point level. Various examples showed that the evolution of temperature as well as the temperature dependence of the stress can be captured very well by our material model. In a future work, we will discuss the model's performance for entire material specimens when it is evaluated within a finite element framework and the artificial assumption of an adiabatic process will not have to be made.

Table 7.1: Transformation strains for cubic to monoclinic transforming NiTi after [194]. $\bar{\alpha} = 0.02381$, $\bar{\beta} = -0.02480$, $\bar{\delta} = 0.07528$, $\bar{\epsilon} = 0.04969$

$$\boldsymbol{\eta}_1 = \begin{pmatrix} \bar{\alpha} & \bar{\delta} & \bar{\epsilon} \\ \bar{\delta} & \bar{\alpha} & \bar{\epsilon} \\ \bar{\epsilon} & \bar{\epsilon} & \bar{\beta} \end{pmatrix} \quad \boldsymbol{\eta}_2 = \begin{pmatrix} \bar{\alpha} & \bar{\delta} & -\bar{\epsilon} \\ \bar{\delta} & \bar{\alpha} & -\bar{\epsilon} \\ -\bar{\epsilon} & -\bar{\epsilon} & \bar{\beta} \end{pmatrix} \quad \boldsymbol{\eta}_3 = \begin{pmatrix} \bar{\alpha} & -\bar{\delta} & -\bar{\epsilon} \\ -\bar{\delta} & \bar{\alpha} & \bar{\epsilon} \\ -\bar{\epsilon} & \bar{\epsilon} & \bar{\beta} \end{pmatrix}$$

$$\boldsymbol{\eta}_4 = \begin{pmatrix} \bar{\alpha} & -\bar{\delta} & \bar{\epsilon} \\ -\bar{\delta} & \bar{\alpha} & -\bar{\epsilon} \\ \bar{\epsilon} & -\bar{\epsilon} & \bar{\beta} \end{pmatrix} \quad \boldsymbol{\eta}_5 = \begin{pmatrix} \bar{\alpha} & \bar{\epsilon} & \bar{\delta} \\ \bar{\epsilon} & \bar{\beta} & \bar{\epsilon} \\ \bar{\delta} & \bar{\epsilon} & \bar{\alpha} \end{pmatrix} \quad \boldsymbol{\eta}_6 = \begin{pmatrix} \bar{\alpha} & -\bar{\epsilon} & \bar{\delta} \\ -\bar{\epsilon} & \bar{\beta} & -\bar{\epsilon} \\ \bar{\delta} & -\bar{\epsilon} & \bar{\alpha} \end{pmatrix}$$

$$\boldsymbol{\eta}_7 = \begin{pmatrix} \bar{\alpha} & -\bar{\epsilon} & -\bar{\delta} \\ -\bar{\epsilon} & \bar{\beta} & \bar{\epsilon} \\ -\bar{\delta} & \bar{\epsilon} & \bar{\alpha} \end{pmatrix} \quad \boldsymbol{\eta}_8 = \begin{pmatrix} \bar{\alpha} & \bar{\epsilon} & -\bar{\delta} \\ \bar{\epsilon} & \bar{\beta} & -\bar{\epsilon} \\ -\bar{\delta} & -\bar{\epsilon} & \bar{\alpha} \end{pmatrix} \quad \boldsymbol{\eta}_9 = \begin{pmatrix} \bar{\beta} & \bar{\epsilon} & \bar{\epsilon} \\ \bar{\epsilon} & \bar{\alpha} & \bar{\delta} \\ \bar{\epsilon} & \bar{\delta} & \bar{\alpha} \end{pmatrix}$$

$$\boldsymbol{\eta}_{10} = \begin{pmatrix} \bar{\beta} & -\bar{\epsilon} & -\bar{\epsilon} \\ -\bar{\epsilon} & \bar{\alpha} & \bar{\delta} \\ -\bar{\epsilon} & \bar{\delta} & \bar{\alpha} \end{pmatrix} \quad \boldsymbol{\eta}_{11} = \begin{pmatrix} \bar{\beta} & -\bar{\epsilon} & \bar{\epsilon} \\ -\bar{\epsilon} & \bar{\alpha} & -\bar{\delta} \\ \bar{\epsilon} & -\bar{\delta} & \bar{\alpha} \end{pmatrix} \quad \boldsymbol{\eta}_{12} = \begin{pmatrix} \bar{\beta} & \bar{\epsilon} & -\bar{\epsilon} \\ \bar{\epsilon} & \bar{\alpha} & -\bar{\delta} \\ -\bar{\epsilon} & -\bar{\delta} & \bar{\alpha} \end{pmatrix}$$

Table 7.2: Expectation values for the elastic constants for austenite and martensite in NiTi, based on the experiments in [151] and [194], calculated in [93]

$$\mathbb{C}_0 = \begin{pmatrix} 149.36 & 105.32 & 105.32 & 0 & 0 & 0 \\ 105.32 & 149.36 & 105.32 & 0 & 0 & 0 \\ 105.32 & 105.32 & 149.36 & 0 & 0 & 0 \\ 0 & 0 & 0 & 44.04 & 0 & 0 \\ 0 & 0 & 0 & 0 & 44.04 & 0 \\ 0 & 0 & 0 & 0 & 0 & 44.04 \end{pmatrix} \text{GPa}$$

$$\mathbb{C}_{i>0} = \begin{pmatrix} 205.05 & 120.78 & 120.78 & 0 & 0 & 0 \\ 120.78 & 205.05 & 120.78 & 0 & 0 & 0 \\ 120.78 & 120.78 & 205.05 & 0 & 0 & 0 \\ 0 & 0 & 0 & 84.28 & 0 & 0 \\ 0 & 0 & 0 & 0 & 84.28 & 0 \\ 0 & 0 & 0 & 0 & 0 & 84.28 \end{pmatrix} \text{GPa}$$

8 Estimation of the dissipated energy and model calibration

Published as: *P. Junker, S. Jaeger, O. Kastner, G. Eggeler, K. Hackl*: Variational prediction of the mechanical behavior of shape memory alloys based on thermal experiments, *J. Mech. Phys. Solids* **80: 86–102 (2015)**

In this work we present simulations of shape memory alloys which serve as first examples demonstrating the predicting character of energy-based material models. We begin with a theoretical approach for the derivation of the caloric parts of the Helmholtz free energy. Afterwards, experimental results for DSC measurements are presented. Then, we recall a micromechanical model based on the principle of the minimum of the dissipation potential for the simulation of polycrystalline shape memory alloys. The previously determined caloric parts of the Helmholtz free energy closes the set of model parameters without the need of parameter fitting. All quantities are derived directly from experiments. Finally, we compare finite element results for tension tests to experimental data and show that the model identified by thermal measurements can predict mechanically induced phase transformations and thus rationalize global material behavior without any further assumptions.

8.1 Introduction

There exist many different ways to establish models that describe the material behavior in terms of mathematical equations. Considering the concept of internal variables, material models can be formulated, for instance, by defining phenomenological laws that display the material reaction without considering the underlying processes or by introducing yield functions and deriving afterwards the evolution equations (which can be challenging if the model has to fulfill complex constraints). On the other hand, variational models may be derived in which the physical processes are taken into account by means of energetic formulations. A famous procedure that belongs to the latter method is the principle of the minimum of the dissipation potential (see e.g. [198, 67, 103]). There exist no physical law that demands this principle to hold. On the other hand, it does not violate the thermodynamic laws.

In previous works, different authors claimed that the energetic character of material models derived by means of that principle of the minimum of the dissipation potential would be rather "universal" (see e.g. [67, 93, 103]). This means that calibrating the model parameters to one experiment would be sufficient in order to predictively simulate the material for different geometries or boundary conditions. Until today, at least a first example, that justifies this hope, is missing.

In this paper we take an existing variational material model for shape memory alloys, published in [93], in order to give that first example on the "universal" applicability of energy-based material models. The material behavior of shape memory alloys involves nonlinear coupling of mechanical and thermodynamic field variables. Their thermo-mechanical properties result from lattice transformations between two generic phases, austenite and martensite, called martensitic transformations, which represent a specific class of non-diffusive solid-solid phase transformations. These are stimulated by temperature change or mechanical loading and evolve by nucleation- and growth processes. Hence, the transformation processes are localized and exhibit transient character.

Engineering applications of shape memory alloys often do not require resolving the micromechanical detail. Continuum models therefore consider phase mixtures of austenite and (variants of) martensite and introduce respective phase fractions as internal variables. Accordingly, global stress/strain/temperature responses of the material are modelled as initial/boundary value problems. In this context, constitutive equations are required capable of representing the functional and structural relation between stress, strain and temperature.

At the length scale of continuum thermodynamics, different routes to the governing constitutive equations were discussed in the literature. The models may be roughly divided into plasticity-based and energy-based ones. The first group of models are rooted in the classical theory of plasticity [78, 141, 6, 159]. These models modify techniques known from plasticity which yields, for instance, the effect of pseudoelasticity without detailed description of the crystallographic microstructure. While such models are very successful and especially suited for large-scale computations, they are often reliable only within their circumscribed boundaries [182, 121, 4, 174, 22, 25]. The second group is based on free-energy descriptions of the material [142, 47, 158, 113, 77, 144, 164, 50, 88, 107]. These energy-based models represent the underlaying phase transformation processes in terms of direct microstructural quantities. Therefore, they do not experience difficulties to the identification of parameters as much as the first class of models. On the other hand, they are computationally more expensive.

The model we are investigating in this contribution belongs to the group of energy-based models and employs specific principles to derive evolution equations for the internal variables [67, 125, 103]. The approach presented here is based on a model for shape memory alloys by Junker [93] and it is evaluated in the framework of the finite element method (FEM). In this contribution we show how the model may be equipped with a thermodynamically sound representation of the caloric part of the Helmholtz free energy which is needed to close the material description. With this approach, the caloric model parameters can be determined by differential scanning calorimetry (DSC) measurements of thermally-induced transformation processes in unloaded specimens. Thermodynamic considerations presented in this work indicate that despite this, the model should to be valid also for the case of load-induced phase transformation processes. Our simulations prove that this is indeed the case for such processes at various temperatures in the materials investigated.

8.2 Material model

8.2.1 The principle of the minimum of the dissipation potential

The principle of the minimum of the dissipation potential is a method to derive evolution equations for internal variables in an efficient way, especially if additional constraints have to be taken into account. It is consistent with the first and second law of thermodynamics but cannot be derived from those. For a detailed exposition see [67]. It can be stated in the form

$$\mathcal{L} = \dot{\psi} + \Delta \rightarrow \min_{\dot{\boldsymbol{z}}} \ . \tag{8.1}$$

In Eq. (8.1) the dot $\dot{()}$ as usual indicates derivative with respect to time, $\psi(\boldsymbol{x}, \boldsymbol{z})$ is the volume-specific Helmholtz free energy (with respect to the austenitic reference configuration), and $\Delta(\boldsymbol{z}, \dot{\boldsymbol{z}})$ denotes the so-called dissipation potential, introduced for the first time in [44]. Here $\boldsymbol{x}$ represents all external state variables, determined by equilibrium conditions, while all internal state variables are collected

in $\boldsymbol{z}$. The minimization in (8.1) possesses the stationarity condition

$$\mathbf{0} \in \frac{\partial \psi}{\partial \boldsymbol{z}} + \frac{\partial \Delta}{\partial \dot{\boldsymbol{z}}}, \tag{8.2}$$

which is an evolution equation for $\boldsymbol{z}$. In general Eq. (8.2) is a so-called differential inclusion because in many cases Δ is non-differentiable at $\boldsymbol{z} = \mathbf{0}$, see e.g. [67] but also A.2.2 and A.2.3. The principle has the distinct advantage that only two scalar potentials, ψ and Δ, have to be specified in order to determine the entire kinetics of the system considered.

8.2.2 Model for polycrystalline shape memory alloys

In the present work, the material model developed by Junker [93] is used which is a mathematically condensed version of the micromechanical models introduced in [71, 70, 97]. Due to a simplified description of the polycrystalline orientation distribution function of the martensitic strain (which must not be confused with an orientation distribution function for the grains or texture) this model proves to be numerically very efficient. It represents the microstructure of the aggregate by two sets of variables, $\boldsymbol{z} = \{\boldsymbol{\lambda}, \boldsymbol{\alpha}\}$. Here $\boldsymbol{\lambda} = \{\lambda_0, \ldots, \lambda_n\}$ collects the local volume fractions (with respect to the austenitic reference configuration) of the various crystallographic phases ($i = 0$ for austenite and $i > 0$ for the martensitic variants), and n is the total number of martensitic variants (12 for NiTi). The second internal variable $\boldsymbol{\alpha} = \{\varphi, \nu, \omega\}$ is the set of three Euler angles giving the local mean orientation of the martensitic strain in the entire polycrystal.

We will assume the dissipation potential as

$$\Delta = r_\lambda |\dot{\boldsymbol{\lambda}}| + r_\alpha \|\dot{\boldsymbol{Q}} \cdot \boldsymbol{Q}^{-1}\| = r_\lambda |\dot{\boldsymbol{\lambda}}| + \sqrt{2}\, r_\alpha \left(\dot{\varphi}^2 + \dot{\nu}^2 + 2\cos\nu\, \dot{\varphi}\, \dot{\omega} + \dot{\omega}^2\right)^{1/2} . \tag{8.3}$$

with two constant dissipation parameters r_λ and r_α. Here $\boldsymbol{Q}(\boldsymbol{\alpha})$ denotes the rotation matrix defined by the Euler angles $\boldsymbol{\alpha}$, see A.2.2. The potential defined by Eq. (8.3) is homogeneous of first order in the rates of the internal variables which results in rate-independent material behavior, see [67]. We do not consider any dissipation due to heat flux since it is not relevant for this work. Otherwise a corresponding term would have to be included in the formula above, see [69, 68, 103]. In previous works we were only able to determine the dissipation parameters by fitting the experimentally observed stress-strain curves. As will be shown, we will now be able to calculate them directly from experimentally obtained values.

Following [93] we assume the Helmholtz free energy to decompose into a mechanical and a caloric contribution as

$$\psi = \psi_{\mathrm{mech}}(\boldsymbol{\varepsilon}, \boldsymbol{\lambda}, \boldsymbol{\alpha}) + \psi_{\mathrm{cal}}(\boldsymbol{\lambda}, T), \tag{8.4}$$

with

$$\psi_{\mathrm{mech}}(\boldsymbol{\varepsilon}, \boldsymbol{\lambda}, \boldsymbol{\alpha}) = \frac{1}{2}(\boldsymbol{\varepsilon} - \boldsymbol{Q}^T \cdot \bar{\boldsymbol{\eta}} \cdot \boldsymbol{Q}) : \bar{\mathbb{C}} : (\boldsymbol{\varepsilon} - \boldsymbol{Q}^T \cdot \bar{\boldsymbol{\eta}} \cdot \boldsymbol{Q}), \tag{8.5}$$

and

$$\psi_{\mathrm{cal}}(\boldsymbol{\lambda}, T) = \sum_{i=0} \lambda_i \psi_{i,\mathrm{cal}}(T). \tag{8.6}$$

Here $\boldsymbol{\varepsilon}$ is the strain tensor, $\bar{\boldsymbol{\eta}}$ the effective transformation strain, $\bar{\mathbb{C}}$ the tensor of effective elastic

constants, and T the absolute temperature. The effective quantities can be calculated according to

$$\bar{\boldsymbol{\eta}} = \sum_{i=0}^{n} \lambda_i \boldsymbol{\eta}_i \,, \qquad \bar{\mathbb{C}} = \left[\sum_{i=0}^{n} \lambda_i \left(\mathbb{C}_i \right)^{-1} \right]^{-1} . \tag{8.7}$$

The transformation strains of the specific variants $\boldsymbol{\eta}_i$, Table 8.1, as well as the the anisotropic stiffness tensors $\mathbb{C}_i$, Table 8.2, may be determined by experiments, or calculated using ab initio simulations, see [86, 194]. The transformation *strain* matrices $\boldsymbol{\eta}_i$ must not be confused with the transformation matrices, often termed by $\boldsymbol{U}_i$ (see e.g. [19]). Consequently, the Euler angles serve as the averaged *martensite strain* orientation distribution function and no orientation of martensitic lattices.

The caloric part of the Helmholtz free energy $\psi_{i,\mathrm{cal}}$ is identical for all martensitic variants as $\psi_{i>0,\mathrm{cal}}$ but different for austenite as $\psi_{0,\mathrm{cal}}$. A theoretical estimation of these terms will be given in Sec. 8.3. As will be shown in Sec. 8.4, knowledge of the caloric part of the Helmholtz free energy will allow to determine the dissipation parameter r_λ.

Free energy and dissipation potential being specified, we are able to derive evolution equations for $\boldsymbol{\lambda}$ and $\boldsymbol{\alpha}$ via Eq. (8.2). Matters are complicated by the fact that we have to respect constraints of mass conservation and positivity of the volume fractions. We refer to A.2.2 and A.2.3 for details of the calculations and summarize the results here only. For an extensive derivation see [70, 93]. Let us define the thermodynamic driving forces for the evolution of volume fractions and Euler angles as

$$\boldsymbol{p}^\lambda := -\frac{\partial \psi}{\partial \boldsymbol{\lambda}} \qquad \text{and} \qquad \boldsymbol{p}^\alpha := \begin{pmatrix} p_\varphi - p_\omega \cos\nu \\ p_\nu (1 - \cos^2 \nu) \\ p_\omega - p_\varphi \cos\nu \end{pmatrix} \tag{8.8}$$

where $p_\varphi := -\partial\Psi/\partial\varphi$, $p_\nu := -\partial\Psi/\partial\nu$ and $p_\omega := -\partial\Psi/\partial\omega$, see A.2.3. Then the evolution equations can be written in the form

$$\dot{\boldsymbol{\lambda}} = \rho_\lambda \left(\mathrm{dev}_{\mathcal{A}} \boldsymbol{p}^\lambda \right)_{\mathcal{A}} , \tag{8.9}$$

$$\dot{\boldsymbol{\alpha}} = \rho_\alpha \boldsymbol{p}^\alpha , \tag{8.10}$$

where the *active deviator* is defined as $\mathrm{dev}_{\mathcal{A}} \boldsymbol{p}^\lambda := \boldsymbol{p}^\lambda - 1/n_{\mathcal{A}} \sum_{k \in \mathcal{A}} p_k^\lambda \boldsymbol{I}$, and $\mathcal{A}$ denotes the *active set* of variants, see A.2.2 for details. We introduced the so-called consistency parameters ρ_λ and ρ_α. The entire set of evolution equations is closed by the Kuhn-Tucker conditions

$$\rho_\lambda \geq 0, \qquad \Phi_\lambda \leq 0, \qquad \rho_\lambda \, \Phi_\lambda = 0, \tag{8.11}$$

$$\rho_\alpha \geq 0, \qquad \Phi_\alpha \leq 0, \qquad \rho_\alpha \, \Phi_\alpha = 0, \tag{8.12}$$

and the consistency condition

$$\left(\mathrm{dev}_{\mathcal{A}} \boldsymbol{p}^\lambda \right)_i \leq 0 \qquad \text{for} \quad i \notin \mathcal{A}. \tag{8.13}$$

Here we have introduced two yield-functions defined by

$$\Phi_\lambda(\boldsymbol{p}^\lambda) = |\mathrm{dev}_{\mathcal{A}} \boldsymbol{p}^\lambda|_{\mathcal{A}} - r_\lambda \,, \qquad \Phi_\alpha(\boldsymbol{p}^\alpha) = |\boldsymbol{p}^\alpha| - r_\alpha \,, \tag{8.14}$$

where $|\boldsymbol{p}|_{\mathcal{A}} = \left(\sum_{i \in \mathcal{A}} p_i^2 \right)^{1/2}$ denotes the *active norm*.

Observe that no direct information about upper and lower plateau stresses or problem dependent

assumptions on transformation strains enter the material model. It is solely based on energetic arguments.

In the next section, an explicit expression for the caloric part of the Helmholtz free energy is derived. This allows to evaluate the driving forces within the evolution equations. However, the dissipation parameters still remain undetermined. As shown in [93], the value of r_α has only minor influence on the mechanical behavior. In contrast, the value of r_λ directly determines the shape and size of the hysteresis in the stress/strain diagram. We present a thermodynamically motivated approach how to derive an analytical expression for r_λ in Sec. 8.4.

8.3 Thermodynamics

8.3.1 Clausius-Clayperon equation

The fundamental thermo-mechanical material properties must reflect the phase stability of the crystal lattice as function of temperature and mechanical loading. Phase equilibria between austenite "A" and (variants of) martensite "M" are established across separating interfaces, considered as singular surfaces which are oriented by the normal vectors $\boldsymbol{n}$. At equilibrium, the following well-known mechanical and thermodynamical conditions must be satisfied, see for example [76, 143, 26]:

$$[\boldsymbol{\sigma}]_{\mathrm{E}} \cdot \boldsymbol{n} = \boldsymbol{0} \,, \tag{8.15}$$

$$[\boldsymbol{F}] = \boldsymbol{a} \otimes \boldsymbol{n} \,, \tag{8.16}$$

$$\boldsymbol{n} \cdot \left[(u - Ts)\, \boldsymbol{I} - \frac{1}{\varrho} \boldsymbol{\sigma} \right]_{\mathrm{E}} \cdot \boldsymbol{n} = 0 \,. \tag{8.17}$$

The operator $[x] \coloneqq x^{\mathrm{M}} - x^{\mathrm{A}}$ denotes the differences of the bracketed quantities between martensite and austenite while the suffix "E" indicates that these conditions refer to equlibria: mechanical equilibrium, Eq. (8.15), requires the normal components of the stress tensor $\boldsymbol{\sigma}$ to be continuous across the interface. Phase equilibrium, Eq. (8.17), requires the double normal component of the tensor of free enthalpy ($(u - Ts)\, \boldsymbol{I} - \boldsymbol{\sigma}/\varrho$) to be continuous across the interface ($\boldsymbol{I}$ denotes the unit tensor). The quantities u and s denote the mass-specific internal energy and entropy, respectively, T is the temperature, and ϱ the mass density.

The strain fields of austenite and martensite must obey kinematic compatibility along the interface, represented by a rank one relationship between the two deformation gradients $\mathbf{F}$ of austenite and martensite, where $\boldsymbol{a}$ is a vector representing the amplitude of the displacement jump across the interface (Hardamard condition). This condition restricts the geometry of the interface between austenite and martensite, which is represented as an invariant "habit" plane. Additional crystallographic considerations constrain the components of $\boldsymbol{a} \otimes \boldsymbol{n}$ [197, 19].

At phase equilibrium, condition (8.17) establishes the relationship between transformation stress and temperature. For convinience, we may define the nominal transformation stress $\hat{\sigma}(T)$ which effectively acts across the interface by

$$\hat{\sigma}(T) = \boldsymbol{n} \cdot \boldsymbol{\sigma}|_{\mathrm{E}} \cdot \boldsymbol{n} \quad . \tag{8.18}$$

This quantity represents an analog to the vapor pressure $p(T)$ in phase mixtures of liquid and vapor.

And like the vapor pressure, the transformation stress is coupled to temperature as long as phases coexist. The relation to temperature is given by the Clausius-Clapeyron equation, which states a consequence of the phase equilibrium condition (8.17), see A.1:

$$\left.\frac{\mathrm{d}\,\hat{\sigma}}{\mathrm{d}\,T}\right|_{\mathrm{E}} = \varrho\frac{s^{\mathrm{A}} - s^{\mathrm{M}}}{\operatorname{tr}\boldsymbol{\eta}} = -\rho\frac{[s]}{\operatorname{tr}\boldsymbol{\eta}} \quad . \tag{8.19}$$

Here, the transformation stress $\hat{\sigma}(T)$ is related to the entropy difference $[s] = (s^M - s^A)$ between austenite and martensite, and to the trace of transformation strain $\operatorname{tr}\boldsymbol{\eta}$. Thermo-mechanical experiments prove that $\mathrm{d}\hat{\sigma}/\mathrm{d}T|_{\mathrm{E}} > 0$, (see e.g. [151]). Furthermore, the trace of transformation strains is always positive which yields $s^{\mathrm{A}} > s^{\mathrm{M}}$.

8.3.2 Transformation entropies

Phase transformations in general occur as the result of competing preferences of (inner) energy and entropy: the preference of energy to minimize and the tendency of entropy to maximize under given thermal and/or mechanical constraints [145]. The stability criterion resulting from this competition, provided in the Introduction, revealed the relationship between transformation stress and temperature through the Clausius-Clapeyron relation, see Equation (8.19). Tensile experiments reveal that the transformation stress is always increasing with temperature [187], therefore the right hand side of the Clausius-Clapeyron relation (8.19) must be positive. We proceed to discuss the consequences of this phenomenological observation and append an atomistic interpretation based on [104, 106, 105].

To guarantee for positive transformation stress/temperature sensitivity of the Clausius-Clapeyron Equation (8.19), the entropy change $[s] = (s^{\mathrm{M}} - s^{\mathrm{A}})$ hence must be negative,

$$s^{\mathrm{A}} > s^{\mathrm{M}} \, . \tag{8.20}$$

An explanation of this experimental finding is rooted in the statistical interpretation of entropy. According to statistical thermodynamics, the mass-specific free energy of an N-atomic assembly at constant temperature is given by

$$f = -\frac{R}{M_{\mathrm{r}}} T \log Z \, , \tag{8.21}$$

where R is the gas constant and M_{r} the relative atom mass. The quantity Z denotes the canonical partition function. Positions $\mathbf{x}_j$ and velocities $\dot{\mathbf{x}}_j$ $(j = 1, ..., N)$ of the atoms in the sample contribute to the overall energy $\hat{u}$ through the potential and the kinetic energy,

$$\hat{u} = \hat{u}_{\mathrm{pot}}(\mathbf{x}_1, \ldots, \mathbf{x}_N) + \underbrace{\sum_{j=1}^{N} \frac{m_j}{2} |\dot{\mathbf{x}}_j|^2}_{\hat{u}_{\mathrm{kin}}} \, , \tag{8.22}$$

and the canonical partition function is defined by

$$Z = \sum_{\mathbf{x}_1} \ldots \sum_{\mathbf{x}_N} \sum_{\dot{\mathbf{x}}_1} \ldots \sum_{\dot{\mathbf{x}}_N} \exp\left(-\frac{\hat{u}}{kT}\right) \, . \tag{8.23}$$

To calculate the partition function, the potential energy $\hat{u}_{\mathrm{pot}}$ must be known as function of the atomic positions. Here, we select a particular simple ansatz suggested by Einstein:

$$\hat{u}_{\mathrm{pot}} = \sum_{j=1}^{N} \hat{u}_j^0 + \frac{\beta}{2} \left| \mathbf{x}_j - \mathbf{x}_j^0 \right|^2 \ . \tag{8.24}$$

The underlying idea is that individual atoms oscillate independently of one another in a parabolic mean-field potential with curvature β about their mean lattice position $\mathbf{x}_j^0$. The zero-point energy of the atom at this position is denoted by $\hat{u}_j^0$. This harmonic potential may be interpreted as an effective mean field provided by the interactions with the remaining collective of atoms. The advantage is that the partition function of such a harmonic crystal can be calculated analytically, see [105]. Skipping the calculus here, we represent the resulting free energy

$$f_{\mathrm{harm}} = \underbrace{3\frac{R}{M_{\mathrm{r}}}T + \hat{u}^0}_{u_{\mathrm{harm}}} \underbrace{-T\left(\frac{3}{2}\frac{R}{M_{\mathrm{r}}}\log T + \frac{R}{M_{\mathrm{r}}}\log\left(\frac{4}{3}\pi\left(\frac{3kT}{\beta}\right)^{3/2}\right) + C\right)}_{s_{\mathrm{harm}}}, \tag{8.25}$$

where $\hat{u}^0$ denotes the mean zero-point energy of the atoms per mass unit. The respective contributions to the internal energy and entropy are indicated by u_{harm} and s_{harm}, respectively. Besides a generic integration constant C, the entropy exhibits two logarithmic terms. The first represents the lattice invariant temperature dependence of entropy, while the second one depends on the specific lattice structure through the curvatures β of the respective mean-field interaction potentials. These curvatures differ between austenite and martensite. The argument $\frac{4}{3}\pi\left(\frac{3kT}{\beta}\right)^{3/2}$ of the second logarithm represents the spherical space an atom j may sweep on average at a thermal activation given by kT. The smaller the potential's curvature β — that is, the softer the potential — the larger this space. Softer atomic interaction potentials allow the realisation of more atomic microstates than stronger ones at the same temperature and accordingly, the entropy is bigger for a softer potential. With this we may return to the phenomenological findings of Eq. (8.20) and conclude that the austenitic lattice provides "softer" interactions than the martensitic one, since

$$s_{\mathrm{harm}}^{\mathrm{A}} > s_{\mathrm{harm}}^{\mathrm{M}} \quad \rightarrow \quad \beta^{\mathrm{M}} > \beta^{\mathrm{A}} \ . \tag{8.26}$$

Employing this result, the difference $[f]_{\mathrm{harm}}$ of the harmonic free energy between martensite and austenite at constant temperature reads

$$[f]_{\mathrm{harm}} = (\hat{u}^{0,\mathrm{M}} - \hat{u}^{0,\mathrm{A}}) - \frac{3}{2}\frac{RT}{M_{\mathrm{r}}}\log\frac{\beta^{\mathrm{A}}}{\beta^{\mathrm{M}}} \ . \tag{8.27}$$

This result clearly motivates that $[f]_{\mathrm{harm}}$ may be approximated by a linear function of temperature. We proceed to explain how the specific contributions of the internal energy $[u]_{\mathrm{harm}}$ and of entropy $[s]_{\mathrm{harm}}$,

$$[u]_{\mathrm{harm}} = \hat{u}^{0,M} - \hat{u}^{0,A} \ , \tag{8.28}$$

$$[s]_{\mathrm{harm}} = \frac{3}{2}\frac{R}{M_{\mathrm{r}}}\log\frac{\beta^{\mathrm{A}}}{\beta^{\mathrm{M}}} \tag{8.29}$$

may be determined by experimental measurements with unloaded samples. We emphasise that for the application of the material model exactly only this difference in the caloric part of the Helmholtz

free energy $[f]_{\mathrm{harm}}$ is needed.

8.3.3 Determination of $[u]$ and $[s]$ by DSC measurements

During martensitic transformations, latent heat is released (for A→M) or absorbed (for M→A) by the lattice. Assuming that during the transformation processes, the temperature and the transformation stress remain approximately constant, integration of the energy balance yields

$$\left[u - \frac{\hat{\sigma}(T)}{\varrho}\right]_{\mathrm{E}} = q_{\mathrm{latent}} \ . \tag{8.30}$$

This equation states that the specific latent heat q_{latent} is related to the difference of the specific enthalpy of the two phases. This quantity can be detected from DSC (differential scanning calorimetry) measurements, as explained below. Such DSC measurements are carried out at absent external loading of the specimen such that $\hat{\sigma}(T) = 0$. Hence,

$$[u]_{\mathrm{E}} = q_0 \ , \tag{8.31}$$

where $q_0 = q_{\mathrm{latent}}(\hat{\sigma} = 0)$ and the transformation temperature thus detected refers to unloaded conditions, too. We may use this relation to determine $[u]_{\mathrm{harm}}$ in Eq. (8.27). The entropic term $[s]_{\mathrm{harm}}$ may then be calculated from the phase equilibrium condition (8.17) for an unloaded specimen, yielding

$$[s]_{\mathrm{E}} = \frac{q_0}{T_{\mathrm{E}}} \ . \tag{8.32}$$

The DSC curves of shape memory alloys are characterised by the austenite start (A_{s}) and finish (A_{f}) temperatures of M→A transformations during heating and the martensite start (M_{s}) and finish (M_{f}) temperatures of the reverse transformation during cooling. The austenite peak temperature A_{p} and the martensite peak temperature M_{p} indicate the respective temperatures of the DSC peaks where maximum heat flows. The peak areas indicate the latent heats of the endothermal (M→A) and exothermal (A→M) reactions during the phase transformation. We refer to the latent heat for the endothermal and exothermal process by q^{M} and q^{A}, respectively (see Fig. 8.1). Here, the DSC signal of binary Ni51.0Ti49.0 alloy is shown as detected employing an instrument of type DSC 204 F1 Phönix. The ingot was prepared by arc melting with Ni pellets and Ti pieces as starting materials. Subsequent solution annealing and water quenching following the procedure developed at the Department of Materials Science at the Ruhr-University in Bochum were performed [48]. The heating and cooling rates were 10 K/min. Further details on thermal analysis have been published in [109]. Figure 8.1 shows the DSC chart for a binary NiTi alloy with 51.0 at.-% Nickel.

From the DSC curves in Fig. 8.1 we see that the individual transformation processes are spread over certain temperature intervals $(A_{\mathrm{s}}, A_{\mathrm{f}})$ around A_{p} and $(M_{\mathrm{s}}, M_{\mathrm{f}})$ around M_{p} and incorporate a temperature hysteresis. Therefore, it is by no means obvious how to interpret the thermodynamic phase equilibrium temperature $T_{\mathrm{E}}(\hat{\sigma} = 0)$ in view of this laboratory experiment. In this situation we refer to the generally accepted suggestion of Tong and Wayman [187] who proposed a geometrical construction to define the phase equilibrium temperature T_E by

$$T_{\mathrm{E}} = \frac{M_{\mathrm{p}} + A_{\mathrm{p}}}{2} \ . \tag{8.33}$$

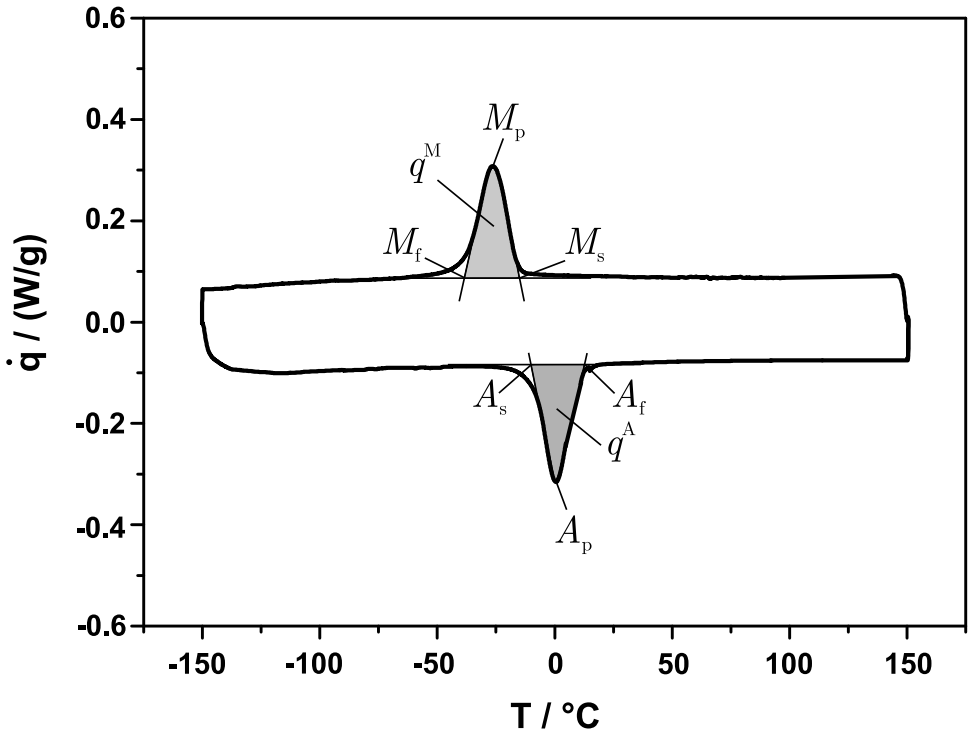

Figure 8.1: DSC chart of a binary NiTi alloy with 51.0 at.-% Nickel. The peak temperatures of the forward and reverse transformation are denoted by A_p and M_p, the respective transformation start and finish temperatures read M_f, M_s, A_s and A_f. The latent heats for the M→A transformation is indicated by q^M and that for the A→M transformation by q^A.

Table 8.3 shows the phase transformation temperatures (M_s, M_p, M_f, A_s, A_p, A_f) and the values of latent heat which were experimentally measured by DSC for the Ni51.0Ti49.0 alloy (see Fig. 8.1). Additionally, the subsequently calculated equilibrium temperature T_E and the resulting coefficients $[u]_\mathrm{harm}$ and $[s]_\mathrm{harm}$ are presented there.

8.4 Calculation of the dissipation parameters

The parameter r_λ is related to the dissipation due to phase transformation. In the experiment described in Sec. 8.3.3, a stress-free specimen of NiTi was subjected to phase transformation induced by temperature. Since there is no mechanical constraint, the transformation from austenite to martensite and vice versa evolves in a completely uniform way. All martensitic variants have the same volume fraction during the entire process. This allows to use this experiment for calculation of r_λ.

The material model investigated here uses a novel approach for the martensite strain orientation distribution function which is necessary to account for the polycrystalline aspect: the martensite strain orientation information carried by different grains is combined to one evolving averaged martensite strain orientation of transforming grains (which is described in terms of $\boldsymbol{\alpha}$). Thus, the quantities λ_i measure the volume fractions of the respective crystallographic variants averaged over all possible orientations of grains. There might occur inner stresses in grains and along grain boundaries in reality. However, we assume that these stresses are averaged out by our specific modeling approach. Then, because of the assumed stress-free state of the specimen only the caloric part of the free energy remains. Employing the harmonic approximation introduced in Sec. 8.3.2, and using the relation $\psi = \varrho^\mathrm{A} f$ (remember, ψ is defined with respect to the austenitic reference configuration), the volume-specific free energy can be written in the form

$$\psi = \lambda_0 \, \varrho^\mathrm{A} (u^\mathrm{A}_\mathrm{harm} - T s^\mathrm{A}_\mathrm{harm}) + \sum_{i=1}^{n} \lambda_i \, \varrho^\mathrm{A} (u^\mathrm{M}_\mathrm{harm} - T s^\mathrm{M}_\mathrm{harm}) \, . \tag{8.34}$$

According to Eq. (8.8) the driving forces are given as

$$p^\lambda_i = -\varrho^\mathrm{A} \begin{cases} u^\mathrm{A}_\mathrm{harm} - T s^\mathrm{A}_\mathrm{harm} & \text{for } i = 0 \, , \\ u^\mathrm{M}_\mathrm{harm} - T s^\mathrm{M}_\mathrm{harm} & \text{for } i > 0 \, . \end{cases} \tag{8.35}$$

As can be seen, the driving forces for all martensitic variants are identical and there is only a difference between those of austenite and martensite. Consequently the rates of the volume fractions are the same for all martensitic variants and mass conservation gives

$$\dot{\lambda}_i = -\frac{1}{n} \, \dot{\lambda}_0 \qquad \text{for } i > 0 \, . \tag{8.36}$$

In our case all variants are active ($n_\mathcal{A} = n + 1$), hence we obtain for the active deviator

$$\left(\mathrm{dev}_\mathcal{A} \boldsymbol{p}^\lambda \right)_i = \varrho^\mathrm{A} \left([u]_\mathrm{harm} - T [s]_\mathrm{harm} \right) \begin{cases} \frac{n}{n+1} & \text{for } i = 0 \, , \\ -\frac{1}{n+1} & \text{for } i > 0 \, , \end{cases} \tag{8.37}$$

and for its active norm

$$|\mathrm{dev}_\mathcal{A} \boldsymbol{p}^\lambda|_\mathcal{A} = \sqrt{\frac{n}{n+1}} \, \varrho^\mathrm{A} \left| [u]_\mathrm{harm} - T [s]_\mathrm{harm} \right| . \tag{8.38}$$

While the transformation takes place, the driving forces are located on the yield surface. Considering the Kuhn-Tucker conditions Eq. (8.11) we have $\rho_\lambda > 0$ and consequently $\Phi_\lambda = 0$. Employing Eqs. (8.14) and (8.38) this gives

$$r_\lambda = \sqrt{\frac{n}{n+1}}\, \varrho^{\mathrm{A}} \left| [u]_{\mathrm{harm}} - T[s]_{\mathrm{harm}} \right| . \tag{8.39}$$

Strictly, the equation above makes only sense if r_λ is assumed as temperature dependent quantity. For constant r_λ Eq. (8.39) has to be averaged over the temperature interval $[T_0, T_1]$ by integration. The expression $[u]_{\mathrm{harm}} - T[s]_{\mathrm{harm}}$ does not change its sign during the transformation process. Thus integration over the entire transformation process gives

$$r_\lambda = \sqrt{\frac{n}{n+1}}\, \varrho^{\mathrm{A}} \left| [u]_{\mathrm{harm}} - \frac{1}{2}\,(T_1 + T_0)[s]_{\mathrm{harm}} \right| , \tag{8.40}$$

where $T_0 = \{M_{\mathrm{s}}, A_{\mathrm{s}}\}$ and $T_1 = \{M_{\mathrm{f}}, A_{\mathrm{f}}\}$ are the respective start and finish temperatures. For symmetric DSC-peaks we have $(T_1 + T_0)/2 = T_p$, the respective peak temperature ($T_p = \{M_{\mathrm{p}}, A_{\mathrm{p}}\}$).

Inserting the experimentally determined values for $[u]_{\mathrm{harm}}$ and $[s]_{\mathrm{harm}}$ yields $r_\lambda = 0.0065\,\mathrm{GPa}$ with $n = 12$ for NiTi which is very comparable to the results given in [92].

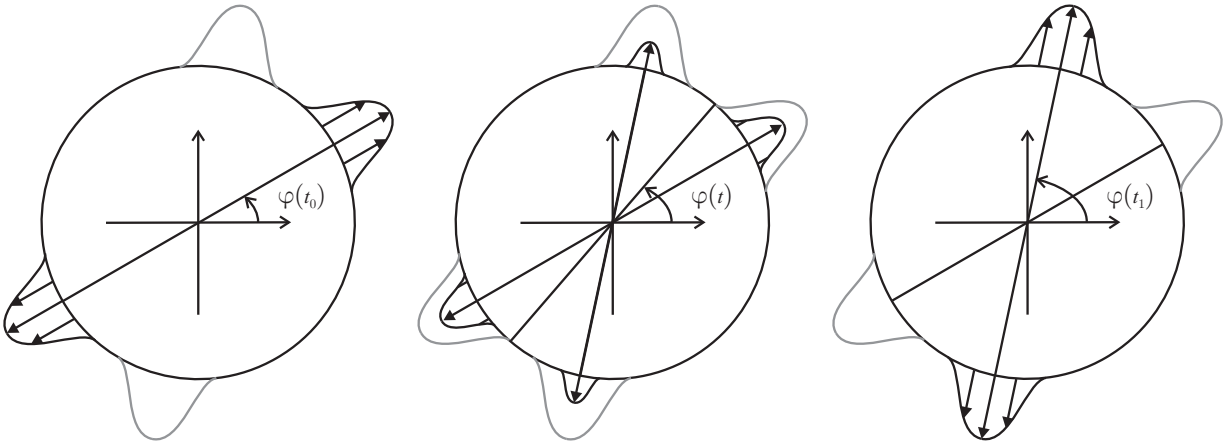

Figure 8.2: Schematic plot of two microstructural states over time: same final state can be described in terms of varying volume fractions $\boldsymbol{\lambda}$ or equivalently in terms of varying average martensite strain orientation of phase-transforming grains, indicated by $\varphi = \varphi(t)$.

A final calculation of the dissipation parameter r_α is complicated and remains for future closer investigation. For now, we postulate the following approximation: consider a material state in which only one martensitic variant is present. This means we have for example $\boldsymbol{\lambda}(t_0) = (0, 1, 0, \ldots, 0)$. Then we alter the polycrystalline microstructure in such a way that a different Bain-strain is predominant now, e.g. $\boldsymbol{\lambda}(t_1) = (0, 0, 1, \ldots, 0)$. The total dissipation produced by this process is given by

$$D_\lambda = \int_{t_0}^{t_1} r_\lambda |\dot{\boldsymbol{\lambda}}|\, \mathrm{d}t = \sqrt{2}\, r_\lambda \, . \tag{8.41}$$

The same change of the polycrystalline configuration can be described, however, by imposing a rotation of the martensite strain by a specific angle, see Figure 8.2. The transformation strain of martensite

one is given in its diagonal form by $\hat{\boldsymbol{\eta}}_1$ (compare to $\boldsymbol{\eta}_1$ given in Table 8.1)

$$\hat{\boldsymbol{\eta}}_1 = \begin{pmatrix} 0.130822 & 0 & 0 \\ 0 & -0.05653 & 0 \\ 0 & 0 & -0.05147 \end{pmatrix} \tag{8.42}$$

In the same basis, the transformation strain of variant two reads

$$\hat{\boldsymbol{\eta}}_2 = \begin{pmatrix} 0.02539 & 0.09294 & 0 \\ 0.09294 & 0.04890 & 0 \\ 0 & 0 & -0.05147 \end{pmatrix} \tag{8.43}$$

Basic calculation reveals that a rotation of $\varphi = 48.60° \cong \pi/4$ around the z axis in its Eigensystem transforms the martensite variant one to the variant two. Thus, same microstructural process of a transition from pure martensite one to pure martensite two can be described in the current model by the mentioned rotation, i.e. we have $\varphi(t_0) = \{0, 0, 0\}$ and $\varphi(t_1) = \{\pi/4, 0, 0\}$. This produces a dissipation of

$$D_\alpha = \int_{t_0}^{t_1} r_\alpha \| \dot{\boldsymbol{Q}} \cdot \boldsymbol{Q}^{-1} \| \, \mathrm{d}t = \sqrt{2}\, \pi/4\, r_\alpha \, . \tag{8.44}$$

Since both processes result in the same material state we claim the corresponding values of dissipation to be equivalent: $D_\lambda = D_\alpha$. This yields the relation

$$r_\alpha = \frac{4}{\pi} r_\lambda \, . \tag{8.45}$$

8.5 Finite element simulations of tension tests

The previous sections proved that all missing model parameters, $[u]_{\mathrm{harm}}$ and $[s]_{\mathrm{harm}}$ as well as r_λ and r_α, can be derived from thermal experiments. We will now present finite element solutions of mechanical tests where these parameters are used. Once again, we emphasize that we did not perform any parameter fitting and that the experiment from which the parameters are derived is a thermal one – in contrast to the numerical results where isothermal tension tests are simulated.

The implementation of the material model into finite elements is of standard manner: it is evaluated for each integration point where, spatially discretized, the volume fractions may evolve individually. A detailed excursion into implementation issues for polycrystalline shape memory can be found in [97]. Let us mention that the result of any finite element calculation is an approximation the minimizer of the Gibbs free energy $\mathcal{G}$, defined as

$$\mathcal{G} := \int_\Omega \psi(\boldsymbol{\varepsilon}, \boldsymbol{\lambda}, \boldsymbol{\alpha}, T) \, \mathrm{d}V - \int_\Omega \boldsymbol{b} \cdot \boldsymbol{u} \, \mathrm{d}V - \int_{\partial\Omega} \boldsymbol{t}^\star \cdot \boldsymbol{u} \, \mathrm{d}A \to \min_{\boldsymbol{u}} \, . \tag{8.46}$$

Here, Ω denotes the body's volume and $\partial\Omega$ its surface, $\boldsymbol{b}$ denotes the external body-forces, e.g. due to gravitation, and $\boldsymbol{t}^\star$ are the tractions. Inserting the Helmholtz free energy according to Eq. (8.5) in Eq. (8.46), applying the material model to update the microstructure, and using a finite element discretization for the displacements $\boldsymbol{u}$ provides the numerical results presented in the following. The

displacements are the prescribed quantities, along with a varying homogeneous and for the respective examples constant temperature. The reaction force at the nodes with prescribed displacements is used later to calculate the stresses. Both for strain and stress calculations, we apply the same "technique" as has been done in the experiments.

We investigate three cases: a NiTi wire at 323.15 K and at 333.15 K, and a NiTi stripe at 295.15 K. Note that NiTi is pseudoelastic at these temperatures. All of the results are compared with experimental findings. Temperature dependence is included in the model by setting the (constant) difference in the caloric part of the Helmholtz free energies according to the respective room temperature, $[\psi]_{\text{harm}}(323.15\text{K})$, $[\psi]_{\text{harm}}(333.15\text{K})$ and $[\psi]_{\text{harm}}(295.15\text{K})$.

All simulations are performed using tri-linear shape functions (3D hexahedra elements with 8 nodes per element).

8.5.1 Wire at 323.15 K

As first case, we chose a NiTi wire at 323.15 K which implies $[\psi]_{\text{harm}}(323.15\text{K}) = -0.032575$ GPa. It is clamped at both sides and tension is applied by moving one fixed side, see Fig. 8.3. The free length is 35 mm (total length 38.88 mm) and the diameter is 1.18 mm. Thus, the cross section is $A_{\text{w}} = 1.0936\ \text{mm}^2$. We discretize the wire with 240 elements and apply 2000 time steps to reach the maximum displacement of 2.1 mm which corresponds to a total strain of 6%. We calculate the resultant force F as sum of all nodal forces at those nodes where the displacements are prescribed. As done in the experimental tests, we introduce the engineering stress as $\sigma := F/A_{\text{w}}$. The engineering strain is displacement over free length, $\epsilon = u/(35\ \text{mm})\,[-]$.

A comparison between the numerically calculated and experimentally measured stress-strain-curve is given in Fig. 8.4.

Figure 8.3: Finite element mesh for the wire, side and top view. Nodes with prescribed displacements are indicated by $\mathbf{x}$.

8.5.2 Wire at 333.15 K

This simulation is identical to the first one, except the room temperature is now 333.15 K, and therefore $[\psi]_{\text{harm}}(333.15\text{K}) = -0.037575\,\text{GPa}$. All boundary conditions are kept the same. The resultant stress/strain curve is presented in Fig. 8.5.

8.5.3 Stripe at 295.15 K

A NiTi stripe is simulated at 295.15 K ($[\psi]_{\text{harm}}(295.15\text{K}) = -0.018575\,\text{GPa}$). It is discretized with 234 elements (one layer of elements in the thickness direction). The nodes with prescribed displacements

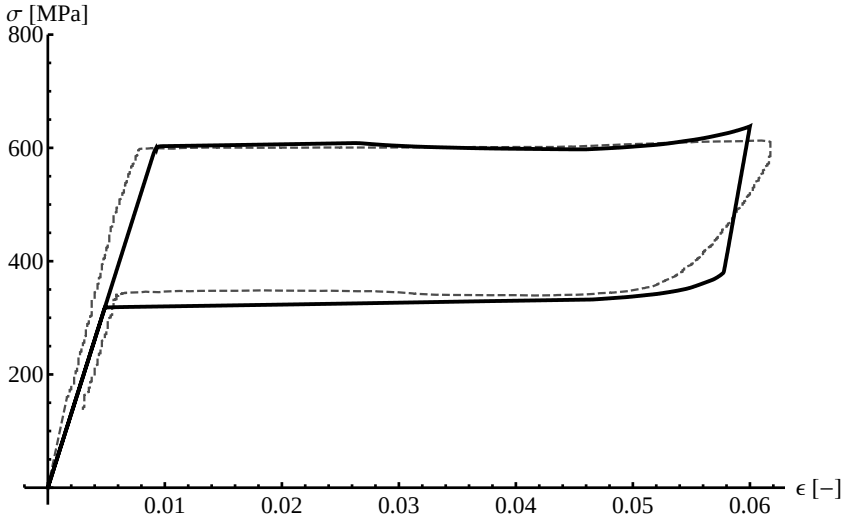

Figure 8.4: Stress-strain diagram for a NiTi wire at 323.15 K. The dashed curve is the experimental result after [192], the solid line is the numerical result of the finite element simulation with the parameters obtained from the DSC measurement.

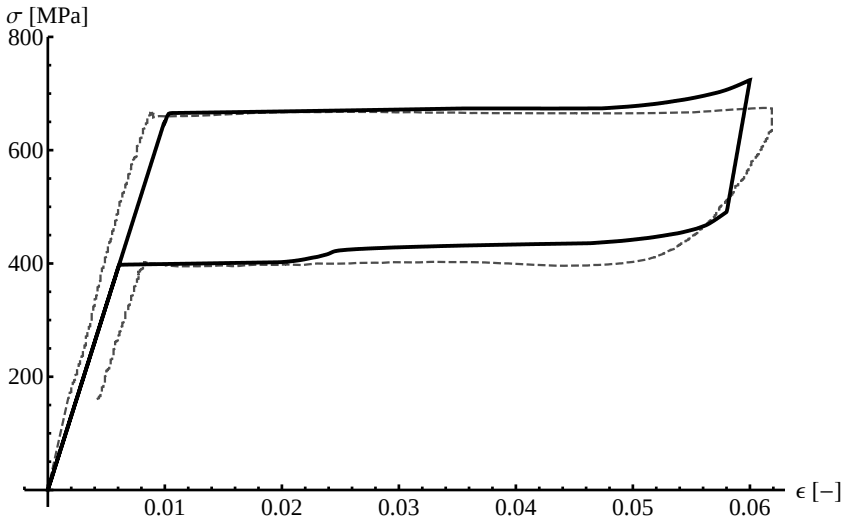

Figure 8.5: Stress/strain diagram for a NiTi wire at 333.15 K. The dashed curve is the experimental result after [192], the solid line is the numerical result of the finite element simulation with the parameters obtained from the DSC measurement.

(zero at the left hand side and non zero at the right hand side) are indicated in Fig. 8.6. Again, the free length is 35 mm and after 2000 time steps a maximum displacement of 2.1 mm is reached, giving a maximum strain of 6% as before. The cross section of the stripe is $A_s = 3.3 \cdot 0.68$ mm^2. Consequently, stress is defined for this geometry as $\sigma := F/A_s$. The resultant stress/strain curve is presented in Fig. 8.7.

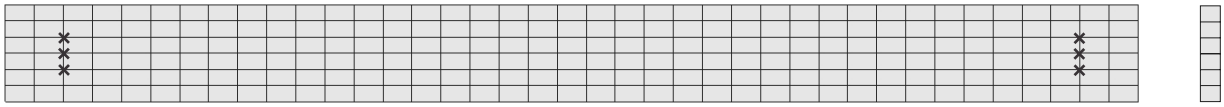

Figure 8.6: Finite element mesh for the stripe. Nodes with prescribed displacements are indicated by **x**.

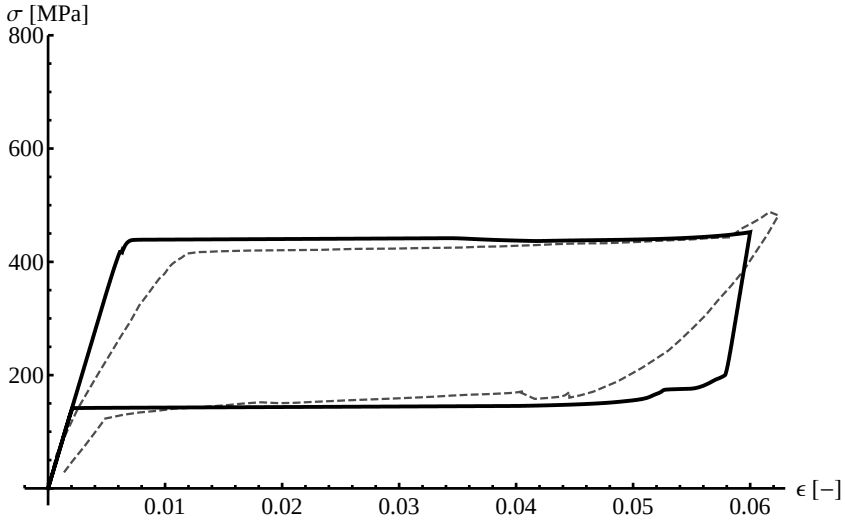

Figure 8.7: Stress/strain diagram for a NiTi stripe at 323.15 K. The dashed curve is the experimental result after [162], the solid line is the numerical result of the finite element simulation with the parameters obtained from the DSC measurement.

8.6 Discussion

In the beginning, the presented numerical results for the tension tests of the respective specimens show a linear behavior in the stress/strain diagrams. In contrast to the wires, where temperature was more elevated compared to the stripe, the experimental material reaction is – even before the stress plateau is reached – slightly different than the numerical prediction. An explanation for this is that the current material model does not account for any R-phase transformation which occurs at lower temperatures and influences even the part in the stress/strain diagram where the principal transformation is not initialized.

However, it holds true for all numerical experiments that after the linear material reaction the well documented stress plateau establishes and phase transformation evolves. When the load is reduced again, first the material behaves linearly until a lower threshold value is reached and stress stays constant. During this, the material transforms from a martensitic configuration back into its original austenitic configuration.

The respective curves are obviously characterized by specific stress values which are the upper and the lower stress plateau or the mean value and its deviation. Indirectly, in energetic terms, the current model uses this later information: the difference of caloric parts of the Helmholtz free energy $[\psi]_{\text{harm}}$ serves as mean value and the dissipation parameter is the difference in upper and lower deviation. However, the exact value for the mean value and its deviation is not given to the model in terms of stresses, as it can be seen from a comparison of their numeric values to their counterparts in the stress/strain diagram. Still, beside the deviation at lower temperatures, the numerical results show a very good compliance to the experiments. This is even more remarkable since we did not fit any parameters to the mechanical tension tests. The parameters calculated from the DSC measurements are completely sufficient to predict the mechanical material behavior without any further modifications. Hence, the results prove empirically that the basic assumptions for the model derivation are correct: this is true both for the Helmholtz free energy and dissipation. For the first time, to our knowledge, the principle of the minimum of the dissipation potential has been applied where the dissipation parameter was no fitting parameter. Due to the transferability of the dissipation parameter for the thermal DSC measurements to the mechanical tension tests, a first example is given that the basic concept of variational modeling owns the advantage that the resultant material models may have a predictive character.

The results show that a physical, or better to say, thermodynamical interpretation of the dissipation parameter is possible: it is a measure for the total amount of dissipated energy, hence the total dissipation.

8.7 Conclusions

In the present work, we further investigate a material model for polycrystalline shape memory alloys which was derived using the principle of the minimum of the dissipation potential. We explain how one can derive missing input parameters which were simply taken to be fit parameters in previous studies: the difference between the caloric parts of the Helmholtz free energies and the dissipation parameter. We show how one can estimate the difference between the caloric parts of the Helmholtz free energies from load and geometry independent thermal DSC experiments. We use this results to calculate the dissipation parameter. Inserting these parameters into the model, we perform finite element simulations for tension tests where phase transformations are induced mechanically and are load and geometry dependent. A comparison between these simulation results (for different geometries at various temperatures) with the experimental findings shows that simulation and experiment are in excellent agreement.

As an alternative interpretation is that one calibration of the material model on an energetic level is sufficient to extend the model application to other more complex cases for which it also makes realistic predictions. Our results show for shape memory alloys that parameter free material models based on energetic methods can make realistic predictions. The advantage of our approach as compared to other modeling techniques is obvious: models based on physically derived input parameters are more reliable than fit parameters obtained from experiments to predict material behavior in a realistic and safe manner.

Of course, although the model in the presented form is free of fitting parameters, it still lacks several important features that are observed in experiments: the well-known functional fatigue, R-phase

nucleation and plasticity, to mention just a few, are not included in the model. However, for the "simple" case of pure martensitic phase transformation a first example is given that variational material models may be defined in a parameter-free manner. For even more complex considerations, further investigations will be focus of future work.

A Appendix

A.1 Derivation of Clausius-Clapeyron equation

For the derivation of the Clausius-Clapeyron equation given in Eq. (8.19), we may assume for simplicity that both phases are isotropic, linear-elastic continua with constant mass density ϱ. As one may see in the following, these assumptions simplify the notation to great degree although they hold true even for the anisotropic case.

Stress composes from the isotropic nominal transformation stress $\hat{\sigma}$ that is identical for both phases austenite and martensite, and a part due to elastic deformation. Introducing the Lamé parameters $\hat{\mu}^{\mathrm{A/M}}$ and $\hat{\lambda}^{\mathrm{A/M}}$ for austenite and martensite, repsectively, stress is given as

$$\boldsymbol{\sigma}^{\mathrm{A/M}} = \hat{\sigma}\,\boldsymbol{I} + 2\,\hat{\mu}^{\mathrm{A/M}}\,\boldsymbol{\varepsilon}^{\mathrm{A/M}} + \hat{\lambda}^{\mathrm{A/M}}\,\mathrm{tr}\,\boldsymbol{\varepsilon}^{\mathrm{A/M}}\,\boldsymbol{I} \tag{8.47}$$

where $\boldsymbol{\varepsilon}^{\mathrm{A/M}}$ are the strain tensors in the respective phases. They share the property $\boldsymbol{\varepsilon}^{\mathrm{M}} = \boldsymbol{\varepsilon}^{\mathrm{A}} + \boldsymbol{\eta}$ with the transformation strain $\boldsymbol{\eta}$. Mass density is assumed to be constant. Then, the trace of $\boldsymbol{\varepsilon}^{\mathrm{A}}$ is zero and we find $\mathrm{tr}\,\boldsymbol{\varepsilon}^{\mathrm{M}} = \mathrm{tr}\,\boldsymbol{\eta}$ (and additionally $\mathrm{tr}\,\boldsymbol{\eta} > 0$ from experimental observations).

The inner energy $u^{\mathrm{A/M}}$ and entropy $s^{\mathrm{A/M}}$ are given for the respective phases as

$$\begin{aligned} u^{\mathrm{A/M}} &= c^{\mathrm{A/M}}(T - T_{\mathrm{ref}}) + \frac{1}{\varrho}\left(\hat{\sigma}\,\mathrm{tr}\,\boldsymbol{\varepsilon}^{\mathrm{A/M}} + \hat{\mu}^{\mathrm{A/M}}\boldsymbol{\varepsilon}^{\mathrm{A/M}} : \boldsymbol{\varepsilon}^{\mathrm{A/M}} + \frac{1}{2}\hat{\lambda}^{\mathrm{A/M}}(\mathrm{tr}\,\boldsymbol{\varepsilon}^{\mathrm{A/M}})^2\right) \\ &\quad + u_{\mathrm{ref}}^{\mathrm{A/M}} \end{aligned} \tag{8.48}$$

$$s^{\mathrm{A/M}} = c^{\mathrm{A/M}} \log\frac{T}{T_{\mathrm{ref}}} + s_{\mathrm{ref}}^{\mathrm{A/M}} \tag{8.49}$$

with the heat capacities $c^{\mathrm{A/M}}$, reference temperature T_{ref}, and reference values $u_{\mathrm{ref}}^{\mathrm{A/M}}$ and $s_{\mathrm{ref}}^{\mathrm{A/M}}$. From this, the caloric part of the free energy can be identified to be

$$f_{\mathrm{c}}^{\mathrm{A/M}} = c^{\mathrm{A/M}}(T - T_{\mathrm{ref}}) + u_{\mathrm{ref}}^{\mathrm{A/M}} - T\left(c^{\mathrm{A/M}} \log\frac{T}{T_{\mathrm{ref}}} + s_{\mathrm{ref}}^{\mathrm{A/M}}\right) \tag{8.50}$$

where we define $[\![f_{\mathrm{c}}]\!] := f_{\mathrm{c}}^{\mathrm{M}} - f_{\mathrm{c}}^{\mathrm{A}}$.

Mechanical equilibrium, Eq. (8.15), implies for constant mass density that $\boldsymbol{n}\cdot[\![\boldsymbol{\sigma}]\!]_{\mathrm{E}}\cdot\boldsymbol{n}/\varrho = 0$ (second term in Eq. (8.17)). This yields for the remaining first part of Eq. (8.17)

$$\begin{aligned} \varrho[\![f_{\mathrm{c}}]\!] &= \hat{\sigma}(T)\,\mathrm{tr}\,\boldsymbol{\eta} + \hat{\mu}^{\mathrm{M}}\boldsymbol{\varepsilon}^{\mathrm{M}} : \boldsymbol{\varepsilon}^{\mathrm{M}} + \frac{1}{2}\hat{\lambda}^{\mathrm{M}}(\mathrm{tr}\,\boldsymbol{\varepsilon}^{\mathrm{M}})^2 - \hat{\mu}^{\mathrm{A}}\boldsymbol{\varepsilon}^{\mathrm{A}} : \boldsymbol{\varepsilon}^{\mathrm{A}} - \frac{1}{2}\hat{\lambda}^{\mathrm{A}}(\mathrm{tr}\,\boldsymbol{\varepsilon}^{\mathrm{A}})^2 \\ \Rightarrow\quad \hat{\sigma}(T) &= \frac{\varrho[\![f_{\mathrm{c}}]\!] - \hat{\mu}^{\mathrm{M}}\boldsymbol{\varepsilon}^{\mathrm{M}} : \boldsymbol{\varepsilon}^{\mathrm{M}} - \frac{1}{2}\hat{\lambda}^{\mathrm{M}}(\mathrm{tr}\,\boldsymbol{\varepsilon}^{\mathrm{M}})^2 + \hat{\mu}^{\mathrm{A}}\boldsymbol{\varepsilon}^{\mathrm{A}} : \boldsymbol{\varepsilon}^{\mathrm{A}} + \frac{1}{2}\hat{\lambda}^{\mathrm{A}}(\mathrm{tr}\,\boldsymbol{\varepsilon}^{\mathrm{A}})^2}{\mathrm{tr}\,\boldsymbol{\eta}} \end{aligned} \tag{8.51}$$

Assumption that strains have a way smaller dependence on temperature than the caloric energies results in

$$\frac{\mathrm{d}\hat{\sigma}}{\mathrm{d}T} = \frac{\varrho}{\operatorname{tr}\boldsymbol{\eta}} \frac{\mathrm{d}}{\mathrm{d}T}[f_\mathrm{c}] \tag{8.52}$$

where

$$\begin{aligned} \frac{\mathrm{d}}{\mathrm{d}T}[f_\mathrm{c}] &= \frac{\mathrm{d}}{\mathrm{d}T}\left((c^\mathrm{M}-c^\mathrm{A})(T-T_\mathrm{ref}) + (u^\mathrm{M}_\mathrm{ref}-u^\mathrm{A}_\mathrm{ref}) - T(c^\mathrm{M}-c^\mathrm{A})(T-T_\mathrm{ref})\log\frac{T}{T_\mathrm{ref}} - T(s^\mathrm{M}_\mathrm{ref}-s^\mathrm{A}_\mathrm{ref})\right) \\ &= \underbrace{(c^\mathrm{M}-c^\mathrm{A}) - T(c^\mathrm{M}-c^\mathrm{A})\frac{1}{T}}_{=0} \underbrace{-(c^\mathrm{M}-c^\mathrm{A})\log\frac{T}{T_\mathrm{ref}} - (s^\mathrm{M}_\mathrm{ref}-s^\mathrm{A}_\mathrm{ref})}_{=s^\mathrm{A}-s^\mathrm{M}} \quad . \end{aligned} \tag{8.53}$$

Finally, we find

$$\frac{\mathrm{d}\hat{\sigma}}{\mathrm{d}T} = \frac{\varrho}{\operatorname{tr}\boldsymbol{\eta}}\left(s^\mathrm{A}-s^\mathrm{M}\right) \quad . \tag{8.54}$$

A.2 Material model

A.2.1 Expectation values for the elastic constants The expectation values can be calculated according to

$$\mathbb{C}_i = \left[\frac{\pi}{(2\pi)^3}\int_{\varphi=0}^{2\pi}\int_{\nu=0}^{\pi}\int_{\omega=0}^{2\pi} \boldsymbol{Q}_{6\times6}\cdot\left(\mathbb{C}^0_i\right)^{-1}\cdot\boldsymbol{Q}^T_{6\times6}\,\sin\nu\,\mathrm{d}\varphi\,\mathrm{d}\nu\,\mathrm{d}\omega\right]^{-1} , \tag{8.55}$$

[66, 93], where $\boldsymbol{Q}_{6\times6}$ is the representation of $\boldsymbol{Q}$ in the six dimensional space of the Mehrabadi-Cowin notation, [132]. The results are presented in Tab. 8.2.

A.2.2 Constraints for the material model There are two constraints for this material: mass shall be conserved during phase transformation which in terms of the rates of the volume fractions (with respect to the austenitic reference configuration) yields

$$\sum_{i=0}^{n}\dot{\lambda}_i = 0 \, , \tag{8.56}$$

and all volume fractions are supposed to be non-negative, thus

$$\lambda_i \geq 0 \, . \tag{8.57}$$

There are no restrictions on the Euler angles. Let us introduce a Lagrange parameter for the constraint of mass conservation, termed κ, and Kuhn-Tucker parameters for the constraint of non-negativity, called γ_i, with

$$\gamma_i = \begin{cases} 0 & \text{for } \lambda_i > 0 \vee \left(\lambda_i = 0 \wedge \dot{\lambda}_i \geq 0\right) \\ \bar{\gamma}_i > 0 & \text{else} \, . \end{cases} \tag{8.58}$$

The functional $\mathcal{L}$ defined in Eq. (8.1) has to be minimized with respect to the rates of the volume fractions and Euler angles. Hence, the dependence of the free energy ψ on the strains has no influence

and we find

$$\mathcal{L} = \frac{\partial \psi}{\partial \boldsymbol{\lambda}} : \dot{\boldsymbol{\lambda}} + \frac{\partial \psi}{\partial \boldsymbol{\alpha}} \cdot \dot{\boldsymbol{\alpha}} + r_\lambda |\dot{\boldsymbol{\lambda}}| + r_\alpha ||\boldsymbol{\Omega}|| + \kappa \sum_{i=0}^{n} \dot{\lambda}_i - \sum_{i=0}^{n} \gamma_i \dot{\lambda}_i \to \min_{\dot{\boldsymbol{\lambda}}, \dot{\boldsymbol{\alpha}}} \tag{8.59}$$

where we introduced the skew symmetric matrix of angular velocities as $\boldsymbol{\Omega} = \dot{\boldsymbol{Q}} \cdot \boldsymbol{Q}^{-1}$.

A.2.3 Evolution equations In order to obtain the evolution equations for the internal variables, $\boldsymbol{\lambda}$ and $\boldsymbol{\alpha}$, we have to evaluate the stationarity conditions of Eq. (8.59) which are for the rates of volume fractions

$$\frac{\partial \Psi}{\partial \lambda_i} + r_\lambda \frac{\dot{\lambda}_i}{|\dot{\boldsymbol{\lambda}}|} + \kappa - \gamma_i = 0 \,, \tag{8.60}$$

and for the rates of Euler angles

$$\frac{\partial \Psi}{\partial \varphi} + \sqrt{2} r_\alpha \frac{\dot{\varphi} + \dot{\omega} \cos \nu}{||\boldsymbol{\Omega}||} = 0 \,, \tag{8.61}$$

$$\frac{\partial \Psi}{\partial \nu} + \sqrt{2} r_\alpha \frac{\dot{\nu}}{||\boldsymbol{\Omega}||} = 0 \,, \tag{8.62}$$

$$\frac{\partial \Psi}{\partial \omega} + \sqrt{2} r_\alpha \frac{\dot{\omega} + \dot{\varphi} \cos \nu}{||\boldsymbol{\Omega}||} = 0 \,. \tag{8.63}$$

Solving Eqs. (8.61) to (8.63) for the rates yields

$$\dot{\varphi} = \rho_\alpha (p_\varphi - p_\omega \cos \nu) \tag{8.64}$$

$$\dot{\nu} = \rho_\alpha p_\nu (1 - \cos^2 \nu) \tag{8.65}$$

$$\dot{\omega} = \rho_\alpha (p_\omega - p_\varphi \cos \nu) \tag{8.66}$$

with $\rho_\alpha := ||\boldsymbol{\Omega}|| / (\sqrt{2} r_\alpha (1 - \cos^2 \nu))$.

We assumed that the volume fractions as well as the Euler angles evolve in a rate-independent manner. This leads to dissipation terms which are non-differentiable at the origins $\dot{\boldsymbol{\lambda}} = \mathbf{0}$, and $\dot{\boldsymbol{\alpha}} = \mathbf{0}$ respectively. All (hyper-)planes are possible tangents and the Eqs. (8.60) to (8.63) are indeed set-valued: $\mathbf{0} \in \partial \mathcal{L} / \partial \dot{\boldsymbol{\lambda}}$, $\mathbf{0} \in \partial \mathcal{L} / \partial \dot{\boldsymbol{\alpha}}$. For details see e.g. [67, 70].

We take the constraint of positivity into account by application of an active set strategy. For this purpose, let us introduce the passive set $\mathcal{B}$ which collects all volume fractions with a value of zero and vanishing rate. The active set $\mathcal{A}$ is defined as the complement of $\mathcal{B}$. This reads

$$\mathcal{B} = \left\{ i \,|\, \lambda_i = 0 \text{ and } \dot{\lambda}_i = 0 \right\} \,, \tag{8.67}$$

$$\mathcal{A} = \left\{ i \,|\, \lambda_i > 0 \text{ or } \dot{\lambda}_i > 0 \right\} \,. \tag{8.68}$$

Application of this active set strategy allows us to reformulate Eq. (8.60) by summing up over all indices that are part of $\mathcal{A}$ which yields

$$\kappa = -\frac{1}{n_\mathcal{A}} \sum_{k \in \mathcal{A}} \frac{\partial \Psi}{\partial \lambda_k} \,, \tag{8.69}$$

with $n_{\mathcal{A}}$ being the number of active elements in $\mathcal{A}$. Equation (8.60) turns into

$$\begin{cases} p_i^\lambda - \dfrac{1}{n_{\mathcal{A}}} \displaystyle\sum_{k\in\mathcal{A}} p_k^\lambda = r_\lambda \dfrac{\dot\lambda_i}{|\dot{\boldsymbol\lambda}|} & , \quad i \in \mathcal{A} \text{ and } |\dot{\boldsymbol\lambda}| \neq \mathbf{0} \\ p_i^\lambda - \dfrac{1}{n_{\mathcal{A}}} \displaystyle\sum_{k\in\mathcal{A}} p_k^\lambda = -\gamma_i < 0 & , \quad i \notin \mathcal{A} \text{ and } |\dot{\boldsymbol\lambda}| \neq \mathbf{0} \end{cases} \tag{8.70}$$

with $\boldsymbol{p}^\lambda := -\partial\Psi/\partial\boldsymbol{\lambda}$. The expression $p_i^\lambda - 1/n_{\mathcal{A}} \sum_{k\in\mathcal{A}} p_k^\lambda =: \mathrm{dev}_{\mathcal{A}} p_i^\lambda$ is termed *active deviator*. Equations (8.64) to (8.66) and (8.70) constitute a complete system of evolution equations already ($\rho_\lambda := |\dot{\boldsymbol\lambda}|/r_\lambda$). However, for mathematical simplification, we perform a Legendre transformation of the respective dissipation functionals $r_\lambda|\dot{\boldsymbol\lambda}|$ and $r_\alpha\|\boldsymbol\Omega\|$, Eq. (8.59). This results in

$$\mathcal{J}_\lambda = \sup_{\dot\lambda_i\in\mathcal{A}} \left\{\boldsymbol{p}^\lambda \cdot \dot{\boldsymbol\lambda} - r_\lambda\right\} = \sup_{\dot\lambda_i\in\mathcal{A}} \left\{ \frac{|\dot{\boldsymbol\lambda}|}{r_\lambda} \underbrace{\left(\textstyle\sum_{i\in\mathcal{A}} \left(\mathrm{dev}_{\mathcal{A}} p_i^\lambda\right)^2 - r_\lambda^2\right)}_{=:\,\Phi_\lambda(\boldsymbol{p}^\lambda) \le 0} \right\} \tag{8.71}$$

for the rates of the volume fractions, and

$$\begin{aligned} \mathcal{J}_\alpha &= \sup_{\dot{\boldsymbol\alpha}} \left\{ p_\varphi\dot\varphi + p_\nu\dot\nu + p_\omega\dot\omega - \sqrt{2} r_\alpha \left(\dot\varphi^2 + \dot\nu^2 + 2\cos\nu\,\dot\varphi\,\dot\omega + \dot\omega^2\right)^{1/2} \right\} \\ &= \sup_{\dot{\boldsymbol\alpha}} \left\{ \frac{\|\boldsymbol\Omega\|}{\sqrt{2} r_\alpha (1-\cos\nu)} \right. \\ &\qquad \left. \underbrace{\left(p_\varphi^2 + p_\nu^2(1-\cos^2\nu) + p_\omega^2 - 2p_\varphi p_\omega \cos\nu - \sqrt{2} r_\alpha^2 (1-\cos^2\nu)\right)}_{=:\,\Phi_\alpha(\boldsymbol{p}^\alpha) \le 0} \right\} \end{aligned} \tag{8.72}$$

for the rates of the Euler angles, [93]. The two limiting conditions, Φ_λ and Φ_α, may be interpreted as yield functions, indicating whether phase transformation and/or re-orientation takes place.

A.2.4 Driving forces The driving forces remain to be calculated. For the volume fractions they are

$$\begin{aligned} p_i^\lambda = &\left(\boldsymbol{Q}^T \cdot \boldsymbol{\eta}_i \cdot \boldsymbol{Q}\right) : \bar{\mathbb{C}} : \left(\boldsymbol{\varepsilon} - \boldsymbol{Q}^T \cdot \bar{\boldsymbol\eta} \cdot \boldsymbol{Q}\right) \\ &+ \frac{1}{2} \left(\boldsymbol{\varepsilon} - \boldsymbol{Q}^T \cdot \bar{\boldsymbol\eta} \cdot \boldsymbol{Q}\right) : \left[\bar{\mathbb{C}} : (\mathbb{C}_i)^{-1} : \bar{\mathbb{C}}\right] : \left(\boldsymbol{\varepsilon} - \boldsymbol{Q}^T \cdot \bar{\boldsymbol\eta} \cdot \boldsymbol{Q}\right) - \Psi_{i,\mathrm{cal}}(T) \,, \end{aligned} \tag{8.73}$$

see [93], also [71]. The driving forces for the angles are (note that $\Psi = \Psi(\boldsymbol{Q}(\boldsymbol\alpha))$)

$$p_\varphi = -\frac{\partial\Psi}{\partial\varphi} = -\frac{\partial\Psi}{\partial\boldsymbol{Q}} : \frac{\partial\boldsymbol{Q}}{\partial\varphi} \,, \tag{8.74}$$

$$p_\nu = -\frac{\partial\Psi}{\partial\nu} = -\frac{\partial\Psi}{\partial\boldsymbol{Q}} : \frac{\partial\boldsymbol{Q}}{\partial\nu} \,, \tag{8.75}$$

$$p_\omega = -\frac{\partial\Psi}{\partial\omega} = -\frac{\partial\Psi}{\partial\boldsymbol{Q}} : \frac{\partial\boldsymbol{Q}}{\partial\omega} \,. \tag{8.76}$$

The first factor of the expressions above is identical for all forces as

$$-\frac{\partial \Psi}{\partial \boldsymbol{Q}} = 2\left[\bar{\boldsymbol{\eta}} \cdot \boldsymbol{Q} \cdot \bar{\mathbb{C}} : \left(\boldsymbol{\varepsilon} - \boldsymbol{Q}^T \cdot \bar{\boldsymbol{\eta}} \cdot \boldsymbol{Q}\right)\right], \tag{8.77}$$

whereas the second factor $\partial \boldsymbol{Q}/\partial \boldsymbol{\alpha} := (\partial \boldsymbol{Q}/\partial \varphi, \partial \boldsymbol{Q}/\partial \nu, \partial \boldsymbol{Q}/\partial \omega)$ depends on the specific parametrization of $\boldsymbol{Q}$ by Euler angles. We choose

$$\boldsymbol{Q}(\boldsymbol{\alpha}) = \begin{pmatrix} \cos\varphi\cos\omega - \cos\nu\sin\varphi\sin\omega & -\cos\nu\cos\omega\sin\varphi - \cos\varphi\sin\omega & \sin\nu\sin\varphi \\ \cos\omega\sin\varphi + \cos\nu\cos\varphi\sin\omega & \cos\nu\cos\varphi\cos\omega - \sin\varphi\sin\omega & -\cos\varphi\sin\nu \\ \sin\nu\sin\omega & \cos\omega\sin\nu & \cos\nu \end{pmatrix} \tag{8.78}$$

giving

$$\frac{\partial \boldsymbol{Q}}{\partial \varphi} = \begin{pmatrix} -\cos\omega\sin\varphi - \cos\nu\cos\varphi\sin\omega & -\cos\nu\cos\varphi\cos\omega + \sin\varphi\sin\omega & \cos\varphi\sin\nu \\ \cos\varphi\cos\omega - \cos\nu\sin\varphi\sin\omega & -\cos\nu\cos\omega\sin\varphi - \cos\varphi\sin\omega & \sin\nu\sin\varphi \\ 0 & 0 & 0 \end{pmatrix},$$

$$\frac{\partial \boldsymbol{Q}}{\partial \nu} = \begin{pmatrix} \sin\nu\sin\varphi\sin\omega & \cos\omega\sin\nu\sin\varphi & \cos\nu\sin\varphi \\ -\cos\varphi\sin\nu\sin\omega & -\cos\varphi\cos\omega\sin\nu & -\cos\nu\cos\varphi \\ \cos\nu\sin\omega & \cos\nu\cos\omega & -\sin\nu \end{pmatrix},$$

$$\frac{\partial \boldsymbol{Q}}{\partial \omega} = \begin{pmatrix} -\cos\nu\cos\omega\sin\varphi - \cos\varphi\sin\omega & -\cos\varphi\cos\omega + \cos\nu\sin\varphi\sin\omega & 0 \\ \cos\nu\cos\varphi\cos\omega - \sin\varphi\sin\omega & -\cos\omega\sin\varphi - \cos\nu\cos\varphi\sin\omega & 0 \\ \cos\omega\sin\nu & -\sin\nu\sin\omega & 0 \end{pmatrix}.$$

Table 8.1: Transformation strains for cubic to monoclinic transforming NiTi after [194]. $\bar{\alpha} = 0.02381$, $\bar{\beta} = -0.02480$, $\bar{\delta} = 0.07528$, $\bar{\epsilon} = 0.04969$. The factor ξ takes the model behavior into account: the martensitic strain orientation function evolves in a way that finally the transformation strain of single crystals in the optimal way are present. However, this is not in agreement with experiments which prove that polycrystals –which are supposed to be simulated here– possess far lower transformation strains than [110] single crystals (see [52]). Therefore, the factor ξ is set to 0.52 in order to capture this effect.

$$\boldsymbol{\eta}_1 = \xi \begin{pmatrix} \bar{\alpha} & \bar{\delta} & \bar{\epsilon} \\ \bar{\delta} & \bar{\alpha} & \bar{\epsilon} \\ \bar{\epsilon} & \bar{\epsilon} & \bar{\beta} \end{pmatrix} \quad \boldsymbol{\eta}_2 = \xi \begin{pmatrix} \bar{\alpha} & \bar{\delta} & -\bar{\epsilon} \\ \bar{\delta} & \bar{\alpha} & -\bar{\epsilon} \\ -\bar{\epsilon} & -\bar{\epsilon} & \bar{\beta} \end{pmatrix} \quad \boldsymbol{\eta}_3 = \xi \begin{pmatrix} \bar{\alpha} & -\bar{\delta} & -\bar{\epsilon} \\ -\bar{\delta} & \bar{\alpha} & \bar{\epsilon} \\ -\bar{\epsilon} & \bar{\epsilon} & \bar{\beta} \end{pmatrix}$$

$$\boldsymbol{\eta}_4 = \xi \begin{pmatrix} \bar{\alpha} & -\bar{\delta} & \bar{\epsilon} \\ -\bar{\delta} & \bar{\alpha} & -\bar{\epsilon} \\ \bar{\epsilon} & -\bar{\epsilon} & \bar{\beta} \end{pmatrix} \quad \boldsymbol{\eta}_5 = \xi \begin{pmatrix} \bar{\alpha} & \bar{\epsilon} & \bar{\delta} \\ \bar{\epsilon} & \bar{\beta} & \bar{\epsilon} \\ \bar{\delta} & \bar{\epsilon} & \bar{\alpha} \end{pmatrix} \quad \boldsymbol{\eta}_6 = \xi \begin{pmatrix} \bar{\alpha} & -\bar{\epsilon} & \bar{\delta} \\ -\bar{\epsilon} & \bar{\beta} & -\bar{\epsilon} \\ \bar{\delta} & -\bar{\epsilon} & \bar{\alpha} \end{pmatrix}$$

$$\boldsymbol{\eta}_7 = \xi \begin{pmatrix} \bar{\alpha} & -\bar{\epsilon} & -\bar{\delta} \\ -\bar{\epsilon} & \bar{\beta} & \bar{\epsilon} \\ -\bar{\delta} & \bar{\epsilon} & \bar{\alpha} \end{pmatrix} \quad \boldsymbol{\eta}_8 = \xi \begin{pmatrix} \bar{\alpha} & \bar{\epsilon} & -\bar{\delta} \\ \bar{\epsilon} & \bar{\beta} & -\bar{\epsilon} \\ -\bar{\delta} & -\bar{\epsilon} & \bar{\alpha} \end{pmatrix} \quad \boldsymbol{\eta}_9 = \xi \begin{pmatrix} \bar{\beta} & \bar{\epsilon} & \bar{\epsilon} \\ \bar{\epsilon} & \bar{\alpha} & \bar{\delta} \\ \bar{\epsilon} & \bar{\delta} & \bar{\alpha} \end{pmatrix}$$

$$\boldsymbol{\eta}_{10} = \xi \begin{pmatrix} \bar{\beta} & -\bar{\epsilon} & -\bar{\epsilon} \\ -\bar{\epsilon} & \bar{\alpha} & \bar{\delta} \\ -\bar{\epsilon} & \bar{\delta} & \bar{\alpha} \end{pmatrix} \quad \boldsymbol{\eta}_{11} = \xi \begin{pmatrix} \bar{\beta} & -\bar{\epsilon} & \bar{\epsilon} \\ -\bar{\epsilon} & \bar{\alpha} & -\bar{\delta} \\ \bar{\epsilon} & -\bar{\delta} & \bar{\alpha} \end{pmatrix} \quad \boldsymbol{\eta}_{12} = \xi \begin{pmatrix} \bar{\beta} & \bar{\epsilon} & -\bar{\epsilon} \\ \bar{\epsilon} & \bar{\alpha} & -\bar{\delta} \\ -\bar{\epsilon} & -\bar{\delta} & \bar{\alpha} \end{pmatrix}$$

Table 8.2: Expectation values for the elastic constants of austenite and martensite in NiTi calculated from the anisotropic data from [151] and [194].

$$\mathbb{C}_0^{\mathrm{NiTi}} = \begin{pmatrix} 149.36 & 105.32 & 105.32 & 0 & 0 & 0 \\ 105.32 & 149.36 & 105.32 & 0 & 0 & 0 \\ 105.32 & 105.32 & 149.36 & 0 & 0 & 0 \\ 0 & 0 & 0 & 44.04 & 0 & 0 \\ 0 & 0 & 0 & 0 & 44.04 & 0 \\ 0 & 0 & 0 & 0 & 0 & 44.04 \end{pmatrix} \text{GPa}$$

$$\mathbb{C}_{i>0}^{\mathrm{NiTi}} = \begin{pmatrix} 205.05 & 120.78 & 120.78 & 0 & 0 & 0 \\ 120.78 & 205.05 & 120.78 & 0 & 0 & 0 \\ 120.78 & 120.78 & 205.05 & 0 & 0 & 0 \\ 0 & 0 & 0 & 84.28 & 0 & 0 \\ 0 & 0 & 0 & 0 & 84.28 & 0 \\ 0 & 0 & 0 & 0 & 0 & 84.28 \end{pmatrix} \text{GPa}$$

Table 8.3: Some characteristic transformation parameters for a binary NiTi alloy. M_f, M_s, A_s, A_f, M_p and A_p denote the phase transformation temperatures of the DSC experiment, $[q]$ is the latent heat under and above the DSC peak. T_e, $[u]_\mathrm{harm}$ and $[s]_\mathrm{harm}$ are the equilibrium temperature and the entropy and enthalpy constants, respectively. The dissipation parameters are r_λ and r_α, ρ_0 is the material's density.

M_f	235 K	M_s	257 K
A_s	264 K	A_f	284 K
M_p	246 K	A_p	274 K
T_e	260 K	$[q]$	20 J/g
$[u]_\mathrm{harm}$	0.129 GPa	$[s]_\mathrm{harm}$	0.000496 GPa/K
r_λ	0.0065 GPa	r_α	0.0085 GPa
ϱ_0	6450 kg/m^3		

9 Model reduction, calibration formulas, and advanced industrial simulations

Published as: *P. Junker*: An accurate, fast and stable material model for shape memory alloys, *Smart Mater. Struct.* **23 (11): 115010 (2014)**

Shape memory alloys possess several features that make them interesting for industrial applications. However, due to their complex and thermo-mechanically coupled behavior, direct use of shape memory alloys in engineering construction is problematic. There is thus a demand for tools to achieve realistic, *predictive* simulations that are numerically robust when computing complex, coupled load states, are fast enough to calculate geometries of industrial interest, and yield realistic and reliable results without the use of fitting curves.

In this paper a new and numerically fast material model for shape memory alloys is presented. It is based solely on energetic quantities, which thus creates a quite universal approach. In the beginning, a short derivation is given before it is demonstrated how this model can be easily calibrated by means of tension tests. Then, several examples of engineering applications under mechanical and thermal loads are presented to demonstrate the numerical stability and high computation speed of the model.

9.1 Introduction

Shape memory alloys are a class of materials with high potential for industrial applications. Depending on the specific alloy composition, construction components may deform reversibly by up to 8 % at relatively high temperatures, whereas they seem to be permanently deformed at lower temperatures. However, this apparently permanent deformation is restored when the specimen is heated and subsequently cooled. This deformation-heating-cooling process, in which the material behaves pseudoplastically, is referred to as the one-way effect and these materials are thus known as shape *memory* alloys. The first behavior described is termed pseudoelasticity.

Both material reactions occur because the microstructural state evolves during loading (mechanical and thermal). At high temperatures, shape memory alloys develop an austenite crystal lattice, which is cubic and thus highly symmetric. At low temperatures, a different crystal configuration evolves due to shearing and shuffling, which is termed martensite. Obviously, this deformation state is not uniquely defined so that different martensitic variants may be present. In contrast to other metallic materials that may form the crystal lattices of austenite and martensite, shape memory alloys transform from austenite to martensite, and vice versa, also during mechanical loading.

Both, pseudoelasticity and pseudoplasticity are dissipative processes: stress for forward and backward transformation are not equal and consequently a hysteresis is observed in stress/strain/temperature diagrams. Furthermore, the transformation stresses are not constant, but depend on temperature. Transformation stresses increase at higher temperatures. If pseudoplastic behavior is present due to a low ambient temperature, further cooling does not change the transformation stresses any more. Detailed information about shape memory alloys can be found e.g. in [152, 19, 151], or [112].

Due to their different properties, shape memory alloys are interesting for industrial applications.

However, not only do they behave very non-linearly, but the coupling effect of mechanical and thermal loads also has a major influence on the resulting material behavior. This makes direct use of shape memory alloys for industrial products problematic. One way to overcome this is to use material models that can be evaluated in an appropriate numerical framework, for example using the finite element method (FEM), which enables the non-linear and thermo-mechanically coupled material behavior to be investigated, even for complex geometries used in engineering construction. This lowers costs by reducing the amount of prototyping (experiments), and construction components can be numerically optimized and adapted to individual requirements.

Numerical investigations require material models for shape memory alloys, a variety of which already exists. These models are sometimes grouped into phenomenological and micromechanical ones. Phenomenological models are described to focus mainly on calculation of a prescribed stress/strain "curve" without taking the physical processes directly into account. This makes these models numerically very fast, particularly if appropriate numerical schemes are applied, [173]; however, their drawback is that they require a lot of experimental data to calculate the corresponding material behavior for different geometries and loads. Furthermore, these models are sometimes not as stable as desired, which is obviously problematic if complex construction components are to be computed. On the other hand, micromechanical models are based on the physical processes that evolve during phase transformations and try to display these. They have a more universal applicability. Unfortunately, these models need usually high computational effort, which also makes them problematic for industrial use.

A completely clear and commonly accepted classification of a model to be phenomenological or micromechanical is quite difficult. The transition between phenomenological and micromechanical models, instead, is rather smooth. For example, in the early model of Brinson, [25], the evolution of martensite was directly assumed by a phenomenological ansatz. Also the model of Boyd and Lagoudas, [23] and later [115], belongs rather to the phenomenological ones although their model was one of the first models using a postulated free energy function and dissipation. Another very famous model for shape memory alloys is the one by Auricchio and Taylor, [8], which shares some similarities with the modeling of plasticity. In a comparable manner to Boyd and Lagoudas, Bouvet *et al.* derived their model in 2004, [22].

In this overview, material models with reduced assumptions for the driving forces are referred to as micromechanical ones. In this vein, the model of Govindjee and Hall is the first one mentioned. They proposed a model based on probability concepts, [58]. In [71], a model for shape memory alloys using the principle of the dissipation potential was presented, which was extended to polycrystals in [70] and implemented into finite elements in [97]. In contrast to the first two research groups mentioned, the latter three works share the property that the driving force for phase transformations can be directly derived from the Helmholtz free energy. A more complex hull for the energy of shape memory alloys is given in [12], whereas a comparable and numerically robust approach also in the context of finite deformations was presented in [178]. The classification presented in this work is not unique: there are models acting on a smaller scale, such as e.g. [155, 156], and thus include much more micromechanical information than material point models which are discussed here. In such a context, a re-classification would be necessary. Hence, for all applications it is necessary to make a clear decission about the scale investgiated and the properties a model should possess.

Aiming to lessen the dilemma between phenomenological and micromechanical models, a new energy-based material model for shape memory alloys that reduces both drawbacks is presented in this work: it is very fast and also numerically stable so that complex geometries with challenging loading states

can be calculated easily. The model also has the advantage of being applicable in a quite universal sense due to its energetic character: if all quantities are determined in terms of energies, which are naturally orientation-independent, then orientation-dependent loading states can be predictively computed when the model is calibrated to one orientation-dependent load case, e.g. to a tension test.

The model presented in this paper is based on previous works in [71], [70] and [97]. An improved model was published in [93], in which a new approach to an orientation distribution function was proposed that results in a huge reduction of the necessary calculation time. In [102], it was shown that the model is able to predict mechanical behavior of shape memory alloys after it has been calibrated to thermal digital scattering calometry tests (DSC tests). Since all model parameters can be derived from physically well-identified quantities, for example latent heat and caloric energies, it was proven empirically that the model is quite parameter-free. A similar model that takes account of full thermo-mechanical coupling was presented in [98].

In this work a further progress is presented: an additional model reduction provides drastic decrease in the numerical effort even compared to the previous work in [93]. Additionally, the new model is derived in an elasto-viscoplastic manner that is numerically stable for all possible loading conditions and numerical discretization, such as step size for instance. Compared to the rate-independent evolution equations used in the previous works, which require to find a root of an associated yield function, rate-dependent evolution equations may be integrated in time directly without encountering complex numerical treatments (see e.g. one of the most important works on the differences of evolution equations given by Simo and Hughes, [169]; they explain the differences in the respective numerical treatment in a very detailed way.) Finally, simple formulas are presented to derive the model parameters from easily performed tension tests. To this end, these three aspects of the novel model presented here increase the applicability in industrial situations. For conclusion, several numerical results for complex loading states (mechanical and thermal) applied to industrially relevant geometries are provided.

9.2 Material model

The material model is based on the principle of the minimum of the dissipation potential. Details of this modeling technique can be found in [30, 67, 123, 138, 137, 146] and [147]. An extension to the principle of the minimum of the dissipation potential for non-isothermal processes is given in [103], which presents a generalized heat conduction equation. The key idea of this principle, which belongs to the so-called variational concepts, is formulation of the model solely in terms of energies using a mathematical potential. This means that constraints can be taken into account very easily. In the case of shape memory alloys for which the reduced material model is derived, the principle reads [93]

$$\mathcal{L} = \dot{\Psi} + \mathcal{D} + \text{cons} \rightarrow \min_{\dot{\boldsymbol{\lambda}}, \dot{\boldsymbol{\alpha}}} \tag{9.1}$$

where Ψ is the Helmholtz free energy, $\mathcal{D}$ is the dissipation functional for which an appropriate approach has to be made, and cons are constraints for mass conservation and positivity. The Langrangean $\mathcal{L}$ is minimized with respect to the rates of the internal variables volume fractions $\dot{\boldsymbol{\lambda}}$ and Euler angles $\dot{\boldsymbol{\alpha}}$. The volume fractions are collected in a vector $\boldsymbol{\lambda}$ that contains the austenite phase λ_0 and one martensitic variant in each Cartesian direction $\lambda_1, \lambda_2, \lambda_3$. Of course, the tetragonal transformation structure does not hold for all shape memory alloys, for example CuAlNi or NiTi. However, by

considering only that (simple) kind of transformation kinematic, the different martensitic twins are averaged in advance that may evolve in shape memory alloys with more complex transformation kinematics. As will be shown later, for simulation of construction components this homogenized approximation has no remarkable influence on the global material reaction. The three Euler angles are comprised to $\boldsymbol{\alpha} = \{\varphi, \vartheta, \omega\}$. A formula for the Helmholtz energy is given as [93]

$$\Psi(\boldsymbol{\varepsilon}, \boldsymbol{\lambda}, \boldsymbol{\alpha}, \theta) = \frac{1}{2}\left(\boldsymbol{\varepsilon} - \boldsymbol{Q}^T \cdot \bar{\boldsymbol{\eta}} \cdot \boldsymbol{Q}\right) : \bar{\mathbb{C}} : \left(\boldsymbol{\varepsilon} - \boldsymbol{Q}^T \cdot \bar{\boldsymbol{\eta}} \cdot \boldsymbol{Q}\right) + \bar{c}(\theta) \tag{9.2}$$

with a rotation matrix $\boldsymbol{Q} = \boldsymbol{Q}(\boldsymbol{\alpha})$ and the effective quantities for transformation strain, elastic constants, and caloric energy, respectively

$$\bar{\boldsymbol{\eta}} = \sum_{i=0}^{3} \lambda_i \, \boldsymbol{\eta}_i \,, \qquad \bar{\mathbb{C}} = \left[\sum_{i=0}^{3} \lambda_i \, (\mathbb{C}_i)^{-1}\right]^{-1} \,, \qquad \bar{c}(\theta) = \sum_{i=0}^{3} \lambda_i \, c_i(\theta) \tag{9.3}$$

where θ is the absolute temperature. The choice for the dissipation functional $\mathcal{D}$ basically determines the form of the resulting evolution equations for the internal variables. In contrast to previous studies, now a different approach for the dissipation functional is used. In particular, the aim is to find rate-dependent evolution equations for the Euler angles and equations that are of an elasto-viscoplastic type for the volume fractions. Therefore, one may define

$$\begin{aligned} \mathcal{D} &:= r_1 |\dot{\boldsymbol{\lambda}}| + \frac{r_2}{2} |\dot{\boldsymbol{\lambda}}|^2 + \frac{r_\alpha}{2(1 - \cos^2 \vartheta)} \|\boldsymbol{\Omega}\|^2 \\ &= r_1 |\dot{\boldsymbol{\lambda}}| + \frac{r_2}{2} |\dot{\boldsymbol{\lambda}}|^2 + \sqrt{2} \, \frac{r_\alpha}{2(1 - \cos^2 \vartheta)} \left(\dot{\varphi}^2 + \dot{\vartheta}^2 + 2\dot{\varphi}\,\dot{\omega} \, \cos\vartheta + \dot{\omega}^2\right) \end{aligned} \tag{9.4}$$

in which the skew-symmetric matrix of angular velocities denoted by $\boldsymbol{\Omega}$ is used in order to fulfill objectivity. The arbitrary factor $1/(1 - \cos^2 \vartheta)$ simplifies the following equations.

The constraints for mass conservation, $\sum_{i=0}^{3} \dot{\lambda}_i = 0$, and positivity, $\lambda_i \geq 0 \; \forall \, i$, are taken into account by the Lagrange parameter β and the Kuhn-Tucker parameters γ_i, which are collected in $\boldsymbol{\gamma} = \gamma_i \, \boldsymbol{e}_i$. There are no constraints that act on the Euler angles. Consequently, one finds for the Lagrangean $\mathcal{L}$ in (9.1)

$$\begin{aligned} \mathcal{L} &= \frac{\partial \Psi}{\partial \boldsymbol{\lambda}} \cdot \dot{\boldsymbol{\lambda}} + \frac{\partial \Psi}{\partial \boldsymbol{\alpha}} \cdot \dot{\boldsymbol{\alpha}} \\ &\quad + r_1 |\dot{\boldsymbol{\lambda}}| + \frac{r_2}{2} |\dot{\boldsymbol{\lambda}}|^2 + \sqrt{2} \, \frac{r_\alpha}{2(1 - \cos^2 \vartheta)} \left(\dot{\varphi}^2 + \dot{\vartheta}^2 + 2\dot{\varphi}\,\dot{\omega} \, \cos\vartheta + \dot{\omega}^2\right) \\ &\quad + \beta \sum_{i=0}^{3} \dot{\lambda}_i - \boldsymbol{\gamma} \cdot \dot{\boldsymbol{\lambda}} \to \min_{\boldsymbol{\lambda}, \boldsymbol{\alpha}} \end{aligned} \tag{9.5}$$

in which the derivatives of Ψ with respect to strains and temperature have been dropped, because they are constants during minimizations for $\dot{\boldsymbol{\lambda}}$ and $\dot{\boldsymbol{\alpha}}$. The necessary conditions for minimizing $\mathcal{L}$ are

$\partial\mathcal{L}/\partial\dot{\boldsymbol{\lambda}} = \mathbf{0}$ and $\partial\mathcal{L}/\partial\dot{\boldsymbol{\alpha}} = \mathbf{0}$ and read

$$\frac{\partial\mathcal{L}}{\partial\dot{\boldsymbol{\lambda}}} = \frac{\partial\Psi}{\partial\boldsymbol{\lambda}} + r_1 \underbrace{\frac{\dot{\boldsymbol{\lambda}}}{|\dot{\boldsymbol{\lambda}}|}}_{=:\,\operatorname{sgn}\dot{\boldsymbol{\lambda}}} + r_2\,\dot{\boldsymbol{\lambda}} + \boldsymbol{\beta} - \boldsymbol{\gamma} \ni \mathbf{0} \tag{9.6}$$

$$\frac{\partial\mathcal{L}}{\partial\dot{\varphi}} = \frac{\partial\Psi}{\partial\varphi} + \sqrt{2}\,\frac{r_\alpha}{1-\cos^2\vartheta}\left(\dot{\varphi} + \dot{\omega}\cos\vartheta\right) = 0 \tag{9.7}$$

$$\frac{\partial\mathcal{L}}{\partial\dot{\vartheta}} = \frac{\partial\Psi}{\partial\vartheta} + \sqrt{2}\,\frac{r_\alpha}{1-\cos^2\vartheta}\,\dot{\vartheta} = 0 \tag{9.8}$$

$$\frac{\partial\mathcal{L}}{\partial\dot{\omega}} = \frac{\partial\Psi}{\partial\omega} + \sqrt{2}\,\frac{r_\alpha}{1-\cos^2\vartheta}\left(\dot{\omega} + \dot{\varphi}\cos\vartheta\right) = 0 \tag{9.9}$$

where $\boldsymbol{\beta} = \beta\,\mathbf{1}$. Equations (9.7,9.8,9.9) can be solved for the rates of the three Euler angles which yields the evolution equations

$$\dot{\varphi} = \frac{1}{\sqrt{2}\,r_\alpha}\left(p_\varphi - p_\omega\cos\vartheta\right) \tag{9.10}$$

$$\dot{\vartheta} = \frac{1}{\sqrt{2}\,r_\alpha}\,p_\vartheta\left(1-\cos^2\vartheta\right) \tag{9.11}$$

$$\dot{\omega} = \frac{1}{\sqrt{2}\,r_\alpha}\left(p_\omega - p_\varphi\cos\vartheta\right) \tag{9.12}$$

defining the driving forces $p_\varphi := -\partial\Psi/\partial\varphi$, $p_\vartheta := -\partial\Psi/\partial\vartheta$, and $p_\omega := -\partial\Psi/\partial\omega$. In accordance with previous studies [70, 93], it is convenient to use an active set strategy for fulfillment of the positivity by introducing

$$\mathcal{A} = \{i|\lambda_i \neq 0\} \cup \left\{i|\lambda_i = 0 \wedge \dot{\lambda}_i > 0\right\} \tag{9.13}$$

Summation of elements in (9.6) that are in the active set $\mathcal{A}$ yields

$$\beta = \frac{1}{n_\mathcal{A}} \sum_{k\in\mathcal{A}} p_{\lambda,k} \tag{9.14}$$

with the number of active phases $n_\mathcal{A}$ and the driving forces for the volume fractions $p_{\lambda,k} := -\partial\Psi/\partial\lambda_k$. Inserting β into (9.6) allows to define the active deviator as

$$\operatorname{dev}_\mathcal{A} p_{\lambda,i} := p_{\lambda,i} - \frac{1}{n_\mathcal{A}} \sum_{k\in\mathcal{A}} p_{\lambda,k} \tag{9.15}$$

Equation (9.6) remains complicated to solve for the rates of the volume fractions. Therefore, the Clausius-Duheme inequality is used, [34], which follows from the second law of thermodynamics. This gives

$$\hat{\mathcal{D}} = \theta\dot{s} = \boldsymbol{\sigma} : \dot{\boldsymbol{\varepsilon}} - \dot{\Psi} - s\dot{\theta} - \frac{1}{\theta}\boldsymbol{q}\cdot\nabla\theta \geq 0 \;\Big|\; \text{cons} \tag{9.16}$$

where $\hat{\mathcal{D}}$ is the dissipation, s is the entropy, $\boldsymbol{\sigma}$ is the stress, and $\boldsymbol{q}$ is the vector of heat flux. From this inequality, the constitutive equations for stress and entropy are derived, as well as the direction of heat flux. In the present case, in which internal variables are also used, (9.16) reduces to

$$\dot{\boldsymbol{\lambda}}\cdot\operatorname{dev}_\mathcal{A}\boldsymbol{p}_\lambda + \dot{\boldsymbol{\alpha}}\cdot\boldsymbol{p}_\alpha \geq 0 \tag{9.17}$$

Volume fractions and Euler angles may evolve independently at first glance. Thus, positivity of

dissipation in (9.17) demands

$$\dot{\boldsymbol{\lambda}} \cdot \operatorname{dev}_{\mathcal{A}} \boldsymbol{p}_{\lambda} \geq 0 \tag{9.18}$$

or equivalently

$$|\dot{\boldsymbol{\lambda}}|\,|\operatorname{dev}_{\mathcal{A}} \boldsymbol{p}_{\lambda}|\,\frac{\dot{\boldsymbol{\lambda}}}{|\dot{\boldsymbol{\lambda}}|} \cdot \frac{\operatorname{dev}_{\mathcal{A}} \boldsymbol{p}_{\lambda}}{|\operatorname{dev}_{\mathcal{A}} \boldsymbol{p}_{\lambda}|} \geq 0 \tag{9.19}$$

from which finally follows

$$\operatorname{sgn} \dot{\boldsymbol{\lambda}} = \operatorname{sgn} \left(\operatorname{dev}_{\mathcal{A}} \boldsymbol{p}_{\lambda} \right) \tag{9.20}$$

This result is used to simplify (9.6) to

$$\dot{\boldsymbol{\lambda}} = \frac{1}{r_2} \left(\operatorname{dev}_{\mathcal{A}} \boldsymbol{p}_{\lambda} - r_1 \operatorname{sgn} \left(\operatorname{dev}_{\mathcal{A}} \boldsymbol{p}_{\lambda} \right) \right) \tag{9.21}$$

Equation (9.21) remains rather unwieldy. Therefore, it is convenient to perform a Legendre transformation of the part of the dissipation functional that depends on $\dot{\boldsymbol{\lambda}}$. This gives

$$\begin{aligned}
\mathcal{D}_{\lambda}^{\star} &= \sup_{\dot{\boldsymbol{\lambda}}} \left\{ \dot{\boldsymbol{\lambda}} \cdot \operatorname{dev}_{\mathcal{A}} \boldsymbol{p}_{\lambda} - \mathcal{D}_{\dot{\lambda}} \right\} \\
&= \sup_{\dot{\boldsymbol{\lambda}}} \left\{ \dot{\boldsymbol{\lambda}} \cdot \operatorname{dev}_{\mathcal{A}} \boldsymbol{p}_{\lambda} - r_1 |\dot{\boldsymbol{\lambda}}| - \frac{r_2}{2} |\dot{\boldsymbol{\lambda}}|^2 \right\} \\
&= \sup_{\dot{\boldsymbol{\lambda}}} \left\{ \frac{|\dot{\boldsymbol{\lambda}}|}{r_1} \left(\frac{r_1}{|\dot{\boldsymbol{\lambda}}|} \dot{\boldsymbol{\lambda}} \cdot \operatorname{dev}_{\mathcal{A}} \boldsymbol{p}_{\lambda} - r_1^2 \right) - \frac{r_2}{2} |\dot{\boldsymbol{\lambda}}|^2 \right\} \\
&= \sup_{\dot{\boldsymbol{\lambda}}} \left\{ \underbrace{\frac{|\dot{\boldsymbol{\lambda}}|}{r_1}}_{>0} \underbrace{\left(|\operatorname{dev}_{\mathcal{A}} \boldsymbol{p}_{\lambda}|^2 - r_1^2 \right)}_{=: \Phi \leq 0} \underbrace{- \frac{|\dot{\boldsymbol{\lambda}}|}{r_1} r_2 \underbrace{\dot{\boldsymbol{\lambda}} \cdot \operatorname{dev}_{\mathcal{A}} \boldsymbol{p}_{\lambda}}_{\geq 0}}_{<0} \underbrace{- \frac{r_2}{2} |\dot{\boldsymbol{\lambda}}|^2}_{\leq 0} \right\}
\end{aligned} \tag{9.22}$$

in which (9.21) and (9.6) have been inserted. In order to bound the supremum, the expression Φ has to be less than or equal to zero. Consequently, it may be identified as an indicator function that separates the transforming and non-transforming regimes. The roots of Φ remain unchanged by redefining

$$\Phi := |\operatorname{dev}_{\mathcal{A}} \boldsymbol{p}_{\lambda}| - r_1 \tag{9.23}$$

Comparison of (9.23) and (9.21) yields the final evolution equation for the volume fractions

$$\dot{\boldsymbol{\lambda}} = \frac{1}{r_2} \left(|\operatorname{dev}_{\mathcal{A}} \boldsymbol{p}_{\lambda}| - r_1 \right)_{+} \operatorname{sgn} \left(\operatorname{dev}_{\mathcal{A}} \boldsymbol{p}_{\lambda} \right) \tag{9.24}$$

The direction of evolution is determined by the signum of the active deviator, whereas the length of the rate vector is defined by the positive deviation from the yield surface quantified by r_1. The factor r_2 can thus be identified as the viscous parameter that defines the velocity of volume change.

It remains to calculate the driving forces. For the volume fractions, these are

$$\begin{aligned}
p_{\lambda,i} = -\frac{\partial \Psi}{\partial \lambda_i} &= \left(\boldsymbol{Q}^T \cdot \boldsymbol{\eta}_i \cdot \boldsymbol{Q} \right) : \bar{\mathbb{C}} : \left(\boldsymbol{\varepsilon} - \boldsymbol{Q}^T \cdot \bar{\boldsymbol{\eta}} \cdot \boldsymbol{Q} \right) \\
&\quad + \frac{1}{2} \left(\boldsymbol{\varepsilon} - \boldsymbol{Q}^T \cdot \bar{\boldsymbol{\eta}} \cdot \boldsymbol{Q} \right) : \left[\bar{\mathbb{C}} : (\mathbb{C}_i)^{-1} : \bar{\mathbb{C}} \right] : \left(\boldsymbol{\varepsilon} - \boldsymbol{Q}^T \cdot \bar{\boldsymbol{\eta}} \cdot \boldsymbol{Q} \right) \\
&\quad - c_i(\theta)
\end{aligned} \tag{9.25}$$

For the Euler angles, one rotation matrix has to be chosen first because there are different variants to define orthonormal matrices. In analogy to [93], it is chosen as

$$\boldsymbol{Q}(\boldsymbol{\alpha}) = \begin{pmatrix} \cos\varphi\cos\omega - \cos\vartheta\sin\varphi\sin\omega & -\cos\vartheta\cos\omega\sin\varphi - \cos\varphi\sin\omega & \sin\vartheta\sin\varphi \\ \cos\omega\sin\varphi + \cos\vartheta\cos\varphi\sin\omega & \cos\vartheta\cos\varphi\cos\omega - \sin\varphi\sin\omega & -\cos\varphi\sin\vartheta \\ \sin\vartheta\sin\omega & \cos\omega\sin\vartheta & \cos\vartheta \end{pmatrix} \tag{9.26}$$

The driving forces for the Euler angles are thus derived as

$$p_\varphi = -\frac{\partial\Psi}{\partial\varphi} = -\frac{\partial\Psi}{\partial\boldsymbol{Q}} : \frac{\partial\boldsymbol{Q}}{\partial\varphi} \tag{9.27}$$

$$p_\vartheta = -\frac{\partial\Psi}{\partial\vartheta} = -\frac{\partial\Psi}{\partial\boldsymbol{Q}} : \frac{\partial\boldsymbol{Q}}{\partial\vartheta} \tag{9.28}$$

$$p_\omega = -\frac{\partial\Psi}{\partial\omega} = -\frac{\partial\Psi}{\partial\boldsymbol{Q}} : \frac{\partial\boldsymbol{Q}}{\partial\omega} \tag{9.29}$$

The first part of the driving forces is identical for all angles and yields

$$-\frac{\partial\Psi}{\partial\boldsymbol{Q}} = 2\left[\bar{\boldsymbol{\eta}}\cdot\boldsymbol{Q}\cdot\bar{\mathbb{C}} : \left(\boldsymbol{\varepsilon} - \boldsymbol{Q}^T\cdot\bar{\boldsymbol{\eta}}\cdot\boldsymbol{Q}\right)\right] \tag{9.30}$$

The entries for $\partial\boldsymbol{Q}/\partial\boldsymbol{\alpha} = (\partial\boldsymbol{Q}/\partial\varphi, \partial\boldsymbol{Q}/\partial\vartheta, \partial\boldsymbol{Q}/\partial\omega)$ depend on the choice of $\boldsymbol{Q}$ and follow from (9.26) as

$$\frac{\partial\boldsymbol{Q}}{\partial\varphi} = \begin{pmatrix} -\cos\omega\sin\varphi - \cos\vartheta\cos\varphi\sin\omega & -\cos\vartheta\cos\varphi\cos\omega + \sin\varphi\sin\omega & \cos\varphi\sin\vartheta \\ \cos\varphi\cos\omega - \cos\vartheta\sin\varphi\sin\omega & -\cos\vartheta\cos\omega\sin\varphi - \cos\varphi\sin\omega & \sin\vartheta\sin\varphi \\ 0 & 0 & 0 \end{pmatrix} \tag{9.31}$$

$$\frac{\partial\boldsymbol{Q}}{\partial\vartheta} = \begin{pmatrix} \sin\vartheta\sin\varphi\sin\omega & \cos\omega\sin\vartheta\sin\varphi & \cos\vartheta\sin\varphi \\ -\cos\varphi\sin\vartheta\sin\omega & -\cos\varphi\cos\omega\sin\vartheta & -\cos\vartheta\cos\varphi \\ \cos\vartheta\sin\omega & \cos\vartheta\cos\omega & -\sin\vartheta \end{pmatrix} \tag{9.32}$$

$$\frac{\partial\boldsymbol{Q}}{\partial\omega} = \begin{pmatrix} -\cos\vartheta\cos\omega\sin\varphi - \cos\varphi\sin\omega & -\cos\varphi\cos\omega + \cos\vartheta\sin\varphi\sin\omega & 0 \\ \cos\vartheta\cos\varphi\cos\omega - \sin\varphi\sin\omega & -\cos\omega\sin\varphi - \cos\vartheta\cos\varphi\sin\omega & 0 \\ \cos\omega\sin\vartheta & -\sin\vartheta\sin\omega & 0 \end{pmatrix} \tag{9.33}$$

The evolution equations for volume fractions, (9.24), and Euler angles, (9.10, 9.11, 9.12), presented in this paper have a different structure to those presented in [93], in which rate-independent behavior was assumed that yield evolution equations of Kuhn-Tucker type which are naturally much more sensitive to numerical aspects such as step size. In contrast, evolution equations haven been derived here that are very stable from a numerical point of view: it is not necessary to find any roots of yield functions and only need to perform a direct integration in time, which can be executed by a forward Euler scheme for sake of simplicity. Of course, one may argue whether a rate-dependent approach for the Euler angles can be motivated physically. The same questions may be posed for the elasto-viscoplastic evolution of the volume fractions. Both microstructural adaptations take place in experiments with the velocity of sound. This makes a formulation in a rate-independent way more justifiable from a physical standpoint. However, the intention of the model is to be as robust as possible. One may argue

here that the numerical behavior has higher importance than being physically more accurate in the form of the equations, because past experience has shown that even the faster model from [93] is still quite slow due to small step sizes. The numerical examples presented in the next sections will show that even with this viscous approach results may be obtained that are physically quite convincing.

9.3 Parameter identification

The model parameters can be grouped into two fields: there are physically motivated parameters and parameters that basically control the numerical performance. The later ones are the dissipation parameters r_2 and r_α that control the viscous behavior: larger values will decrease the rates, whereas smaller values result in faster evolutions. In particular, if the parameter r_2 tends to zero, the material model becomes more and more rate-independent. This yields lower numerical stability.

$\mathbb{C}$, $\boldsymbol{\eta}_i$, $c_i(\theta)$ and r_1 are the physical model parameters. One may assume for polycrystalline shape memory alloys that the material behaves isotropically. This may not be completely true. However, the elastic constants for isotropic materials are much more easily derived from experiments than for anisotropic materials. Therefore, they read in the common Voigt notation

$$\mathbb{C}_i = \frac{E_i}{1+\nu_i} \begin{pmatrix} \frac{1-\nu_i}{1-2\nu_i} & \frac{\nu_i}{1-2\nu_i} & \frac{\nu_i}{1-2\nu_i} & 0 & 0 & 0 \\ \frac{\nu_i}{1-2\nu_i} & \frac{1-\nu_i}{1-2\nu_i} & \frac{\nu_i}{1-2\nu_i} & 0 & 0 & 0 \\ \frac{\nu_i}{1-2\nu_i} & \frac{\nu_i}{1-2\nu_i} & \frac{1-\nu_i}{1-2\nu_i} & 0 & 0 & 0 \\ 0 & 0 & 0 & \frac{1}{2} & 0 & 0 \\ 0 & 0 & 0 & 0 & \frac{1}{2} & 0 \\ 0 & 0 & 0 & 0 & 0 & \frac{1}{2} \end{pmatrix} \tag{9.34}$$

with the Young's moduli E_A and E_M, and the Poisson's ratios ν_A and ν_M for austenite (A) and martensite (M), respectively.

As already indicated, only three martensitic variants are assumed, one in each Cartesian direction. This yields for the transformation strains

$$\boldsymbol{\eta}_1 = \hat{\eta} \begin{pmatrix} 1 & 0 & 0 \\ 0 & -\hat{\nu} & 0 \\ 0 & 0 & -\hat{\nu} \end{pmatrix}, \quad \boldsymbol{\eta}_2 = \hat{\eta} \begin{pmatrix} -\hat{\nu} & 0 & 0 \\ 0 & 1 & 0 \\ 0 & 0 & -\hat{\nu} \end{pmatrix}, \quad \boldsymbol{\eta}_3 = \hat{\eta} \begin{pmatrix} -\hat{\nu} & 0 & 0 \\ 0 & -\hat{\nu} & 0 \\ 0 & 0 & 1 \end{pmatrix} \tag{9.35}$$

where $\hat{\eta}$ is the scalar maximum transformation strain and $\hat{\nu}$ is Poisson's ratio for phase transformation. Whereas $\hat{\nu}$ has to be assumed, the maximum transformation strain $\hat{\eta}$ can be read in a stress/strain diagram for a tension test in which mainly a one-dimensional stress state is present. This experiment can also be used to find approximation formulas for the caloric energy $\Delta c(\theta) := c_\mathrm{A}(\theta) - c_\mathrm{M}(\theta)$ (note that all martensitic variants possess the same caloric energy) and for the dissipation parameter r_1 that serves as transformation criterion. For this purpose, the driving forces for phase transformations according to (9.25) are reduced to the one-dimensional case. One can identify the stresses in (9.25) that can be reduced to $\bar{\mathbb{C}} : (\boldsymbol{\varepsilon} - \boldsymbol{Q}^T \cdot \bar{\boldsymbol{\eta}} \cdot \boldsymbol{Q}) \to \sigma$. Shape memory alloys are most sensitive to shear stresses. Consequently, for the inverse of the elastic constants the inverse of the shear modulus G_i is

used: $(\mathbb{C}_i)^{-1} \rightarrow (G_i)^{-1} = (2(1+\nu_i))/E_i$. The transformation strains reduce to $\boldsymbol{\eta}_i \rightarrow \hat{\eta}_i$ because in one dimension – due to symmetry of energy – only two martensitic variants exist, possessing $-\hat{\eta}_i$ and $\hat{\eta}_i$ as transformation strains. During tension only one variant becomes active, yielding $n_{\mathcal{A}} = 2$ (austenite plus one martensite variant). By inserting these findings into (9.25), the driving forces reduce to

$$p_{\lambda,i} = \hat{\eta}_i \, \sigma + \frac{1}{2} \frac{\sigma^2}{G_i} - c_i(\theta) \tag{9.36}$$

Thus, one finds for the austenite ($\hat{\eta}_{\mathrm{A}} = 0$ and calculating the caloric energy with respect to the martensite phase which implies $c_{\mathrm{A}}(\theta) = \Delta c(\theta)$ and $c_{\mathrm{M}}(\theta) = 0$)

$$p_{\lambda,\mathrm{A}} = \frac{1}{2} \frac{\sigma^2}{G_{\mathrm{A}}} - \Delta c(\theta) \tag{9.37}$$

and for the martensite phase

$$p_{\lambda,\mathrm{M}} = \hat{\eta} \, \sigma + \frac{1}{2} \frac{\sigma^2}{G_{\mathrm{M}}} \tag{9.38}$$

The active deviator takes for this one-dimensional example the form

$$\mathrm{dev}_{\mathcal{A}} \, p_{\lambda,i} = p_{\lambda,i} - \frac{1}{2} \left(p_{\lambda,\mathrm{A}} + p_{\lambda,\mathrm{M}} \right) \tag{9.39}$$

which yields

$$\mathrm{dev}_{\mathcal{A}} \, p_{\lambda,\mathrm{A}} = \frac{1}{2} \left(p_{\lambda,\mathrm{A}} - p_{\lambda,\mathrm{M}} \right) \tag{9.40}$$

$$\mathrm{dev}_{\mathcal{A}} \, p_{\lambda,\mathrm{M}} = \frac{1}{2} \left(p_{\lambda,\mathrm{M}} - p_{\lambda,\mathrm{A}} \right) \tag{9.41}$$

During transformation, the yield function Φ equals zero. This implies

$$\begin{aligned} & \sqrt{\left(\mathrm{dev}_{\mathcal{A}} \, p_{\lambda,\mathrm{A}}\right)^2 + \left(\mathrm{dev}_{\mathcal{A}} \, p_{\lambda,\mathrm{M}}\right)^2} && = r_1 \\ \Leftrightarrow \quad & \tfrac{1}{2} \sqrt{\left(p_{\lambda,\mathrm{A}} - p_{\lambda,\mathrm{M}}\right)^2 + \left(p_{\lambda,\mathrm{M}} - p_{\lambda,\mathrm{A}}\right)^2} && = r_1 \\ \Rightarrow \quad & \tfrac{1}{\sqrt{2}} \left| p_{\lambda,\mathrm{A}} - p_{\lambda,\mathrm{M}} \right| && = r_1 \end{aligned} \tag{9.42}$$

The difference in the caloric energies $\Delta c(\theta)$ can be interpreted as an energetic measure for the average transformation stress. The dissipation parameter r_1 is the energetic deviation of the average stress in the upper and lower directions, which yields a hysteresis. For the one-dimensional tension test, the upper transformation stress is defined as σ_{u} and the lower one as σ_{l}. Furthermore, for a first analysis, an isothermal process is considered for which $\Delta c(\theta) = \mathrm{const} = \Delta c$. Then, the deviation in the upper and lower directions is equal, which means $r_{1,\mathrm{u}} = r_{1,\mathrm{l}} = \mathrm{const} = r_1$. This allows to write

$$\left| p_{\lambda,\mathrm{A,u}} - p_{\lambda,\mathrm{M,u}} \right| = \sqrt{2} \, r_1 = \left| p_{\lambda,\mathrm{A,l}} - p_{\lambda,\mathrm{M,l}} \right| \tag{9.43}$$

By inserting (9.37,9.38) into (9.43), and using σ_{u} and σ_{l}, one finds

$$\Delta c = -\frac{\sigma_{\mathrm{u}} + \sigma_{\mathrm{l}}}{2} \, \hat{\eta} + \frac{\sigma_{\mathrm{u}}^2 + \sigma_{\mathrm{l}}^2}{4} \left(\frac{1}{G_{\mathrm{A}}} - \frac{1}{G_{\mathrm{M}}} \right) \tag{9.44}$$

Thus, for the case with equal elastic constants, the difference in the caloric energies can be expressed,

for fixed temperature, as the (specific) work produced by mean transformation stress multiplied by transformation strain. Inserting this result into (9.42) gives the threshold work for phase transformation

$$r_1 = \frac{1}{\sqrt{2}} \left(\frac{\sigma_u - \sigma_l}{2} \hat{\eta} - \frac{\sigma_u^2 - \sigma_l^2}{4} \left(\frac{1}{G_A} - \frac{1}{G_M} \right) \right) \tag{9.45}$$

The approximation formulas in (9.44) and (9.45) can be used to calibrate the material model in a very easy way based on simple tension tests.

It is known from experiments, e.g. [152] or [151], that the width of the hysteresis stays constant for different temperatures, whereas the upper and lower transformation stresses vary linearly when the temperature changes. For the model parameters, this means that Δc should be a linear function in temperature, whereas the threshold work r_1 should be more or less constant. An examination of the approximation formulas for Δc and r_1 (9.44,9.45) shows that there is a quadratic dependence on the plateau stresses and thus on the temperature, which is surprising at first glance. In Section 9.4, which is dedicated to numerical results, this property is analyzed specifically with respect to the experimental data. As one will see there, a linear interpolation will receive numerical results with acceptable agreement with experiments. For this purpose, a second tension test at a different temperature has to be performed that yields a different value for Δc. A linear interpolation between the two different values for Δc at different temperatures finally gives the linear function for $\Delta c(\theta)$.

9.4 Numerical results

9.4.1 Numerical treatment

In contrast to previous works [70, 93], the numerical treatment of the model presented here is – as intended to be – rather simple, see also the algorithm presented in [93]. Resulting from the new elasto-viscoplastic type of the evolution equations, a direct integration in time is feasible. Employing a regular forward integration scheme, also in e.g. [93] and [75], the update of the two internal variables, volume fractions and Euler angles, may be computed by

$$\boldsymbol{\lambda}^{n+1} = \boldsymbol{\lambda}^n + \Delta t \; \dot{\boldsymbol{\lambda}}(\boldsymbol{\varepsilon}^{n+1}, \theta^{n+1}, \boldsymbol{\lambda}^n, \boldsymbol{\alpha}^n) \tag{9.46}$$

$$\boldsymbol{\alpha}^{n+1} = \boldsymbol{\lambda}^n + \Delta t \; \dot{\boldsymbol{\alpha}}(\boldsymbol{\varepsilon}^{n+1}, \theta^{n+1}, \boldsymbol{\lambda}^n, \boldsymbol{\alpha}^n) \tag{9.47}$$

where the rates of the internal variables are give in Equations (9.24) and (9.10-9.12), respectively. The index $(\cdot)^{n+1}$ refers to the current load step, whereas $(\cdot)^n$ indicates the previous one. Due to the transient character of the equations, a time increment Δt has to be chosen, which, of course, influences the numerical solution. Along with the time increment, as usual a load increment Δu (in terms of prescribed displacements in the context of finite elements) has to be specified. A quantity related to the (experimental loading) velocity may then be defined as $v := \Delta u / \Delta t$. If that loading velocity is kept constant, similar numerical results may be expected, even for different choices for the time and the load increment.

As already stated, the great benefit of rate-dependent evolution equations is a huge numerical stability. On the other hand, by introducing a time increment an additional parameter has to be defined. In the case of the material model presented here, too "high" loading velocities v result in an increase of stress plateaus. The underlying physical cause of this experimentally observed material behavior, see e.g.

[166, 62], is not taken into account by the model presented here. Appropriate models for simulating the thermo-mechanically coupling which has to be taken into account at "high" strain rates can be found for instance in [98, 75, 165]. In a one-dimensional case, as presented in the following, the strain rate $\dot{\varepsilon}$ should be less than 1×10^{-3} [1/s] to receive reliable results.

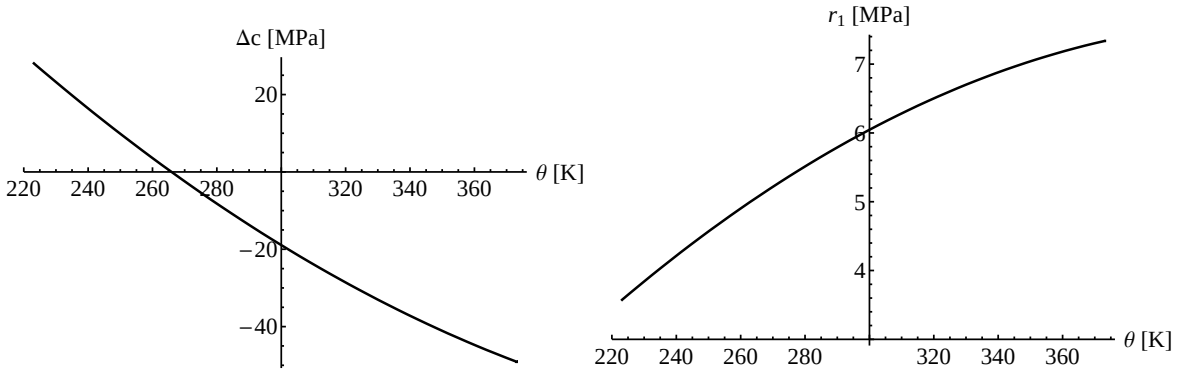

Figure 9.1: Left: caloric part of the energy Δc as function of temperature θ calculated by means of (9.44). Right: threshold energy r_1 as function of temperature. Both curves are determined using the experimental values for NiTi given in Table 9.1.

9.4.2 Tension tests

First, the parameters for the example material Ni50.9Ti49.1 are specified by using the experimental data from [192] and [162], before several complex examples for construction components are presented. In [192], wires at 323.15 K and 333.15 K were investigated, and in [162] a strip was tested at 293.15 K, all under tension. The elastic constants are 83 GPa for austenite and 40 GPa for martensite, both possessing a Poisson's ratio of 0.35, a maximum transformation strain $\hat{\eta} = 0.055$ [-] and a Poisson's ratio for transformation $\hat{\nu} = 0.45$ [-]. The numerical parameters are set to $r_2 = 10$ [MPa], $r_\alpha = 10$ [MPa], and the time increment for numerical discretization $\Delta t = 1$ [s]. For all subsequent simulations, the load increment is smaller than $\Delta u \leq 0.075$ [mm], yielding $v \leq 0.075$ [mm/s] and for the tension tests $\dot{\varepsilon} = 8 \times 10^{-4}$ [1/s] ($\dot{\varepsilon} = \Delta u/(l_0\ \Delta t)$ with $\Delta u = 2.8 \times 10^{-2}$ [mm] and $l_0 = 35$ [mm]), which is small enough to neglect inner heat production due to phase transformations for which thermo-mechanically coupled models have to be applied. The plateau stresses and resulting model parameters are collected in Table 9.1. Analyzing the parameters r_1, one sees a (small) temperature dependence that could be

	Strip @ 293.15 K	Wire @ 323.15 K	Wire @ 333.15 K
σ_u [MPa]	400	600	660
σ_l [MPa]	140	340	400
r_1 [MPa]	5.92	6.57	6.76
Δc [MPa]	-16.42	-30.01	-34.36

Table 9.1: Plateau stresses and parameters r_1 and Δc at various temperatures.

surprising at first glance. However, as indicated by (9.45), the difference between the upper and lower plateau stresses of the two varies for different values of σ_u and σ_l, even if their difference is constant. A

comparison with previous studies, [98], which discuss formulas for the dissipation parameter based on other approaches, reveals that a temperature dependence of r_1 could be investigated there also. Here, values for r_1 for three different temperatures have been found, which allows to give a closed form for the quadratic function $r_1(\theta)$. The same can be carried out for the caloric energy. It is then possible to search for the roots, which are $\Delta c(\theta) = 0 \Leftrightarrow \theta = \{265.89, 718.53\}\,[\mathrm{K}]$. Obviously, the second one is so high that the material does not show any shape memory effect and the material model loses its range of applicability. In contrast, the first root is very close to the experimental equilibrium temperature (defined as the average between the two peak temperatures), which is about 260 K.

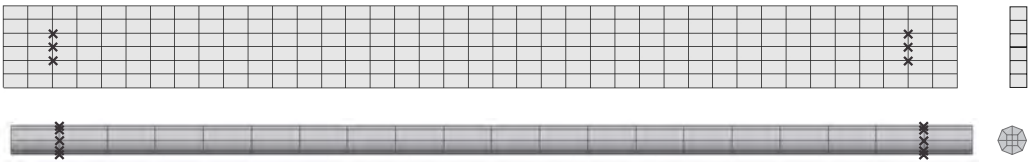

Figure 9.2: Upper: finite element mesh for the strip, side and top view. Nodes with prescribed displacements are indicated by **x**. Lower: finite element mesh for the wire, side and top view. Nodes with prescribed displacements are indicated by **x**.

A similar analysis of (9.44) for the caloric energy Δc shows that it is a quadratic function in plateau stresses and thus temperature. This is in contrast to experimental observations which prove that the dependence should be linear. However, both formulas in (9.44, 9.45) are just approximation formulas for a first guess of the energetic material parameters. Furthermore, Figure 9.1 shows that the non-linear character of (9.44) is less intense for the temperature interval [223, ... ,333] K.

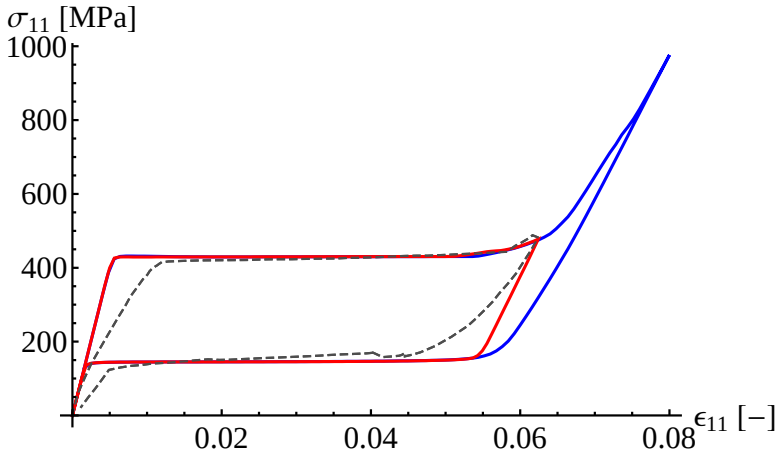

Figure 9.3: Stress/strain diagram for the strip at 293.15 K using the material parameter given in Table 9.1. The gray curve is from experimental data reported in [162] and the red and blue curves are numerical results. The red curve corresponds to same maximum strain as applied in the experiment, the blue one results for 8 % maximum strain.

The three examples for characterization (2 × wire, strip) are calculated using the parameters given in Table 9.1 and three-linear shape functions for the finite element method. The respective meshes are presented in Figure 9.2. The reaction forces are divided by the respective cross-sections (wire: $A_\mathrm{d} = 1.09359\,\mathrm{mm}^2$, strip: $A_\mathrm{s} = 2.244\,\mathrm{mm}^2$) yielding the stress measure as equivalent to experimental procedure. The prescribed displacement is divided by the free length, which is 35 mm for all cases and which serves as strain measure. Stress versus strain for the three cases is plotted respectively in

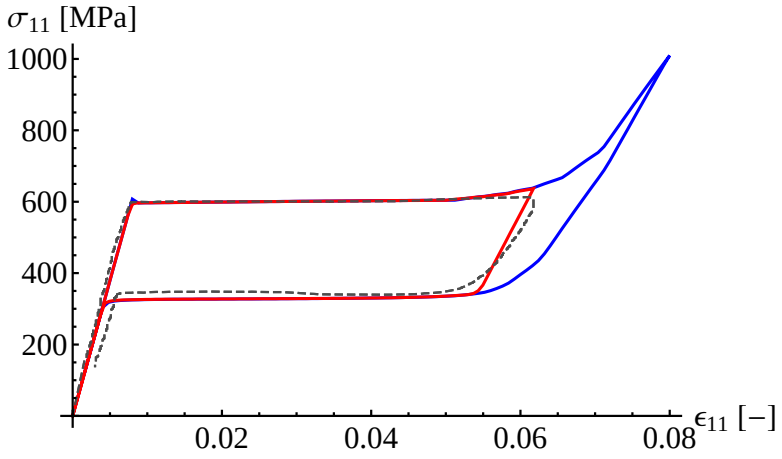

Figure 9.4: Stress/strain diagram for the wire at 323.15 K using the material parameter given in Table 9.1. The gray curve is from experimental data reported in [192] and the red and blue curves are numerical results. The red curve corresponds to same maximum strain as applied in the experiment, the blue one results for 8 % maximum strain.

Figures 9.3, 9.4, and 9.5, together with the experimental results. It is obvious that without defining a specific transformation stress, as necessary for plasticity-based models, the approximation formulas in (9.44,9.45) yield results that are very close to experimental findings. Of course, due to the supports in the finite element results, the stress state is far more complex than being one-dimensional. However, due to the energetic character of the model and the model parameters, the one-dimensional approximation formulas are sufficient to predict the experimental material behavior to a high degree.

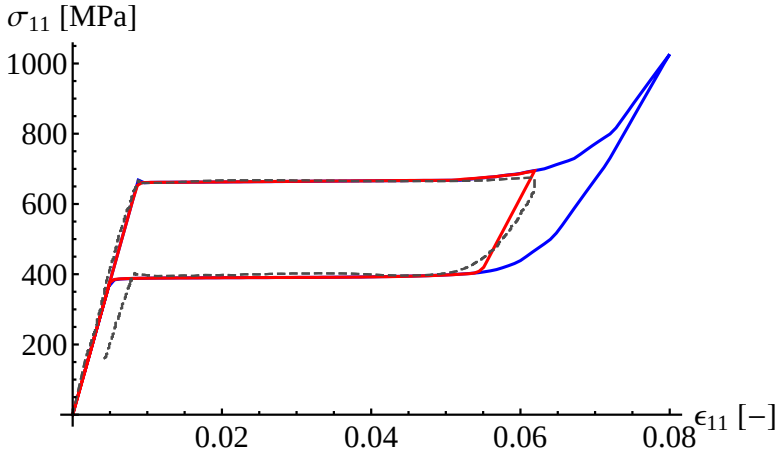

Figure 9.5: Stress/strain diagram for the wire at 333.15 K using the material parameter given in Table 9.1. The gray curve is from experimental data reported in [192] and the red and blue curves are numerical results. The red curve corresponds to same maximum strain as applied in the experiment, the blue one results for 8 % maximum strain.

9.4.3 Plate with notch

The presented material model is numerically very stable. As an exemplary illustration, a plate with a notch is calculated. In this case, very high stress peaks are present at the notch tip, which constitutes as a numerically difficult boundary value problem. From now on, the values for the caloric energies are taken to interpolate the linear function in temperature. A plot for the linear approximation of caloric energy is given in Figure 9.6. The function is $\Delta c(\theta) = (136.06 - 0.51\,\theta)[\mathrm{MPa}]$.

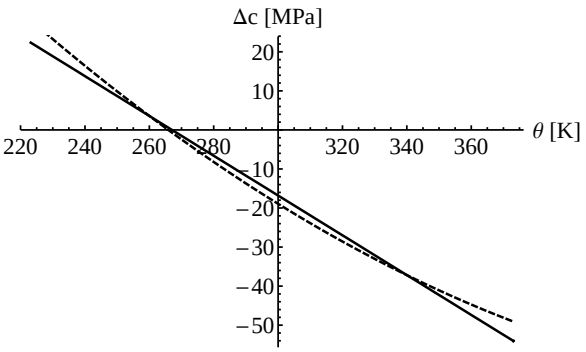

Figure 9.6: Caloric part of the energy Δc as function of temperature θ calculated with (9.44) (dashed line) and its linear interpolation (straight line).

The dissipation parameter r_1, which is used for all subsequent calculations is obtained by averaging over the temperature interval [293.15,...,333.15]. This is

$$\bar{r}_1 := \frac{1}{333.15 - 293.15} \int_{293.15}^{333.15} r(\theta)\,\mathrm{d}\theta = 6.34\,[\mathrm{MPa}] \tag{9.48}$$

The plate is discretized by use of 720 finite elements with only one element in the thickness direction. It is quadratic in the x- and y-directions with length 100 mm and thickness 5 mm in z-direction, the angle of the notch is 2 degree in positive and negative direction of the horizontal axis. The plate is fixed at the bottom and a linearly increasing tension is applied at the top for the first 400 load steps (maximum displacement is 0.75 mm). During the second 400 load steps (800 in total), the prescribed displacement is held at maximum while temperature is increased homogeneously (thus, the heat conduction equation is not solved, but just temperature is increased in all Gauß points simultaneously). The spacial distribution of the austenite phase is presented in Figure 9.7, a zoomed view of the notch tip is given in Figure 9.8, and the force/displacement/temperature diagram is given in Figure 9.9. When tension is applied, first an elastic material reaction is present. After reaching a certain threshold value, phase transformation initializes where stress is the highest, which is – of course – at the notch tip. The transformation zone has a kidney-like shape which is also known for the stress field investigated in fracture mechanics. Increasing the external displacement results in an enlargement of the transformation zone where, in the limit, two transformation "rays" evolve that point to the edges of the plate. In the detailed sketch of the notch tip, see Figure 9.8, it can be seen that the austenite transforms to martensite during tension. When the mechanical load in terms of displacements is fixed and the temperature is increased, the microstructural configuration in the material stays unaffected for the first 200 thermal load steps (see load step 600). However, once the thermal driving forces and thus the differences in the caloric energies are high enough, the austenite phase starts to increase at the expense of the martensitic phases. The gap between increasing temperature and phase transformation results from the fact that the initial configuration for that loading step (400) "lies" on the upper

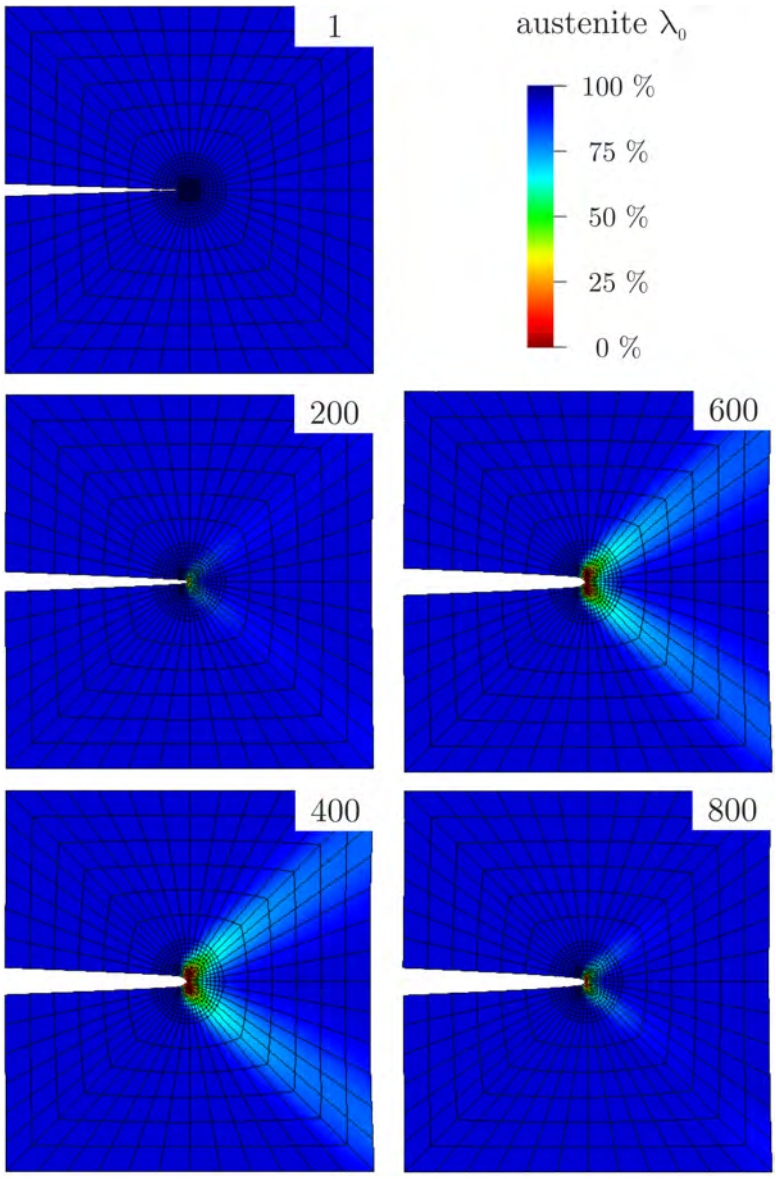

Figure 9.7: Spatial distribution of austenite at different points in time. Deformation is increased by a factor of 5. Initial configuration (1, θ = 283.15 [K]) is put under tension (load steps 1 to 400). Subsequently (load steps 400 to 800), the temperature is linearly increased (800: θ = 373.15 [K]).

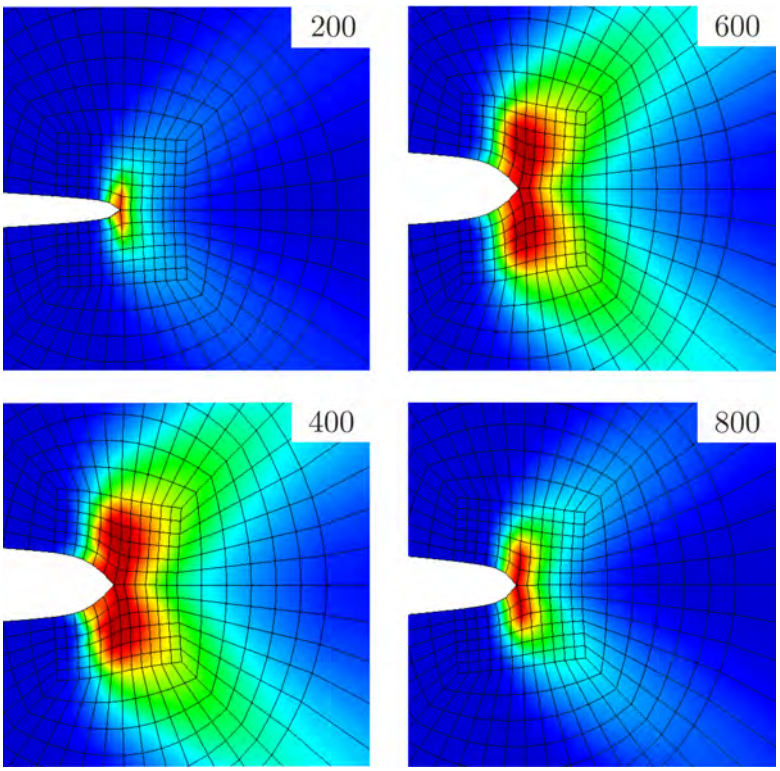

Figure 9.8: Spatial distribution of austenite at different points in time and zoomed on the notch tip. The legend is given in Figure 9.7; deformation is increased by a factor of 5. Initial configuration (1, θ = 283.15 [K]) is put under tension (load steps 200 to 400). Subsequently (load steps 400 to 800), the temperature is linearly increased (800: θ = 373.15 [K]).

branch of the hysteresis. This means, only when the hysteresis is lifted high enough that the initial states constitutes as being created during mechanical *un*loading, phase transformation is triggered due to temperature. The global behavior of the entire construction components is displayed in its

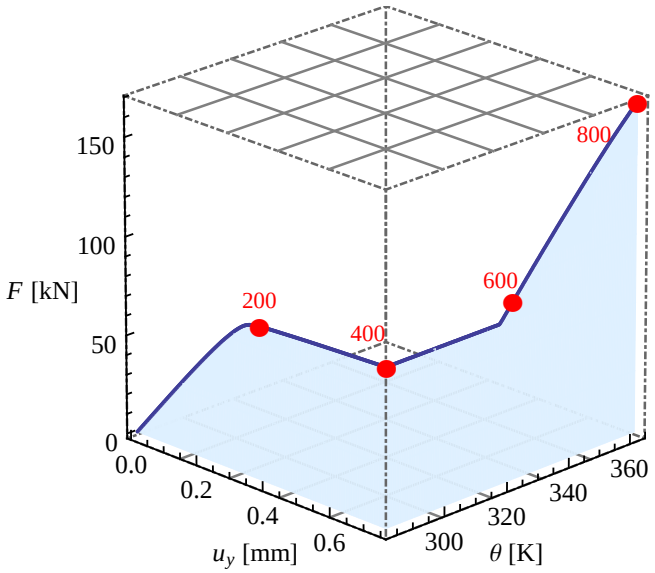

Figure 9.9: Force/displacement/temperature diagram for the plate with notch. The respective loading steps in Figures 9.7 and 9.8 are indicated in red.

corresponding force/displacement/temperature diagram in Figure 9.9. The gap between the curve and the displacement/temperature plane is colored in blue. Thus, the curve runs parallel to the displacement axis for the first 400 load steps and then (steps 401 to 800) follows only the direction of temperature axis. In this global context, one can identify the elastic region at the beginning and constant forces during (mechanically induced) phase transformation. In contrast to the initial tension tests, Figures 9.3, 9.4, and 9.5, the transition from the linear-elastic part of the curve to the constant one is much smoother. The applied tension is too small to trigger phase transformation in the majority of the construction component. Consequently, one stays in the force plateau. When the temperature is increased, no phase transformation initially takes place, as discussed above. At a temperature of about 340 K, the austenite returns and thus the material contracts, which results in an increase in forces.

9.4.4 Spring with two materials

Evaluation of the material model in a finite element setting easily allows for consideration of construction components that are made of different materials. As an example, the geometry of a spring is chosen and 1440 finite elements are used. Springs serve often as actuator devices and thus constitute as important construction component in industrial settings, see e.g. [152, 41, 85, 54, 14, 134] and the impressive paper of Sun *et al.* [179]. The wire radius is 1 mm, the inner coil radius is 2 mm, and the escaping arc is 30 degree. The left-hand half of the spring is made of NiTi, the right-hand half is made of brass (elastic modulus is 78 GPa, Poisson's ratio is 0.37). Similar to the plate with notch, tension is applied for the first 400 load steps and subsequently the temperature is increased while keeping the maximum displacement constant at 7.5 mm. Figure 9.10 shows a plot of the distribution of austenite.

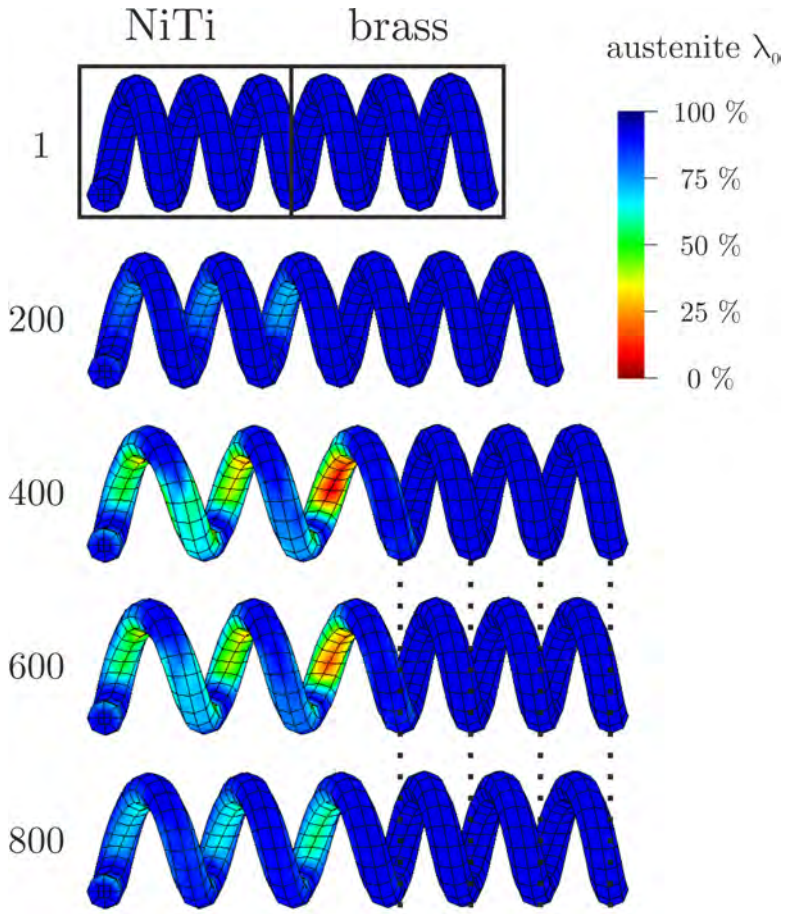

Figure 9.10: Spatial distribution of austenite at different points in time. Initial configuration (1, θ = 283.15 [K]) is put under tension (load steps 1 to 400). Subsequently (load steps 400 to 800), the temperature is linearly increased (800: θ = 373.15 [K]).

Owing to the boundary conditions that are induced by the brass part of the spring, phase transformation is triggered in the NiTi part close to the center, where a mixture state of austenite and martensite evolves that is softer than the austenitic one. Consequently, the NiTi part of the spring behaves like a combination of stiffer regions (where pure austenite is present) and softer regions (with the mixture state). This forces the NiTi part of the spring to transform inhomogeneously. When temperature is

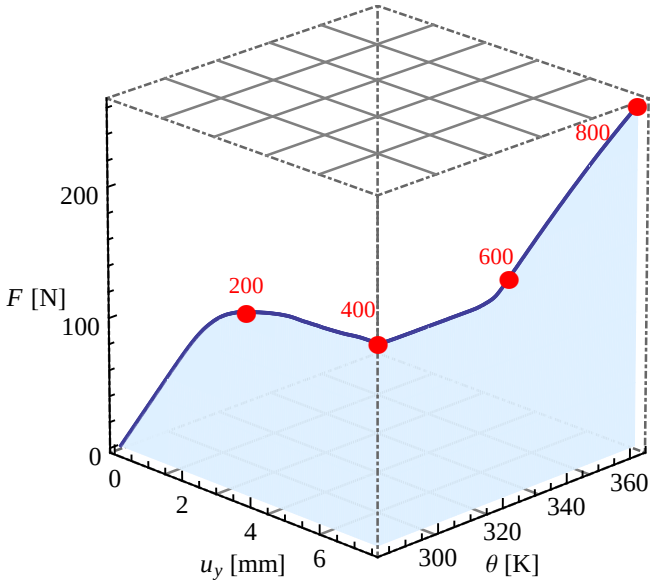

Figure 9.11: Force/displacement/temperature diagram for the spring made of NiTi and brass. The respective loading steps in Figure 9.10 are indicated in red.

increased, austenite is re-established. The resultant inner forces are large enough to deform the brass part of the spring: the end position of this part moves to the left while austenite contracts, such as the rest does for the brass part. This is demonstrated by the dashed lines indicating the initial state for thermal loading (beginning with load step 401).

Again, the global material reaction is presented in a force/displacement/temperature diagram, which is given in Figure 9.11. The entire behavior is comparable to that one observed for the plate with notch. However, the transition into the force plateau is still smoother to some extent, and the temperature-driven increase of force initializes earlier. This is very reasonable because this starting time is determined by the overall amount of austenite. For the NiTi part of the spring, this is obviously lower than in the plate with notch. Consequently, more material is sensitive to the temperature-induced driving forces. Of course, due to other geometric effects, the resultant global forces for the entire construction component differ from the plate with notch. This is an automatic result for a finite-element-based simulation and simplifies engineering efforts drastically.

9.4.5 Clamping ring

The last example presented in this work is a clamping ring whose general mode of operation is used in many different industrial devices, e.g. [179, 15, 49, 80, 118]. The loading conditions are, in principle, all the same as for the plate with notch and the spring made of NiTi and brass. The specific boundary conditions here are fixed displacements for the nodes at the bottom and prescribed displacements for

the nodes at the top. The clamping ring is compressed in the beginning, as it would be the case during assembly with a screw, and it is subsequently heated to the application temperature. The geometry of the ring is quite complex: it has a trigonometric slope in the circumferential direction with seven periods. In total, 630 elements are used for discretization. The inner radius is 3.3 mm, the width is 0.125 mm in the axial direction and 0.5 mm in the radial direction. The spatial distribution

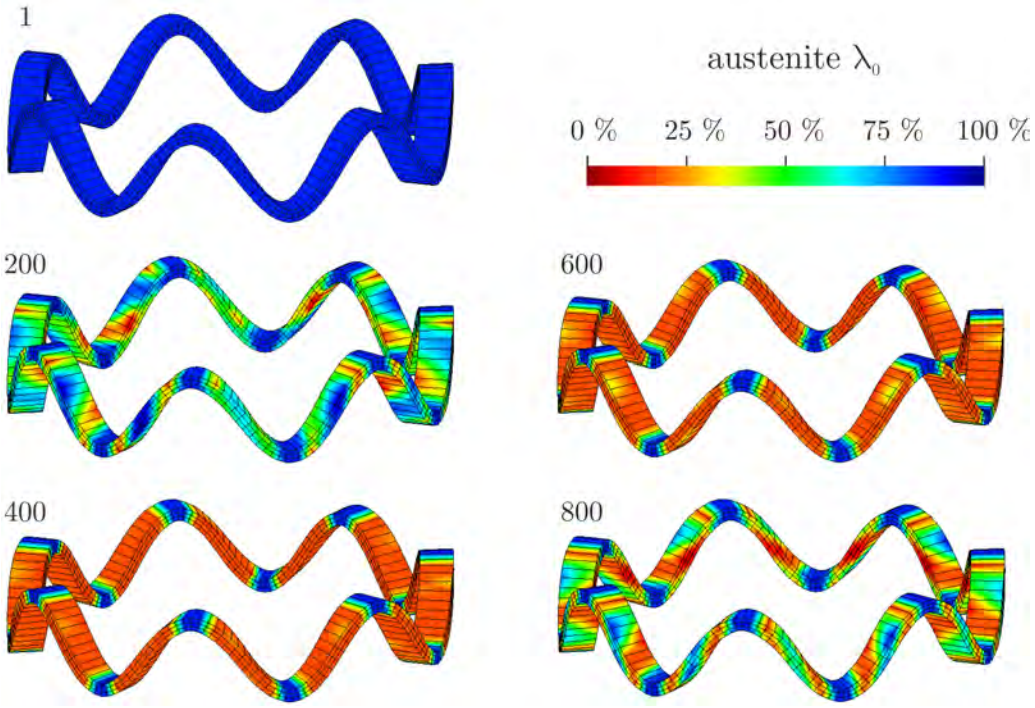

Figure 9.12: Spatial distribution of austenite at different points in time. Initial configuration (1, θ = 283.15 [K]) is put under compression (load steps 1 to 400). Subsequently (load steps 400 to 800), the temperature is linearly increased (800: θ = 373.15 [K]).

of austenite is displayed in Figure 9.12. Due to the rather complex geometry, quite complex stress states are present (tension in several directions and bending around several axes). That particular stress state triggers the phase transformation to take place in quite localized way, but periodically in the circumferential direction (see load step 200). At maximum compression (load step 400), the bar-like parts have completely transformed, except for the tips, due to less intense stresses. While the temperature is increased, again the back-transformation initializes somewhat localized (load step 600) until, finally, a quite inhomogeneously distributed configuration of the crystallographic phases is present. In the corresponding force/displacement/temperature diagram in Figure 9.13, after the linear region at the beginning, one again sees a constant force for increasing displacements. At approximately u_y = 0.07 mm, the plateau is left and the resultant force is decreased (increase in absolute value). The non-constant force over increasing displacement indicates that the majority of the material has transformed to martensite and consequently the construction component behaves linearly again, but now with the mechanical properties of martensite. This observation agrees with the distribution of austenite in Figure 9.12 which shows that almost all the austenite has vanished.

Subsequently, the temperature is increased again and once the driving forces have become large enough, the absolute value of the resultant force increases further. In a real application, this means that the ring can be assembled at relatively low temperatures, yielding a clamping force of approximately 920

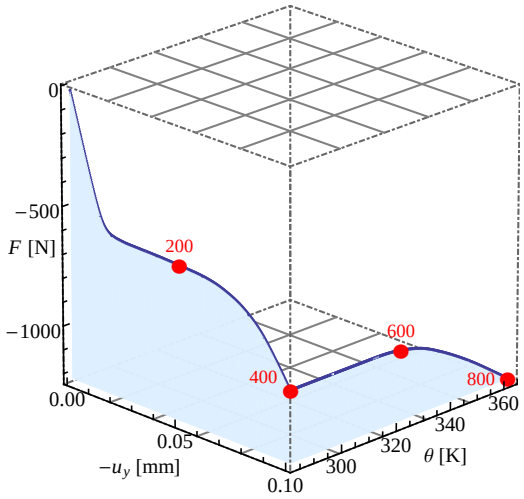

Figure 9.13: Force/displacement/temperature diagram for the clamping ring. The respective loading steps in Figure 9.12 are indicated in red.

N. If the entire construction is used at 360 K, the clamping force increases to 1220 N which is a boost of 33 %.

An analysis of all the presented numerical simulations reveals that the physical behavior of shape memory alloys is displayed quite well by the presented material model: the simplifications of considering only three martensitic variants as well as treating the model equations in a transient way do not yield questionable results. The global material behavior that is determined by local phase transformations induced by both mechanical and thermal loads agrees, as compared to validation data, quite well with experiments. Also for the more complex examples, the numerical results are quite reasonable without any re-calibration of the material model.

9.4.6 Calculation times

The presented material model is fast. In order to prove this empirically, the calculation times for the individual boundary value problems are listed in Table 9.2 (note that variations in element numbering, solvers, and other aspects may influence the calculation times). All computations were executed on an Intel i7 with 2.93 GHz and a 64 bit system. The model itself was programmed in a user-defined element routine in the finite element program FEAP. No parallelization techniques were applied. The

	Strip	Wire	Plate	Spring	Ring
No. of nodes	560	357	1526	2057	1680
No. of elements	234	240	720	1440	630
CPU time [s]	380	175	2482	1861	1127

Table 9.2: Calculation times for the presented boundary value problems.

strip and the wire were only mechanically loaded, thus 200 load steps were used in total. This is only

5 % of the number of loading steps that would be necessary using the first version of the model in [93]. In this study, the total number of load steps for the tension tests was 4000. Mention that the relative high number of load steps for the rate-independent model were chosen only due to numerical reasons: higher increments, yielding smaller numbers of load steps, cause numerical instabilities and the calculation of the old model had to be aborted. Here, in contrast, larger load increments are numerically possible with smaller numbers of load steps. Even if the reduced effort of the presented model is neglected, comparing the number of load steps indicates directly that simulations based on the new model are much faster due to the much smaller number of load steps. The plate, the spring, and the ring were subjetced to both mechanical and thermal loadings (each 400 load steps) with a total number of 800 load steps. These examples exhibited much more complicated stress states, and it is quite likely that the load increment has to be reduced even more than 5 % for the old model in [93].

Although not all relevant information for comparison is provided in the recent paper of Stebner and Brinson, [173], it is still possible to use their work for valuation of the model's numerical performance. In [173], an improved three-dimensional model is presented and it is applied to boundary value problems, which are solved using the finite element program ABAQUS on a DELL T5500 Intel Xeon single core. Unfortunately, neither the exact number of load steps nor the exact number of elements is given. However, both the processor as well as the finite element program are faster than the ones deployed here. They compute a mechanically induced phase transformation in a two-dimensional strip with hole using finite elements with reduced integration (CPS4R element; the dimensions of the strip are 3 mm × 25 mm and it can be estimated that the elements have a minimal size of 0.1 mm × 0.1 mm: thus, if coarsening of the elements and the hole are not considered, the maximum number of elements is less than $(3{\times}25)/(0.1{\times}0.1) = 7500$). Performing a reduced integration implies that the material model has to be evaluated only once per element and iteration step. In contrast, the results presented here have been computed by application of full integration of tri-linear elements demanding the model to be evaluated eight times per element and iteration step (comparable to C3D8 element in ABAQUS). Thus, a comparable number of 3D-elements of the example in [173] would be $7500/8 \approx 940$ for measuring the numerical effort for calling the respective material model. Along with the factor eight between reduced and full integration, the numerical effort to calculate the displacement field in two dimensions is less than for three-dimensional problems which increases the total calculation time. The computation of the strip in [173] was completed in 4.5 h, whereas the simulations presented here completed in 0.5 h maximum. Thus, without discussing more details, the model in this paper is at least as fast as the one presented in [173].

With regard to the simple numerical implementation (no parallelization, no step size control) and the complexity of the boundary value problems of the plate, the spring, and the ring, the resultant calculation times are very satisfactory.

9.5 Conclusions and outlook

In this paper a new material model for the mechanically and thermally induced phase transformation in shape memory alloys has been derived. The model is formulated in an energetic framework. In order to be as fast and also as numerically stable as possible, the number of martensitic variants was reduced to three and an elasto-viscoplastic approach was chosen for the evolution of internal variables. The theoretical section finished with a presentation of simple formulas that enable approximation of

the rather abstract quantities “dissipation parameter” and “difference in caloric energies” (compared to plateau stresses, for instance). Tension tests were used to demonstrate the calibration of the model in a finite element setting. Interestingly, formulation of the model parameters for an artificial one-dimensional state was accurate enough to predict the experimental results of the tension tests at various temperatures and for different geometries. Three much more sophisticated examples were calculated and discussed: one proved the numerical stability of the material model (plate with notch), one showed the applicability to interaction of different materials (spring with two materials), and the last one served as real application example with a complex geometry that can also be found in a comparable manner in stents (clamping ring). All examples were evaluated with respect to both mechanical and thermal loadings and showed physically reasonable results without the need for re-calibration of the model for different temperatures or geometries, which simplifies engineering processes to a great degree. Owing to very limited number of internal variables and the simple mathematical framework, the model is fast, stable and quite accurate for modeling shape memory alloys in an industrial setting.

Although the model is able to predict the pseudoelastic and the pseudoplastic material behavior as well as the one-way effect and the two-way effect, it does not include R-phase transformation or functional fatigue. These topics will be part of future work.

10 Modeling the long-life behavior of shape memory alloys

Published as: *J. Waimann, P. Junker, K. Hackl*: A coupled dissipation functional for modeling the functional fatigue in polycrystalline shape memory alloys, *Eur. J. Mech. A-Solid* ***accepted for publication*** **(2015)**

The pseudoelastic material behavior is one outstanding feature of shape memory alloys. This effect comes along with the forming of two plateaus in the stress/strain diagram of a tension test. Cyclic loading leads to a decrease particularly of the upper stress-plateau due to the evolution of plastic deformations which also implies fatigue of the material. In this work, we develop a variational material model which is able to predict the effect of fatigue using a novel approach for the dissipation potential that couples the evolutions of phase transformations and plastic strains.

10.1 Introduction

The unique properties of shape memory alloys (SMAs), referred to as pseudoplasticity and pseudoelasticity, are a result of crystallographic phase transformations. These solid/solid transformations are diffusionless and take place between the austenite and martensite phases (see e.g. [152] or [151]). Compared to other materials that may form the austenite and martensite phases, e.g. steel, this reversible phase transformation is not only induced by thermal loads but also by mechanical ones. Due to their (thermo-)mechanical properties, SMAs are very promising materials for future technical developments. An interesting review on the versatile applications is given in [140].

The austenitic phase is stable at higher temperatures and has a cubic crystal structure. The martensite is stable at lower temperatures and exists in several different variants which can transform into each other by rotation and reflection. The transformation is characterized by a transformation strain (tensor) $\boldsymbol{\eta}$ which is material-dependent and can be determined experimentally. At lower temperatures, the material is purely martensitic and it behaves pseudoplastically. At higher temperatures, the material is austenitic and the effect of pseudoelasticity takes place. Consequently, the material behavior strongly depends on the current ambient temperature.

There exist a lot of experimental work regarding fatigue effects in shape memory alloys and we will just mention a few of them. One of the earliest investigations was done by Miyazaki *et al.* [139] who explained the fatigue effect as a result of developing dislocations in the martensitic phase. In Ibarra *et al.* [89], the microstructural changes during cyclic compression were analyzed under the consideration of different dislocation types. Gall and Maier [51] investigated the influence of the crystallographic orientation and precipitates on the material behavior. An introduction to the fatigue effects and investigations on the temperature's influence on the fatigue life is given in Eggeler *et al.* [45]. In Wagner *et al.* [193], the effect of healing treatments on the material's fatigue life is examined. These experimental findings give rise to a classification of the underlying micromechanical effects that trigger fatigue in shape memory alloys: on the one hand, it is the accumulation of plastic deformation which can also be identified in a global stress/strain diagram in terms of residual "plastic" strains. On the other hand, the production of dislocations at the grain level constitute as a second source for fatigue. This later effect is referred to as micro-plasticity and can be healed according to Wagner *et al.* [193].

Figure 10.1 recalls the schematic material behavior for a cycled tension test as presented in Wagner [192]. The initially purely austenitic material behaves linear elastically until it reaches a critical stress

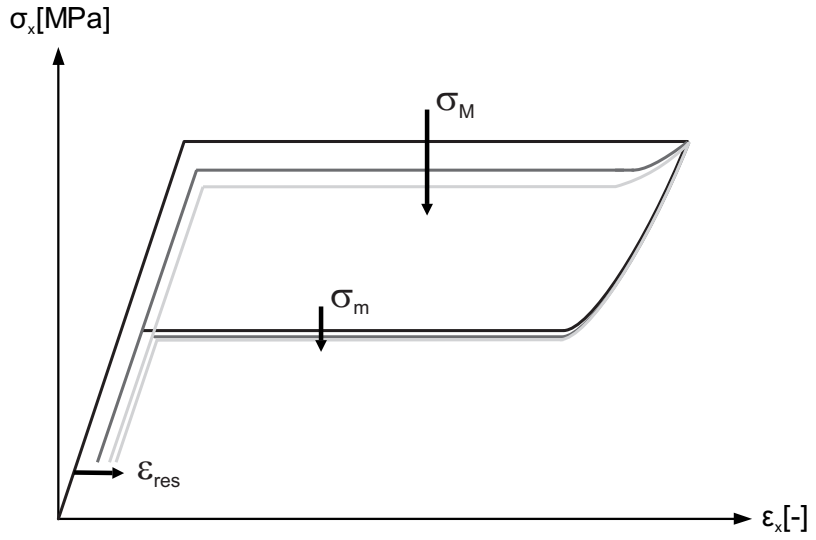

Figure 10.1: Schematic stress/strain diagram for a cycled tension test [192].

value indicated by σ_{M}. Further increasing the external load forces the material to transform from the austenite to the martensite phase. During this process, stress remains constant until the transformation is completed. During unloading the material initially exhibits fairly linear elastic behavior until reaching another threshold value for the stress σ_{m}, whereby $\sigma_{\mathrm{m}} < \sigma_{\mathrm{M}}$. When reaching this second threshold value σ_{m}, the reverse transformation from martensite to austenite is initiated during which stress remains constant again. It behaves linearly again when the material has transformed back. It is known that austenite and martensite share an incoherent interface (see e.g. [152] or [151]). Due to this incoherence, dislocations are formed during phase transformation which accumulate to (macroscopically) measurable irreversible plastic strains. The local stress increase, which accompanies every dislocation, serves as nucleus for phase transformation. Consequently, if the number of dislocations increases with increasing load cycle, the number of nuclei increases. The macroscopic effect is that the mentioned plateau stresses σ_{M} and σ_{m} decrease with every load cycle until they converge towards some constant values. Additionally, the irreversible strain $\varepsilon_{\mathrm{res}}$, which results from the occurring fatigue effects and the plastic deformations, tends to some limit value.

There exist many different concepts for modeling SMAs which consider different aspects of the complex material behavior. Brinson [25] developed one of the first empirical material model for SMAs, followed by other phenomenological models, e.g. by Bouvet *et al.* [22] and Lexcellent *et al.* [120]. Other approaches model the material behavior based on techniques that show some similarities to plasticity modeling. To name but a few, we mention here the rate-dependent and hardening effects considering model of Hartl *et al.* [75] which is modified by Lagoudas *et al.* [115] regarding rate-independence. The model by Auricchio and Taylor [8] considers irreversible strains whereas Helm and Haupt [79] focused on the thermo-mechanically coupling. The last approach mentioned here that is used for the modeling of SMAs grounds on variational concepts. Stupkiewicz and Petryk examined the transition between the micro and the macro scale [177] and developed a model under assumption of a simplified

microstructure for small and finite deformations [178]. Other examples for variational material models are the models by Govindjee and Miehe [60], by Stein and Sagar [174] for large deformations and by Mielke *et al.* [138] which is based on the idea of dissipation functional relaxation. Additionally, Kružík and Otto developed a material model for polycrystalline SMAs [111] in which they discretized the polycrystal with use of a finite element implementation. In [59] Govindjee and Kasper developed a probabilistic model that accounts for plasticity but without the development of plastic deformations during the transformation process. Bartel [13] also used probabilistic concepts to examine the influence of plasticity on martensitic phase transformations.

Modeling of fatigue in SMAs was also part of earlier works. Tanaka *et al.* [183] described the functional fatigue by use of three internal variables: the residual stress and strain along with an irreversible martensitic volume fraction. Lexcellent and Bourbon [119] developed the concept of instantaneous residual martensite. They modified the free energy by use of the residual martensite as an internal variable. Abeyaratne and Kim [2] developed a one-dimensional continuum model based on Abeyaratne *et al.* [3]. They defined a critical value for the Gibb's energy that has to be overcome before the microstructural change can start and which depends on the number of loading cycles. Bo and Lagoudas [20] described the fatigue effect during thermal loading by taking plastic deformations into account. This model was later enhanced by Lagoudas and Entchev [114]. Additionally, Auricchio *et al.* [7] derived a material model where the fatigue effect is modeled by consideration of a permanent inelastic strain. Saint-Sulpice *et al.* [161] developed a rather phenomenological material model based on [22] in which the material behavior is directly influenced by the load cycle's number.

In this work, we focus on the inclusion of appropriate modifications of an earlier model of our research group such that we can account for the structural and functional fatigue of a pseudoelastically behaving material. In this vein, we propose an extension of the dissipation functional that is used to derive an energy-based material model. The model was developed in [71] and [70]. An thermo-mechanically coupled extension was presented in [99]. In Section 10.2 we present an advanced material model that is able to predict the functional fatigue in cyclically loaded SMAs. Therefore, we introduce an additional internal variable which describes the plastic deformation in each phase of each grain of the polycrystalline material. Thereby, we are able to account for the aforementioned effect of micro-plasticity. For the non-conservative microstructural evolution, we propose a coupled ansatz for the dissipation functional and a combined Voigt/Reuß energy bound. One single yield function results which is valid for both the plastic deformation and the phase transformation. Subsequently, we show some numerical examples for our material model in Section 10.4 and give a final conclusion and outlook in Section 10.5.

10.2 Material Model

10.2.1 A variational modeling approach

Material models based on internal variables can be derived using different methodical techniques. One possible technique is the principle of the minimum of the dissipation potential which is associated to Hamilton's principle if no gradients of the internal variables are present. Then, evaluation of the stationarity condition of an associated Lagrange functional results in the governing evolution equations

(comparable to Biot's equation)

$$\mathcal{L} := \dot{\Psi} + \bar{\mathcal{D}} + \text{cons} \rightarrow \operatorname*{stat}_{\dot{\Lambda}} \tag{10.1}$$

where $\Psi = \Psi(\boldsymbol{\varepsilon}, \Lambda)$ is the Helmholtz free energy which depends on the strains $\boldsymbol{\varepsilon}$ and the internal variables Λ. $\bar{\mathcal{D}} = \bar{\mathcal{D}}(\Lambda, \dot{\Lambda})$ is the dissipation functional which is chosen in an appropriate manner such that the desired type of evolution equation results (e.g. rate-independent, viscos, elasto-viscoplastic). The great advantage of this modeling technique is the easy inclusion of material- (and thus model-) dependent constraints cons and it is used by "simple" definition of the Helmholtz free energy Ψ and the dissipation functional $\bar{\mathcal{D}}$. Particularly for the rate-independent and the elasto-viscoplastic approach, usually a Legendre transformation of $\bar{\mathcal{D}}$ is applied afterward for mathematical simplification. This results in yield functions of identical kind as they are known e.g. from plasticity. However, if complex constraints have to be fulfilled by the material model, for instance mass conservation, it turns out that the direct formulation of an appropriate yield function is a challenging issue (from the yield function the evolution equation can be derived using the orthogonality rule). This aspect is remarkably simplified using variational modeling techniques in which constraints can be taken into account by simple addition to the associated Lagrange functional. Further details may be taken from e.g. [30, 67] while the principle of the minimum of the dissipation potential for non-isothermal processes is presented in [103].

The presented material model is developed on the basis of works in [71] and [70]. Condensed versions can be found in [93, 92] and for the thermo-mechanically coupled case in [98] where the principle of the minimum of the dissipation potential for non-isothermal processes [103] has been applied. The micromechanical state for shape memory alloys undergoing functional fatigue is described by use of two internal variables for both the phases $\boldsymbol{\lambda}$ and the irreversible strains $\boldsymbol{\varepsilon}^{\mathrm{p}}$: $\Lambda = \{\boldsymbol{\lambda}, \boldsymbol{\varepsilon}^{\mathrm{p}}\}$. Hence,

$$\mathcal{L} = \dot{\Psi}\left(\boldsymbol{\varepsilon}, \boldsymbol{\lambda}, \boldsymbol{\varepsilon}^{\mathrm{p}}\right) + \bar{\mathcal{D}}\left(\dot{\boldsymbol{\lambda}}, \dot{\boldsymbol{\varepsilon}}^{\mathrm{p}}\right) + \text{cons} \quad \rightarrow \quad \operatorname*{stat}_{\dot{\boldsymbol{\lambda}}, \dot{\boldsymbol{\varepsilon}}^{\mathrm{p}}} \tag{10.2}$$

(see also [71, 70]).

10.2.2 Polycrystalline shape memory alloys

We examine a polycrystalline shape memory alloy on the material point level consisting of N differently oriented grains, Figure 10.2. The index j denotes quantities concerning the grain with orientation j which is characterized by three randomly chosen Euler angles β^j, ϕ^j and γ^j. The jth grain has a volume fraction ξ^j. The index i denotes the austenitic ($i = 0$) and the martensitic ($0 < i \leq n$) phases which are identified by means of their respective experimentally observed transformation strains $\boldsymbol{\eta}_i$. Choosing austenite as reference configuration leads to $\boldsymbol{\eta}_0 = \mathbf{0}$. Additionally, the phases possess different elastic constants that are comprised in the respective tensors $\mathbb{C}_i$. The polycrystalline character of the model is realized by rotating both the transformation strains and the elastic constants into each of the N assumed directions. Therefore, rotation matrices $\boldsymbol{R}^j$ are created using randomly chosen Euler angles. Finally, we calculate

$$\boldsymbol{\eta}_i^j = \left(\boldsymbol{R}^j\right)^T \cdot \boldsymbol{\eta}_i \cdot \boldsymbol{R}^j, \quad \mathbb{C}^j_{i,mnop} = R^j_{qm} R^j_{rn} R^j_{so} R^j_{tp} \mathbb{C}_{i,qrst} \tag{10.3}$$

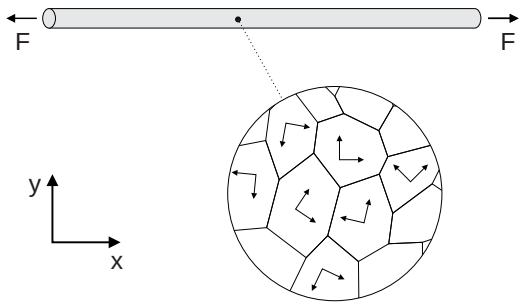

Figure 10.2: Material point level with different oriented grains.

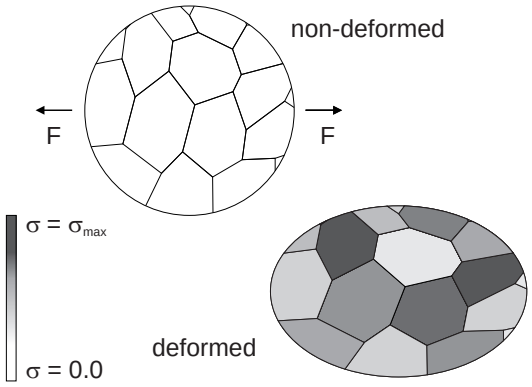

Figure 10.3: Non-deformed and deformed material point.

10.2.3 Energy, energy rate and driving forces

The used energetic approach is outgoing from a combined Voigt/Reuß bound. On the grain level, we assume that stress is constant in each single grain but may differ between the individual grains. This assumption implies a Reuß bound on the grain level. In contrast, on the material point level, thus for a homogenized ensemble of single grains that form in combination the polycrystal, we assume a Voigt bound: all grains possess the same averaged strain (that may change between in the respective phases within one grain). This procedure is motivated by the consideration that all grains in the material point perform the same displacements under load and thus a constant strain $\boldsymbol{\varepsilon}$ is present in all grains. This results in a variable stress for each grain, see Figure 10.3.

Considering the Voigt bound, the energy can be written in the form

$$\Psi = \sum_{j=1}^{N} \xi^j \left(\frac{1}{2} \left(\boldsymbol{\varepsilon} - \boldsymbol{\varepsilon}^{\mathrm{p}j}_{\mathrm{eff}} - \boldsymbol{\eta}^j_{\mathrm{eff}} \right) : \mathbb{C}^j_{\mathrm{eff}} : \left(\boldsymbol{\varepsilon} - \boldsymbol{\varepsilon}^{\mathrm{p}j}_{\mathrm{eff}} - \boldsymbol{\eta}^j_{\mathrm{eff}} \right) + c^j_{\mathrm{eff}} \right) \tag{10.4}$$

The variables marked like $(\cdot)^j_{\mathrm{eff}}$ are the effective values for the single orientations. They can be calculated by averaging the single quantities

$$\begin{aligned} \boldsymbol{\eta}^j_{\mathrm{eff}} &= \sum_{i=0}^{n} \lambda^j_i \boldsymbol{\eta}^j_i \qquad & \mathbb{C}^j_{\mathrm{eff}} &= \left(\sum_{i=0}^{n} \lambda^j_i \left(\mathbb{C}^j_i \right)^{-1} \right)^{-1} \\ c^j_{\mathrm{eff}} &= \sum_{i=0}^{j} \lambda^j_i c_i \qquad & \boldsymbol{\varepsilon}^{\mathrm{p}j}_{\mathrm{eff}} &= \sum_{i=0}^{n} \lambda^j_i \boldsymbol{\varepsilon}^{\mathrm{p}j}_i \end{aligned} \tag{10.5}$$

which results from a Reuß bound for each grain (see [71]). The plastic strains $\boldsymbol{\varepsilon}^{\mathrm{p}j}_i$ refer to the irreversible deformations of *each phase* in *each grain*. Thus, they describe the effect of micro-plasticity as explained in the introduction in Section 10.1. Of course, the use of plastic strains instead of a dislocation density corresponds to a homogenized description in terms of scales. However, we assume that this rough ansatz agrees well to the original model. The accumulation of plastic deformation is given in a macroscopic sense by the global plastic strain $\boldsymbol{\varepsilon}^{\mathrm{p}}_{\mathrm{eff}} = \left(\sum_{j=1}^{N} \xi^j \mathbb{C}^j_{\mathrm{eff}} \right)^{-1} : \left(\sum_{j=1}^{N} \xi^j \mathbb{C}^j_{\mathrm{eff}} : \boldsymbol{\varepsilon}^{\mathrm{p}j}_{\mathrm{eff}} \right)$. Following [87], the variable c_i denotes the caloric and thus temperature-dependent part of the energy

of phase i. The caloric energy for the austenite is denoted by c_0 and is zero for the martensitic variants. Furthermore, the time derivative of the energy in Equation (10.2) can be calculated with use of the chain rule

$$\dot{\Psi} = \frac{\partial \Psi}{\partial \boldsymbol{\varepsilon}} : \dot{\boldsymbol{\varepsilon}} + \sum_{j=1}^{N} \sum_{i=0}^{n} \frac{\partial \Psi}{\partial \lambda_i^j} \dot{\lambda}_i^j + \sum_{j=1}^{N} \sum_{i=0}^{n} \frac{\partial \Psi}{\partial \boldsymbol{\varepsilon}_i^{\mathrm{p}j}} : \dot{\boldsymbol{\varepsilon}}_i^{\mathrm{p}j} \tag{10.6}$$

Due to the later minimization of the Lagrange functional with respect to the rate of the internal variables, the first summand can be neglected in the Lagrange functional.

As usual, the thermodynamic force $\boldsymbol{P}$ acting on a thermodynamical flux $\dot{\Lambda}$ can be identified as $\boldsymbol{P} := -\frac{\partial \Psi}{\partial \Lambda}$. In the context of internal variables, $\boldsymbol{P}$ is termed driving force. Thus, the driving forces for volume fraction i in grain with orientation j, defined by $P_{\mathrm{t}i}^j$, and analogously for the corresponding plastic strain, defined by $\boldsymbol{P}_{\mathrm{p}i}^j$, can be calculated as

$$\begin{aligned} P_{\mathrm{t}i}^j &= -\frac{\partial \Psi}{\partial \lambda_i^j} \\ &= \xi^j \left[\frac{1}{2} \left(\boldsymbol{\sigma}^j \right)^{\mathrm{T}} : \left(\mathbb{C}_i^j \right)^{-1} : \boldsymbol{\sigma}^j + \left(\boldsymbol{\varepsilon}_i^{\mathrm{p}j} + \boldsymbol{\eta}_i^j \right) : \boldsymbol{\sigma}^j - c_i \right] \\ \boldsymbol{P}_{\mathrm{p}i}^j &= -\frac{\partial \Psi}{\partial \boldsymbol{\varepsilon}_i^{\mathrm{p}j}} = \xi^j \lambda_i^j \boldsymbol{\sigma}^j \end{aligned} \tag{10.7}$$

in which $\boldsymbol{\sigma}^j$ is the grain specific stress and volume averaging results in the total stress $\boldsymbol{\sigma}$

$$\boldsymbol{\sigma}^j = \mathbb{C}_{\mathrm{eff}}^j : \left(\boldsymbol{\varepsilon} - \boldsymbol{\varepsilon}_{\mathrm{eff}}^{\mathrm{p}j} - \boldsymbol{\eta}_{\mathrm{eff}}^j \right), \quad \boldsymbol{\sigma} = \sum_{j=1}^{N} \xi^j \boldsymbol{\sigma}^j \tag{10.8}$$

10.2.4 Dissipation functional

The quantity $\bar{\mathcal{D}}$ in Equation (10.2) is called dissipation functional. It has to be chosen appropriately so that evolution equations of a desired type result from the related stationarity problem (see Equation (10.2)). There exists no unique formulation for $\bar{\mathcal{D}}$. However, it is related to the amount of dissipated energy and it is used in comparable form in Hamilton's principle for the inclusion of dissipative forces. The only constraint in formulating a specific choice for $\bar{\mathcal{D}}$ is that $\bar{\mathcal{D}} \geq 0 \ \forall \Lambda, \dot{\Lambda}$ (see e.g. [30, 67]). A time-integration of $\bar{\mathcal{D}}$ equals the total amount of dissipated energy as has been shown in [102] where thermal experiments served as sole input for (non-cyclic) mechanical tension tests of NiTi wires. The simulated mechanical stress/strain relation equaled the experimentally observed one without any further model calibration.

For the current model, we assume that phase transformation and plastic strain evolve *in parallel* (which is also proven by experiments). Consequently, we chose an approach for $\bar{\mathcal{D}}$ which ensures evolution equations of quasi-static type (which requires $\bar{\mathcal{D}}$ to be homogeneous of order one). Then, the fundamental form of $\bar{\mathcal{D}}$ that fulfills the aforementioned requirements reads

$$\bar{\mathcal{D}} = \sum_{j=1}^{N} \xi^j r^j \sqrt{\sum_{i=0}^{n} \left(\dot{\lambda}_i^j \right)^2 + \alpha^j \sum_{i=0}^{n} \dot{\boldsymbol{\varepsilon}}_i^{\mathrm{p}j} : \dot{\boldsymbol{\varepsilon}}_i^{\mathrm{p}j}} \tag{10.9}$$

which yields a coupled evolution of $\boldsymbol{\lambda}$ and $\boldsymbol{\varepsilon}^{\mathrm{p}}$ as desired. The parameter r^j in Equation (10.9) is called dissipation parameter which is specified in 10.2.7. As can be seen later, it serves as an energetic threshold value that has to be overcome before an evolution of micostructure may take place. The parameter α^j accounts for the different energetic levels of the internal variables. It can be calculated by

$$\alpha^j = \left(\frac{Y_0}{r^j}\right)^2 \tag{10.10}$$

where Y_0 is the energetic barrier that has to be overcome before the plastic deformation without phase transformation can start. Thus, it is comparable with the material's plastic yield limit.

10.2.5 Constraints

Finally, the constraints cons in the Lagrange functional (10.2) need to be specified. In our case, there are three constraints: on the one hand the mass conservation

$$\sum_{i=0}^{n} \dot{\lambda}_i^j = 0 \quad \forall\ j \tag{10.11}$$

and the non-negativity of the volume fractions

$$\lambda_i^j \geq 0 \quad \forall\ i,j \tag{10.12}$$

on the other hand the volume preservation of the plastic strains

$$\dot{\boldsymbol{\varepsilon}}_i^{\mathrm{p}j} : \boldsymbol{I} = 0 \quad \forall\ i,j \tag{10.13}$$

where $\boldsymbol{I}$ denotes the unity tensor. These constraints can be taken into account by use of Lagrange parameters (κ_{t}^j and $\kappa_{\mathrm{p}i}^j$) and Kuhn-Tucker parameters γ_i^j.

10.2.6 Evolution equations and yield function

With use of Equations (10.6), (10.7) and (10.9) and the consideration of the constraints in Equations (10.11-10.13) the Lagrange functional in Equation (10.2) can be written as

$$\begin{aligned}
\mathcal{L} \;=\; & -\sum_{j=1}^{N}\sum_{i=0}^{n} P_{\mathrm{t}}^j \dot{\lambda}_i^j - \sum_{j=1}^{N}\sum_{i=0}^{n} \boldsymbol{P}_{\mathrm{p}i}^j : \dot{\boldsymbol{\varepsilon}}_i^{\mathrm{p}j} \\
& + \sum_{j=1}^{N} \xi^j r^j \sqrt{\sum_{i=0}^{n}\left(\dot{\lambda}_i^j\right)^2 + \alpha^j \sum_{i=0}^{n} \dot{\boldsymbol{\varepsilon}}_i^{\mathrm{p}j} : \dot{\boldsymbol{\varepsilon}}_i^{\mathrm{p}j}} \\
& + \sum_{j=1}^{N} \kappa_{\mathrm{t}}^j \sum_{i=0}^{n} \dot{\lambda}_i^j - \sum_{j=1}^{N}\sum_{i=0}^{n} \gamma_i^j \dot{\lambda}_i^j + \sum_{j=1}^{N}\sum_{i=0}^{n} \kappa_{\mathrm{p}i}^j \dot{\boldsymbol{\varepsilon}}_i^{\mathrm{p}j} : \boldsymbol{I}
\end{aligned} \tag{10.14}$$

Minimization of Equation (10.14) with respect to the rates of the internal variables leads to their evolution equations

$$\dot{\lambda}_i^j = \rho^j \frac{1}{\xi^j} \mathrm{dev}_{\mathcal{A}^j} P_{\mathrm{t}i}^j \ , \quad \dot{\boldsymbol{\varepsilon}}_i^{\mathrm{p}j} = \rho^j \frac{1}{\xi^j \alpha^j} \mathrm{dev} P_{\mathrm{p}i}^j \ , \quad \forall i \in \mathcal{A}^j \tag{10.15}$$

where a consistency parameter $\rho^j := \sqrt{\sum_{i=0}^{n}\left(\dot{\lambda}_i^j\right)^2 + \alpha^j \sum_{i=0}^{n} \dot{\boldsymbol{\varepsilon}}_i^{\mathrm{p}j} : \dot{\boldsymbol{\varepsilon}}_i^{\mathrm{p}j}}\Big/(\xi^j r^j)$ was introduced.

For the calculation, an active-set strategy is used. Therefore, $n_{\mathcal{A}^j}$ denotes the number of active phases in the active set $\mathcal{A}^j$ that fulfill the constraint in Equation (10.12)

$$\mathcal{A}^j = \left\{ i \,|\, \lambda_i^j > 0 \right\} \cup \left\{ i \,|\, \lambda_i^j = 0 \wedge \dot{\lambda}_i^j > 0 \right\} \tag{10.16}$$

The active deviator $\mathrm{dev}_{\mathcal{A}^j} P_{\mathrm{t}i}^j$ and the deviator of the plastic strains $\mathrm{dev} P_{\mathrm{p}i}^j$ are defined as

$$\mathrm{dev}_{\mathcal{A}^j} P_{\mathrm{t}i}^j := P_{\mathrm{t}i}^j - \frac{1}{n_{\mathcal{A}^j}} \sum_{k \in \mathcal{A}^j} P_{\mathrm{t}k}^j \,, \quad \mathrm{dev} P_{\mathrm{p}i}^j := \boldsymbol{P}_{\mathrm{p}i}^j - \frac{1}{3}\left(\boldsymbol{P}_{\mathrm{p}i}^j : \boldsymbol{I}\right)\boldsymbol{I} \tag{10.17}$$

Subsequently, the use of a Legendre transformation results in one yield function for every grain

$$\Phi^j = \frac{1}{\xi^j} \sum_{i=0}^{n} \left(\mathrm{dev}_{\mathcal{A}^j} P_{\mathrm{t}i}^j \right)^2 + \frac{1}{\xi^j \alpha^j} \sum_{i=0}^{n} \left(\mathrm{dev} P_{\mathrm{p}i}^j : \mathrm{dev} P_{\mathrm{p}i}^j \right) - \xi^j \left(r^j \right)^2 \overset{!}{\leq} 0 \tag{10.18}$$

In addition, the Kuhn-Tucker conditions $\rho^j \geq 0$, $\Phi^j \leq 0$ and $\rho^j \Phi^j = 0$ have to be fulfilled for every grain orientation j.

The current material model has only one consistency parameter ρ^j and one yield function Φ^j for every grain that describe the coupled evolution of plastic deformations on the one hand and the phase transformations on the other hand. Hence, the approach describes the physical effects in a realistic manner: phase transformation automatically leads to plastic deformation.

10.2.7 Dissipation parameter

Due to the incompatibility between the parent phase of austenite and martensite, dislocations, which are synthesized in the plastic strains $\boldsymbol{\varepsilon}^{\mathrm{p}}$ in the current modeling approach, are produced during phase transformation. The remaining dislocations cause a stress field which triggers phase transformation to start here. In an energetic consideration, this phenomenon can be taken into account that –locally– the amount of external energy provided to the system can be reduced in order to initiate phase transformation or identically that the amount of dissipated energy is reduced. This is also the reason for the decrease of the stress plateau in a mesoscopic setting. This aspect is included into our model in terms of the dissipation functional $\bar{\mathcal{D}}$. Hence, an approach for the dissipation parameter r^j is necessary to predict the material's functional fatigue. The motivation are cyclic DSC measurements by Burow [27] and the investigations in Junker *et al.* [102], that show that the material parameter r^j evolves under cyclic loading, in combination with the examined martensite stabilizing feature of the dislocations formed during the transformation process, e.g. [192]. The dislocations are a result of martensitic needles developing in the material, see Figure 10.4 and [172]. Stress was assumed to be constant in every grain orientation j. Thus, dislocations of a previous load step serve as nuclei for the entire grain so that the number of dislocations determines the reduction of energetic effort to trigger phase transformations. As a result, the dissipation parameter is updated for every load step.

Due to the fact, that the plastic strain is not an experimentally measurable quantity and that the function of r^j has to be valid for every initial value of the plastic strain, $r = r\left(\varepsilon_{\mathrm{eff}}^{\mathrm{p}j}\right)$ is not explicitly

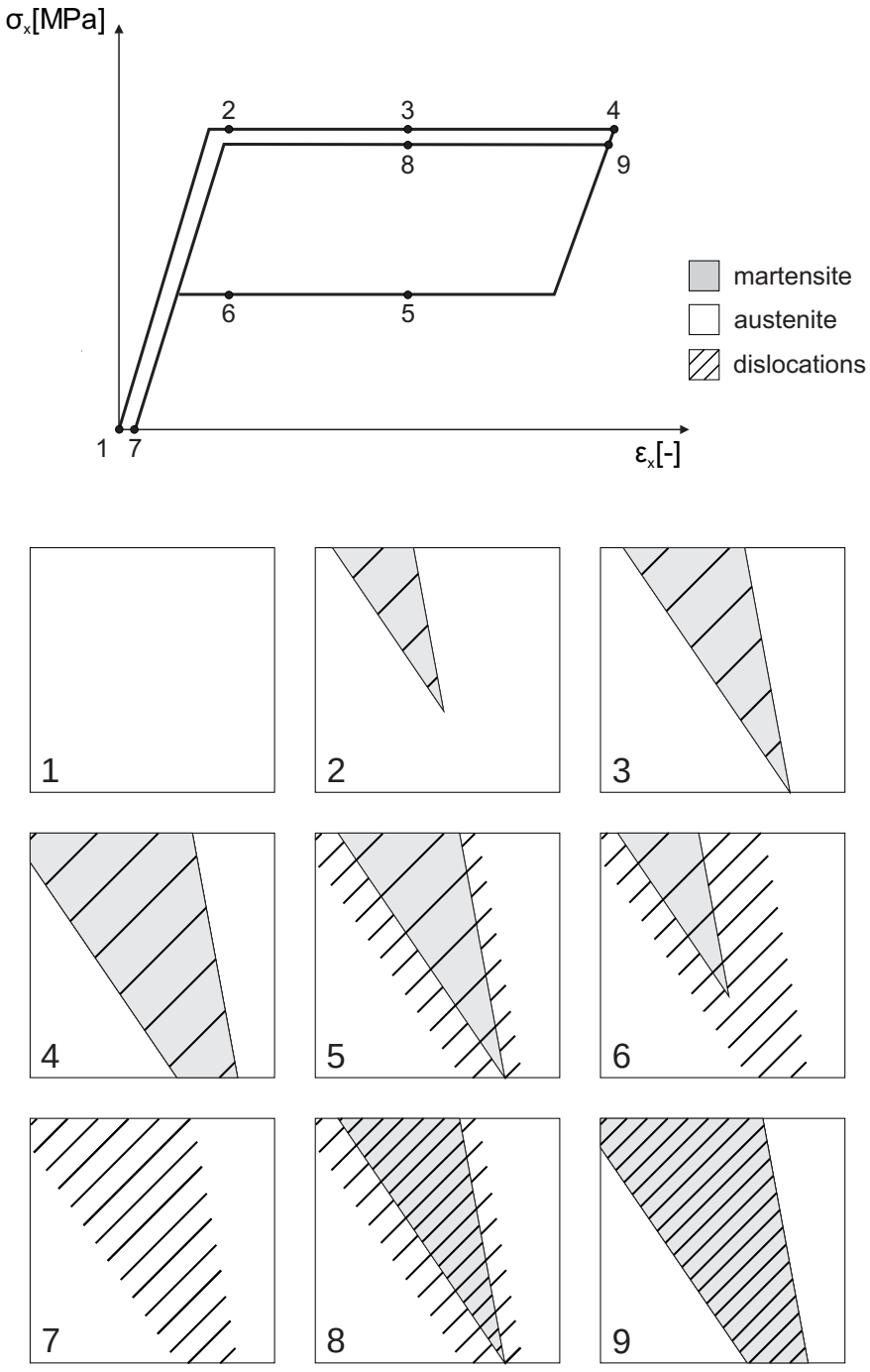

Figure 10.4: Dependency of the dislocation development on the phase transformation. Schematic plots after the experimental investigations provided by Simon *et al.* in [172].

expressible. Therefore, we formulate r^j as a function of the plastic strain's rate and integrate it over time. The result is the necessary function of the evolved plastic strain. With respect to the mentioned stabilization of martensite due to the formed dislocations, we assume that the dislocations favor the transformation from austenite to martensite and delay the back transformation. Following (10.15), the transformation direction is given by the active deviator of the austenite $\mathrm{dev}_{\mathcal{A}^j} P^j_{\mathrm{t0}}$.

On the other hand, and based on the dislocation theory, e.g. [116, 184], the higher the number of dislocations is the more energy is necessary for the development of new dislocations. Therefore, the factor α^j is likewise chosen as a function of the plastic strain. Because of the converging character of the SMAs' material behavior and considering Equation (10.10), we chose the following functions for the two parameters

$$\begin{aligned} r^j &= r^{j,0}\left[\left(\frac{1}{2} - \frac{\arctan\left(s\ \mathrm{dev}_{\mathcal{A}^j} P^j_{\mathrm{t0}}\right)}{\pi}\right) f_{\mathrm{I}}\left(\varepsilon^{\mathrm{p}j}_{\mathrm{eff}}\right) + \left(\frac{1}{2} + \frac{\arctan\left(s\ \mathrm{dev}_{\mathcal{A}^j} P^j_{\mathrm{t0}}\right)}{\pi}\right) f_{\mathrm{II}}\left(\varepsilon^{\mathrm{p}j}_{\mathrm{eff}}\right)\right] \\ \alpha^j &= \left(\frac{Y_0}{r^j}\right)^2 f_{\mathrm{III}}\left(\varepsilon^{\mathrm{p}j}_{\mathrm{eff}}\right) \end{aligned} \tag{10.19}$$

where $r^{j,0}$ denotes the initial value of the dissipation parameter. The approach for r^j accounts for a varying dissipation, depending on the sign of the rate of austenite (which is given in terms of $\mathrm{dev}_{\mathcal{A}^j} P^j_{\mathrm{t0}}$). The arctan function allows for a smooth transition between both evolution directions, while the parameter s controls the width of the jump. The functions f_{I}, f_{II} and f_{III} have the following character

$$\begin{aligned} f_{\mathrm{I}}\left(\varepsilon^{\mathrm{p}j}_{\mathrm{eff}}\right) &= \exp\left(-b_{\mathrm{I}}|\varepsilon^{\mathrm{p}j}_{\mathrm{eff}}|\right) \\ f_{\mathrm{II}}\left(\varepsilon^{\mathrm{p}j}_{\mathrm{eff}}\right) &= 1 + b_{\mathrm{II}}\left(1 - f_{\mathrm{I}}\left(\varepsilon^{\mathrm{p}j}_{\mathrm{eff}}\right)\right) \\ f_{\mathrm{III}}\left(\varepsilon^{\mathrm{p}j}_{\mathrm{eff}}\right) &= -\left(\frac{1}{b_{\mathrm{III}}}|\varepsilon^{\mathrm{p}j}_{\mathrm{eff}}| - 1\right)^{-1} \end{aligned} \tag{10.20}$$

and are numerically specified in Section 10.4.

10.3 Algorithmic implementation

The complex material behavior is described by the evolution equations (10.15), the yield function (10.18), the Kuhn-Tucker conditions, and the adaptations of the model parameters as presented in Equation (10.19) which constitutes as a non-linear system of differential equations including constraints. For a numerical analysis, a time integration has to be executed whereas the yield functions are solved using a Newton scheme. A detailed description of the numerical treatment is presented in Algorithm 2.

Due to the fact that we are using very small load steps, it is possible to further discretize (10.19) and thus, update r^j and α^j with respect to the prior load step's internal variables (operator split).

Outgoing from start values of the internal variables and a given value for the strain $\boldsymbol{\varepsilon}^{l+1}$ at the load step $l+1$, the yield function Φ^j is calculated for every grain. When a zero tolerance tol is exceeded, Newton's method is used to calculate the internal variables for the current load step which ensures

$\Phi^j < \text{tol}$. The updated internal variables serve as input parameters for the next load step.

Input: $\varepsilon^{\text{l+1}}$, $\boldsymbol{\lambda}^{\text{l}}$,$\varepsilon^{\text{p,l}}$
Calc: $\left(\text{dev}_{\mathcal{A}^j} P_{\text{t}i}^j\right)^{\text{l}} = \left(\text{dev}_{\mathcal{A}^j} P_{\text{t}i}^j\right)^{\text{l}} \left(\varepsilon^{\text{l+1}}, \boldsymbol{\lambda}^{\text{l}}, \varepsilon^{\text{p,l}}\right)$
Calc: $\left(\text{dev} P_{\text{p}i}^j\right)^{\text{l}} = \left(\text{dev} P_{\text{p}i}^j\right)^{\text{l}} \left(\varepsilon^{\text{l+1}}, \boldsymbol{\lambda}^{\text{l}}, \varepsilon^{\text{p,l}}\right)$
Calc: $\left(r^j\right)^{\text{l+1}} = \left(r^j\right)^{\text{l+1}} \left(\varepsilon^{\text{p,l}}, \left(\text{dev}_{\mathcal{A}^j} P_{\text{t}0}^j\right)^{\text{l}}\right)$, $\left(\alpha^j\right)^{\text{l+1}} = \left(\alpha^j\right)^{\text{l+1}} \left(\left(r^j\right)^{\text{l+1}}, \varepsilon^{\text{p,l}}\right)$
Calc: $\Phi^j = \Phi^j \left(\varepsilon^{\text{l+1}}, \boldsymbol{\lambda}^{\text{l}}, \varepsilon^{\text{p,l}}\right)$

Set: $\boldsymbol{\lambda}^{\text{l+1}} = \boldsymbol{\lambda}^{\text{l}}$, $\varepsilon^{\text{p,l+1}} = \varepsilon^{\text{p,l}}$, $\rho^j = 0$

if $\Phi^j \leq \text{tol} \forall j$ **then**
  CONTINUE with next load step: l+1 → l+2
end
else
  while $\exists j : \Phi^j > \text{tol}$ **do**
    $\lambda_i^{j,\text{l+1}} = \lambda_i^{j,\text{l}} + \dfrac{\rho^j}{\xi^j} \left(\text{dev}_{\mathcal{A}^j} P_{\text{t}i}^j\right)^{\text{l}} \quad \forall\ i \in \mathcal{A}^j$
    $\left(\varepsilon_i^{\text{p},j}\right)^{\text{l+1}} = \left(\varepsilon_i^{\text{p},j}\right)^{\text{l}} + \dfrac{\rho^j}{\xi^j \left(\alpha^j\right)^{\text{l+1}}} \left(\text{dev} P_{\text{p}i}^j\right)^{\text{l}} \quad \forall\ i \in \mathcal{A}^j$
    Calc: $\left(\text{dev}_{\mathcal{A}^j} P_{\text{t}i}^j\right)^{\text{l+1}} = \left(\text{dev}_{\mathcal{A}^j} P_{\text{t}i}^j\right)^{\text{l+1}} \left(\varepsilon^{\text{l+1}}, \boldsymbol{\lambda}^{\text{l+1}}, \varepsilon^{\text{p,l+1}}\right)$
    Calc: $\left(\text{dev} P_{\text{p}i}^j\right)^{\text{l+1}} = \left(\text{dev} P_{\text{p}i}^j\right)^{\text{l+1}} \left(\varepsilon^{\text{l+1}}, \boldsymbol{\lambda}^{\text{l+1}}, \varepsilon^{\text{p,l+1}}\right)$
    Calc: $\Phi^j = \Phi^j \left(\varepsilon^{\text{l+1}}, \boldsymbol{\lambda}^{\text{l+1}}, \varepsilon^{\text{p,l+1}}\right)$
    if $\exists j : \Phi^j > \text{tol}$ **then**
      $\lambda_i^{j,\text{nt}} = \lambda_i^{j,\text{l}} + \dfrac{\rho^j + \text{tol}_{\text{nt}}}{\xi^j} \left(\text{dev}_{\mathcal{A}^j} P_{\text{t}i}^j\right)^{\text{l}} \quad \forall\ i \in \mathcal{A}^j$
      $\left(\varepsilon_i^{\text{p},j}\right)^{\text{nt}} = \left(\varepsilon_i^{\text{p},j}\right)^{\text{l}} + \dfrac{\rho^j + \text{tol}_{\text{nt}}}{\xi^j \left(\alpha^j\right)^{\text{l+1}}} \left(\text{dev} P_{\text{p}i}^j\right)^{\text{l}} \quad \forall\ i \in \mathcal{A}^j$
      Calc: $\left(\text{dev}_{\mathcal{A}^j} P_{\text{t}i}^j\right)^{\text{nt}} = \left(\text{dev}_{\mathcal{A}^j} P_{\text{t}i}^j\right)^{\text{nt}} \left(\varepsilon^{\text{l+1}}, \boldsymbol{\lambda}^{\text{nt}}, \varepsilon^{\text{p,nt}}\right)$
      Calc: $\left(\text{dev} P_{\text{p}i}^j\right)^{\text{nt}} = \left(\text{dev} P_{\text{p}i}^j\right)^{\text{nt}} \left(\varepsilon^{\text{l+1}}, \boldsymbol{\lambda}^{\text{nt}}, \varepsilon^{\text{p,nt}}\right)$
      Calc: $\Phi^{j,\text{nt}} = \Phi^{j,\text{nt}} \left(\varepsilon^{\text{l+1}}, \boldsymbol{\lambda}^{\text{nt}}, \varepsilon^{\text{p,nt}}\right)$
      $\rho^j = \rho^j - \dfrac{\Phi^j}{\Phi^{j,\text{nt}} - \Phi^j} \text{tol}_{\text{nt}} \quad \forall j : \Phi^j > \text{tol}$
      if $\exists j : \rho^j < -\text{tol}$ **then**
        ABORT
      end
    end
  end
end

Update: $\lambda_i^{j,\text{l}} = \lambda_i^{j,\text{l+1}}$, $\left(\varepsilon_i^{\text{p},j}\right)^{\text{l}} = \left(\varepsilon_i^{\text{p},j}\right)^{\text{l+1}}$

Algorithm 2: Algorithmic implementation.

10.4 Numerical results

10.4.1 Uniform orientation distribution function

We present numerical simulations for the SMA NiTi. The material data (elastic constants and transformation strains) is taken from [194]. For demonstration, a cycled tri-axial tension test with a maximum strain of 0.06 is simulated. Thus,

$$\boldsymbol{\varepsilon} = \hat{\varepsilon} \begin{pmatrix} 1 & 0 & 0 \\ 0 & -0.41 & 0 \\ 0 & 0 & -0.41 \end{pmatrix} \tag{10.21}$$

with $\hat{\varepsilon} \in [0, 0.06]$.

The start value of the dissipation parameter is $r^{j,0} = 0.011\,\mathrm{GPa}$, the temperature dependent part for the austenitic phase is $c_0 = -0.046\,\mathrm{GPa}$ and the factor Y_0 is $3.0\,\mathrm{GPa}$. For the moment, we are not able to provide experimental data for the parameters in the functions f_{I}, f_{II} and f_{III}. Hence, we chose them to be

$$\begin{aligned} f_{\mathrm{I}}\left(\boldsymbol{\varepsilon}_{\mathrm{eff}}^{\mathrm{p}j}\right) &= \exp\left(-700|\boldsymbol{\varepsilon}_{\mathrm{eff}}^{\mathrm{p}j}|\right) \\ f_{\mathrm{II}}\left(\boldsymbol{\varepsilon}_{\mathrm{eff}}^{\mathrm{p}j}\right) &= 1 + 0.7\left(1 - f_{\mathrm{I}}\left(\boldsymbol{\varepsilon}_{\mathrm{eff}}^{\mathrm{p}j}\right)\right) \\ f_{\mathrm{III}}\left(\boldsymbol{\varepsilon}_{\mathrm{eff}}^{\mathrm{p}j}\right) &= -\left(\frac{1}{0.004}|\boldsymbol{\varepsilon}_{\mathrm{eff}}^{\mathrm{p}j}| - 1\right)^{-1} \end{aligned} \tag{10.22}$$

The transition parameter for the evolution directions is set to $s = 10^6$.

For a first investigation, we assume a uniform orientation distribution function for the individual grains which implies $\xi^j = \mathrm{const}\ \forall j$. The results for 20 different oriented grains ($\Rightarrow \xi^j = 1/20$) and 10 load cycles are presented in Figures 10.5, 10.6 and 10.7: precisely, Figure 10.5 shows the stress/strain diagram. Compared with the experimental findings of [192] presented in Figure 10.1, the calculation shows similar effects: particularly the upper stress plateau decreases and in addition, there is an irreversible strain which increases with every load cycle. Also the convergence of the plastic strain growth and the plateau decrease is visible. However, there are also some differences compared to the experiment: on the one hand there is a softer transition between the linear elastic regions and the stress plateaus; on the other hand the stress does not remain constant but it is still increasing during phase transformations. This phenomenon can be investigated with increased physical reliability first during future finite element simulations in which boundary value problems correctly associated to experiments provide a more realistic setting compared to the prescribed strain state here. On the other hand, the choice of the fixed grain orientation distribution function might play also a role which is discussed in the next section.

Figure 10.6 shows the development of the effective plastic strain's component in tensile direction $\varepsilon_{\mathrm{eff},xx}^{\mathrm{p}}$. The plastic strain increases with every load cycle. Interestingly, the plastic strain also decreases during unloading. This effect begins in the third cycle and intensifies with every following cycle. At first glance this might seem surprising. However, there exists one possible physical explanation for this phenomenon: the dislocations develop in different directions and thus, with increasing number of dislocations, the possibility increases that two dislocations collide that possess opposite signs. In

this case, they extinguish each other which reduces the (macroscopic) plastic strain. On the other hand, this aspect has not been taken into account "directly" by our model since it does not include dislocation theory. Hence, a comparison to dislocation-based models has to be performed in future investigations. Figure 10.7 shows the development of the austenitic volume fraction. As can be seen, the phase transformation is fairly identical for the respective load cycles.

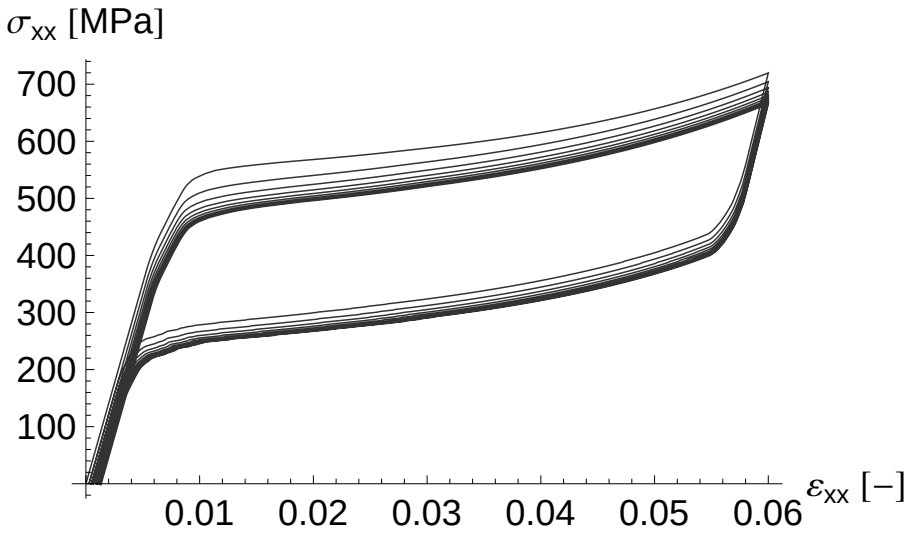

Figure 10.5: Tension test, stress/strain diagram, 20 orientations, 10 load cycles ($q = 0$).

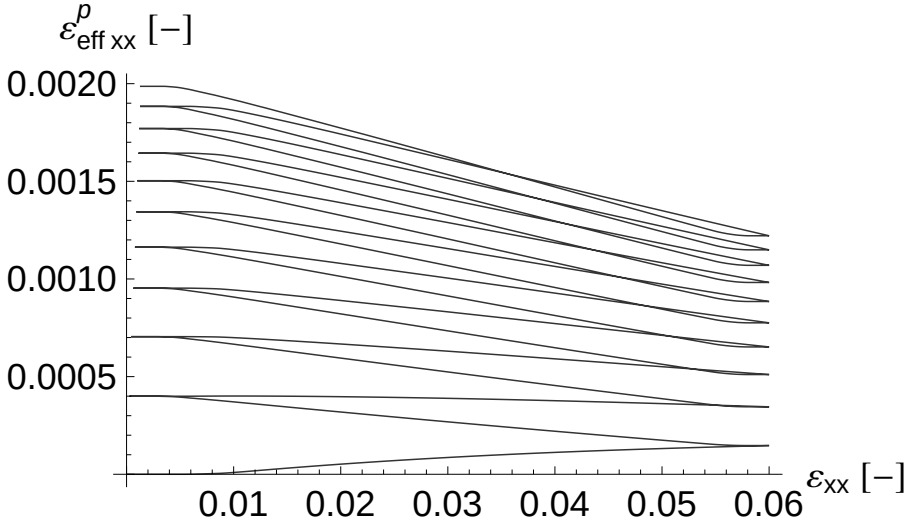

Figure 10.6: Tension test, development of plastic strains, 20 orientations, 10 load cycles ($q = 0$).

To examine the effect of the increasing stress during phase transformation, we simulated a tension test for 20 orientations and one load cycle. Figure 10.8 shows the stress/strain diagrams of the 20 orientations individually. Due to the concept of the combined Voigt/Reuß bound, the stress is not constant in the entire material point and the phase transformations in the grains take place at different loads.

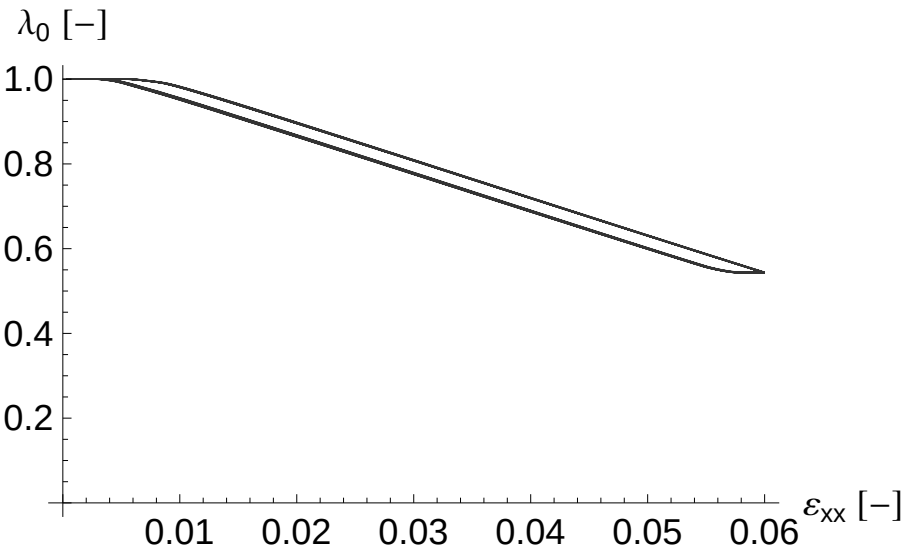

Figure 10.7: Tension test, development of austenitic volume fraction, 20 orientations, 10 load cycles ($q = 0$).

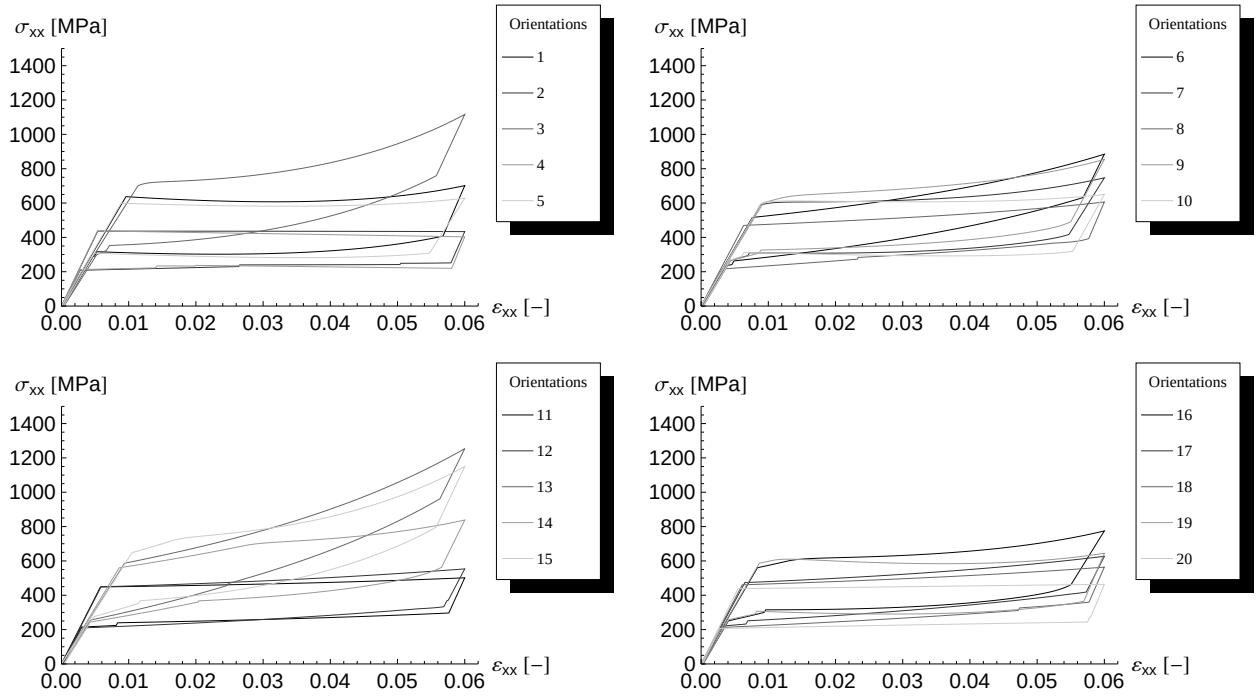

Figure 10.8: Tension test, stress/strain diagrams for the respective orientations ($q = 0$).

10.4.2 Orientation distribution function including stochastic fluctuations

Every orientation of the first two simulation examples has the same volume fraction $\xi^j = \text{const}$. In contrast, the grain orientation's distribution of a real NiTi is not as equally distributed as implied by a constant ξ^j for all grain orientations. This might influence the local and consequently the global stress response. To account for this, we adapt in this subsection the approach in [70] to calculate the Young measure for the volume fraction of grains ξ^j by

$$\bar{\xi}^j = \max_{k=1,\dots,6} \left[\boldsymbol{n}_{\text{pref}} \cdot \boldsymbol{R}^j \cdot \boldsymbol{n}_{\{1,0,0\},k} \right]^{-q} \tag{10.23}$$

with the set of $\{1,0,0\}$-austenite normal vectors

$$\boldsymbol{n}_{\{1,0,0\},k} \in \left\{ \begin{pmatrix} \pm 1 \\ 0 \\ 0 \end{pmatrix}, \begin{pmatrix} 0 \\ \pm 1 \\ 0 \end{pmatrix}, \begin{pmatrix} 0 \\ 0 \\ \pm 1 \end{pmatrix} \right\} \tag{10.24}$$

The exponent q in Equation (10.23) is a measure for the stochastic influence. In the following, it is assumed to be 5. The quantity $\boldsymbol{n}_{\text{Pref}}$ is the given preferred orientation and $\boldsymbol{R}^j$ is the rotation matrix of orientation j. Due to the condition $\sum_{j=1}^{N} \xi^j = 1$, the volume fractions are normalized by

$$\xi^j = \frac{\bar{\xi}^j}{\sum_{j=1}^{N} \bar{\xi}^j} \tag{10.25}$$

The stress/strain diagrams for the different orientations correspond to Figure 10.8. The macroscopic stress/strain diagram, which results of the homogenized behavior of the individual grains [see Equation (10.8)], is presented in Figure 10.9. The unequally distributed volume fractions for the grains, given in terms of ξ^j, are illustrated in Figure 10.10.

Obviously, the consideration of the material's stochastic fluctuation leads to results that are more expected from experimental observations of tension tests than the previous simulation: the stress plateau is nearly horizontal and there is a more distinct transition between the elastic regions and the stress-plateaus. This aspect has also to be investigated further in future finite element simulations. Figure 10.11 shows the stress/strain diagram resulting from a tension test with stochastic fluctuation and 20 orientations for ten load cycles.

Finally, same simulations but with 100 load cycles show the convergence of the stress plateaus and the plastic strain. The referring diagrams are presented in Figures 10.12 and 10.13. They prove empirically that both the plateau stresses and the amount of plastic strains tends to some limit values.

10.4.3 Parameter study

The modeling of the functional fatigue is based on the rather phenomenological assumptions for the parameters in Equations (10.19) and (10.20). We now examined the influence of the model parameters Y_0, b_{I}, b_{II}, and b_{III}. The single parameters are varied separately, therefore the other parameters are fixed. The basic values for the model parameters are shown in Table 10.1. The results are presented

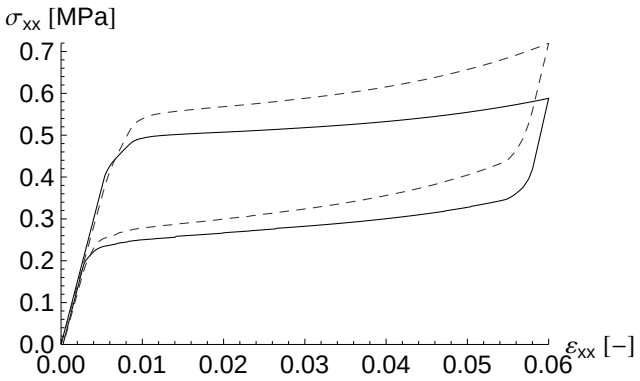

Figure 10.9: Tension test, stress/strain diagram, 20 orientations, 1 load cycle, without (dashed) and with stochastic fluctuation ($q = 5$).

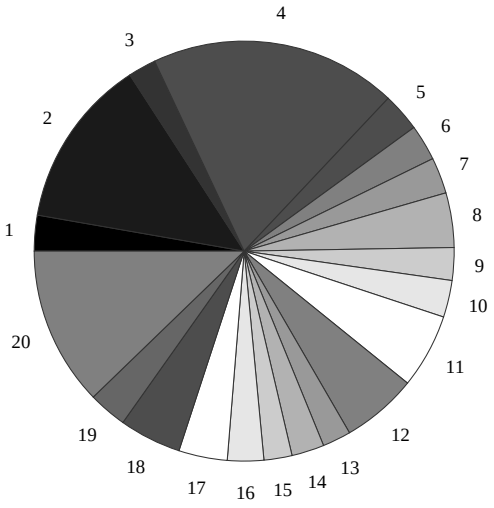

Figure 10.10: Orientation distribution, with stochastic fluctuation ($q = 5$).

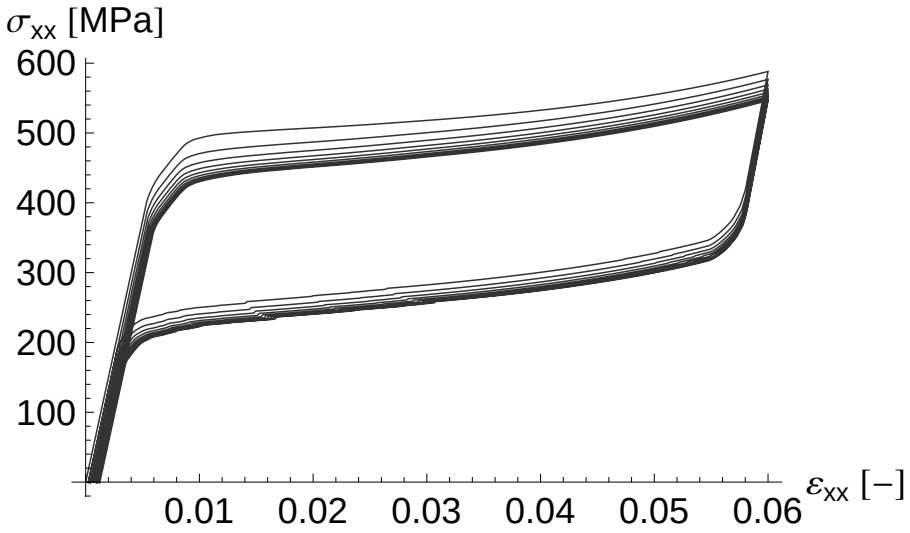

Figure 10.11: Tension test, stress/strain diagram, 20 orientations, 10 load cycles, with stochastic fluctuation ($q = 5$).

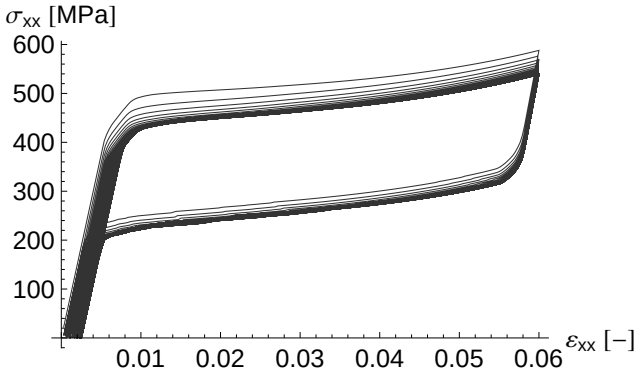

Figure 10.12: Tension test, stress/strain diagram, 20 orientations, 100 load cycles, with stochastic fluctuation ($q = 5$).

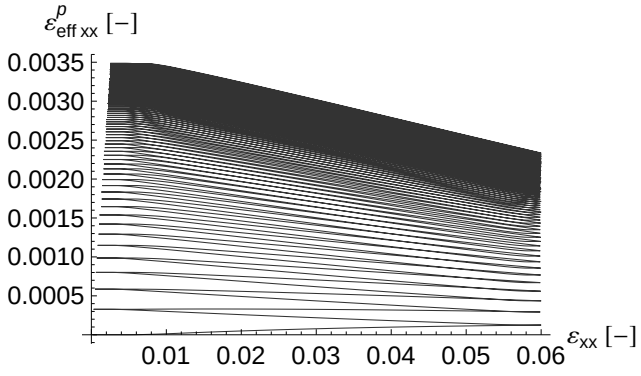

Figure 10.13: Tension test, development of plastic strains, 20 orientations, 100 load cycles, with stochastic fluctuation ($q = 5$).

in Figures 10.14 to 10.17 in which the central results are always those from Figures 10.5 and 10.6 to provide an easy comparison.

The variation of the yield limit for the purely plastic deformation Y_0 shows that the smaller Y_0 the more plastic strain is developed, which also results in a faster convergence of the plateau decrease due to the parallel converging character of the functions (10.20) (see Figure 10.14). The model parameters b_{I} and b_{II} have a similar influence on the material behavior: with an increasing factor b_{I}, the effect of functional fatigue – precisely the decrease of the stress plateaus – becomes stronger (see Figure 10.15). The parameter b_{II} also influences the strength of the plateau decrease but only of the lower one (see Figure 10.16). The factor b_{III} directly influences the amount of produced plastic strain. The higher b_{III} the more plastic strain evolves and the stronger the effect of fatigue is (see Figure 10.17).

Y_0	3.0 GPa
b_{I}	700 [-]
b_{II}	0.7 [-]
b_{III}	0.004 [-]

Table 10.1: Basic values for the separately varied parameters.

10.5 Conclusions and Outlook

In this paper, we developed an advanced material model for the functional fatigue in polycrystalline shape memory alloys. With use of a coupled dissipation functional we developed evolution equations for the volume fractions and the plastic strain in a way that both internal variables develop in parallel. Thus, phase transformation is directly connected with developing dislocations (modeled in terms of plastic strains) and only one yield function and one consistency parameter are used. The model is completed by phenomenological functions that account for the cycle-dependent character of the material behavior. The model quantity that "counts" the number of cycles is the plastic strain which is more realistic than the real cycle number. We investigated the influence of the grain orientation

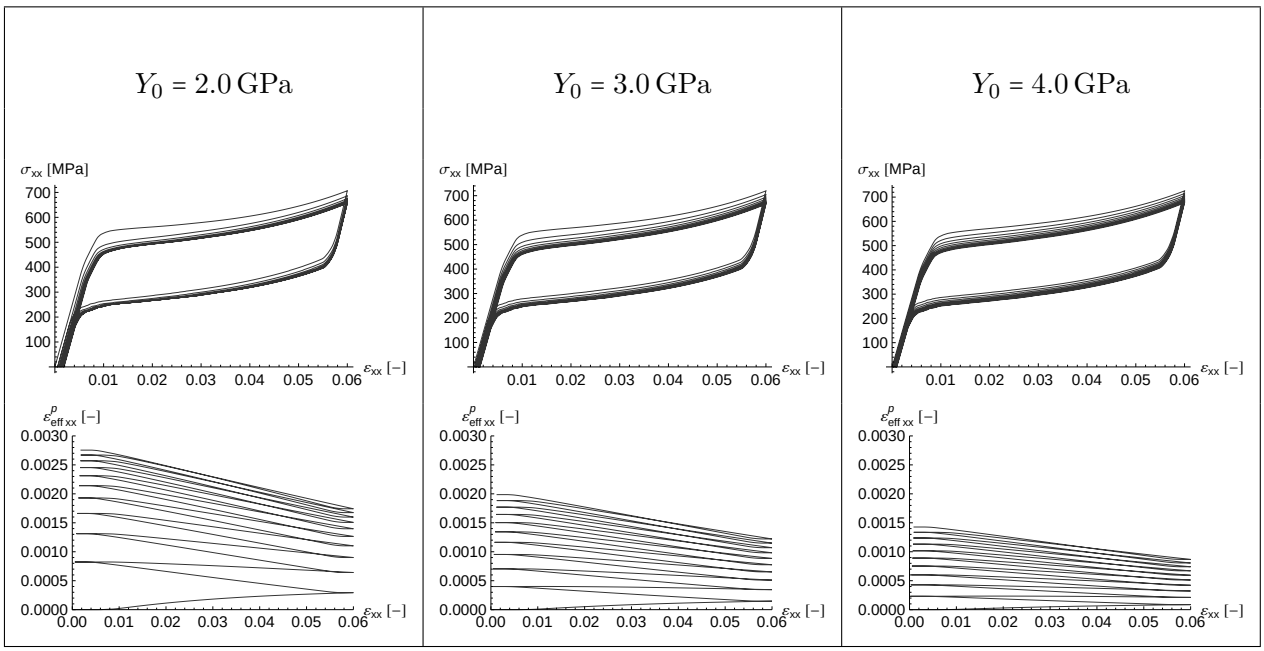

Figure 10.14: Variation of Y_0 with fixed values for b_I, b_II and b_III, see Table 10.1. Central result equals Figures 10.5 and 10.6.

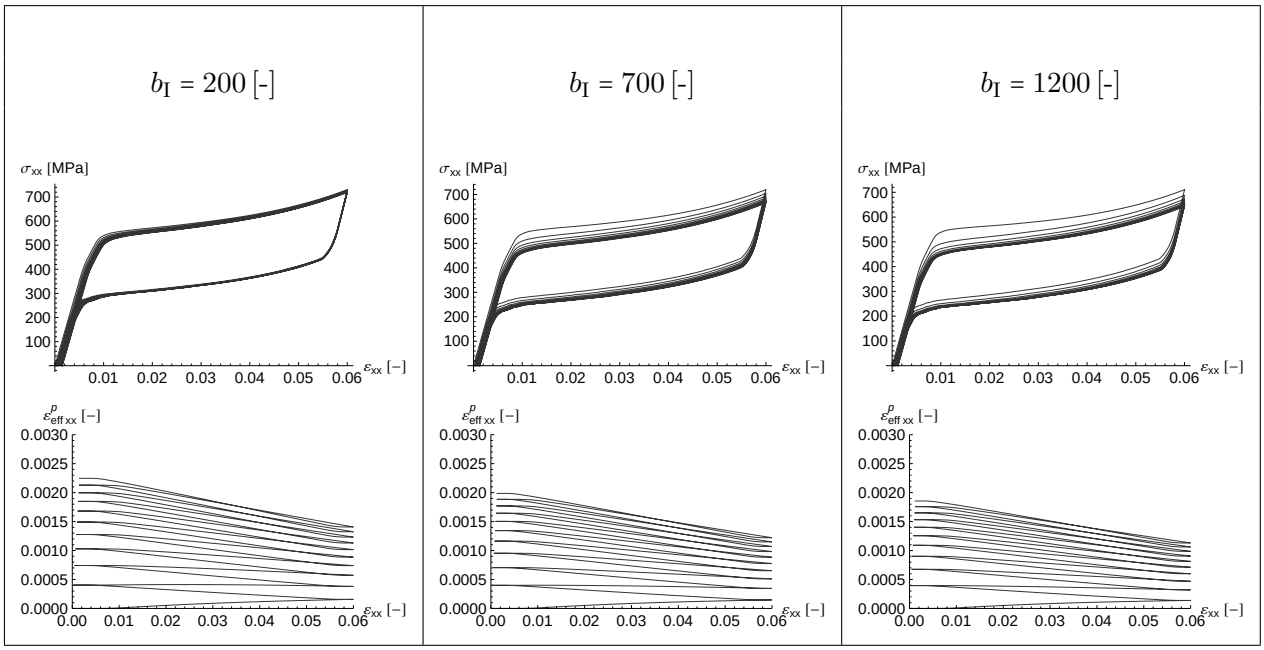

Figure 10.15: Variation of b_I with fixed values for Y_0, b_II and b_III, see Table 10.1. Central result equals Figures 10.5 and 10.6.

distribution function via numerical experiments and examined the impact of the phenomenological model parameters. These results, particularly the results with stochastic fluctuation, showed a good agreement with the experimentally observed material behavior at least in a qualitatively manner.

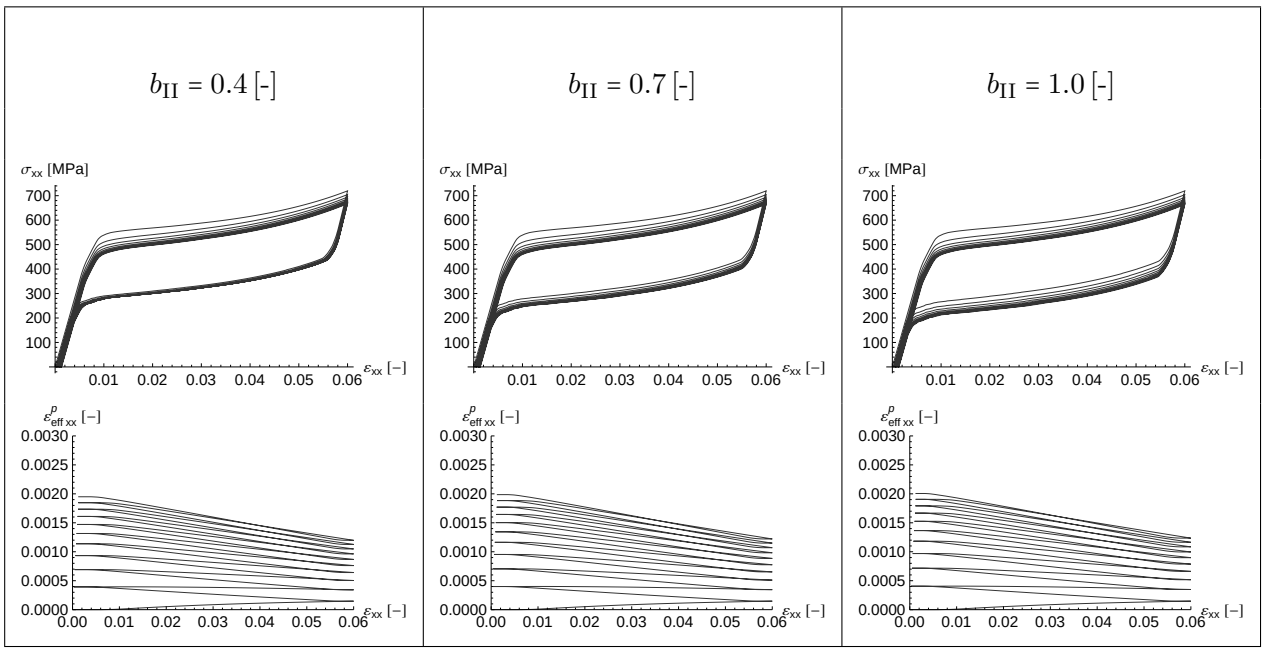

Figure 10.16: Variation of b_{II} with fixed values for Y_0, b_{I} and b_{III}, see Table 10.1. Central result equals Figures 10.5 and 10.6.

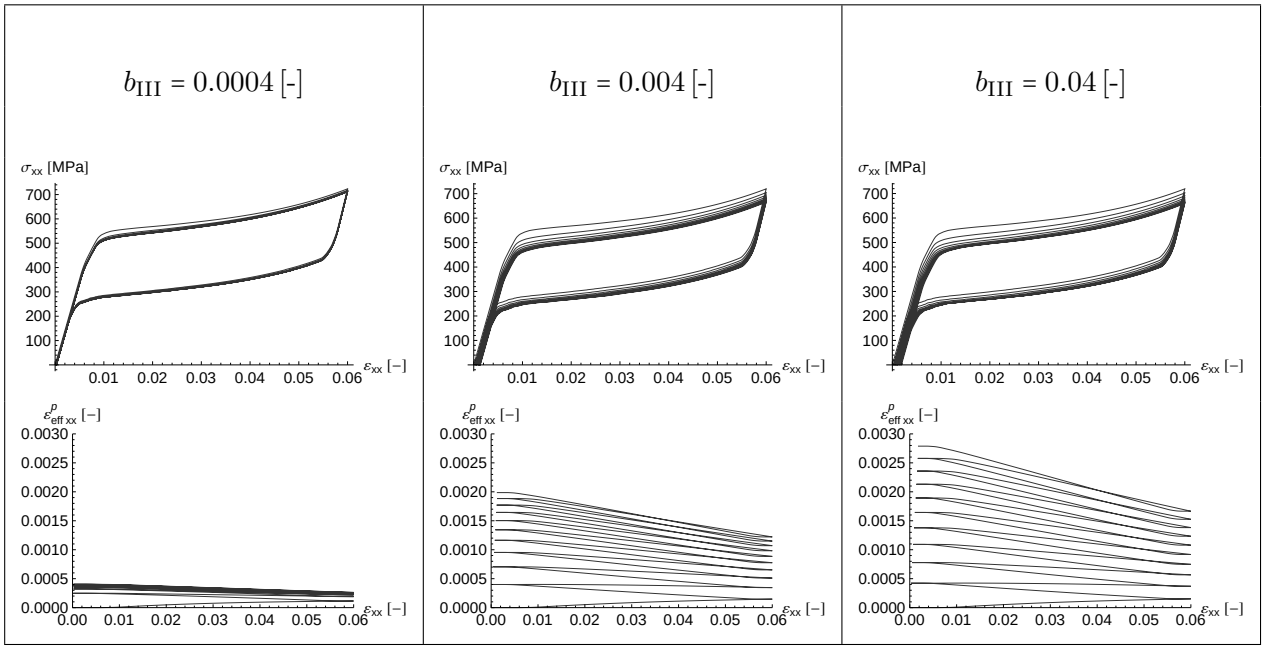

Figure 10.17: Variation of b_{III} with fixed values for Y_0, b_{I} and b_{II}, see Table 10.1. Central result equals Figures 10.5 and 10.6.

Furthermore, the new combined Voigt/Reuß energy allowed an investigation of the material behavior in different grains in which different stresses may be present for identical strains. This is also a more realistic modeling as compared to our previous works.

In future works we will extend our model from the material point level to a finite element code. Additionally, we will reduce the phenomenological approaches for the material parameters and take structural fatigue in a more complete way into account.

11 Conclusions

Variational material models require the specification of the material processes in energetic quantities, e.g. in terms of the Helmholtz free energy and the dissipation functional, which was discussed in Chapter 1. On the one hand, these energy-based formulations allow for a fairly simplified inclusion of complex constraints into a material model which is a remarkable advantage from a technical point of view. On the other hand, a sufficiently accurate formulation of the microstructural state and its evolution in the rather abstract energy space may seem less intuitive as compared to a formulation in the stress space, for instance. Furthermore, the definition of the dissipative material parameters which enter the associated indicator functions is (much) more challenging than in terms of stress measures. It has been shown in this thesis that for shape memory alloys both problems mentioned can be solved and furthermore that a universal applicability can be expected from energy-based material models.

Evaluation of the original model in a finite element context showed that the key characteristics of shape memory alloys could already be simulated well: examples are on the one hand the hysteresis and stress plateaus in the isothermal setting (see Chapter 2); on the other hand, the complex thermo-mechanically coupled behavior which can also lead to multiple transformation fronts was a natural result (see Chapters 3 and 4). However, an application of the original material model in an industrial context demanded an improvement in terms of the fundamental formulation: the numerical evaluation of the model in a finite element routine, as presented in Chapter 2, revealed that it was far too slow and consumed to much computational effort. This drawback became even more evident in a thermo-mechanically coupled setting (Chapters 3 and 4): the evaluation of the material behavior in a huge number of discretizations of the orientation distribution function, which was necessary to obtain reproducible results, was identified as the bottleneck in the numerical simulations. Thus, the material model was reinvented in a condensed form: the approach for the static evaluation of a huge number of discretizations of the orientation distribution function was completely replaced by a dynamically evolving orientation distribution function. To this end, it was parameterized by the Euler angles in Chapter 5 which served as additional internal variables. The necessary additional evolution equations could also be derived by variational techniques which resulted in a material model with a comparable information density as the original one at the mesoscopic level but at highly increased numerical efficiency. This opened the field for further model analysis and an application to boundary value problems of industrial interest.

The principle of maximum dissipation was applied for the non-isothermal setting in all previous works. However, this technique required a slightly cumbersome treatment as presented in Chapters 3 and 4. The application of the principle of the minimum dissipation potential, in turn, promised to be more intuitive. Unfortunately, it was solely formulated for isothermal problems. To overcome this drawback, the principle of the minimum of the dissipation potential was analyzed in its general form in Chapter 6 which revealed that it can also be applied to non-isothermal processes: only a small reformulation was necessary which generalized this modeling technique to include temperature effects and also to derive a generalized heat conduction equation. This extended modeling approach was employed to the condensed material model in Chapter 7 which demonstrated two characteristics: first, the principle of the minimum of the dissipation potential for non-isothermal processes is even valid for complex materials (to which shape memory alloys belong). Second, the condensed material model including the dynamically evolving orientation distribution function is also valid for non-isothermal conditions.

Although the material model performed qualitatively well for different physical boundary conditions

(isothermal and non-isothermal, Chapters 5 and 7), a link between the theoretical model derivation, in which dissipation plays an important role, to experiments, in which dissipation is measured directly, was still missing. In other words, the model calibration was less intuitive and less convincing than it was expected: the dissipation parameter which indicates whether phase transformation takes place or not turned out to be a real energetic quantity in contrast to the example of perfect plasticity presented in Chapter 1: here, the dissipation parameter could be identified as the deviator-type norm of the yield stresses. This, in contrast, was not possible for shape memory alloys yet. In order to find this missing link, the condensed material model was analyzed further in Chapter 8. The yield function and the driving forces could be simplified for a purely temperature-induced phase transformation which allowed for a closed theoretical formula for the dissipation parameter. DSC experiments were used to quantify the dissipation for a purely temperature-driven phase transformation which could directly be related to the formula for the dissipation parameter. Subsequently performed finite element simulations for different specimens at various ambient temperatures proved that the dissipation parameter and consequently the variational material modeling approach shows a rather universal applicability: comparison of the finite element results to experimental observations showed that the dissipation parameter, which was calculated by means of DSC measurements, was also valid for purely mechanically induced phase transformations. This result constituted a drastic improvement of the material model, because a calibration could now be performed without any parameter fitting. Furthermore, this research showed for the first time that modeling based on variational concepts owns a rather universal character which is very promising for future research in various directions.

A calculation of the dissipation parameter based on stress/strain curves, which should be possible in general, was also appreciated since it further improved the applicability of the model. This task was investigated and solved in Chapter 9: after introducing volume fractions for only the twinned martensitic variants in each Cartesian direction, which improved simultaneously the numerical performance of the model, simple formulas for the dissipation parameter and also for the caloric energy for a specific ambient temperature could be derived. The numerical values for both material parameters agreed well with the values obtained from the DSC experiments in Chapter 8. This completed the model in terms of applicability: complex thermo-mechanically coupled boundary value problems could be solved in a reasonable amount of computation time. However, an important characteristic of shape memory alloys was not considered yet by all models discussed: functional fatigue which becomes visible in the stress/strain diagram in terms of a decrease of particularly the upper plateau stress for cyclic loading. This material behavior plays a key role in the simulation-based lifetime prediction of construction parts. Therefore, a fist inclusion of this aspect into the model was presented in Chapter 10. Although this model equipment was a rather brute-force approach, it still demonstrated that the model is able to display the aspect of functional fatigue.

In future research, the aspect of functional fatigue has to be investigated further and more "physics-driven" approaches have to be developed. For instance, by considering reversible and irreversible parts of the volume fractions in combination with a modified assumption for the dissipation functional, an even more convincing inclusion of functional fatigue into the material model is very likely to be expected. In turn, cyclic DSC measurements can be used to reveal the interrelation between the measured (evolving) dissipation (rate) and the novel dissipation parameter(s) in the modified material model. Due to the smooth derivation for the dissipation parameter for the single cycle case in Chapter 8, an adapted and analogous derivation seems to be possible also for the high cycle behavior.

The characteristic of an universal applicability of variational material models also influences the modeling of other materials than shape memory alloys. For instance, damage models can be derived also

purely in the energy space which might disclose possibilities to solve the problem of localization and (consequently) dependence on the finite element mesh without the need for complex regularization schemes. Even for approaches which are less devoted to the modeling of materials but rather to the optimization of topologies under complex constraints variational techniques can successfully be applied. First examples are given in [100] and [101].

References

[1] Feap – a finite element analysis program. *http.//www.ce.berkeley.edu/ rtl/*.

[2] R Abeyaratne and SJ Kim. Cyclic effects in shape-memory alloys: a one-dimensional continuum model. *International journal of solids and structures*, 34(25):3273–3289, 1997.

[3] R Abeyaratne, SJ Kim, and JK Knowles. A one-dimensional continuum model for shape-memory alloys. *International Journal of Solids and Structures*, 31(16):2229–2249, 1994.

[4] F Auricchio. A robust integration-algorithm for a finite-strain shape-memory-alloy superelastic model. *International Journal of plasticity*, 17(7):971–990, 2001.

[5] F Auricchio, A Mielke, and U Stefanelli. A rate-independent model for the isothermal quasi-static evolution of shape-memory materials. *Mathematical Models and Methods in Applied Sciences*, 18(01):125–164, 2008.

[6] F Auricchio and L Petrini. A three-dimensional model describing stress-temperature induced solid phase transformations: solution algorithm and boundary value problems. *International Journal for Numerical Methods in Engineering*, 61(6):807–836, 2004.

[7] F Auricchio, A Reali, and U Stefanelli. A three-dimensional model describing stress-induced solid phase transformation with permanent inelasticity. *International Journal of Plasticity*, 23(2):207–226, 2007.

[8] F Auricchio and RL Taylor. Shape-memory alloys: modelling and numerical simulations of the finite-strain superelastic behavior. *Computer Methods in Applied Mechanics and Engineering*, 143(1):175–194, 1997.

[9] CD Bailey. The unifying laws of classical mechanics. *Foundations of Physics*, 32(1):159–176, 2002.

[10] JM Ball and RD James. Fine phase mixtures as minimizers of energy. In *Analysis and Continuum Mechanics*, pages 647–686. Springer, 1989.

[11] T Bartel and K Hackl. A micromechanical model for single-crystal shape-memory-alloys. *PAMM*, 4(1):298–299, 2004.

[12] T Bartel and K Hackl. A micromechanical model for martensitic phase-transformations in shape-memory alloys based on energy-relaxation. *ZAMM-Journal of Applied Mathematics and Mechanics/Zeitschrift für Angewandte Mathematik und Mechanik*, 89(10):792–809, 2009.

[13] T Bartel, A Menzel, and B Svendsen. Thermodynamic and relaxation-based modeling of the interaction between martensitic phase transformations and plasticity. *Journal of the Mechanics and Physics of Solids*, 59(5):1004–1019, 2011.

[14] RJ Baumbick. Shape memory alloy actuator, November 28 2000. US Patent 6,151,897.

[15] F Baumgart, G Bensmann, J Haasters, J Hartwig, J Jorde, M Muller, and KF Schlegel. Method for implanting and subsequently removing mechanical connecting elements from living tissue, October 16 1979. US Patent 4,170,990.

[16] R Becker and S Panchanadeeswaran. Crystal rotations represented as rodrigues vectors. *Textures and Microstructures*, 10(3):167–194, 1989.

[17] A Bedford. *Hamilton's principle in continuum mechanics*, volume 139. Pitman Advanced Publishing Program, 1985.

[18] V Berdichevsky. *Variational Principles of Continuum Mechanics: I. Fundamentals*. Springer Science & Business Media, 2009.

[19] K Bhattacharya. *Microstructure of martensite: why it forms and how it gives rise to the shape-memory effect*, volume 2. Oxford University Press, 2003.

[20] Z Bo and DC Lagoudas. Thermomechanical modeling of polycrystalline smas under cyclic loading, part iii: Evolution of plastic strains and two-way shape memory effect. *International Journal of Engineering Science*, 37(9):1175–1203, 1999.

[21] T Böhlke, G Risy, and A Bertram. Finite element simulation of metal forming operations with texture based material models. *Modelling and Simulation in Materials Science and Engineering*, 14(3):365, 2006.

[22] C Bouvet, S Calloch, and C Lexcellent. A phenomenological model for pseudoelasticity of shape memory alloys under multiaxial proportional and nonproportional loadings. *European Journal of Mechanics-A/Solids*, 23(1):37–61, 2004.

[23] JG Boyd and DC Lagoudas. A thermodynamical constitutive model for shape memory materials. part i. the monolithic shape memory alloy. *International Journal of Plasticity*, 12(6):805–842, 1996.

[24] PW Bridgman. *The nature of physical theory*. Dover Publications New York, 1936.

[25] LC Brinson. One-dimensional constitutive behavior of shape memory alloys: thermomechanical derivation with non-constant material functions and redefined martensite internal variable. *Journal of intelligent material systems and structures*, 4(2):229–242, 1993.

[26] G Buratti, Y Huo, and I Müller. Eshelby tensor as a tensor of free enthalpy. In *The Rational Spirit in Modern Continuum Mechanics*, pages 101–112. Springer, 2004.

[27] J Burow. *Herstellung, Eigenschaften und Mikrostruktur von ultrafeinkörnigen NiTi-Formgedächtnislegierungen*. urn:nbn:de:hbz:294-29048, 2010.

[28] D Capecchi and G Ruta. A historical perspective of menabrea's theorem in elasticity. *Meccanica*, 45(2):199–212, 2010.

[29] S Carnot. *Reflections on the motive power of fire: And other papers on the second law of thermodynamics*. Courier Corporation, 2012.

[30] C Carstensen, K Hackl, and A Mielke. Non–convex potentials and microstructures in finite–strain plasticity. *Proceedings of the Royal Society of London. Series A: Mathematical, Physical and Engineering Sciences*, 458(2018):299–317, 2002.

[31] A Castigliano. Nuova teoria intorno all'equilibrio dei sistemi elastici. *Atti R. Accad. delle Sci. di Torino*, 11(1875):132, 1875.

[32] R Clausius. Über die bewegende kraft der wärme und die gesetze, welche sich daraus für die wärmelehre selbst ableiten lassen. *Annalen der Physik*, 155(3):368–397, 1850.

[33] BD Coleman. Thermodynamics of materials with memory. *Archive for Rational Mechanics and Analysis*, 17(1):1–46, 1964.

[34] BD Coleman. Memories of clifford truesdell. In *The Rational Spirit in Modern Continuum Mechanics*, pages 1–13. Springer, 2004.

[35] BD Coleman and ME Gurtin. Thermodynamics with internal state variables. *The Journal of Chemical Physics*, 47(2):597–613, 1967.

[36] BD Coleman and W Noll. The thermodynamics of elastic materials with heat conduction and viscosity. *Archive for Rational Mechanics and Analysis*, 13(1):167–178, 1963.

[37] B Dacorogna. *Direct methods in the calculus of variations*, volume 78. Springer Science & Business Media, 2007.

[38] EH Dill. Simple materials with fading memory. *Academic, New York*, 1975.

[39] B Dimitrijevic and K Hackl. A method for gradient enhancement of continuum damage models. *Tech. Mech*, 28(1):43–52, 2008.

[40] B Dimitrijevic and K Hackl. A regularization framework for damage–plasticity models via gradient enhancement of the free energy. *International Journal for Numerical Methods in Biomedical Engineering*, 27(8):1199–1210, 2011.

[41] M Dolce, D Cardone, and R Marnetto. Implementation and testing of passive control devices based on shape memory alloys. *Earthquake engineering & structural dynamics*, 29(7):945–968, 2000.

[42] PMM Duhem. *The aim and structure of physical theory*, volume 13. Princeton University Press, 1991.

[43] C Eckart. The thermodynamics of irreversible processes. iii. relativistic theory of the simple fluid. *Physical review*, 58(10):919, 1940.

[44] DGB Edelen. On the existence of symmetry relations and dissipation potentials. *Archive for Rational Mechanics and Analysis*, 51(3):218–227, 1973.

[45] Gg Eggeler, E Hornbogen, A Yawny, A Heckmann, and MFX Wagner. Structural and functional fatigue of niti shape memory alloys. *Materials Science and Engineering: A*, 378(1):24–33, 2004.

[46] LD Elsgolc. *Calculus of variations*. Courier Corporation, 2012.

[47] F Falk. Model free energy, mechanics, and thermodynamics of shape memory alloys. *Acta Metallurgica*, 28(12):1773–1780, 1980.

[48] J Frenzel, EP George, A Dlouhy, C Somsen, MFX Wagner, and G Eggeler. Influence of ni on martensitic phase transformations in niti shape memory alloys. *Acta Materialia*, 58(9):3444–3458, 2010.

[49] TW Friedland. Surgical fastening clip formed of a shape memory alloy, a method of making such a clip and a method of using such a clip, December 15 1992. US Patent 5,171,252.

[50] S Fu, Y Huo, and I Müller. Thermodynamics of pseudoelasticity—an analytical approach. *Acta mechanica*, 99(1-4):1–19, 1993.

[51] K Gall and HJ Maier. Cyclic deformation mechanisms in precipitated niti shape memory alloys. *Acta Materialia*, 50(18):4643–4657, 2002.

[52] K Gall, H Sehitoglu, YI Chumlyakov, and IV Kireeva. Tension–compression asymmetry of the stress–strain response in aged single crystal and polycrystalline niti. *Acta Materialia*, 47(4):1203–1217, 1999.

[53] P Germain, QS Nguyen, and P Suquet. Continuum thermodynamics. *Journal of Applied Mechanics*, 50(4b):1010–1020, 1983.

[54] JA Giacomel. Shape memory alloy actuator, October 6 1998. US Patent 5,816,306.

[55] JW Gibbs. *A method of geometrical representation of the thermodynamic properties of substances by means of surfaces*. Connecticut Academy of Arts and Sciences, 1873.

[56] M Goodarzi and K Hackl. A model for martensitic microstructure, its geometry and interface effects. *PAMM*, 12(1):345–346, 2012.

[57] S Govindjee, K Hackl, and R Heinen. An upper bound to the free energy of mixing by twin-compatible lamination for n-variant martensitic phase transformations. *Continuum Mechanics and Thermodynamics*, 18(7-8):443–453, 2007.

[58] S Govindjee and GJ Hall. A computational model for shape memory alloys. *International Journal of Solids and Structures*, 37(5):735–760, 2000.

[59] S Govindjee and EP Kasper. Computational aspects of one-dimensional shape memory alloy modeling with phase diagrams. *Computer Methods in Applied Mechanics and Engineering*, 171(3):309–326, 1999.

[60] S Govindjee and C Miehe. A multi-variant martensitic phase transformation model: formulation and numerical implementation. *Computer Methods in Applied Mechanics and Engineering*, 191(3):215–238, 2001.

[61] S Govindjee, A Mielke, and GJ Hall. The free energy of mixing for n-variant martensitic phase transformations using quasi-convex analysis. *Journal of the Mechanics and Physics of Solids*, 51(4):1–26, 2003.

[62] C Grabe and OT Bruhns. On the viscous and strain rate dependent behavior of polycrystalline niti. *International Journal of Solids and Structures*, 45(7):1876–1895, 2008.

[63] AE Green and PM Naghdi. A unified procedure for construction of theories of deformable media. ii. generalized continua. In *Proceedings of the Royal Society of London A: Mathematical, Physical and Engineering Sciences*, volume 448, pages 357–377. The Royal Society, 1995.

[64] ME Gurtin. The linear theory of elasticity. In *Linear Theories of Elasticity and Thermoelasticity*, pages 1–295. Springer, 1973.

[65] K Hackl. Generalized standard media and variational principles in classical and finite strain elastoplasticity. *Journal of the Mechanics and Physics of Solids*, 45(5):667–688, 1997.

[66] K Hackl. On the representation of anisotropic elastic materials by symmetric irreducible tensors. *Continuum Mechanics and Thermodynamics*, 11(6):353–369, 1999.

[67] K Hackl and FD Fischer. On the relation between the principle of maximum dissipation and inelastic evolution given by dissipation potentials. *Proceedings of the Royal Society A: Mathematical, Physical and Engineering Science*, 464(2089):117–132, 2008.

[68] K Hackl, FD Fischer, and J Svoboda. Addendum: A study on the principle of maximum dissipation for coupled and non-coupled non-isothermal processes in materials. *Proceedings: Mathematical, Physical and Engineering Sciences*, pages 2422–2426, 2011.

[69] K Hackl, FD Fischer, and J Svoboda. A study on the principle of maximum dissipation for coupled and non-coupled non-isothermal processes in materials. *Proceedings: Mathematical, Physical and Engineering Sciences*, pages 1186–1196, 2011.

[70] K Hackl and R Heinen. A micromechanical model for pretextured polycrystalline shape-memory alloys including elastic anisotropy. *Continuum Mechanics and Thermodynamics*, 19(8):499–510, 2008.

[71] K Hackl, M Schmidt-Baldassari, and W Zhang. A micromechanical model for polycrystalline shape-memory alloys. *Materials Science and Engineering: A*, 378(1):503–506, 2004.

[72] B Halphen and QS Nguyen. Sur les matériaux standard généralisés. *Journal de mécanique*, 14:39–63, 1975.

[73] WR Hamilton. On a general method in dynamics; by which the study of the motions of all free systems of attracting or repelling points is reduced to the search and differentiation of one central relation, or characteristic function. *Philosophical transactions of the Royal Society of London*, 124:247–308, 1834.

[74] WR Hamilton. Second essay on a general method in dynamics. *Philosophical Transactions of the Royal Society of London*, 125:95–144, 1835.

[75] DJ Hartl, G Chatzigeorgiou, and DC Lagoudas. Three-dimensional modeling and numerical analysis of rate-dependent irrecoverable deformation in shape memory alloys. *International Journal of Plasticity*, 26(10):1485–1507, 2010.

[76] W Heidug and FK Lehner. Thermodynamics of coherent phase transformations in nonhydrostatically stressed solids. *pure and applied geophysics*, 123(1):91–98, 1985.

[77] R Heinen and K Hackl. On the calculation of energy-minimizing phase fractions in shape memory alloys. *Computer methods in applied mechanics and engineering*, 196(21):2401–2412, 2007.

[78] D Helm. *Formgedächtnislegierungen: Experimentelle Untersuchung, phänomenologische Modellierung und numerische Simulation der thermomechanischen Materialeigenschaften*. PhD thesis, Zugl.: Kassel, Univ., Diss., 2001, 2001.

[79] D Helm and P Haupt. Shape memory behaviour: modelling within continuum thermomechanics. *International Journal of Solids and Structures*, 40(4):827–849, 2003.

[80] T Hesse, M Ghorashi, and DJ Inman. Shape memory alloy in tension and compression and its application as clamping-force actuator in a bolted joint: Part 1 – experimentation. *Journal of intelligent material systems and structures*, 15(8):577–587, 2004.

[81] GA Holzapfel. Nonlinear solid mechanics. 2000. *John Wiley&Sons., Ltd.*

[82] H Horikawa, S Ichinose, K Morii, S Miyazaki, and K Otsuka. Orientation dependence of $\beta 1 \rightarrow \beta 1'$ stress-induced martensitic transformation in a cu-ai-ni alloy. *Metallurgical Transactions A*, 19(4):915–923, 1988.

[83] MF Horstemeyer and DJ Bammann. Historical review of internal state variable theory for inelasticity. *International Journal of Plasticity*, 26(9):1310–1334, 2010.

[84] M Huang, X Gao, and LC Brinson. A multivariant micromechanical model for smas part 2. polycrystal model. *International Journal of Plasticity*, 16(10):1371–1390, 2000.

[85] W Huang. On the selection of shape memory alloys for actuators. *Materials & design*, 23(1):11–19, 2002.

[86] X Huang, GJ Ackland, and KM Rabe. Crystal structures and shape-memory behaviour of niti. *Nature materials*, 2(5):307–311, 2003.

[87] Y Huo and I Müller. Nonequilibrium thermodynamics of pseudoelasticity. *Continuum Mechanics and Thermodynamics*, 5(3):163–204, 1993.

[88] Y Huo, I Müller, and S Seelecke. Quasiplasticity and pseudoelasticity in shape memory alloys. In *Phase transitions and hysteresis*, pages 87–146. Springer, 1994.

[89] A Ibarra, J San Juan, EH Bocanegra, and ML Nó. Evolution of microstructure and thermomechanical properties during superelastic compression cycling in cu–al–ni single crystals. *Acta materialia*, 55(14):4789–4798, 2007.

[90] JP Joule. Philosophical magazine 23, 263. *Scientific Papers*, 123, 1843.

[91] P Junker. *Simulation of shape memory alloys – material modeling using the principle of maximum dissipation*. PhD thesis, Ruhr-Universität Bochum, urn:nbn:de:hbz:294-33862, 2011.

[92] P Junker. An accurate, fast and stable material model for shape memory alloys. *Smart Materials and Structures*, 23(11):115010, 2014.

[93] P Junker. A novel approach to representative orientation distribution functions for modeling and simulation of polycrystalline shape memory alloys. *International Journal for Numerical Methods in Engineering*, 98(11):799–818, 2014.

[94] P Junker and K Hackl. Numerical simulations of poly-crystalline shape-memory alloys based on a micromechanical model. *PAMM*, 9(1):339–340, 2009.

[95] P Junker and K Hackl. On the numerical simulation of material inhomogeneities due to martensitic phase transformations in poly-crystals. *Proceedings of ESOMAT*, pages 1–9, 2009.

[96] P Junker and K Hackl. About the influence of heat conductivity on the mechanical behavior of poly-crystalline shape memory alloys. *The International Journal of Structural Changes in Solids*, 3(1):49–62, 2011.

[97] P Junker and K Hackl. Finite element simulations of poly-crystalline shape memory alloys based on a micromechanical model. *Computational Mechanics*, 47(5):505–517, 2011.

[98] P Junker and K Hackl. A condensed variational model for thermo-mechanically coupled phase transformations in polycrystalline shape memory alloys. *Journal of the Mechanical Behavior of Materials*, 22(3-4):111–118, 2013.

[99] P Junker and K Hackl. A thermo-mechanically coupled field model for shape memory alloys. *Continuum Mechanics and Thermodynamics*, pages 1–19, 2014.

[100] P Junker and K Hackl. A variational growth approach to topology optimization. *Structural and Multidisciplinary Optimization*, pages 1–12, 2015.

[101] P Junker and K Hackl. A discontinuous phase field approach to variational growth-based topology optimization. *Structural and Multidisciplinary Optimization, accepted for publication.*

[102] P Junker, S Jaeger, O Kastner, G Eggeler, and K Hackl. Variational prediction of the mechanical behavior of shape memory alloys based on thermal experiments. *Journal of the Mechanics and Physics of Solids*, 80:86–102, 2015.

[103] P Junker, Jerzy M, and K Hackl. The principle of the minimum of the dissipation potential for non-isothermal processes. *Continuum Mechanics and Thermodynamics*, 26(3):259–268, 2014.

[104] O Kastner. Molecular-dynamics of a 2d model of the shape memory effect. *Continuum Mechanics and Thermodynamics*, 18(1-2):63–81, 2006.

[105] O Kastner. *First principles modelling of shape memory alloys: molecular dynamics simulations*, volume 163. Springer Science & Business Media, 2012.

[106] O Kastner, G Eggeler, W Weiss, and GJ Ackland. Molecular dynamics simulation study of microstructure evolution during cyclic martensitic transformations. *Journal of the Mechanics and Physics of Solids*, 59(9):1888–1908, 2011.

[107] O Kastner, F Richter, and G Eggeler. Multivariant formulation of the thermomechanically coupled müller-achenbach-seelecke-model for shape memory alloys. In *ASME 2009 Conference on Smart Materials, Adaptive Structures and Intelligent Systems*, pages 45–52. American Society of Mechanical Engineers, 2009.

[108] J Kestin and JR Rice. Paradoxes in the application of thermodynamics to strained solids. *A Critical Review of Thermodynamics, ed by EB Stuart (Mono Book Corp., Baltimore, 1970)*, pages 275–280, 1970.

[109] J Khalil-Allafi, A Dlouhy, and G Eggeler. Ni 4 ti 3-precipitation during aging of niti shape memory alloys and its influence on martensitic phase transformations. *Acta Materialia*, 50(17):4255–4274, 2002.

[110] RV Kohn. The relaxation of a double-well energy. *Continuum Mechanics and Thermodynamics*, 3(3):193–236, 1991.

[111] M Kružík and F Otto. A phenomenological model for hysteresis in polycrystalline shape memory alloys. *ZAMM-Journal of Applied Mathematics and Mechanics/Zeitschrift für Angewandte Mathematik und Mechanik*, 84(12):835–842, 2004.

[112] DC Lagoudas. *Shape memory alloys: modeling and engineering applications*. Springer, 2008.

[113] DC Lagoudas, Z Bo, and A Bhattacharyya. A thermodynamic constitutive model for gradual phase transformation of sma materials. *Mathematics And Control In Smart Structures-Smart Structures And Materials, ed. by VV Varadan, J. Chandra*, 2715:482–493, 1996.

[114] DC Lagoudas and PB Entchev. Modeling of transformation-induced plasticity and its effect on the behavior of porous shape memory alloys. part i: constitutive model for fully dense smas. *Mechanics of Materials*, 36(9):865–892, 2004.

[115] DC Lagoudas, D Hartl, Y Chemisky, L Machado, and P Popov. Constitutive model for the numerical analysis of phase transformation in polycrystalline shape memory alloys. *International Journal of Plasticity*, 32:155–183, 2012.

[116] KC Le. *Introduction to Micromechanics*. Nova Science, 2010.

[117] KC Le and P Junker. A thermodynamically consistent model of static and dynamic recrystallization. *Archive of Applied Mechanics*, pages 1–11, 2014.

[118] RS Lee. Nitinol ring marmon clamp, April 2 2013. US Patent 8,408,136.

[119] C Lexcellent and G Bourbon. Thermodynamical model of cyclic behaviour of ti-ni and cu-zn-al shape memory alloys under isothermal undulated tensile tests. *Mechanics of Materials*, 24(1):59–73, 1996.

[120] C Lexcellent, A Vivet, C Bouvet, S Calloch, and P Blanc. Experimental and numerical determinations of the initial surface of phase transformation under biaxial loading in some polycrystalline shape-memory alloys. *Journal of the Mechanics and Physics of Solids*, 50(12):2717–2735, 2002.

[121] C Liang and CA Rogers. One-dimensional thermomechanical constitutive relations for shape memory materials. *Journal of intelligent material systems and structures*, 1(2):207–234, 1990.

[122] IS Liu. Method of lagrange multipliers for exploitation of the entropy principle. *Archive for Rational Mechanics and Analysis*, 46(2):131–148, 1972.

[123] J Lubliner. On the thermodynamic foundations of non-linear solid mechanics. *International Journal of Non-Linear Mechanics*, 7(3):237–254, 1972.

[124] J Lubliner. On the structure of the rate equations of materials with internal variables. *Acta Mechanica*, 17(1-2):109–119, 1973.

[125] J Lubliner. A maximum-dissipation principle in generalized plasticity. *Acta Mechanica*, 52(3-4):225–237, 1984.

[126] G Maier. Some theorems for plastic strain rates and plastic strains(minimum theorems for plastic strain rates and plastic strains governed by holonomic elastoplastic theory utilizing quadratic functions). *Journal de Mécanique*, 8:5–19, 1969.

[127] JB Martin and Alan RS Ponter. *A note on a work inequality in linear viscoelasticity*. Division of Engineering, Brown University, 1965.

[128] GA Maugin. *The thermomechanics of plasticity and fracture*, volume 7. Cambridge University Press, 1992.

[129] GA Maugin. The saga of internal variables of state in continuum thermo-mechanics (1893-2013). *Mechanics Research Communications*, 2015.

[130] GA Maugin and AV Metrikine. Mechanics of generalized continua. *Advances in mechanics and mathematics*, 21, 2010.

[131] JC Maxwell. On the dynamical evidence of the molecular constitution of bodies. *Nature*, 11:357–359, 1875.

[132] MM Mehrabadi and SC Cowin. Eigentensors of linear anisotropic elastic materials. *The Quarterly Journal of Mechanics and Applied Mathematics*, 43(1):15–41, 1990.

[133] LF Menabrea. *Étude de statique physique: Principe général pour déterminer les pressions et les tensions dans un système élastique*. 1868.

[134] M Mernoe. Shape memory alloy actuator, 2003.

[135] C Miehe, Jacques Schotte, and M Lambrecht. Homogenization of inelastic solid materials at finite strains based on incremental minimization principles. application to the texture analysis of polycrystals. *Journal of the Mechanics and Physics of Solids*, 50(10):2123–2167, 2002.

[136] A Mielke. Energetic formulation of multiplicative elasto-plasticity using dissipation distances. *Continuum Mechanics and Thermodynamics*, 15(4):351–382, 2003.

[137] A Mielke and U Stefanelli. A discrete variational principle for rate-independent evolution. *Advances in Calculus of Variations*, 1(4):399–431, 2008.

[138] A Mielke, F Theil, and VI Levitas. A variational formulation of rate-independent phase transformations using an extremum principle. *Archive for Rational Mechanics and Analysis*, 162(2):137–177, 2002.

[139] S Miyazaki, T Imai, Y Igo, and K Otsuka. Effect of cyclic deformation on the pseudoelasticity characteristics of Ti-Ni alloys. *Metallurgical Transactions A*, 17(1):115–120, 1986.

[140] J Mohd Jani, M Leary, A Subic, and MA Gibson. A review of shape memory alloy research, applications and opportunities. *Materials & Design*, 56:1078–1113, 2014.

[141] Ch Müller and OT Bruhns. Modeling of polycrystalline shape memory alloys at finite strains based upon the logarithmic stress rate. In *Journal de Physique IV (Proceedings)*, volume 112, pages 187–190. EDP sciences, 2003.

[142] I Müller. A model for a body with shape-memory. *Archive for Rational Mechanics and Analysis*, 70(1):61–77, 1979.

[143] I Müller. *Eshelby tensor and phase equilibrium*. 1999.

[144] I Müller and S Seelecke. Thermodynamic aspects of shape memory alloys. *Mathematical and Computer Modelling*, 34(12):1307–1355, 2001.

[145] I Müller and W Weiss. Entropy and energy–interaction of mechanics and mathematics, 2005.

[146] L Onsager. Reciprocal relations in irreversible processes. i. *Physical Review*, 37(4):405–426, 1931.

[147] L Onsager. Reciprocal relations in irreversible processes. ii. *Physical Review*, 38(12):2265, 1931.

[148] L Onsager. Theories and problems of liquid diffusion. *Annals of the New York Academy of Sciences*, 46(5):241–265, 1945.

[149] M Ortiz and EA Repetto. Nonconvex energy minimization and dislocation structures in ductile single crystals. *Journal of the Mechanics and Physics of Solids*, 47(2):397–462, 1999.

[150] M Ortiz and L Stainier. The variational formulation of viscoplastic constitutive updates. *Computer methods in applied mechanics and engineering*, 171(3):419–444, 1999.

[151] K Otsuka and X Ren. Physical metallurgy of ti–ni-based shape memory alloys. *Progress in Materials Science*, 50(5):511–678, 2005.

[152] K Otsuka and CM Wayman. *Shape memory materials*. Cambridge University Press, 1999.

[153] H Pan, P Thamburaja, and FS Chau. Multi-axial behavior of shape-memory alloys undergoing martensitic reorientation and detwinning. *International Journal of Plasticity*, 23(4):711–732, 2007.

[154] H Petryk. Incremental energy minimization in dissipative solids. *Comptes Rendus Mecanique*, 331(7):469–474, 2003.

[155] H Petryk and S Stupkiewicz. Interfacial energy and dissipation in martensitic phase transformations. part i: Theory. *Journal of the Mechanics and Physics of Solids*, 58(3):390–408, 2010.

[156] H Petryk, S Stupkiewicz, and G Maciejewski. Interfacial energy and dissipation in martensitic phase transformations. part ii: Size effects in pseudoelasticity. *Journal of the Mechanics and Physics of Solids*, 58(3):373–389, 2010.

[157] H Pulte. Das prinzip der kleinsten wirkung und die kraftkonzeptionen der rationalen mechanik – eine untersuchung zur grundlegungsproblematik bei leonhard euler, pierre louis moreau de maupertuis und joseph louis lagrange. 1989.

[158] B Raniecki and Ch Lexcellent. Thermodynamics of isotropic pseudoelasticity in shape memory alloys. *European Journal of Mechanics-A/Solids*, 17(2):185–205, 1998.

[159] S Reese and D Christ. Finite deformation pseudo-elasticity of shape memory alloys–constitutive modelling and finite element implementation. *International Journal of Plasticity*, 24(3):455–482, 2008.

[160] JR Rice. Inelastic constitutive relations for solids: an internal-variable theory and its application to metal plasticity. *Journal of the Mechanics and Physics of Solids*, 19(6):433–455, 1971.

[161] L Saint-Sulpice, SA Chirani, and S Calloch. A 3d super-elastic model for shape memory alloys taking into account progressive strain under cyclic loadings. *Mechanics of materials*, 41(1):12–26, 2009.

[162] A Schäfer and MFX Wagner. Strain mapping at propagating interfaces in pseudoelastic niti. In *European Symposium on Martensitic Transformations*, page 06031. EDP Sciences, 2009.

[163] P Sedlák, H Seiner, M Landa, V Novák, P Šittner, and Ll Mañosa. Elastic constants of bcc austenite and 2h orthorhombic martensite in cualni shape memory alloy. *Acta Materialia*, 53(13):3643–3661, 2005.

[164] S Seelecke. Modeling the dynamic behavior of shape memory alloys. *International Journal of Non-Linear Mechanics*, 37(8):1363–1374, 2002.

[165] JA Shaw. Simulations of localized thermo-mechanical behavior in a niti shape memory alloy. *International Journal of Plasticity*, 16(5):541–562, 2000.

[166] JA Shaw and S Kyriakides. Thermomechanical aspects of niti. *Journal of the Mechanics and Physics of Solids*, 43(8):1243–1281, 1995.

[167] M Silhavy. *The mechanics and thermodynamics of continuous media*. Springer Science & Business Media, 2013.

[168] JC Simo. A framework for finite strain elastoplasticity based on maximum plastic dissipation and the multiplicative decomposition: Part i. continuum formulation. *Computer methods in applied mechanics and engineering*, 66(2):199–219, 1988.

[169] JC Simo and TJR Hughes. Computational inelasticity. 2008.

[170] JC Simo, JG Kennedy, and S Govindjee. Non-smooth multisurface plasticity and viscoplasticity. loading/unloading conditions and numerical algorithms. *International Journal for Numerical Methods in Engineering*, 26(10):2161–2185, 1988.

[171] JC Simo and Ch Miehe. Associative coupled thermoplasticity at finite strains: formulation, numerical analysis and implementation. *Computer Methods in Applied Mechanics and Engineering*, 98(1):41–104, 1992.

[172] T Simon, A Kröger, C Somsen, A Dlouhy, and G Eggeler. On the multiplication of dislocations during martensitic transformations in niti shape memory alloys. *Acta Materialia*, 58(5):1850–1860, 2010.

[173] AP Stebner and LC Brinson. Explicit finite element implementation of an improved three dimensional constitutive model for shape memory alloys. *Computer Methods in Applied Mechanics and Engineering*, 257:17–35, 2013.

[174] E Stein and G Sagar. Theory and finite element computation of cyclic martensitic phase transformation at finite strain. *International Journal for Numerical Methods in Engineering*, 74(1):1–31, 2008.

[175] M Struwe. *Variational methods*, volume 31999. Springer, 1990.

[176] J Stuelpnagel. On the parametrization of the three-dimensional rotation group. *SIAM review*, 6(4):422–430, 1964.

[177] S Stupkiewicz and H Petryk. Modelling of laminated microstructures in stress-induced martensitic transformations. *Journal of the Mechanics and Physics of Solids*, 50(11):2303–2331, 2002.

[178] S Stupkiewicz and H Petryk. A robust model of pseudoelasticity in shape memory alloys. *International Journal for Numerical Methods in Engineering*, 93(7):747–769, 2013.

[179] L Sun, WM Huang, Z Ding, Y Zhao, CC Wang, H Purnawali, and C Tang. Stimulus-responsive shape memory materials: a review. *Materials & Design*, 33:577–640, 2012.

[180] J Svoboda, FD Fischer, and P Fratzl. Diffusion and creep in multi-component alloys with non-ideal sources and sinks for vacancies. *Acta materialia*, 54(11):3043–3053, 2006.

[181] J Svoboda, FD Fischer, P Fratzl, and A Kroupa. Diffusion in multi-component systems with no or dense sources and sinks for vacancies. *Acta materialia*, 50(6):1369–1381, 2002.

[182] K Tanaka, S Kobayashi, and Y Sato. Thermomechanics of transformation pseudoelasticity and shape memory effect in alloys. *International Journal of Plasticity*, 2(1):59–72, 1986.

[183] K Tanaka, F Nishimura, T Hayashi, H Tobushi, and Ch Lexcellent. Phenomenological analysis on subloops and cyclic behavior in shape memory alloys under mechanical and/or thermal loads. *Mechanics of Materials*, 19(4):281–292, 1995.

[184] GI Taylor. The mechanism of plastic deformation of crystals. part i. theoretical. *Proceedings of the Royal Society of London. Series A, Containing Papers of a Mathematical and Physical Character*, pages 362–387, 1934.

[185] P Thamburaja. Constitutive equations for martensitic reorientation and detwinning in shape-memory alloys. *Journal of the Mechanics and Physics of Solids*, 53(4):825–856, 2005.

[186] W Thomson. Xv.—on the dynamical theory of heat, with numerical results deduced from mr joule's equivalent of a thermal unit, and m. regnault's observations on steam. *Transactions of the Royal Society of Edinburgh*, 20(02):261–288, 1853.

[187] HC Tong and CM Wayman. Characteristic temperatures and other properties of thermoelastic martensites. *Acta Metallurgica*, 22(7):887–896, 1974.

[188] C Truesdell. *Rational thermodynamics*. Springer Science & Business Media, 2012.

[189] C Truesdell and W Noll. *The non-linear field theories of mechanics*. Springer, 2004.

[190] L Truskinovsky. About the "normal growth" approximation in the dynamical theory of phase transitions. *Continuum mechanics and thermodynamics*, 6(3):185–208, 1994.

[191] H von Helmholtz. Ueber die physikalische bedeutung des prinicips der kleinsten wirkung. *Journal für die reine und angewandte Mathematik*, 100:137–166, 1887.

[192] MFX Wagner. *Ein Beitrag zur strukturellen und funktionalen Ermüdung von Drähten und Federn aus NiTi-Formgedächtnislegierungen*. Europ. Univ.-Verlag, 2005.

[193] MFX Wagner, N Nayan, and U Ramamurty. Healing of fatigue damage in niti shape memory alloys. *Journal of Physics D: Applied Physics*, 41(18):185408, 2008.

[194] MFX Wagner and W Windl. Lattice stability, elastic constants and macroscopic moduli of niti martensites from first principles. *Acta Materialia*, 56(20):6232–6245, 2008.

[195] T Waitz, T Antretter, FD Fischer, NK Simha, and HP Karnthaler. Size effects on the martensitic phase transformation of niti nanograins. *Journal of the Mechanics and Physics of Solids*, 55(2):419–444, 2007.

[196] T Waitz, W Pranger, T Antretter, FD Fischer, and HP Karnthaler. Competing accommodation mechanisms of the martensite in nanocrystalline niti shape memory alloys. *Materials Science and Engineering: A*, 481:479–483, 2008.

[197] MS Wechsler, DS Lieberman, and TA Read. On the theory of the formation of martensite. *Trans. AIME*, 197(11):1503–1515, 1953.

[198] Q Yang, L Stainier, and M Ortiz. A variational formulation of the coupled thermo-mechanical boundary-value problem for general dissipative solids. *Journal of the Mechanics and Physics of Solids*, 54(2):401–424, 2006.

[199] H Ziegler. An attempt to generalize onsager's principle, and its significance for rheological problems. *Zeitschrift für angewandte Mathematik und Physik ZAMP*, 9(5-6):748–763, 1958.

[200] H Ziegler. *Some extremum principles in irreversible thermodynamics, with application to continuum mechanics*. Swiss Federal Institute of Technology, 1962.

[201] H Ziegler. *An introduction to thermomechanics*. Elsevier, 2012.

[202] H Ziegler and C Wehrli. The derivation of constitutive relations from the free energy and the dissipation function. *Archive of Applied Mechanics*, 25:183–238, 1987.

Mitteilungen aus dem Institut für Mechanik
RUHR-UNIVERSITÄT BOCHUM
Nr. 171

ISBN 978-3-935892-49-0